technische universität
dortmund

Arbeit zur Erlangung des akademischen Grades eines Doktors der Naturwissenschaften (Dr. rer. nat.)

Stacking Point Source Search for a Neutrino Contribution at 22 Track-Like HESE Positions using Six Years of IceCube Data

Thorben Menne

Dortmund, 2018

Lehrstuhl für Experimentelle Physik V
Fakultät Physik
Technische Universität Dortmund

Erstgutachter:	Prof. Dr. Dr. Wolfgang Rhode
Zweitgutachter:	Prof. Dr. Bernhard Spaan
Abgabedatum:	20.10.2018

Abstract

In this thesis, an approach is presented to probe the locations of track-like high energy starting events (HESE) for an additional clustering of neutrino events within six years of IceCube neutrino data at these positions. Two unbinned Likelihood stacking analyses using both a time-dependent, per-burst and a steady-state neutrino emission scenario are performed. This is done to be sensitive to a collection of weak fluxes, undetectable on their own and to test a rather broad regime of emission scenarios in the light of the unknown, underlying sources types. In both analyses, no significant excess of an additional neutrino contribution was found. However, a slight over-fluctuation of about $1\,\sigma$ in the largest tested time window, with a width of five days, and about $0.7\,\sigma$ in the time-integrated analysis is measured. This mildly indicates a connection to the recent measurement of a correlation between the flaring Blazar TXS 0506+056 and an extremely high energy neutrino starting event, where evidence was found for an additional neutrino emission on timescales of about 110 days, right in between the tested emission scenarios in this thesis.

Kurzfassung

In dieser Arbeit wird die Suche nach einem Neutrinofluss an den Positionen von hochenergetischen, im Detektor startenden Neutrinoereignissen, *High Energy Starting Events* (HESE), in sechs Jahren IceCube Neutrino Daten beschrieben. Es wird ein ungebinnter, gestackter Likelihood-Ansatz benutzt, um nach zusätzlichen Neutrinoereignissen zu suchen, die räumlich korreliert zu den HESE-Ereignissen erzeugt wurden. Da die potentiellen Quellen, aus denen die HESE Ereignisse stammen können unbekannt sind, wird sowohl ein zeitabhängiges, als auch ein stetiges Emissionsszenario getestet. In beiden Analysen konnte kein signifikantes Signal gefunden werden. Allerdings zeigt sowohl die zeitabhängige Messung mit etwa $1\,\sigma$ im größten getesteten Zeitfenster, mit einer Breite von fünf Tagen, als auch die zeitintegrierte Messung mit $0.7\,\sigma$ eine leichte Überfluktuation. Beide Ergebnisse lassen sich damit in den Rahmen der kürzlich entdeckten Korrelation eines extrem hochenergetischen Neutrinos und der erhöhten Aktivität des Blazars TXS 0506+056, bei der eine zusätzliche Neutrinoemission auf einer Zeitskala von etwa 110 Tagen nachgewiesen wurde, einfügen.

Contents

1. Introduction **1**

2. Astroparticle physics **3**
2.1. Astrophysical neutrino production . . . 3
2.2. Possible sources of astrophysical neutrinos . . . 5
2.3. Atmospheric muons and neutrinos . . . 6

3. The IceCube neutrino observatory **9**
3.1. Detection principle . . . 10

4. Datasets **13**
4.1. High energy starting event data . . . 13
4.2. All sky muon neutrino data . . . 20

5. Point source searches with IceCube neutrinos **25**
5.1. Extended unbinned Likelihood . . . 25
5.2. Per event distributions . . . 28
5.3. Time-dependent Likelihood . . . 33
5.4. Time-integrated Likelihood . . . 38
5.5. A priori weight selection . . . 41
5.6. Frequentist methods . . . 46

6. Time-dependent analysis **49**
6.1. Per event distribution modelling . . . 50
6.2. Background estimation and stacking weights . . . 56
6.3. Note on LLH minimization . . . 57
6.4. Trial generation . . . 59
6.5. Performance estimation . . . 66
6.6. Differential performance . . . 69
6.7. Post-trial method . . . 74
6.8. Results . . . 76

7. Time-integrated analysis **79**
7.1. Per event distribution modelling . . . 80
7.2. Stacking and multi-sample weights . . . 84

7.3. Note on LLH minimization . . . 85
7.4. Trial generation . . . 85
7.5. Performance . . . 87
7.6. Results . . . 89

8. Discussion **91**

9. Outlook **99**

A. Further references **103**
A.1. Notes on reproducibility . . . 103
A.2. Acknowledgements . . . 106

B. Supplementary material **107**
B.1. Datasets . . . 107
B.2. Time-dependent analysis . . . 110
B.3. Time-integrated analysis . . . 146
B.4. Discussion . . . 157

Bibliography **161**

List of figures **177**

List of tables **181**

1. Introduction

Since the first proposal in 1960 to use underwater apparatus to detect Cherenkov light from charged particles originating from astrophysical neutrinos, neutrino astronomy has come a long way [Mar60]. In 2013, three years after the IceCube neutrino observatory started operating in its final configuration, the first evidence of a diffuse, astrophysical neutrino flux was found in IceCube data [Aar+13a; Aar+17e]. Although giving the opportunity to probe a broad spectrum of astrophysical and particle physics topics, one of the primary goals of the IceCube detector has been the direct identification of the sources of astrophysical neutrinos ever since [KS12; Gol02]. Despite numerous efforts, including general searches of the whole sky, stacked approaches testing various source catalogues and tests for emission from a extended region like the galactic plane with different event topologies, no significant source of neutrinos has been found so far [AH14; Aar+17a; Aar+13a; Aar+16a; Adr+16b; Aar+16c; Aar+18c; Aar+16d; Abb+09; Aar+14d; Aar+15b]. This changed with the very recent discovery of a blazar flare, measured with the Fermi satellite, coincident with the arrival direction of an extremely high energy neutrino, measured with the IceCube neutrino observatory on September 22nd, 2017 [Kei+18]. In addition to the correlation between these two events, a scan of earlier neutrino data also revealed evidence of a temporally constrained neutrino flux coming from the blazar's position emitted on a 100-day long timescale [Aar+18c].

Despite this detection, the few detected neutrinos coincident with a single source cannot unveil all of the unknown properties of neutrino production mechanisms and the underlying cosmic ray acceleration processes. This justifies the ongoing efforts to further investigate the astrophysical neutrino emission scenarios and identify the fundamental physics at play during the neutrino creation in the source regions. Additionally, it shows that a more comprehensive picture of the internal workings of astrophysical sources can be achieved by the combination of multiple observation channels. Having a collection of observatories that together are able to detect a broad range of astrophysical messengers, including photons in almost every wavelength [Hub+16], charged cosmic rays [BSY14; SW09], the aforementioned neutrinos and most recently even gravitational waves, which are already incorporated in correlation searches [Abb+16; Adr+16a], the way is paved for powerful new analyses [Bra16].

In this thesis, a similar approach is followed. Equivalently to photons and cosmic rays, neutrinos are also measured in a broad energy range and, after having data available

from eight years of operation in its full configuration state, also in great abundance, by the IceCube detector. Instead of testing for correlation with other messenger particles, it is also feasible to try to pinpoint a possible correlation between high energy starting events and a larger set of lower energy neutrino events. The lower energy neutrinos are measured with great abundance but it cannot be safely concluded if a single event is of astrophysical origin or not, due to the large amounts of background events for lower energies. For the aforementioned high energy starting events on the other hand, it can be quite safely concluded that they are of astrophysical origin, for most of them even on a per-event scale. Therefore, if a correlation between higher energy and lower energy events can be identified, it strengthens the case for further efforts in multi-messenger observations at these specific source locations, to identify the underlying sources with better precision.

In this thesis, two analyses for different emission scenarios for a combined, lower energy neutrino clustering at the positions of 22 track-like high energy starting events, measured in six years of IceCube data are presented. It is tested for both a time-dependent emission scenario on short to medium time ranges and a time-independent, steady-state flux scenario. The second chapter gives a short overview of neutrino astroparticle physics and some prominent astrophysical source emission models. In the third chapter, the IceCube detector is described and the detection method explained. The fourth chapter briefly describes the used datasets, consisting of the source data set of track-like high energy starting events and the test data set, made of six years of all-sky muon neutrino track events, that represent the primary channel for neutrino point source searches.

These chapters are held quite short, because of the great abundance of material available dealing in great detail with many aspects of these topics. In this thesis, the focus lies more on the methodical approaches and detailed description of the analysis structure. Therefore, in chapter 5, a detailed derivation of the Likelihood formulas for both analyses is given. In chapters six and seven, both analyses for the time-dependent and the steady state emission scenario are described. These chapters explain in detail how choices for constructing probability density functions or weights used in the Likelihood formulations are made. The aim is to give a good understanding of how such analyses work and enable the reader to reproduce the main aspects of the presented analyses. Chapter eight summarizes the results and presents the main physics results of both analyses. The conclusion and outlook, which puts them into the context of the most recent development of searches for astrophysical neutrino sources can be found in chapter nine and closes this thesis.

2. Astroparticle physics

The universe can not only be observed in visible light but in a variety of different wavelengths and other astrophysical messengers. Typically, three main messenger particles are distinguished, which are photons, cosmic rays and neutrinos [Cir08; Gio09; LM00; Hal16]. Very recently, also gravitational waves are started to be taken into account [Abb+16; Abb+17]. Photon observations range over many decades in wavelength, from radio waves, microwaves, over infrared, visible and ultraviolet light, up to x-rays and the highest gamma-ray energies. Each of these observation windows is used for different purposes and combined to obtain a unified picture of astrophysical processes [WT09; Liu+18; Ada+16; Wer+04; Dal+17; Lal12; Sem99; ODe+10; Aje+17; Tib12; Lau15]

Cosmic rays usually include charged particles as protons, ions or bare nuclei and electrons, as well as uncharged neutrons and are measured using earthbound experiments for the highest energies [Hör16; Yoo+17; All+08; Abr+09]. While charged particles, especially the heavy particles reach up to observed energies in the order of 100 EeV, they usually don't point back to their origin, due to deflection in magnetic fields within the intergalactic or interstellar medium [MGH98]. Photons, on the one hand, are uncharged and can point back to the source regions, but are also attenuated on cosmic distances by various influences on the other hand, which makes it difficult to detect faraway sources, especially for higher photon energies [Gil+09]. Neutrinos only interact weakly with normal matter and carry no electrical charge. This prevents them from getting deflected away from the source position or getting absorbed in dust or plasma, enabling them to travel unimpeded towards earth. However, that apparent advantage makes it necessary to build relatively large detectors to be able to detect a large enough number of neutrinos to obtain the desired information [KS12; Anc+14].

2.1. Astrophysical neutrino production

The neutrino production in astrophysical sources can be explained by basic interactions described in the standard model of elementary particle physics [Pat+16; Her99]. An extensive review of the processes is given in [Gai90; GER16; Gru05] and a short summary is given here. Neutrino production is tightly connected to preceding acceleration of charged particles [Fer49], cosmic rays, powered by some engine mechanism [Net15; BS13; UP95]. If these high energy particles are available and collide with ambient hadronic

matter or radiation fields, the actual creation of neutrinos is primarily explained by the decay of pions through hadronic interaction channels. The primary collisions can either happen in protohadronic

$$pp \to \begin{cases} pp\pi^0 \\ pn\pi^+ \end{cases} \quad \text{or photohadronic channels } p\gamma \to \begin{cases} p + \pi^0 \\ n + \pi^+ \end{cases} . \tag{2.1}$$

For pp collisions up to 60 % of the initial beam energy can be channelled into pions [FGS97]. The subsequent decays then lead to neutrinos via the decaying pions

$$\pi^0 \to 2\gamma \tag{2.2}$$
$$\pi^+ \to \mu^+\nu_\mu \to e^+\nu_e\bar{\nu}_\mu\nu_\mu \tag{2.3}$$
$$\pi^- \to \mu^-\bar{\nu}_\mu \to e^-\bar{\nu}_e\nu_\mu\bar{\nu}_\mu \ , \tag{2.4}$$

where the charged pion decays in $> 99.9\,\%$ of the time in the depicted channel [Pat+16]. A similar process happens via the the kaon decay [Gai12]

$$K^+ \to \mu^+\nu_\mu \text{ and } K^- \to \mu^-\bar{\nu}_\mu \ . \tag{2.5}$$

Those main decay chains also lead to the assumption of having a neutrino flavour ratio of

$$\nu_e : \nu_\mu : \nu_\tau = 1 : 2 : 0 \tag{2.6}$$

directly at the sources. Through neutrino oscillations over cosmic distances, this leads to an expected expected flavour mixture at earth of $1 : 1 : 1$ [AKL06; AJY00].

The energy spectrum of the primary cosmic ray population follows a power law, $\sim E^{-\gamma}$, in first order. This universal behaviour can be explained by first-order Fermi shock acceleration [MD01; Bar97; Bel78b; Bel78a]. The cosmic ray spectrum measured at earth is subject to losses as well as propagation effects and can be approximately described with a spectral index of $\gamma = 2.7$ until a steepening at roughly 1 PeV occurs, possibly due to particle leakage from the the galactic disc [Mos03; Str+09; GST13; Gai10; Hör03; Gru05; GIT96]. Depending on the initial energy distribution at the source, the neutrino spectrum closely follows the spectral form of the cosmic rays because neutrinos do not suffer any substantial losses during their travel to earth. Usually, a spectral index of $\gamma = 2$ resembles a generic choice for a reasonable range of scenarios and can be derived from only a few basic assumptions in the shock acceleration regions [Lip08; Bel78b; Gai90]. However, recent measurements from IceCube in different flavour channels yielded a range of different indices from $\gamma = 2.19$ [HW18] for muon tracks from the northern sky, over 2.48 [NX18] for the cascade channel to 2.92 [Kop18] for all flavour, high energy starting events. So the production mechanisms of astrophysical neutrinos remain not completely understood.

2.2. Possible sources of astrophysical neutrinos

Though the first neutrino emitting source has recently been identified from the connection of the extremely-high-energy neutrino event and the flaring blazar TXS 0506+056 [Aar+18b] there are many other candidates that in theory may emit neutrinos. An overview plot for various neutrino emitter candidates and limits from neutrino searches can be seen in figure (2.1a), but with the assumption that the observed diffuse flux can be explained by the depicted source classes alone [Kow15]. Some prominent examples from the pool of possible emitters are given below in a short review extracted from [Gru05; GER16; Mes17; DG16; Der07; MRT17; JB12; UP95].

Active galactic nuclei (AGN) is the general term for active central engines in the hearts of galaxies. These accelerators are powered by a super-massive black hole accreting matter from a surrounding disc of matter and forming a relativistic jet outflow perpendicular to the disc. Depending on the exact formation of the jets and the ambient material, multiple particle acceleration mechanisms are possible. AGNs show a variety of different characteristics, which largely depend on the viewing angle between the observer on earth and the direction of the jet emission. A schematic representation of the unified AGN classification scheme can be seen in figure (2.1b) AGN emission spectra can range over a broad frequency region from low energy radio waves to the highest gamma-ray energies. Models for the particle acceleration describe leptonic, hadronic, or leptohadronic interaction types, depending which particle makes up the main amount of electromagnetic emission from a source.

As protons get accelerated in each scenario, neutrinos may be emitted from each of these objects. For blazars, which are a subclass of AGNs, the line of sight is less than 10° from the jet direction. Therefore, an observer at earth sees straight into the jet, perpendicular to the disc area. The jet axis is parallel to the acceleration direction which leads to the detection of strong, high energy gamma-ray fluxes. This indicates that also neutrinos should be created in the processes leading to the high energy gamma rays and emitted in the same direction, which makes blazars a promising neutrino point source candidate. As the detection of the observation of an extremely-high-energy neutrino from the direction of TXS 0506+056 shows, at least one blazar seems to correspond to the prediction [Kei+18; Gao+18]. However a variety of other searches across blazar catalogues remained unsuccessful so far [MR18; HK18].

While AGNs do show a time variability, there are other, purely transient events that are also candidates for neutrino emission. Gamma-ray bursts for example output enormous energies on timescales from milliseconds to minutes. These events are likely created by stellar collapse events, either massive star hypernovae or compact binary mergers. Highly relativistic jets emerge from the collapse region, giving rise to high energy particle shock accelerations [Bia+07]. Though dedicated IceCube searches for neutrinos from these

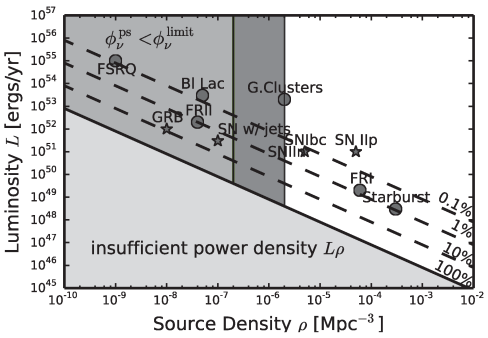

(a) Constraints on possible neutrino sources under the assumption to be responsible for the diffuse astrophysical flux detected by IceCube.

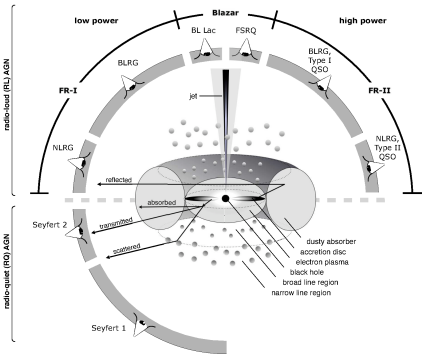

(b) Unified AGN classification scheme. For the discussed blazars, the observer looks more or less directly into the jet region.

Figure 2.1.: Neutrino source constraints and scheme of the unified AGN model. Left image taken from [Kow15], colours removed. Right image taken from [BS13].

objects remained inconclusive [Aar+16a; Abb+10], GRBs remain objects of high interest for probing neutrino production in most extreme environments [SMM16]. Other classes of transient neutrino sources may be tidal disruption events or white dwarf mergers. In the processes leading to tidal disruption events, stars get torn apart by gravitational tidal forces when they come too close to the central black hole. The accreted gas may then either externally collide with the outflow of the existing black hole's jet or provide enough accretion material for a strong jet breakout [Mat+18]. White dwarf mergers are estimated to have a reasonably high merger rate to be detected as a quasi-diffuse neutrino flux. During a merger, particle acceleration may occur due to magnetic flux line reconnection [Xia+16].

2.3. Atmospheric muons and neutrinos

Apart from the astrophysical flux of neutrinos, a far greater neutrino flux component dominates the observed neutrino flux on earth up to energies of some 100 TeV [ERS08; GH02]. When cosmic rays hit the upper atmosphere they interact with nuclei in the air and produce extensive air showers when the interchanged energy is cascaded to down to the final reaction products [GER16].

The processes that produce neutrinos in these showers are basically the same as the ones inside the source regions as described in section 2.1 so mainly from pion and kaon decay. The dominant component of the atmospheric neutrino flux goes hand in hand with the atmospheric muon flux and is often called "conventional" atmospheric neutrino

flux [GH02; GIT96]. A secondary component originating from mesons with charm components is called "prompt", but is sub-dominant to the conventional and also to the astrophysical flux and plays no role in this thesis [ERS08; HW18]. Pions and kaons have decay times in the order of 10^{-8} s [Pat+16] and can interact during their relatively long livetime with other particles at the high energies considered in this thesis. That leads to a steepened spectral index with respect to the incident cosmic ray spectrum so that the conventional atmospheric neutrino flux follows a power law with a spectral index of $\gamma_{\nu_{\mathrm{atmo}}} = \gamma_{\mathrm{CR}} + 1 = 3.7$ [GIT96].

3. The IceCube neutrino observatory

The low interaction cross section of neutrinos with matter makes them not only a suitable astrophysical messenger particle pointing back to production regions, but also hard to detect when they arrive on earth. Thus there is the need for large detection volumes countering the low interaction possibilities with larger instrumented volumes [KS12]. As the detection principle is based on the photoelectric detection of Cherenkov light in the blue part of the visible spectrum, a detector medium which is optically transparent is required. Building a large detection volume artificially from scratch is not feasible, so natural resources need to be exploited. Multiple neutrino observatories have been built by instrumenting naturally occurring sites with the needed properties, for example in the Mediterranean sea or, in the case of IceCube, in the clear Antarctic ice at the South Pole [KS12].

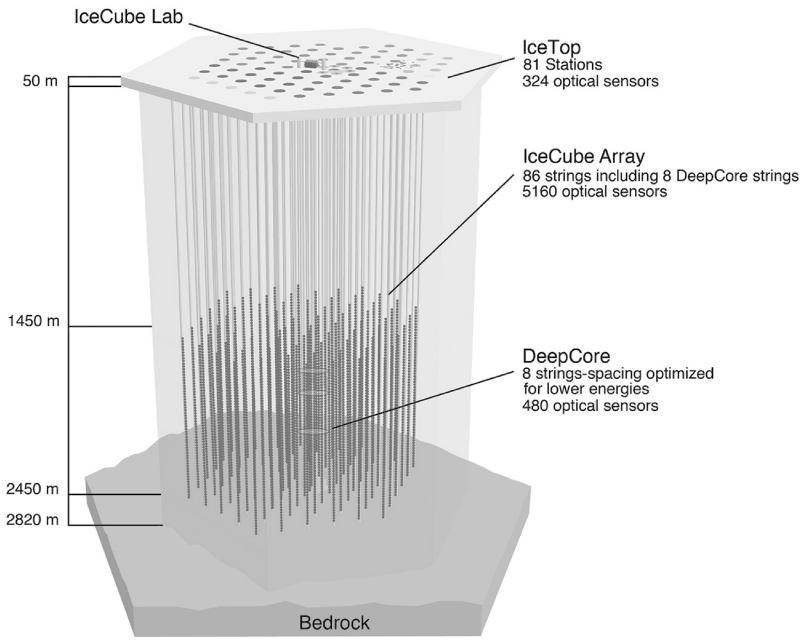

Figure 3.1.: Schematic view of the IceCube detector in its full configuration. Image taken from [Col18] and slightly adapted.

IceCube is currently the largest neutrino observatory, instrumenting roughly one cubic kilometre of Antarctic ice at the geographic South Pole. Instrumentation is realized by an approximately hexagonal grid of 86 strings, each carrying 60 digital optical modules (DOMs). The DOMs are deployed in depths from 1450 m to 2450 m below the ground with a vertical spacing of 17 m. It has to be further distinguished between 78 regular strings with a horizontal spacing of about 125 m in the hexagonal grid and eight additional DeepCore strings which make up the DeepCore sub-detector. These strings are more densely packed with a string distance of about 75 m and a vertical spacing of 10 m for ten DOMs above a naturally occurring dust layer at 2000 m below ground in the ice and the remaining 50 DOMs with a spacing of 7 m below the dust layer, starting at 2100 m. For a schematic view of the detector, see figure (3.1). The denser packing of the photodetectors reduces the energy threshold in the sub-array to about 10 GeV suitable to probe atmospheric neutrino oscillation properties [Aar+17e; Wie09]. Additionally, there is also a surface detection array of small, ice-filled tanks containing two photomultipliers each, covering an area of roughly 1 km^2 on the surface above the IceCube detector. This air shower detection array, called IceTop, can be used for cosmic ray studies or as a veto layer for atmospheric particles travelling down to the IceCube array alongside any astrophysical neutrinos [Abb+13]. Therefore, the complete IceCube detector is suitable to detect neutrinos in a wide range of energies, starting at the aforementioned 10 GeV and reaching to the highest energies of cosmogenic neutrinos up to multiple EeV with events lighting up almost the complete detection volume [Aar+13c].

Each digital optical module consists of a spherical glass unit withstanding the pressure of the surrounding ice and protecting the electronic components inside. The main detection instrument is a single 25 cm diameter, downward-facing photomultiplier tube per DOM. The signal is digitized and sent to the surface data acquisition system, the IceCube Lab, via the string cable. The main trigger system yields a combined trigger rate of approximately 2.8 Hz [Aar+17e]. Construction of the detector began in the Antarctic summer 2004 deploying a single string and ended in 2011 after partial configurations of 1, 9, 22, 40, 59 and 79 strings with the deployment of the last strings to complete the 86 string array. The sub-arrays deployed each season were already operational so data taking started with the very first configuration[Aar+17e].

3.1. Detection principle

Neutrinos come in three lepton flavours, electron-, muon- and tau-neutrino together with their corresponding antiparticles. As neutrinos only interact via the electroweak force with all other standard model particles, they cannot be detected directly [Pat+16]. Therefore, IceCube detects neutrinos indirectly via the Cherenkov effect. Neutrinos can

undergo neutral (NC) and charged (CC) current interactions with matter in the detection volume [FS82]. The interactions are the same for all three lepton flavours l:

$$\nu_l + N \to Z^0 \to \nu_l' + X' \text{ and } \nu_l + N \to W \to l + X' \ . \tag{3.1}$$

For the energies considered at IceCube, the interactions are dominated by deep inelastic scattering [CMS11]. Combined CC and NC cross sections are in the order of $10^{-35}\,\mathrm{cm}^2$ for a 1 TeV or $10^{-33}\,\mathrm{cm}^2$ for a 1 PeV neutrino. For example, a 1 TeV neutrino has an interaction length of roughly $2.5 \cdot 10^6$ km in water [Gan+96].

In neutral current interactions, neutrinos interact via an intermediate Z boson with a nucleus, generally noted as N in the reaction equation (3.1). The Z boson carries no charge resulting in an unchanged flavour neutrino final state. These interactions produce rather spherical, cascade-like signatures in the detector, for which it is virtually indistinguishable from which flavour they originated.

In charged current interactions, the exchange particle is the charged W boson, thus changing the initial neutrino state ν_l to a final lepton state l with the same flavour. These interactions can produce vastly different event signatures in the detector depending on the primary neutrino energy and flavour. In general, electron final states produce neutral current-like cascades due to their short mean free path and rapid energy loss. Muon final states usually produce track-like signatures and, with enough energy, are able to traverse through the whole detector [KS12]. Tau leptons can produce various different signatures depending on the initial energy and particle location. A unique pattern would be the so-called double bang signature, in which a first cascade is produced in the initial charged current interaction and a second one when the tau lepton decays, depositing energy in the detector medium [CI07]. Two exemplary event displays of a cascade and a track-like event are shown in figure (3.2).

Despite the different interaction types, the detection principle remains the same for all signatures mentioned above. When energy is deposited in the detector, secondary charged particles are created which, at the high energies considered here, travel through the matter faster than the effective speed of light in the medium. During their passage through matter, Cherenkov light gets emitted along their path. The light is emitted at an angle given in first order by the relation

$$\Theta = \arccos\left(\frac{1}{\beta n}\right) \tag{3.2}$$

with the refractive index n of the traversed medium an $\beta = v/c$ the particle speed in units of the vacuum speed of light c [Che37; Mea58]. Typical interactions of the charged primary lepton are ionization, photonuclear, pair production and Bremsstrahlung losses where the latter three start to dominate the energy loss for muon energies higher than

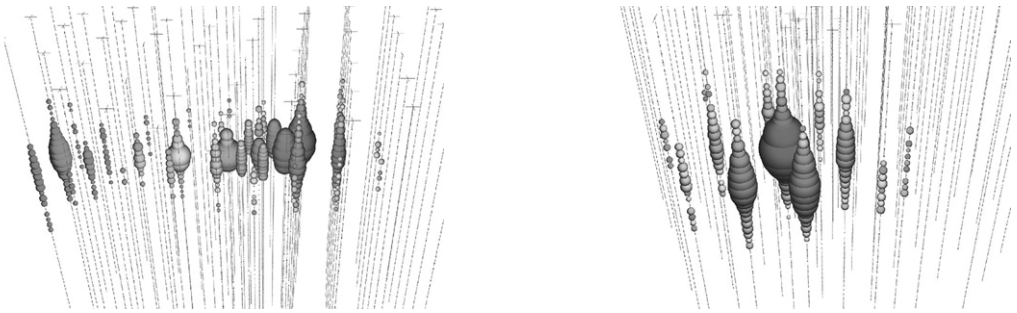

(a) Track-like event **(b)** Cascade-like event

Figure 3.2.: Two event displays from very high energy events [Aar+13a]. Each sphere represents a DOM and the size of each sphere corresponds to the detected photons in each photomultiplier. The track-like event starts on the right side within the detector and travels to the left continuously leaving traces from energy losses along the way. The particle causing the cascade event interacts in the upper region of the detector and loses all its energy on length scales unresolvable by the detector, so the light spreads out spherically.

some 10 TeV. The combined Cherenkov light yield from the secondary charged particles originating from the lepton interaction points is typically higher than the yield from the primary lepton itself [Koe+13; RW13].

The Cherenkov photons travel through the ice and may be detected in one of the photomultiplier tubes inside the DOMs which are able to detect single photon hits. The Antarctic ice as a natural medium is not perfectly isotropic and has depth and direction dependent absorption and scattering properties, which was observed by using artificially injected light signals from LEDs built into the DOM cases. Additionally, a dust layer between a depth of roughly 2000 m and 2100 m in which the mean free photon path is drastically reduced compared to the clear ice in other layers, is present within the IceCube detection volume. Furthermore, there is a directional dependence of the ice scattering coefficient due to environmental influences during the ice sheet formation and a vertical tilt of ice layers due to slow glacier movement of the detection volume. Different ice models have been developed and adapted to account for these different effects as good as possible [Cas+14; Bay+10; Aar+13b; Chi11].

4. Datasets

Two distinct datasets are used in a so far unique way in the analyses done in this thesis. Here, two different event selections serve as a test and as a source dataset. In both sets, six years of IceCube data is used. Usually, in point source searches, locations of sources measured from other experiments are tested, for example from high energy cosmic ray information or from gamma-ray observations. These are either classic catalogue stacking point source searches, where the external catalogue provides source locations with a sufficiently high precision to treat the sources as point sources with respect to the resolution capabilities of IceCube, which is in the order of 1° [Aar+14c; Bos+15]. Or the analyses incorporate the uncertainty from external sources, usually by expanding the spatial per event uncertainty to $\sigma^2_{\text{tot}} = \sigma^2_{\text{evt}} + \sigma^2_{\text{src}}$, effectively treating the source as an extended emitter[1]. This is problematic when a test for point sources is needed, especially when testing for extragalactic sources that always appear point-like, due to the large cosmic distances[2]. Here, 22 track-like events from six years of the high energy starting event (HESE) selection data are used as potential source candidates. In this chapter, the two different data sets partaking in the analyses are shortly introduced. Also, they need to be slightly adapted from the originally prepared sets to be suitable for the analyses performed here.

In the following, the naming scheme for data taken in each period is following the number of operational strings until the complete detector was operational. After that, the data taking periods are numbered consecutively with the corresponding year the data was taken in. In IceCube, a data taking period starts around May each year, where a new detector configuration set-up may be installed or trigger or filter systems get updated [Aar+17e].

4.1. High energy starting event data

The high energy starting event selection has led to the first-ever detection of a diffuse astrophysical neutrino signal in 2013 [Aar+13a]. Additionally, a dedicated point source search was made using only the HESE event selection, however with no significant

[1] More on the Likelihood formalism in the next chapter.
[2] Maybe with the exception of Centaurus A (NGC 5128) [Yan+12].

detection throughout the years [Aar+13b; Aar+14b; KGK16; Kop18]. The idea behind the data selection is to use the outermost detector units as a veto against events starting outside the detector to reject atmospheric muons from the southern sky. In figure (4.1) the veto region is shown. Each event lighting up a DOM in the shaded areas would be rejected as background and only those passing the layers and start inside the fiducial detection volume are selected[3]. Additionally, to make sure no lower energy muon enters the detector, a total charge of at least 6000 photoelectrons is required to be registered in the whole detector. In six years of data, in data taking seasons 2010–2015, 82 events, possibly including all three neutrino flavours, have been collected. 22 of these events are the track-like starting events with a good angular resolution of about 1° used as sources in this work. Additionally, 60 cascade-like events with a much worse angular resolution were recorded [Kop18]. Unlike in most other point source searches, the positions of the sources are not exactly known due to the reconstruction uncertainties, however, full Likelihood scans of the reconstruction algorithm are available. To include this uncertainty in the analyses performance estimation, the Likelihood scan maps are later used to inject source positions during trial generation. The cascades could potentially also be considered as sources, but this would require a more advanced Likelihood formalism as known to the author to-date to capture the wide-spread source regions properly, preferably by fitting the positions themselves using the Likelihood maps as priors. Therefore, only the track-like events with good pointing capabilities are used in this thesis. See table (4.1) for detailed information of each used, track-like high energy starting event.

4.1.1. HESE reconstruction map handling

To use the HESE track-like events as sources, their positions must be reconstructed first. Instead of determining a single best-fit position, a full Likelihood scan utilizing an advanced reconstruction algorithm is done[4] [Aar+14a]. For the few track-like events recorded this is feasible, even though scanning the whole sky is a slow procedure and takes up several hours of computing time on a distributed system. Since 2016, the scan procedure is running automated to support follow-up observation programs for the IceCube real-time alert system. When a triggered event passes the high energy starting event filter running live at the South Pole, an alert is sent and the event reconstruction starts immediately to make the position available for other observatories [Aar+17f].

For the scan procedure, the sky is binned in a HEALPix [Gor+05] pixelization scheme in a three pass procedure. The HEALPix grid was originally developed for a frequency

[3] Less than three of the first 250 registered photoelectrons are allowed to be recorded in any of the veto DOMS [Kop18].

[4] Internally named “millipede” due to the segmentation of the track hypothesis. For each segment the energy losses are fitted, unfolded and compared to data.

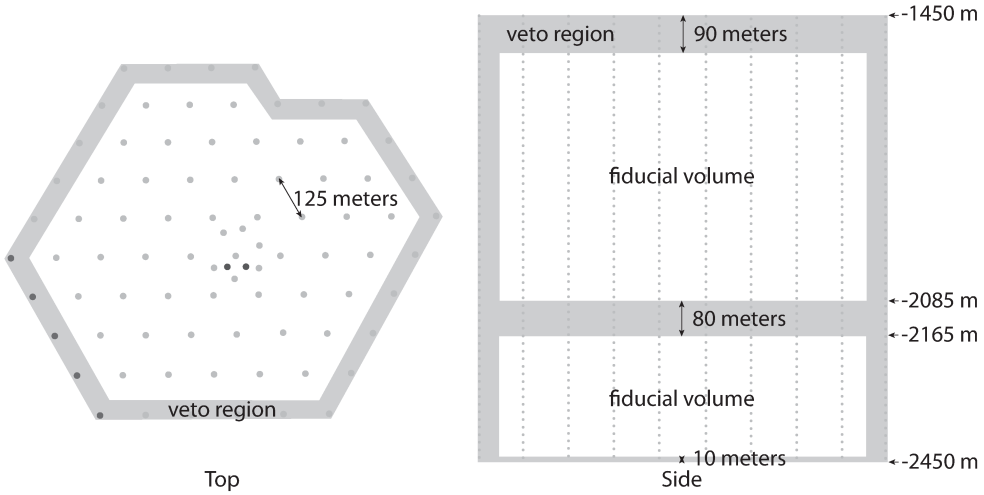

Figure 4.1.: High energy starting event veto region in the main IceCube detector array. The DOMs with a grey background are only used to veto incoming events that don't start within the detector. The top needs to be thicker due to a large number of atmospheric muons entering the detector. The middle layer is due to the light absorbing dust layer, which could cause events to enter the detector horizontally in this region without being vetoed if only the outer layers would be used. Image taken from [Aar+13a], colours removed.

analysis of the cosmic microwave background measured with the Wilkinson Microwave Anisotropy Probe (WMAP) satellite mission [Jar+11]. It tesselates the unit sphere in hierarchical segments, where all pixels for a given resolution have the same area and are distributed on lines of constant latitude. This has the advantage of having a constant normalization in each pixel, instead of using, for example, a rectangular grid, where pixel areas get smaller towards the poles. To get a rough idea of the most likely event direction, at first a coarse scan with only a few pixels is used. At each pixel, the reconstruction algorithm is run with the event positions fixed. It then fits the best matching support point and the energy losses along the track pointing to the fixed direction of the current pixel. As the same fit hypothesis is used across all pixels, the resulting Likelihood values can be directly compared and the highest value, or the minimum if the negative logarithm of the Likelihood is used, can be found from the map of scanned Likelihood values. Then, consecutively only increasing the resolution around a large enough region in the vicinity of the previous best fit pixel to save computation time, a second and a third scan is done. The final resolution would have over three million pixels on the whole sky, being equal to an angular resolution of about 0.5°. The best fit pixel with the highest Likelihood value is then the reported arrival direction. See plots (B.1) and (4.2) for the reconstruction maps and the events positions for each of the 22 tested HESE events.

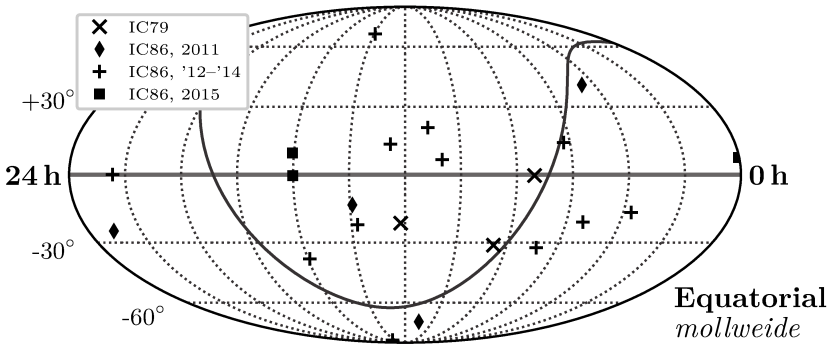

Figure 4.2.: Skymap in equatorial coordinates and Mollweide projection showing the positions of all 22 high energy starting events with additional season information.

The advantage of this method is two-fold. First, the fitting algorithm has to deal with less free parameters in a difficult scenario, making it more stable. The region around the best-fit position can be inspected for failures in the fitting procedures, for example, when sudden drops of the Likelihood value for neighbour pixels occur. Secondly, the scanned Likelihood gives an estimate of the uncertainty of the angular reconstruction by inspection of the Likelihood landscape around the best fit pixel. Though the underlying test statistic, which would allow the needed mapping of Likelihood values to probabilities, is not known here and can only be obtained by extensive and costly re-simulation per event, the uncertainty can be estimated in a first approximation using Wilks' theorem [Wil38; CB02; BZ10]. To factor in possible systematic uncertainties, each map is convolved with a 1° Gaussian smoothing kernel. The 1° is an upper limit of combined systematics effects derived from a study of the cosmic ray shadow of the moon in IceCube [Aar+13a; Aar+14c].

The reconstruction Likelihood is originally scanned in local detector coordinates zenith $\theta \in [0, \pi]$ and azimuth $\varphi \in [0, 2\pi]$. However, source objects are usually described in equatorial coordinates, declination $\delta \in [-\pi/2, \pi/2]$ and right ascension $\alpha \in [0, 2\pi]$ or often also $\alpha \in [0\,\mathrm{h}, 24\,\mathrm{h}]$. The equatorial coordinate system is created by projecting the earth's equator onto the celestial sky for the horizon and the March equinox point is used as the starting point for the perpendicular coordinate, right ascension, in a right-handed system. Far away objects are fixed in these coordinates[5], which is the reason why it has become the standard coordinate system for a broad range of astronomy tasks [Hoh+92]. Though the basic coordinate transformations in IceCube are relatively easy because of the special position directly at the South Pole, for which the approximation $\delta \approx \theta - \pi/2$

[5]At least for a certain time range in which the earth's precession can be neglected. These time periods are given as *epochs*. The current epoch is *J2000*.

holds reasonably well, the full set of transformations including the sun position and other corrections takes a long time to process. Therefore, the local event coordinates from a test dataset are converted to equatorial coordinates beforehand, so their positions can be directly compared to the equatorial source coordinates. To become computationally feasible, also the aforementioned reconstruction maps for the HESE events need to be converted into a fast-to-evaluate equatorial representation.

The used HEALPix maps use an internal coordinate-to-pixel-number conversion scheme, with $\Theta \in [0, \pi]$ and $\Phi \in [0, 2\pi]$, that is easily identifiably with IceCube's local detector coordinates zenith $\theta \in [0, \pi]$ and azimuth $\varphi \in [0, 2\pi]$, so the local maps can directly represent local coordinates for each pixel. The conversion from local to equatorial coordinates depends on the sources' times which fixes the detector location relative to the equatorial coordinate system. Due to IceCube's special location almost directly at the geographic South Pole, the relation between zenith θ and declination δ angle is $\delta \approx \theta - \pi/2$ and only the right ascension values varies strongly over time. To avoid recalculating costly transformations from local map coordinates to equatorial coordinates at runtime, pre-transformed maps in equatorial coordinates are computed beforehand only once. The convention used to efficiently map from HEALPix coordinates to equatorial ones is chosen as

$$\delta = \frac{\pi}{2} - \Theta \text{ and } \alpha = \varphi \ . \tag{4.1}$$

This mapping is not bijective though, because $\delta \approx \theta - \pi/2$ is only an approximation and the number of pixels in each Θ band changes depending on whether being close to the poles or to the horizon. So sometimes two pixels are mapped to one, which means that another pixel stays empty because the number of pixels is fixed. To overcome this, the mapping is done in reverse by transforming the exact pixel coordinates from a map in equatorial convention back to local coordinates. Then the local map is interpolated to the new pixel location and that value is stored in the equatorial map. The maximum error that can happen this way is in the order of a single pixel offset because the above approximation between zenith and declination holds closely enough.

Next, the maps should represent a probability distribution that gives the probability of the true source position being at a specific pixel. For this, the transformed maps are first converted back from the original logarithmic Likelihood space after the scan in local coordinates, to linear Likelihood space by $m \to \exp(m)$. To approximately and conservatively account for unknown systematics, the transformed maps are convolved with a symmetric Gaussian kernel of width 1° as mentioned before. See figure (4.3) for an example of the a smoothed Likelihood map around the best fit position. The smoothing introduces some numerical errors because it is done in spherical harmonics space which has to be truncated numerically [Gor+05]. The artefacts are removed by normalizing the

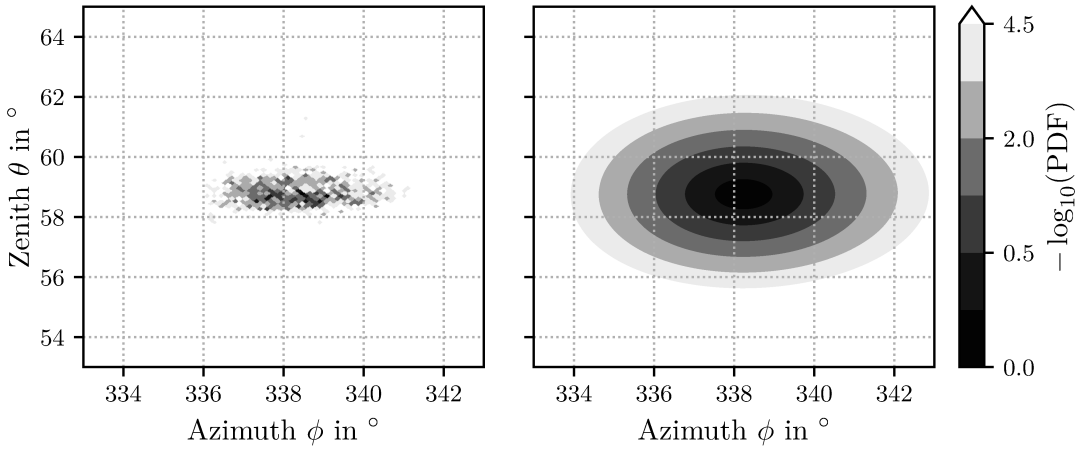

Figure 4.3.: Likelihood reconstruction map of event 1 in local coordinates zoomed to the region of high Likelihood. On the left the original Likelihood map as obtained from the scan procedure. On the right the same map convolved with a 1° Gaussian smoothing kernel to approximately account for unknown systematics.

smoothed maps to have an integral value of

$$\sum_{i=1}^{N_{\mathrm{pix}}} \mathrm{d}A_{\mathrm{pix}} = 1 \tag{4.2}$$

over the unit sphere and setting the resulting map to zero outside the $6\,\sigma$ confidence contour. Due to the lack of a proper test statistic, the Likelihood value $\mathcal{L}_{\mathrm{cut}}$ for the $6\,\sigma$ level can only be estimated from Wilks' theorem with

$$\mathcal{L}_{\mathrm{cut}} = \max_{i=1}^{N_{\mathrm{pix}}}(\mathcal{L}_i) \cdot \left(1 - \int_0^{6^2} \chi_2^2(x)\mathrm{d}x\right) \quad . \tag{4.3}$$

The resulting maps can then be used as spatial PDF maps and are later sampled during the signal injection trials described in the analysis sections 6 and 7. For each event, the tested source position is defined as the direction of the pixel from the smoothed, equatorial PDF map with the highest value. These coordinates are slightly different to the published equatorial HESE coordinates due to the necessary map processing procedure. But this ensures that the sampling procedure from the map does not introduce a bias by sampling the most likely source positions not exactly at the tested ones. See figure (4.4) for an example of the map truncation.

Table 4.1.: Time and angular position for the 22 high energy starting track events used as potential source candidates. In total, 82 HESE events where detected in six years of data, including these 22 track-like events and 60 cascade-like events with a worse angular resolution [Kop18]. For an explanation of the equatorial coordinates δ, α, see the description in the text.

Nr.	HESE ID	Season	Run	MJD	δ in °	α in °
1	3	IC79	116 528	55 451.07	−31.19	127.86
2	5	IC79	116 876	55 512.55	−0.35	110.61
3	8	IC79	117 782	55 608.82	−21.24	182.44
4	13	IC86, 2011	118 435	55 756.11	40.30	67.91
5	18	IC86, 2011	119 196	55 923.53	−24.77	345.59
6	23	IC86, 2011	119 470	55 949.57	−13.18	208.71
7	28	IC86, 2011	120 045	56 048.57	−71.49	164.74
8	37	IC86, 2012	122 152	56 390.19	20.66	167.25
9	38	IC86, 2013	122 604	56 470.11	14.02	93.35
10	43	IC86, 2013	123 326	56 628.57	−21.95	206.64
11	44	IC86, 2013	123 867	56 671.88	0.08	336.68
12	45	IC86, 2013	123 986	56 679.20	−86.20	219.27
13	47	IC86, 2013	124 244	56 704.60	67.45	209.33
14	53	IC86, 2013	124 640	56 767.07	−37.69	238.99
15	58	IC86, 2014	125 071	56 859.76	−32.33	102.09
16	61	IC86, 2014	125 541	56 970.21	−16.45	55.62
17	62	IC86, 2014	125 627	56 987.77	13.33	187.93
18	63	IC86, 2014	125 700	57 000.14	6.58	160.06
19	71	IC86, 2014	126 307	57 140.47	−20.75	80.73
20	76	IC86, 2015	126 838	57 276.57	−0.41	240.23
21	78	IC86, 2015	127 210	57 363.44	7.54	0.34
22	82	IC86, 2015	127 853	57 505.24	9.42	240.83

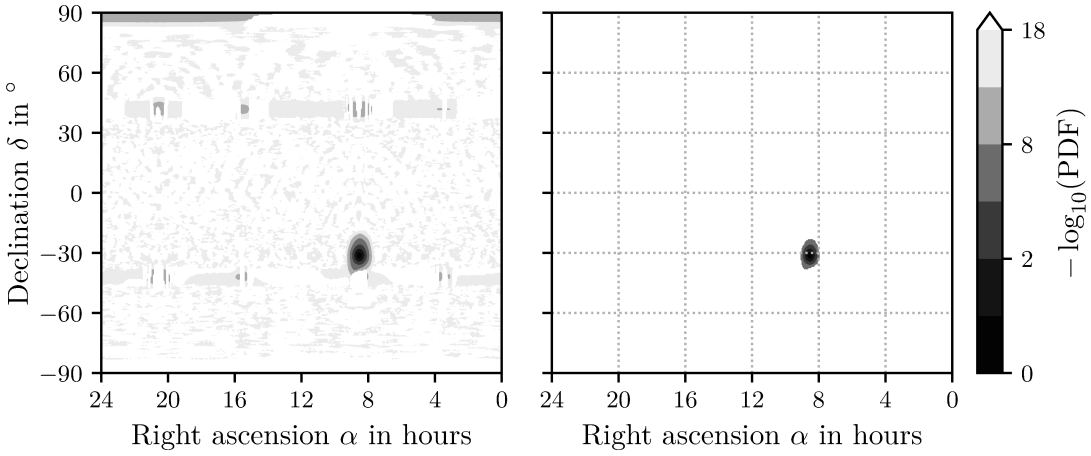

Figure 4.4.: Likelihood reconstruction map of event 1 in equatorial coordinates. On the left the raw map after the smoothing procedure and on the right the same map truncated at $6\,\sigma$ level as described in the text.

4.2. All sky muon neutrino data

The second type of dataset used here is a collection of six years of muon track-like event data. Parts of this dataset have been extensively used to test for various source hypothesis in the past. Here, data from the same detector seasons as for the source events is used, so from IC79 to IC86, 2015. Though the underlying event selection differs slightly for each sample and also the detector configuration changes for certain seasons, the basic steps to arrive at the final event selection is summarized in [Aar+16e] for the IC86, 2015 season, in [Aar+17a] for the IC86, 2012–2014 season, in [Aar+13d] for IC86, 2011 and [Aar+14d] for IC79. The same selection is used for all three years of the IC86, 2012–2014 season, because the detector configuration was not changed. In the following, this three-year dataset is always considered in total, not for each season separately. The number of events in each dataset is shown in table (4.2). The goal of the data selection was to obtain a highly pure muon track sample from the whole sky in each case. Because the background contributions from each hemisphere in the detector are fundamentally different, the samples are usually built for each hemisphere separately and then combined back into a single sample. As depicted in figure (4.5), muons from atmospheric air showers get blocked by the earth and cannot enter the detector from below. However, the main reducible background in the northern sky is still the contribution from wrongly reconstructed atmospheric muons where the reconstruction methods computed false entry angles. In the southern sky, direct muons from the Antarctic atmosphere which enter the detector from the top are the main background contribution. The selection

efficiency is worse in the southern sky, leading to fewer statistics and a higher energy threshold for obtaining a pure muon neutrino sample. The irreducible background in the samples is made of muons induced by atmospheric muon neutrinos produced alongside atmospheric muons in the air showers. Because the particle type is the same, these can't be directly distinguished from muons induced by astrophysical muon neutrinos. However, atmospheric particles are expected to be produced diffusely with no preferred direction in a large production volume. Therefore the Likelihood ansatz described in the next chapter is used to test for a significant clustering of events around the assumed source locations which would be a clear signal of the presence of astrophysical neutrinos.

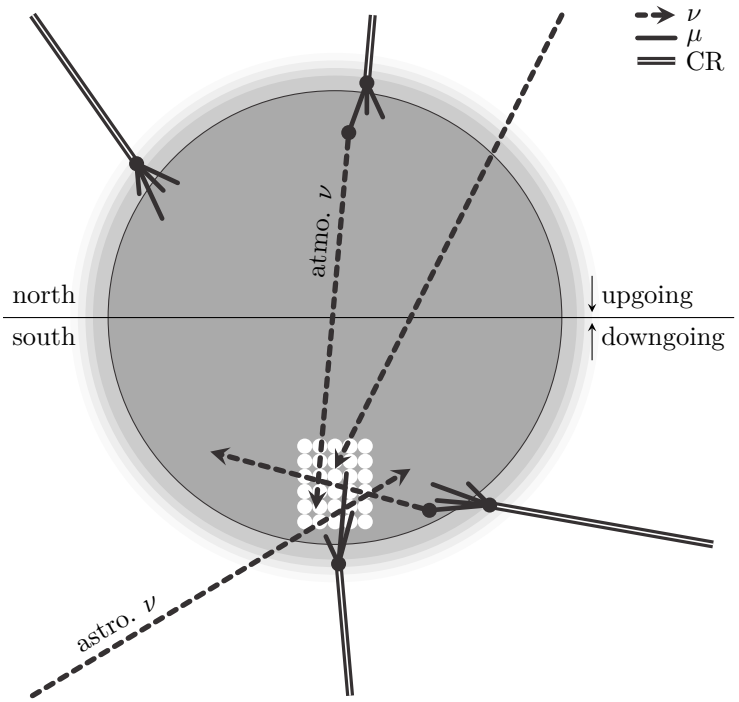

Figure 4.5.: Schematic overview of the different particle contributions going into the six year muon neutrino track sample. In the northern sky, the earth shields the detector from the atmospheric muons, so the main irreducible background are the atmospheric neutrinos. In the souther sky, atmospheric muons are able to enter the detector alongside with the atmospheric and astrophysical neutrino contribution.

A standardized form utilizing a named array structure is used to provide the datasets. The per-event attributes used for experimental data are the reconstructed angular direction in equatorial coordinates declination and right ascension, the logarithm to base 10 of an energy proxy variable, the event times in Modified Julian Date representation

Table 4.2.: Number of events and the lifetime in days in the used muon neutrino track test datasets remaining at the final analysis level for each considered season.

Season	No. of events	Livetime in days
IC79	93 133	315.51
IC86, 2011	136 244	1058.34
IC86, '12–14'	338 590	332.61
IC86, 2015	211 309	364.68
Total	779 276	2071.14

[Hoh+92] and the combined events angular uncertainty σ[6], where the angles and σ are given in radian. The underlying reconstruction algorithms for the energy proxy or the directional reconstruction may differ per or within a sample. However, in general, the reconstruction algorithms for the angles is one of the algorithms described in [Ahr+04], because a time costly scan as done with the HESE events is not feasible for a large number of events. The same reasoning applies to the energy proxy variable, which is one of the faster algorithms from [Aar+14a]. Though the actually used algorithm does not matter, the unbinned Likelihood will perform better, the better the algorithms can reconstruct the true quantities of each event. The per event angular uncertainty σ is either constructed using a coarse Likelihood scan around the best-fit position from the directional reconstruction algorithm and approximating this landscape with a parabola, which justifies its use as a Gaussian uncertainty or, where that scan fails, through a bootstrap procedure.

To built time-dependent Likelihood PDFs, the time ranges in which the detector was set up to actually measure event information is needed too. Usually, this information is tracked in *good run lists*, which note the start and end times of each detector run. Because it was not quite clear which run-list should be used, especially for the older datasets, run information was manually reconstructed from the datasets by using the first and last event per run to estimate each run's livetime. This generally underestimates the livetime, with the underestimation being more severe the fewer events are present at final data level within in a run. If a run only had a single event it was dropped, because the livetime would become zero in this case. However, for the time-dependent analysis done here, this only leads to a slight overestimation of background because of the high statistic in the final samples. Therefore this can only worsen the sensitivity, so the procedure is safe to use, despite not being optimal.

In addition to the experimental data sets, dedicated Monte Carlo simulation tailored to the specific detector configuration is used to estimate the behaviour of signal-like events

[6]Named accordingly with keys `'ra'`, `'dec'`, `'logE'`, `'sigma'`, `'time'`.

from the source regions. The simulation sets are computed by the collaboration using a software based on [GK05]. For the Monte Carlo datasets, additionally the ground simulation truth is available to study the effects of the detection mechanism on the incident neutrino signal. Added are the true neutrino direction in equatorial coordinates, the true neutrino energy and a weight `'ow'`[7] , with the energy in GeV and the angles given in radian. The attribute `'ow'`, short for *OneWeight*, contains a per-event simulation weight that allows mapping the number of produced simulation events to an expectation value for the desired target flux that can be directly compared to measured data. More details on the OneWeight is given in equation (5.72). Just note that OneWeight is already divided by the number of simulated events in total for the standardized datasets used here, which is, in general, not the case for other datasets. The simulation data is used for building the model PDFs in the Likelihood construction, described in the next chapters. Another important step, that is also already included in the standardized datasets, is the so-called *pull correction*. In general, the per event uncertainty reconstruction has an energy-dependent bias which needs to be corrected [Neu06]. This is usually called pull correction, where the pull $^{\Delta\Psi}/_{\sigma}$ is defined by the angular separation of the true neutrino direction and the reconstructed muon direction $\Delta\Psi$ divided by the estimated angular uncertainty σ, where the former is only available from simulation. Because the per event uncertainty is later used in a two-dimensional Gaussian distribution and is also constructed for that use in mind, the median of the energy-dependent pull is corrected to the expected value of 1.1774[8]. Because this can only be computed using the ground truth on simulation data, the same correction formula is applied as-is to the per-event uncertainties on experimental data. See figure (B.2) for effective areas and $\sin(\delta_\nu)$ distribution plots for each used sample.

4.2.1. Decorrelation

In the analyses done here, the HESE events themselves are the sources, but can and do also appear in the test dataset because the original data sample that was used to create both sets are the same. Leaving the HESE events in the experimental test dataset would introduce a large bias because these events have per-definition a large signal over background ratio as they occur exactly at the source positions, at the source times and also have a high energy. To avoid this bias, these events are removed from the data before doing any analysis steps.

Because the simulation datasets also contain events, that are similar to high energy starting event signatures and therefore would also be handled as sources rather than

[7] Named accordingly with keys `'trueRa', 'trueDec', 'trueE', 'ow'`.

[8] The $1\,\sigma$ error ellipse region of a 2D Gaussian contains 39 % of probability. Equivalently, the $1.1774\,\sigma$ contour contains 50 % as expected from the median. In general this can be calculated using $\sigma^2 = \chi^2_{\text{ppf}}(1-p|k)$, where k is the dimension, p the tail probability and χ^2_{ppf} the inverse of the CDF [Sio63].

test events in the analyses done here, they need to be removed from the simulation files. This avoids a bias in the creation of the Likelihood PDFs and in the performance estimation for which the simulation is used. Here, a conservative approach is taken and all HESE-like events are removed from the simulation. A more sensitive estimation of the veto passing fraction of HESE candidates can be found in [Arg+18]. The removal of the events is done by applying the same HESE veto filter module on the simulation datasets as used to originally select the events on data. The IDs of the vetoed events are collected and matched against the full simulation set to remove the HESE-like events from the final simulation sets. Figures (4.6) and (B.3) show the filtered out subsample of the HESE-like events per used sample.

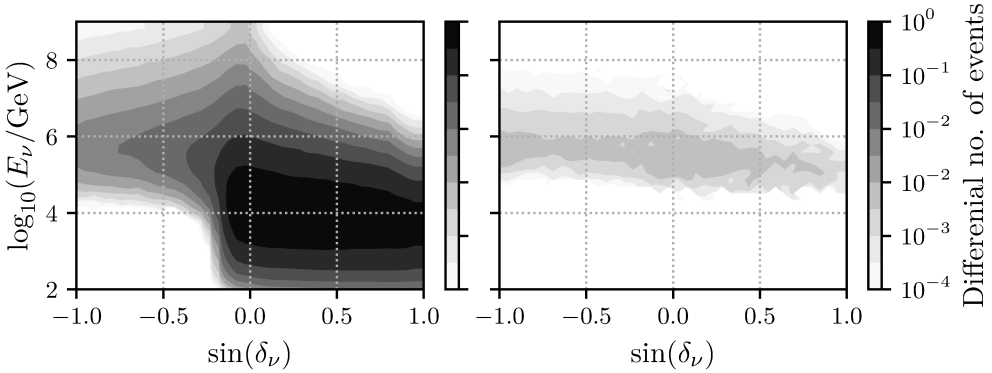

Figure 4.6.: Plot showing the filtered out HESE-like events in the simulation files used for the IC86, 2015 sample on the right and the full simulation sample on the left. As expected the filter removes events with a high energy over all declinations. Note that the plot does not show whether events are starting or not, but only the energy and declination distribution of the removed events. The samples are weighted to the flux model in [HW18] normalized to a livetime of 365 days. To obtain the total number of events, the integral over the parameter space needs to be taken, shown are differential number of events.

5. Point source searches with IceCube neutrinos

In this chapter, the unbinned Likelihood methods used for IceCube point source searches are derived. To identify an astrophysical neutrino signal from a specific source location in the sky, an excess of events from that direction needs to be identified. In general, atmospheric and the sought after extraterrestrial neutrinos cannot be distinguished on a per event basis. However, it is possible to search from a sample based point-of-view by measuring deviations for an ensemble of events with respect to a known background expectation. A simple method could be to define a fixed search region around a direction from which signal is expected, count the number of measured events and compare them to the number of events from a background expectation in the region [LM83]. If the measured number of events is significantly higher than the expected number of background events, that may be a hint for a signal from that direction.

In this thesis, a similar but more advanced approach is used, incorporating multiple pieces of event information to increase the detection sensitivity. Also the usage of pre-defined search regions, often called a binned approach, is replaced with an unbinned version on a per event basis. This has the advantage of avoiding hard search region boundaries which can drop the sensitivity of the approach if e.g. an unknown source is located directly at the border of such a region. Starting from a general unbinned, extended Likelihood approach, the special cases of a time-dependent and time-integrated search for point-like sources are derived. Particular cases handling multiple years of data from different detector configurations and multiple sources for the so-called stacking case are further derived from the basic form. In the following, a single event is consistently noted with index i, a source with index k and a data sample with index j.

5.1. Extended unbinned Likelihood

The extended Likelihood [Bar89] and the corresponding logarithmic extended Likelihood function is defined as

$$\mathcal{L}(\lambda) = \frac{\lambda^N e^{-\lambda}}{N!} \prod_{i=1}^{N} P_i \quad \Rightarrow \quad \ln \mathcal{L}(\lambda) = -\lambda + \sum_{i=1}^{N} \ln(\lambda P_i) \ , \tag{5.1}$$

where the constant term $\ln(N!)$ is dropped in the logarithmic version. Here λ is the expected number of events and N the number of measured events following a Poisson

counting distribution. The per event model distributions P_i, normalized to integral 1 over the defined parameter space, describe the Likelihood of each event under the assumed model and how likely it contributes to the expectation. The use of the Poisson term is justified by a re-normalization of the per event distributions to include the total number of measured events, which is not fixed for multiple experiments of the same kind but may fluctuate around an unknown expectation value.

The tested hypotheses are a priori encoded in the description of the model P. To obtain a fairly general expression to derive the point source special cases from, the expectation model can be split into multiple classes by splitting the expectation and the models accordingly

$$0 \leq \lambda = \sum_{k=1}^{N_{\text{classes}}} \lambda_k \text{ and } P_i = \frac{1}{\sum_{k=1}^{N_{\text{classes}}} \lambda_k} \cdot \sum_{k=1}^{N_{\text{classes}}} \lambda_k P_{i,k} \ . \tag{5.2}$$

The single λ_k can be negative but their sum must not, because it is still a Poisson expectation parameter. Additionally, the new split model is normalized over all classes to arrive at the form

$$\ln \mathcal{L}(\{\lambda_k\}) = -\sum_{k=1}^{N_{\text{classes}}} \lambda_k + \sum_{i=1}^{N} \ln \left(\sum_{k=1}^{N_{\text{classes}}} \lambda_k P_{i,k} \right) \ . \tag{5.3}$$

To further specialize, it is usually desired to test a signal hypothesis against a background one, for N_{srcs} sources in general, for each event i. The above expression (5.3) is thus expanded to include N_{srcs} signal and N_{srcs} background parameters and the corresponding distributions $S_{i,k}$ and $B_{i,k}$:

$$\ln \mathcal{L}(\{\lambda_{k,S}\}, \{\lambda_{k,B}\}) = -\sum_{k=1}^{N_{\text{srcs}}} (\lambda_{k,S} + \lambda_{k,B}) + \sum_{i=1}^{N} \ln \left(\sum_{k=1}^{N_{\text{srcs}}} (\lambda_{k,S} S_{i,k} + \lambda_{k,B} B_{i,k}) \right) \ , \tag{5.4}$$

and from the Poisson condition there is still the constraint

$$0 \leq \sum_{k=1}^{N_{\text{srcs}}} (\lambda_{k,S} + \lambda_{k,B}) \ . \tag{5.5}$$

For testing the significance of a potential signal contribution in the measured data, a Likelihood ratio test is used [9]. The null hypotheses H_0, which means that only background

[9] See section 5.6 for an introduction to frequentist methods.

is expected to be measured, is constructed by using only a portion Θ_0 of the allowed parameter space, here by setting all signal expectations to zero

$$\ln \mathcal{L}_0(\{\lambda_{k,S}=0\},\{\lambda_{k,B}\}) = -\sum_{k=1}^{N_{\text{srcs}}}\left(\lambda_{k,B}\right) + \sum_{i=1}^{N}\ln\left(\sum_{k=1}^{N_{\text{srcs}}}\left(\lambda_{k,B}B_{i,k}\right)\right) \quad . \tag{5.6}$$

The alternative hypothesis H_1 is constructed by using the full Likelihood parameter space Θ

$$\ln \mathcal{L}_1(\{\lambda_{k,S}\},\{\lambda_{k,B}\}) = -\sum_{k=1}^{N_{\text{srcs}}}\left(\lambda_{k,S}+\lambda_{k,B}\right) + \sum_{i=1}^{N}\ln\left(\sum_{k=1}^{N_{\text{srcs}}}\left(\lambda_{k,S}S_{i,k}+\lambda_{k,B}B_{i,k}\right)\right) \quad . \tag{5.7}$$

The Likelihood ratio test statistic Λ for testing the null hypothesis H_0 against the alternative H_1 is defined as [CB02]

$$\ln \hat{\Lambda} = \ln\left(\frac{\sup_{\theta\in\Theta_0}\mathcal{L}(\theta)}{\sup_{\theta\in\Theta}\mathcal{L}(\theta)}\right) = \ln\left(\sup_{\theta\in\Theta_0}\mathcal{L}(\theta)\right) - \ln\left(\sup_{\theta\in\Theta}\mathcal{L}(\theta)\right) \quad . \tag{5.8}$$

where $\hat{\Lambda}$ means the single test statistic value after finding the supremum of both nominator and denominator. This leads to the test statistic considered in this work,

$$\begin{aligned} -2\ln\hat{\Lambda} &= 2\ln(\mathcal{L}_1(\{\hat{\lambda}_{k,S/B}\})) - 2\ln(\mathcal{L}_0(\{\hat{\lambda}^{(0)}_{k,B}\})) \\ &= -2\left(\sum_{k=1}^{N_{\text{srcs}}}\hat{\lambda}_{k,S}+\hat{\lambda}_{k,B}-\hat{\lambda}^{(0)}_{k,B}\right) + 2\sum_{i=1}^{N}\ln\left(\frac{\sum_{k=1}^{N_{\text{srcs}}}\left(\hat{\lambda}_{k,S}S_{i,k}+\hat{\lambda}_{k,B}B_{i,k}\right)}{\sum_{k=1}^{N_{\text{srcs}}}\left(\hat{\lambda}^{(0)}_{k,B}B_{i,k}\right)}\right) \quad , \end{aligned} \tag{5.9}$$

which has been decorated by the factor -2 to be compatible to Wilks' theorem [Wil38; CB02]. Here the parameters $\hat{\lambda}_{k,S/B}$ were introduced, which mean the parameters $\lambda_{k,S/B}$ that maximize the Likelihood $\mathcal{L}_1$ under the complete parameter space and $\hat{\lambda}^{(0)}_{k,B}$ maximizing $\mathcal{L}_0$. As seen in expression (5.9), all best-fit parameters from both hypotheses have to be distinguished. That means it must be differentiated between the best fit parameters $\hat{\lambda}^{(0)}_{k,B}$ from the null hypothesis and $\hat{\lambda}_{k,B}$ from the alternative hypothesis, which are not the same in general.

In the following sections, specific model choices for the signal and background distributions and approximating assumptions are shown, to transform expression (5.9) to more commonly known forms, and to the ones used for the time-dependent and time-integrated search in this thesis.

5.2. Per event distributions

The introduced per event distributions S_i, B_i are the functions that actually define the tested hypothesis of the analysis. Depending on their structure they can describe a single point source search, a stacking search for searching at various source positions at once or a template search, where a whole spatial region is tested for neutrino emission over the expectation. The used PDFs are usually similar for all analysis types and the conventions applied for most point source searches in IceCube are followed here [Bra+10; Bra+08].

The per-event distributions describe the main separation power between signal and background hypotheses in combination with the mixing portions $\lambda_{i,S/B}$ by introducing a priori knowledge in defining signal- and background-like regions in the tested parameter space. The better these distributions are able to separate signal and background regions, the more sensitive the analysis becomes, but also the more bias towards specific model choice is introduced. A common approach with known good separation power is to combine contributions from spatial clustering and energy information, where the first one is inherent to the tested point source hypothesis and the latter providing additional information under certain assumptions of signal flux shapes. For time-dependent analyses, an additional time-dependent part is introduced.

In their general form, the model PDFs S_i and B_i are multi-dimensional composite PDFs. For the common approach using spatial, energy and time information, the resulting PDFs would have five dimensions, being possibly correlated in the variables declination, right ascension, energy proxy, the spatial uncertainty estimator and the event times. However, for most IceCube point source searches, the signal and background contributions are written as independent products of a spatial, an energy and a time-dependent part as

$$S_{i,k} = S(\vec{x}_i, \vec{x}_{\mathrm{src},k}, E_i|\gamma) = S^S(\vec{x}_i, \vec{x}_{\mathrm{src},k}) \cdot S^E(E_i, \delta_i|\gamma) \cdot S^T(t_i, t_k) \tag{5.10}$$

and

$$B_{i,k} = B(\delta_i, E_i|\phi_{\mathrm{BG}}) = B^S(\delta_i) \cdot B^E(E_i, \delta_i|\phi_{\mathrm{BG}}) \cdot B^T(t_i, t_k) \tag{5.11}$$

where γ is the shape parameter of a signal flux usually assumed to be a power law $\propto E^{-\gamma}$ and ϕ_{BG} stands for a flux model of the atmospheric neutrino flux describing the background flux dependency. The event times t_i and source times t_k define the time dependent emission model and δ_i is the declination angle, described in more detail in chapter 4. The choice of splitting the PDF in several independent terms happens for symmetry reasons and to allow the usage of approximate analytic forms of the PDF terms. The first step to arrive at the split PDF form, is to apply the law of total probability [CB02], which dissects the composite PDF into marginal distributions

$$f(x_1, \ldots, x_n) = P(x_1) \cdot P(x_2|x_1) \cdot P(x_3|x_1x_2) \ldots P(x_n|x_1 \ldots x_{n-1}) \ . \tag{5.12}$$

This splits the combined PDF into products of marginal distributions. By neglecting the marginal dependency e.g. of the split off energy PDF on the spatial resolution proxy or the energy dependence on the spatial terms, the standalone PDFs in the following sections can be derived. Because of the special location and the resulting symmetry of the IceCube detector, the right ascension dependency is often dropped. Also, for the spatial PDF, it is chosen to replace the general form with an analytic Gaussian PDF as it resembles the true distribution closely enough but is much easier to handle. Note, that all these simplifications and assumptions influence the shape of the obtained test statistics and may lead to deviations of the expected shape from the application of Wilks' theorem. Also note, that only variables known on experimental data can be used, because no simulation truth is available on actual data.

5.2.1. Spatial distribution

The most important part in the search for neutrino point sources is the spatial clustering of events around a point in the sky. Without the spatial term, the analysis would be insensitive to the main hypothesis of having a localized excess of neutrino events from a certain location in the sky. For data samples used in point source searches, a reconstructed estimate of the per event uncertainty is available. This estimator is built from the positional reconstruction Likelihood fit and is constructed assuming a symmetric, two-dimensional Gaussian distribution describing the reconstruction uncertainty. The value is obtained by scanning the reconstruction Likelihood on a grid and fitting a two-dimensional parabola through the sampled points to be compliant with the assumed underlying Gaussian distribution. To be even easier to apply, it is further assumed that the underlying distribution is symmetric in the two directional angles. To obtain the symmetrized covariance matrix from the generally tilted form, the two-dimensional covariance matrix

$$\begin{pmatrix} \sigma_a^2 & \sigma_b^2 \\ \sigma_b^2 & \sigma_c^2 \end{pmatrix} \tag{5.13}$$

can be transformed in its diagonal form. The new covariance ellipsis axes then have the values

$$\sigma_{1,2}^2 = \frac{\sigma_a^2 + \sigma_b^2}{2} \pm \sqrt{(\sigma_a^2 + \sigma_b^2)^2 + 4\sigma_c^2} \ . \tag{5.14}$$

Demanding that the half-axes are of equal length, the radicand needs to vanish, leaving the relation

$$\sigma_1^2 = \sigma_2^2 = \frac{\sigma_a^2 + \sigma_b^2}{2} \ , \tag{5.15}$$

which is used to circularize the covariances obtained from the grid scan. Because the Gaussian is thus of circular shape, only the radial distance, or space angle, from the

assumed source position the each event's position is needed

$$\cos(\Psi_{i,k}) = \vec{x}_k \cdot \vec{x}_i = \cos(\alpha_i - \alpha_k) \cdot \cos(\delta_i)\cos(\delta_k) + \sin(\delta_i)\sin(\delta_k) \ , \tag{5.16}$$

which can be derived from the scalar product in spherical coordinates with the angles defined by the equatorial coordinate system convention.

Alternatively, the same value can be transformed and used for the symmetric Kent distribution [Ken82] for the per event spatial distribution instead. The Kent distribution is the pendant of the symmetric, two-dimensional Gaussian distribution, but is correctly normalized on the sphere and is useful for larger uncertainties for example when investigating cascade-like events. For tracks, the good angular resolution of about 1° justifies the use of the simpler and more familiar Gaussian distribution as both distributions become virtually indistinguishable for small uncertainties.

In general, the joint probability for an event i to spatially originate from a source k can be obtained by a convolution of the two separate spatial PDFs. One part describes the intrinsic distribution for the source and the other part the intrinsic distribution of the event itself. In a search for point sources at known positions, the distribution of a source position is represented by a delta distribution. In searches for spatially extended sources a Gaussian profile is usually assumed. The per-event probability distribution is assumed to be a Gaussian PDF, which is connected to the construction of the per-event-uncertainty from a parabolic fit of the scanned Likelihood space, as described above or a bootstrap algorithm. The resulting spatial signal distribution, describing the probability of an event being spatially correlated to a given source with density profile $f(\vec{x}_k)$, can thus be expressed as a convolution of the Gaussian per-event part and source distribution for the fixed source position

$$S^S(\vec{x}_i, \vec{x}_k) = \int_\Omega \frac{1}{2\pi\sigma_i^2} \exp\left(-\frac{|\vec{x} - \vec{x}_i|^2}{2\sigma_i^2}\right) \cdot f(\vec{x}_k - \vec{x}) \mathrm{d}\vec{x} \ . \tag{5.17}$$

For the point-source hypothesis, $f(\vec{x}_k)$ can be replaced with a delta distribution $\delta(\vec{x}_k)$ yielding the often used expression

$$S^S(\vec{x}_i, \vec{x}_k) = \frac{1}{2\pi\sigma_i^2} \exp\left(-\frac{|\vec{x}_k - \vec{x}_i|^2}{2\sigma_i^2}\right) \tag{5.18}$$

for the spatial signal PDF. Assuming extended sources with a Gaussian density profile would follow the same scheme and an analytic solution for the convolution of two Gaussian distributions exists, resulting in a substitution of $\sigma_i \to \sqrt{\sigma_i^2 + \sigma_k^2}$ [Bro14]. Note, that the energy dependence of the signal PDF is implicitly included in the per-event uncertainties marginal distribution. The marginal term, that needs to be split-off in the application of

the law of total probability, resembles the energy distribution, which is then dealt with separately.

The spatial background distribution is constructed similarly to the signal case in equation (5.17). Because IceCube is a nearly right ascension symmetric detector at the South Pole, the distribution is assumed to be declination-dependent only, which holds the better the larger the regarded time windows are. This may break down, however, for time scales short enough that the earth's rotation does not smear out the slightly asymmetric distribution in azimuth angle. The declination-dependent PDF is written in a general form here and can, for example, be constructed by computing histograms of experimental data, which is described later in more detail. The spatial background distribution can then be written as

$$B^S(\delta_i) = \frac{1}{2\pi} \cdot P(\sin(\delta_i)) \ , \tag{5.19}$$

where the first factor is the uniform distribution in right ascension and the latter indicating, the often alternatively used, dependence on the sine of declination δ. Note that the background distribution is only depending on the event position, as background events are not expected to have any correlation with a source, by definition. This description neglects the per-event uncertainty though. In principle, the same method that was used to construct the convoluted signal PDF can be applied to the construction of the background distribution. With

$$B^S(\vec{x}_i) = \int_\Omega \hat{B}^S(\vec{x}) \cdot \exp\left(-\frac{|\vec{x} - \vec{x}_i|^2}{2\sigma_i^2}\right) \mathrm{d}\vec{x} \tag{5.20}$$

the per-event declination distribution would be described in full detail. However, as the intrinsic background PDF $\hat{B}^S$ does not change much with declination and a closed form analytic description as in the Gaussian case for the signal PDF in (5.17) is not easily possible with $\hat{B}^S$ derived from histograms, the per-event-uncertainty is neglected.

5.2.2. Energy distribution

In addition to the spatial clustering, the event's energy can also provide a powerful separation argument and lead to a large improvement in sensitivity [Bra+08]. As the energy distribution of atmospheric neutrinos can approximately be described by a power law $\phi_{\mathrm{BG}}(E) \propto E^{-3.7}$ and the astrophysical signal by a harder spectrum around $\phi(E)_S \propto E^{-2}$, higher energy events are more likely to originate from an extraterrestrial source rather than having been created in the atmosphere. In the PDFs, the energy dependence can only be taken into account with energy estimators of the true neutrino energy E_ν because the information must also be available on measured data, not knowing the true neutrino energy. Formally, that mapping can be written as an integration using

the law of total probabilities of the distribution of the energy proxy of the event with the probability of obtaining a true neutrino energy under the current flux hypothesis

$$\hat{S}^E(E,\vec{x}|\gamma) = \int_{E_\nu}\int_{\Omega_\nu} P(E,\vec{x}|E_\nu,\vec{x}_\nu)\cdot P(\vec{x}_\nu,E_\nu|\gamma)\,\mathrm{d}E_\nu d\vec{x}_\nu \ , \tag{5.21}$$

where γ is the shape parameter of an assumed signal power law flux.

For background, the same reasoning applies and the flux model is substituted for one describing the atmospheric neutrino background instead

$$\hat{B}^E(E,\vec{x}|\phi_{\mathrm{BG}}) = \int_{E_\nu}\int_{\Omega_\nu} P(E,\vec{x}|E_\nu,\vec{x}_\nu)\cdot P(\vec{x}_\nu,E_\nu|\phi_{\mathrm{BG}})\,\mathrm{d}E_\nu d\vec{x}_\nu \tag{5.22}$$

to obtain the intrinsic distribution.

In practice, the integrals may be obtained using histograms in reconstructed declination and an energy estimator from simulations for signal and from either simulations or measured data for the background distributions. By computing the histograms on the proxy variables directly, the integrals are obtained automatically in each bin from the simulation procedure. This is because each bin contains the superposition of the fraction of true neutrino energies contributing to the proxy value considered in the bin.

To obtain the convolved PDFs, that also take into account the per event uncertainty for each event in energy and position, the same ansatz as for the signal PDFs in section 5.2.1 can be used

$$S^E(E_i,\delta_i|\gamma) = \int_E\int_\Omega f(\vec{x}_i,E_i)\hat{S}^E\,\mathrm{d}E\mathrm{d}\vec{x} \tag{5.23}$$

$$B^E(E_i,\delta_i|\phi_{\mathrm{BG}}) = \int_E\int_\Omega P(E_i,\delta_i|E_\nu)\cdot P(E_\nu|\phi_{\mathrm{BG}})\mathrm{d}E_\nu \ . \tag{5.24}$$

In the majority of analyses, a delta distribution is used for the per-event function in the last step, for the same reasons quoted for the spatial background PDF. Also, the distribution is normalized independently of the spatial PDFs, although the declination occurs in both of them. This may be done to simplify the computation and housekeeping in the analysis code because it avoids higher dimensional PDF constructions. Additionally, when inferring higher-dimensional PDFs from data, the required statistic may exceed the available number of measured events and a compromise between robust PDF estimation and affordable approximations is considered.

5.2.3. Time dependency

When testing for time-dependent emission models, the time-dependent PDFs $S^T_{i,k}(t_i, t_k)$ and $B^T_{i,k}(t_i, t_k)$ need to be incorporated, which depend on each event's time and their occurrences relative to the temporal evolution of the sources. The assumption is then, that each source only emits neutrinos as given by $S^T_{i,k}(t_i, t_k)$. The background can in general also be time dependent to account e.g. for seasonal variations in the detector rate. Because of the precise timing information available per event, there is no relevant time uncertainty that needs to be convolved into the intrinsic PDFs.

5.3. Time-dependent Likelihood

To test for a time-dependent emission in this analysis, the general extended Likelihood is altered to a form similar to what is usually called *Gamma Ray Burst Likelihood*[10] [Aar+18a; Aar+15a; Aar+17c]. As the name may indicate, the source emission is assumed to be per-burst with a fluence Φ rather than a time-dependent flux, where fluence means the integral form of a time-dependent flux, so particles received per energy and unit area only.

This includes explicit assumptions about the temporal source emission PDFs and simplifications of the general Likelihood formula introduced before. The simplifications need to be applied to ensure the proper handling of small time windows. For relatively small burst time windows, only a few events are left in each window making it hard to fit a larger amount of free model parameters to the data. Therefore the number of free parameters needs to be reduced as much as possible without introducing too many a priori assumptions. That allows to stick to a rather general search method because of the unknown source types.

Here, using the burst model, a rather general assumption about the source emission is made. The time PDFs are therefore constructed using rectangle functions

$$\mathrm{rect}(t) = \Theta\left(t + \frac{1}{2}\right) \cdot \Theta\left(t - \frac{1}{2}\right) = \begin{cases} 1 & \text{, if } |t| \leq \frac{1}{2} \\ 0 & \text{, if } |t| > \frac{1}{2} \end{cases} , \tag{5.25}$$

[10] Named after the original purpose of searching for emission from a Gamma Ray Burst catalogue. The concept can be applied to other sources testing a similar hypothesis of emission within a defined time window.

where Θ is the Heaviside step function [AS74]. This way, each source is having only a non-zero emission contribution within its pre-defined source time window

$$S_{i,k}^{T} = B_{i,k}^{T} = T_k(t_i) \coloneqq \text{rect}\left(\frac{t_i - \frac{t_k^1 - t_k^0}{2}}{t_k^1 - t_k^0}\right) \quad . \tag{5.26}$$

This effectively cuts out a subset of events around the sources time stamps t_k and the corresponding time interval around each source $[t_k^0, t_k^1]$ and is a background rejection technique only, because any underlying temporal dependence on the source emission flux is discarded. The simplest case is then to have each source in its own, non-overlapping time window so that each source has a unique set of events belonging to it. Note again, that no separation power stems from these time PDFs, they are merely used to reduce the background rate under the assumption of a temporally concentrated emission. In this light, a per-burst search is not a "real" time-dependent search. For the ease of use, a time PDF is only defined to effectively cut out the interesting burst regions.

One important simplification of the general Likelihood applied here, is that the background expectations are not fitted, but rather fixed from the integrated off-time data rate over the range of the background time PDFs. This decreases the number of parameters to fit for because it unifies and fixes the background estimators to

$$\hat{\lambda}_{k,B} = \hat{\lambda}_{k,B}^{(0)} = \langle \lambda_{k,B} \rangle \quad . \tag{5.27}$$

The test statistic then turns to the form

$$-2\ln\hat{\Lambda} = -2\sum_{k=1}^{N_{\text{srcs}}} \hat{\lambda}_{k,S} + 2\sum_{i=1}^{N} \ln\left(\frac{\sum_{k=1}^{N_{\text{srcs}}} \hat{\lambda}_{k,S} S_{i,k}}{\sum_{k=1}^{N_{\text{srcs}}} \langle \lambda_{k,B} \rangle B_{i,k}} + 1\right) \quad . \tag{5.28}$$

One further Likelihood simplification is performed, which is necessary because a large number of free parameters cannot be fitted to very few events in a low background analysis. The relative signal expectations of each source are fixed a priori and the Likelihood is only fitted for a total signal expectation value

$$\lambda_{k,S} = n_S \cdot w_k \tag{5.29}$$

with a free global signal strength parameter n_S and weights w_k normalized so that

$$\sum_{k=1}^{N_{\text{srcs}}} w_k = 1 \quad . \tag{5.30}$$

The test statistic can then be expressed by

$$-2\ln\hat{\Lambda} = -2\hat{n}_S + 2\sum_{i=1}^{N} \ln\left(\frac{\hat{n}_S \sum_{k=1}^{N_{\text{srcs}}} w_k S_{i,k}}{\sum_{k=1}^{N_{\text{srcs}}} \langle \lambda_{k,B} \rangle B_{i,k}} + 1\right) \quad . \tag{5.31}$$

The a priori fixed weights resemble the expectation from every single source at the detector. They can, therefore, depend on the explicitly chosen source emission model and the detection efficiency depending on the source locations in the detector. Note that the a priori chosen weights should match the true, but usually unknown, emission scenario as much as possible to obtain a good analysis sensitivity. If the true scenario strongly differs from the assumed weights, the performance of the analysis drops. Generalized assumptions can be made though, in favour of the ability to test a broader range of emission scenarios, but losing performance when nature indeed chose a specific model realisation.

5.3.1. Single sample stacking case

Using the assumption of independent time windows for the sources can further simplify the test statistic. The expression can be rearranged to an explicit sum of logarithms that better resembles the uniqueness of each source in its time window.

Starting from the test statistic expression (5.31) and from the definition of the unique time windows, it can be seen that each event i can only contribute to a single source k. The event belongs to the source in which time window it falls or to no source at all, where the time windows are defined as in (5.26)

$$T_k(t_i) := \mathrm{rect}\left(\frac{t_i - \frac{t_k^1 - t_k^0}{2}}{t_k^1 - t_k^0}\right) \quad . \tag{5.32}$$

The stacking sum then turns to

$$-2\ln\hat{\Lambda} = -2\hat{n}_S + 2\sum_{i=1}^{N}\ln\left(\frac{\hat{n}_S\sum_{k=1}^{N_{\mathrm{srcs}}} w_k S_{i,k}\delta_{\{i,k|T_k(t_i)\neq 0\}}}{\sum_{k=1}^{N_{\mathrm{srcs}}}\left\langle\lambda_{k,B}\right\rangle B_{i,k}\delta_{\{i,k|T_k(t_i)\neq 0\}}} + 1\right) \tag{5.33}$$

$$= -2\hat{n}_S + 2\sum_{i=1}^{N}\ln\left(\frac{\hat{n}_S\left[0+\cdots+0+w_{k^*}S_{i,k^*}+0+\cdots+0\right]}{\left[0+\cdots+0+\left\langle\lambda_{k^*,B}\right\rangle B_{i,k^*}+0+\cdots+0\right]} + 1\right) \tag{5.34}$$

$$= -2\hat{n}_S + 2\sum_{i=1}^{N}\sum_{k=1}^{N_{\mathrm{srcs}}}\ln\left(\frac{\hat{n}_S w_k S_{i,k}}{\left\langle\lambda_{k,B}\right\rangle B_{i,k}} + 1\right) \quad , \tag{5.35}$$

where k^* means the k that fulfils the condition $T_k(t_i) \neq 0$ and in the last step it is used that

$$\ln\left(\frac{\hat{n}_S w_{k\neq k^*} S_{i,k\neq k^*}}{\left\langle\lambda_{k\neq k^*,B}\right\rangle B_{i,k\neq k^*}} + 1\right) = \ln(0+1) = 0 \quad . \tag{5.36}$$

5.3.2. Multiple samples stacking case

To add more sources to the unique time window scenario, data at the times at which the added source events occurred needs to be taken into account. In each IceCube data taking season, there may be a change in the data taking procedure, for example in the trigger system. Also, different sample selection methods may yield different expectation values for the number of events in each sample. These changes and differences must be included in the expectations for the samples used in the single Likelihood test. An additional weighting scheme can be considered to account for the differences. The reasoning is quite similar to the a priori n_S splitting weights w_k for the stacking case for the single sample Likelihood as seen in (5.29).

To add another sample, the individual logarithmic Likelihoods can be summed up, because the tested datasets are independent, which yields the combined test statistic

$$-2\ln\hat{\Lambda} = \sum_{j=1}^{N_{\text{sam}}} -2\ln\hat{\Lambda}_j(\hat{n}_{S,j}) \tag{5.37}$$

$$= \sum_{j=1}^{N_{\text{sam}}} \left[-2\hat{n}_{S,j} + 2\sum_{i=1}^{N_j}\sum_{k=1}^{N_{\text{srcs,j}}} \ln\left(\frac{\hat{n}_{S,j} w_{k,j} S_{i,k,j}}{\langle \lambda_{k,j,B} \rangle B_{i,k,j}} + 1 \right) \right] \ , \tag{5.38}$$

where individual free $n_{S,j}$ signal parameters are introduced and the stacking weights $w_{k,j}$ per source in the sample are constructed like the usual single sample stacking weights w_k and are still normalized over all sources N_{srcs} per sample

$$\sum_{k=1}^{N_{j,\text{srcs}}} w_{k,j} = 1 \ . \tag{5.39}$$

Only the number of events per sample N_j and the sources belonging to sample j are considered for each Likelihood, as well as the weights $w_{k,j}$, PDFs $S_{i,k,j}$ and $B_{i,k,j}$ and the background expectations per source $\langle \lambda_{k,j,B} \rangle$ for each sample. Again, a priori information about the expected number of signal events originating from each sample can be used and a global free signal strength parameter n_S is introduced with

$$n_{S,j} = w_j n_S \ . \tag{5.40}$$

To calculate the a priori weights w_j the law of total probability is applied

$$w_j = P(j) = \sum_{k=1}^{N_{\text{srcs}}} P(j|k) \cdot P(k) = \sum_{k=1}^{N_{\text{srcs}}} \underbrace{P(j,k)}_{\text{unknown}} \ , \tag{5.41}$$

because only the conditional probability contribution $P(j|k)$ from each source k per sample j is known, but not the joint distribution $P(j,k)$. $P(j|k)$ is the probability of getting signal from source k within sample j, normalized over all samples

$$\sum_{j=1}^{N_{\mathrm{sam}}} P(j|k) = 1 \ . \tag{5.42}$$

Additionally, $P(k)$ is the probability of getting signal from source k at all within any sample, separately normalized over all sources

$$\sum_{k=1}^{N_{\mathrm{srcs}}} P(k) = 1 \ . \tag{5.43}$$

These relations can also be written in a concise matrix notation

$$\begin{pmatrix} w_1 \\ \vdots \\ w_{N_{\mathrm{sam}}} \end{pmatrix} = \begin{pmatrix} P(j=0|k=0) & \dots & P(j=0|k=N_{\mathrm{srcs}}) \\ \vdots & \ddots & \vdots \\ P(j=N_{\mathrm{sam}}|k=0) & \dots & P(j=N_{\mathrm{sam}}|k=N_{\mathrm{srcs}}) \end{pmatrix} \cdot \begin{pmatrix} P(k=0) \\ \vdots \\ P(k=N_{\mathrm{srcs}}) \end{pmatrix} \ . \tag{5.44}$$

The unnormalized, conditional signal expectation values can be obtained in each sample by calculating the expected number of events from a signal simulation which usually differs for each detector configuration and sample selection criteria. These values can then be used to normalize the matrix per column and construct the $P(k)$ vector by summing over each column per source k.

The most complex weighting case in this scenario would be having multiple sources that have time PDFs overlapping in their emission region and are also leaking into another data sample. The formalism then still applies, and the sample splitting weights can be obtained by integrating the time emission PDFs per sample to obtain the relative emission strength for the source portions lying in each sample. These are then multiplied with the usual declination dependent weights per sample to form the $P(j|k)$ entries of the matrix in expression (5.44). The weighting within each sample wouldn't be affected and is still constructed as explained in the previous section 5.3.1.

For the special case treated here, with each source having its unique time window and also falling exclusively in a single sample, each column has only a single entry which is 1 after the trivial normalization. The probabilities $P(k)$ can be obtained by using the un-normalized source stacking weights regardless of the sample $\tilde{w}_k$ and re-normalize them over all sources in all samples

$$P(k) = \frac{\tilde{w}_k}{\sum_{m=1}^{N_{\mathrm{srcs}}} \tilde{w}_m} \ . \tag{5.45}$$

Because of the special matrix properties used here, the explicit weights w_j then turn out to be global re-normalizations of the un-normalized single sample weights $\tilde{w}_k$ with

$$w_j = \sum_{k=1}^{N_{\mathrm{srcs}}} P(j|k) \cdot P(k) = \sum_{k=1}^{N_{\mathrm{srcs}}} \delta_{\{k,j|T_j(t_k)\neq 0\}} \cdot \frac{\tilde{w}_k}{\sum_{m=1}^{N_{\mathrm{srcs}}} \tilde{w}_m} \tag{5.46}$$

$$= \sum_{k=1}^{N_{j,\mathrm{srcs}}} \frac{\tilde{w}_{k,j}}{\sum_{m=1}^{N_{\mathrm{srcs}}} \tilde{w}_m} \ , \tag{5.47}$$

where T_j is a unique rectangle function for each sample, equally used as the rectangle function utilized to describe the unique time windows per source in each sample. $\tilde{w}_{k,j}$ are the un-normalized stacking weights per sample.

Now the numerator turns out to be exactly the per sample normalization of the per sample splitting weights, which is the sum of all weights for the subset of all sources that actually are in the sample. The full multi-sample test statistic then reads

$$-2\ln\hat{\Lambda} = -2\hat{n}_S + 2\sum_{j=1}^{N_{\mathrm{sam}}}\sum_{i=1}^{N_j}\sum_{k=1}^{N_{\mathrm{srcs,j}}} \ln\left(\frac{\hat{n}_S \frac{\tilde{w}_{k,j}}{\sum_{m=1}^{N_{\mathrm{srcs}}} \tilde{w}_m} S_{i,k,j}}{\langle\lambda_{k,j,B}\rangle\, B_{i,k,j}} + 1\right) \ , \tag{5.48}$$

where $\tilde{w}_{k,j}$ are the un-normalized weights per source with respect to the expected signal in their corresponding sample and are normalized over all un-normalized source expectations $\tilde{w}_m$ in all samples regarded. This expression nicely demonstrates the circumstances here, namely that each source is independent of each other source and lies completely in a single data sample, so the whole underlying Likelihood completely factorizes in events, sources and samples.

5.4. Time-integrated Likelihood

The standard time integrated Likelihood formula used in IceCube point source searches can also be derived from the general, extended Likelihood formula. A different approximation than in the time-dependent case is used, which takes into account the usually larger statistics in a time-integrated sample as all events count and not only these in temporal coincidence with any source.

5.4.1. Single sample stacking case

Starting again from the general form

$$-2\ln\hat{\Lambda} = -2\left(\sum_{k=1}^{N_{\text{srcs}}}\hat{\lambda}_{k,S}+\hat{\lambda}_{k,B}-\hat{\lambda}_{k,B}^{(0)}\right)+2\sum_{i=1}^{N}\ln\left(\frac{\sum_{k=1}^{N_{\text{srcs}}}\left(\hat{\lambda}_{k,S}S_{i,k}+\hat{\lambda}_{k,B}B_{i,k}\right)}{\sum_{k=1}^{N_{\text{srcs}}}\left(\hat{\lambda}_{k,B}^{(0)}B_{i,k}\right)}\right)\ , \tag{5.49}$$

the following approximation can be used

$$\sum_{k=1}^{N_{\text{srcs}}}\hat{\lambda}_{k,S}+\hat{\lambda}_{k,B}\approx\sum_{k=1}^{N_{\text{srcs}}}\hat{\lambda}_{k,B}^{(0)}\approx N\ . \tag{5.50}$$

This means the Poisson fluctuations of the sample size are neglected. Also, the second part is usually valid if the amount of signal expected in the data is small compared to the amount of background-like events.

These approximations cancel the Poisson term in front of the sum and leave

$$-2\ln\hat{\Lambda} = 2\sum_{i=1}^{N}\ln\left(\frac{\sum_{k=1}^{N_{\text{srcs}}}\left(\hat{\lambda}_{k,S}S_{i,k}+\hat{\lambda}_{k,B}B_{i,k}\right)}{\sum_{k=1}^{N_{\text{srcs}}}\left(\hat{\lambda}_{k,B}^{(0)}B_{i,k}\right)}\right)\ . \tag{5.51}$$

For the time-independent part, the background distributions $B_{i,k}$ are all the same, because they only depend on each event's location and not on any source related parameters anymore. Thus the background PDFs can be written as

$$\hat{\lambda}_{k,B}=\frac{1}{N_{\text{srcs}}}\hat{\lambda}_B\ \text{ and }\ B_{i,k}=B_i \tag{5.52}$$

and with approximation (5.50) the denominator in the logarithm can be simplified to

$$\frac{1}{\sum_{k=1}^{N_{\text{srcs}}}\left(\hat{\lambda}_{k,B}^{(0)}B_{i,k}\right)}=\frac{1}{B_i\sum_{k=1}^{N_{\text{srcs}}}\hat{\lambda}_{k,B}^{(0)}}=\frac{1}{NB_i}\ . \tag{5.53}$$

Using the same argument for the background distributions in the nominator, the stacking test statistic becomes

$$-2\ln\hat{\Lambda} = 2\sum_{i=1}^{N}\ln\left(\frac{\sum_{k=1}^{N_{\text{srcs}}}\left(\hat{\lambda}_{k,S}S_{i,k}+\frac{1}{N_{\text{srcs}}}\hat{\lambda}_B\right)}{NB_i}\right) \tag{5.54}$$

$$= 2\sum_{i=1}^{N}\ln\left(\frac{\sum_{k=1}^{N_{\text{srcs}}}\left(\hat{\lambda}_{k,S}S_{i,k}\right)+\hat{\lambda}_B B_i}{NB_i}\right)\ . \tag{5.55}$$

Using the fixed expectation approximation from (5.50) again, the background parameter $\hat{\lambda}_B$ can be eliminated leaving N_{srcs} free signal parameters, one for each source

$$-2\ln\hat{\Lambda} = 2\sum_{i=1}^{N}\ln\left(\frac{\sum_{k=1}^{N_{\text{srcs}}}\left(\hat{\lambda}_{k,S}S_{i,k}\right)+\left(N-\sum_{k=1}^{N_{\text{srcs}}}\hat{\lambda}_{k,S}\right)B_i}{NB_i}\right) \tag{5.56}$$

$$= 2\sum_{i=1}^{N}\ln\left(\frac{\sum_{k=1}^{N_{\text{srcs}}}\left(\hat{\lambda}_{k,S}S_{i,k}\right)}{NB_i}-\frac{\sum_{k=1}^{N_{\text{srcs}}}\hat{\lambda}_{k,S}}{N}+1\right)\ . \tag{5.57}$$

where in the last step the equation is slightly rearranged to show the commonly used test statistic formula in the general time integrated stacking case.

The N_{srcs} free signal strength parameters $\lambda_{k,S}$ can again be reduced to a single signal strength parameter n_S when a priori knowledge about the source class proportions is used via

$$\lambda_{k,S} = n_S\cdot w_k \ \text{ and } \ \sum_{k=1}^{N_{\text{srcs}}} w_k = 1\ . \tag{5.58}$$

The test statistic can then be further reduced to its final form

$$-2\ln\hat{\Lambda} = 2\sum_{i=1}^{N}\ln\left(\frac{\hat{n}_S\sum_{k=1}^{N_{\text{srcs}}}\left(w_kS_{i,k}\right)}{NB_i}-\frac{\hat{n}_S\sum_{k=1}^{N_{\text{srcs}}}w_k}{N}+1\right) \tag{5.59}$$

$$= 2\sum_{i=1}^{N}\ln\left(\frac{\hat{n}_S}{N}\left(\frac{\sum_{k=1}^{N_{\text{srcs}}}(w_kS_{i,k})}{B_i}-1\right)+1\right)\ . \tag{5.60}$$

Sometimes the signal sum term is abbreviated to

$$S_i^{(\text{tot})} := \sum_{k=1}^{N_{\text{srcs}}}\left(w_kS_{i,k}\right) \tag{5.61}$$

and only in this case, with a priori fixed weights w_k, the replacement of the single source signal term S_i with the summed signal term $S_i^{(\text{tot})}$ is valid

$$\sum_{i=1}^{N}\ln\left(\frac{\hat{n}_S}{N}\left(\frac{S_i}{B_i}-1\right)+1\right)\rightarrow\sum_{i=1}^{N}\ln\left(\frac{\hat{n}_S}{N}\left(\frac{S_i^{(\text{tot})}}{B_i}-1\right)+1\right) \tag{5.62}$$

to quickly change from a single to a stacked source hypothesis.

5.4.2. Multiple samples stacking case

Construction of the multi-sample Likelihood formula in the time-integrated case is done exactly as in the time-dependent case before by starting with the sample weight relation

$$n_{S,j} = n_S\cdot w_j \ \text{ with } \ w_j = P(j) = \sum_{k=1}^{N_{\text{srcs}}} P(j|k)\cdot P(k) \tag{5.63}$$

inserted in the familiar combination of single sample Likelihoods

$$-2\ln\hat{\Lambda} = \sum_{j=1}^{N_{\text{sam}}} -2\ln\hat{\Lambda}_j(\hat{n}_{S,j}) \tag{5.64}$$

$$= \sum_{j=1}^{N_{\text{sam}}} \left[2\sum_{i=1}^{N_j} \ln\left(\frac{\hat{n}_{S,j}}{N_j} \left(\frac{\sum_{k=1}^{N_{\text{srcs}}} (w_{k,j} S_{i,k,j})}{B_{i,j}} - 1 \right) + 1 \right) \right] \tag{5.65}$$

$$= \sum_{j=1}^{N_{\text{sam}}} \left[2\sum_{i=1}^{N_j} \ln\left(\frac{\hat{n}_S \cdot w_j}{N_j} \left(\frac{\sum_{k=1}^{N_{\text{srcs}}} (w_{k,j} S_{i,k,j})}{B_{i,j}} - 1 \right) + 1 \right) \right] \quad . \tag{5.66}$$

The number of events N_j is now related to the number of events per sample j and the number of sources is the same in each sample, because of the steady state emission scenario. Also the PDFs $S_{i,k,j}$, $B_{i,j}$ and stacking weights $w_{k,j}$ are taken and normalized per sample as seen before in the time dependent Likelihood in section 5.3.

Because all sources contribute during all times and thus in all samples, the weights cannot be written out in a simplified, compact form here, but they still represent the relative sensitivity of a single sample to a given source hypothesis combined with the global sensitivity to a single source across all samples. This may also be seen as a special case for the time-dependent Likelihood weights, where all the time windows for signal and background are as large as the sample livetimes and a true flux scenario is used, where the emitted total flux is proportional to the emission time window length.

A notable difference arises if another global fit parameter is introduced alongside the mandatory n_S. This is often done to better adapt to the unknown signal hypothesis and in a time-integrated analysis, the statistics are usually sufficient to reliably fit an additional parameter. Usually, this parameter describes the signal flux hypothesis and is modelled as a single unbroken power law with spectral index γ_k per source in the energy PDF term. This leads to splitting weights that depend on the actual shape of the assumed signal flux because the sensitivity per sample can change when the flux gets harder or softer

$$w_j(\vec{x}_k, \gamma_k) = \frac{T_j \cdot \int_{E_\nu} A_{j,\text{eff}}(E_\nu, \Omega_k) \cdot \phi(E_\nu, \Omega_k|\gamma_k)\,\mathrm{d}E_\nu}{\sum_{m=1}^{N_{\text{srcs}}} T_m \cdot \int_{E_\nu} A_{m,\text{eff}}(E_\nu, \Omega_k) \cdot \phi(E_\nu, \Omega_k|\gamma_k)\,\mathrm{d}E_\nu} \quad . \tag{5.67}$$

More details on how these weights are constructed follow in the next section.

5.5. A priori weight selection

The a priori weights for the expected signal of a source in a specific sample should match the true emission model as closely as possible to gain optimal analysis performance. Note

that the weights resemble the expected relative flux at the detector. For example, for an IceCube-like detector that only measures the Northern sky, all weights for sources on the Southern sky would be zero, regardless of the true intrinsic emission strength, because no signal is ever detected.

To construct the weights that actually distribute the total expected amount of signal to the expected contribution from each source, signal simulation can be used to estimate the signal detection efficiencies. This is done by calculating the total number of expected events from each source from a given emission scenario at detector level. Depending on the assumed emission scenario, the weights might depend on any source parameter, usually the source position, the time and the spectral emission behaviour of the sources. For sources that are not point-like in any parameter but show a functional dependency, the detector response must be convolved with the source parameter distribution to obtain the effective weight.

For the spatial weight contribution, the weights are dependent only on the source positions and the signal response of the detector at their positions. The assumption that IceCube is right ascension symmetric yields stacking weights that only depend on the source declinations. For extended sources the detector response needs to be convolved with the source extension density profile incorporating efficiencies from multiple detector regions.

When using a time-dependent emission scenario the number of expected events varies with the emission type. Because the detector response to signal usually does not vary with time, only the relative differences in the time window functions matter for the stacking weights. For example in a per-burst scenario, the amount of signal events is independent of the considered emission time scale and a time-integrated fluence is assumed rather than a time-dependent flux. The cases regarded in this thesis both lead to a vanishing temporal dependence. In the time-dependent analysis, a fluence scenario is considered and all sources have the same time window length, making the temporal emission equal by design. Even with time windows that differ in length between each other, the expected signal is equal from all bursts by definition. In the time-independent case, all source fluxes have the same linear temporal dependence

$$\int_T \phi \, \mathrm{d}t = T \cdot \phi \tag{5.68}$$

and are expected to steadily emit for the whole sample livetime, making all integrals over the temporal part equal. Only when considering fluxes differential in time with different emission profiles, the integral contributions differ and the stacking weights become truly time-dependent. It is also possible to split time-dependent sources across multiple samples with this formalism. If they are assumed to depend on a flux, then the portion of the flux PDF in each sample can be computed. If using a per-burst scenario

the time evolution information is lost. Therefore, it is not explicitly possible to split a burst time window across multiple samples. A fair and general approach might be to assume a uniform temporal dependency and again see how much of the integral lies in each sample. Repeating sources in per-burst scenarios can be treated by assuming that each burst is a separate source and making sure, that time windows do not overlap. The latter is needed because a source is not expected to emit into two bursts at the same time. The third common scenario is that sources also vary in their energy dependence for their intrinsic flux strengths. Usually, this happens in the form of altering the spectral index of the assumed power-law flux. This means the detector response is additionally depending on the spectral index as the expected number of events per declination changes depending on the spectrum's steepness.

To summarize, note that the source weights should represent the estimated splitting of the single signal strength fit parameter n_S, reflecting the relative, expected number of events for the whole tested parameter space. Therefore, they do not vary per event, but only per source. It is useful to imagine what happens if the proposed source class emits signal events into the detector and what would be recorded after the detection process.

As an example, a dependency on the source positions $\vec{x}_k$ and spectral indices γ_k of the n_S splitting weight per source k is assumed. For actually calculating the signal efficiency and thus the expected number of events per source N_k at detector level and for the final sample event selection from an intrinsic, linearly time-dependent neutrino flux ϕ, the expression

$$N_k(\vec{x}_k, \gamma_k) = T \cdot \int_{E_\nu} \int_{\Omega_\nu} f(\vec{x}_k - \vec{x}) A_{\text{eff}}(E_\nu, \Omega_\nu) \cdot \phi(E_\nu, \Omega_\nu | \gamma_k) \, \mathrm{d}E_\nu \mathrm{d}\Omega_\nu \tag{5.69}$$

is used. Note the usage of the true neutrino energies and directions, as the interest lies in the mapping of intrinsic flux strength to expected events, not in the performance of spatial or energy reconstruction algorithms. Here, the value of γ_k is taken to be exact and for a point-source hypothesis, the function $f(\vec{x})$ can be replaced with a δ distribution for picking only the integral contribution from the single source position. A_{eff} is the hypothetical detector surface area, which would yield the same number of observed events if it would detect 100 % of the incoming flux compared to the real detector and the applied event selection and maps an intrinsic flux to event counts detected at detector level. The integrated A_{eff} is typically in units cm^2, the flux ϕ in $1/(\mathrm{GeV}\,\mathrm{cm}^2\,\mathrm{s}\,\mathrm{sr})$ and the detector livetime T in s. When using a time-integrated fluence Φ model, the livetime is obsolete and the number of events read

$$N_k \to \frac{N_k}{T} \ . \tag{5.70}$$

instead. The normalized weights per source in a single sample can be constructed by

$$w_k = \frac{N_k}{\sum_{m=1}^{N_{\mathrm{srcs}}} N_m} \quad . \tag{5.71}$$

This effective area formulation holds for calculating the multi sample splitting weights as well as for the expected n_S splitting within a single sample, because it is the most general form of calculating the detector efficiency and the expected number of events for a given flux or fluence hypothesis.

In practice, to obtain the desired number of events for a given signal flux or fluence, simulation data is used to approximate the integral (5.69) using Monte Carlo integration by estimating the unknown distribution via sampling methods. A simulation quantity called OneWeight is used to properly weight neutrino simulation to the number of expected events, being able to compare expectation values obtained from simulation directly to measured data. The OneWeight per event i is defined as [GK05]

$$\mathrm{OneWeight}_i = p_{\mathrm{int}} \frac{\int_\Omega \int_{E_0}^{E_1} \Phi_{\mathrm{gen}}(E_i)\mathrm{d}E\mathrm{d}\Omega}{\Phi_{\mathrm{gen}}(E_i)} A_{\mathrm{gen}} \tag{5.72}$$

$$= p_{\mathrm{int}} \frac{\int_{E_0}^{E_1} \Phi_{\mathrm{gen}}(E_i)\mathrm{d}E}{\Phi_{\mathrm{gen}}(E_i)} A_{\mathrm{gen}} \Omega_{\mathrm{gen}} \quad , \tag{5.73}$$

where p_{int} is the interaction probability for neutrinos forced to interact close to the detection volume[11], Φ_{gen} is the energy fluence used to generate the initial neutrino distribution, usually a power law and A_{gen}, Ω_{gen} are the constant surface and the solid angle over which the initial neutrinos are injected. In the last step, the integration over Ω is carried out because usually, the injection fluence is only energy dependent. By this definition, OneWeight is the inverse of the generating fluence in $\mathrm{GeV\,sr\,cm^2}$ combined with the correction factor for the forced neutrino interaction close to the detection volume. To obtain the number of equivalent data events for a given simulation set, the per event weights

$$N = \sum_i w_i = \sum_i \frac{\Phi_i}{\Phi_{i,\mathrm{gen}}} \tag{5.74}$$

need to be summed up. When using OneWeight to express the generating flux, the number of events can be obtained via

$$N = T \cdot \sum_i \frac{\mathrm{OneWeight}_i \cdot \phi_i}{N_{\mathrm{gen}}} \tag{5.75}$$

[11] Otherwise the simulation efficiency would be very low due to the small interaction probabilities of neutrinos.

or for fluences without the livetime T

$$N = \sum_i \frac{\text{OneWeight}_i \cdot \Phi_i}{N_{\text{gen}}} \ , \tag{5.76}$$

where N_{gen} is the generated total number of events summed over both particle and anti-particle types. This scaling makes sure, that the physical expectation value stays the same, regardless of the number of simulated events. The sum can also be taken across subsamples of a whole data set to obtain differential event counts, e.g. per energy or solid angle to obtain approximations for the analytic integration in formula (5.69).

5.5.1. Intrinsic source weights

Additional intrinsic source weights can be introduced to capture differences in the expected, relative fluxes or fluences from the sources themselves. This is decoupled from the actual detection mechanism and the detector efficiency weights expressed by formula (5.71). The weight selection strongly depends on the used catalogue or source category and can, for example, be a gamma-ray flux or distance weighting [HK18; Aar+17d]. These intrinsic source weights w_k^{src} are independently multiplied with the corresponding detector weights w_k^{det} to form the total source weights used in the stacking

$$w_k := w_k^{\text{det}} \cdot w_k^{\text{src}} \ . \tag{5.77}$$

If the intrinsic source properties are not known or not reliably available, the intrinsic source weights are usually assumed to be equal to trade a potentially worsened performance for avoiding too much model specific bias.

5.5.2. Connecting weighting formulas

The connection to the effective area formula (5.69) with the more practical one using simulation weights is shortly depicted below. From the definition of the effective area

$$A_{\text{eff}}(\Delta E, \Delta\Omega) = A_{\text{gen}} \frac{\hat{N}(\Delta E, \Delta\Omega)}{\hat{N}_{\text{gen}}(\Delta E, \Delta\Omega)} \ , \tag{5.78}$$

where ΔE and $\Delta\Omega$ are arbitrary chosen integration intervals in energy and solid angle, because the effective area is only properly defined under the integral, the number of generated events per interval can be obtained from the flux or fluence assumption used to sample the primary simulation particles

$$\phi_{\text{gen}} = \phi_0 \cdot f(E, \Omega) \ . \tag{5.79}$$

The unit-less functional flux dependency is described in the usually energy and solid angle dependent function $f(E, \Omega)$. Because the generating function is usually uniform and independent in solid angle it follows that $f(E, \Omega) \to f(E) \cdot {}^1/_{\Omega_{\text{gen}}}$. The expected number of simulated primaries in the interval is then given by

$$\hat{N}_{\text{gen}}(\Delta E, \Delta\Omega) = N_{\text{gen}} \cdot \frac{\Delta\Omega}{\Omega_{\text{gen}}} \frac{\int_{E'}^{E'+\Delta E} f(E)\,\mathrm{d}E}{\int_{E_0}^{E_1} f(E)\,\mathrm{d}E} \quad . \tag{5.80}$$

For neutrino simulation, where primaries are forced to interact close to the detection volume, the number of events is given by

$$\hat{N}(\Delta E, \Delta\Omega) = \sum_{i=1}^{N_{\text{gen}}} w_{i,\text{sel}} \cdot p_{i,\text{int}} = \sum_{(i|E_i \in \Delta E, \Omega_i \in \Delta\Omega)} p_{i,\text{int}} \quad , \tag{5.81}$$

where $w_{i,\text{sel}}$ is either 0, if the event is not present or 1 if it is present in the final selection in bin ΔE, $\Delta\Omega$. Now replacing $\hat{N}_{\text{gen}}$ and $\hat{N}$ in the effective area definition yields

$$A_{\text{eff}}(\Delta E, \Delta\Omega) = A_{\text{gen}} \cdot \left(\sum_{(i|E_i \in \Delta E, \Omega_i \in \Delta\Omega)} p_{i,\text{int}} \right) \cdot \frac{\Omega_{\text{gen}}}{\Delta\Omega} \cdot \frac{1}{N_{\text{gen}}} \frac{\int_{E_0}^{E_1} f(E)\mathrm{d}E}{\int_{E'}^{E'+\Delta E} f(E)\mathrm{d}E} \quad . \tag{5.82}$$

Identifying and replacing the OneWeight definition from (5.72), the formula to obtain the effective area estimate from a simulation data set becomes

$$A_{\text{eff}}(\Delta E, \Delta\Omega) = \frac{1}{N_{\text{gen}}\Delta\Omega} \cdot \frac{\left(\sum_{(i|E_i \in \Delta E, \Omega_i \in \Delta\Omega)} \text{OneWeight}_i \cdot f(E_i) \right)}{\int_{E'}^{E'+\Delta E} f(E)\mathrm{d}E} \quad . \tag{5.83}$$

Sometimes a slightly modified version

$$A_{\text{eff}}(\Delta E, \Delta\Omega) = \frac{1}{N_{\text{gen}}\Delta\Omega} \cdot \frac{\sum_{(i|E_i \in \Delta E, \Omega_i \in \Delta\Omega)} \text{OneWeight}_i}{\Delta E} \tag{5.84}$$

is used, which is only valid for small integration intervals, because it assumes an approximately constant generating function f within an interval by simplifying

$$\frac{f(E_i)}{\int_{E'}^{E'+\Delta E} f(E)\mathrm{d}E} \approx \frac{f(E_i)}{f(E') \cdot \Delta E} \approx \frac{f(E_i)}{f(E_i) \cdot \Delta E} = \frac{1}{\Delta E} \quad . \tag{5.85}$$

5.6. Frequentist methods

In this thesis, significances for hypothesis tests are obtained using frequentist methods. This section shortly introduces the relevant terminology and is a summary of the extensive

treatments in [CB02; BL13; Bar89]. The methods used are *point estimation* and *interval estimation*. Usually, the result of a model-dependent point source search, as done here, is a single best fit result. This best fit result is the point in the considered space of free parameters that gives the most likely model to describe the measured data. This is called a point estimate. To also obtain an estimate of the region of the true underlying physics parameters, an interval estimation needs to be performed.

Point estimation is directly connected to *hypothesis testing* because for a given best-fit result, the significance of being compatible with the null hypothesis is wanted, to see if the alternative model is favoured. Therefore, the general procedure is to set the null hypothesis to a background-only assumption or the current understanding of the underlying physics. For a given point estimate, an incompatible result can give reason to reject the null hypothesis and thus open the possibility to claim new discoveries. A p-value p gives the probability to obtain the given or a larger test statistic value under the assumption that the null hypothesis holds

$$p := \int_x^\infty f_{H_0}(-2\ln\lambda)\mathrm{d}(x) \ , \tag{5.86}$$

where $f_{H_0}(-2\ln\lambda)$ is the test statistic distribution under the null hypothesis H_0. The test statistic is generated by doing pseudo experiments by drawing samples from a distribution that well resembles the parameter space of the null hypothesis. A small p-value indicates a strong deviation from the test result from the expected behaviour of the null hypothesis. It does not imply the truth of the alternative hypothesis though, but only that it is unlikely for the data to originate from the null hypothesis distribution.

Using an interval estimation, further information on the possible value of the true parameter can be obtained. In general, a frequentist confidence region $[\theta_0, \theta_1]$ for a parameter θ at a confidence level α is defined to have the property of "covering the true parameter $\hat{\theta}$ in a fraction α of random measurements" [CB02]. Note, that the interval itself is a random quantity and may or may not contain the true parameter. Only a statement about ensembles of measurements can be made. By following the definition for a consistent construction of the intervals, it is ensured the desired coverage probability is reached.

A general method to construct confidence intervals is the *Neyman construction* [Ney37]. In a modern language, the method relies on the sampling of the probability space of the defined parameter space, creating sets of samples for which the true parameters are known. For example, a single parameter n_S is fitted in a point source Likelihood, which is an estimator for the true, but unknown signal strength μ. Using a set of experimental data $X = (x_1, ..., x_N)$, a best-fit point estimator can be obtained by finding the parameter

$\hat{n}_S$, that maximises the Likelihood

$$\mathcal{L}(n_S) = \prod_{i=1}^{N} P(n_s|x_i) \ . \tag{5.87}$$

By performing pseudo experiments and creating samples for which the true parameter is scanned in a region of interest, a two-dimensional plane of the true and estimated parameter can be created for the example case here. To construct the confidence interval for μ, first, an interval containing the probability α is created on the sampled statistic for each parameter μ_i. This ensures a consistent treatment of the enclosed probabilities according to the definition. Then the confidence interval for μ from the single point estimate $\hat{n}_S$ at a confidence level α is the set of all μ_i, which have the measured value $\hat{n}_S$ in the previously built interval. Using the histogram analogy, with n_S on the x-axis and μ on the y-axis, the interval $[\mu_0, \mu_1]$ is the vertical line that cuts through the band created by marking the horizontal interval start and end points for each value μ_i.

Interval estimation is closely related to hypothesis testing. Hypothesis testing is used to find the acceptance region for a fixed set of model parameters by probing all possible sample values. In interval estimation, the sample is fixed and the question is, which model parameters plausibly explain the data in the whole parameter space. This can be expressed schematically with

$$(x_1, \dots, x_N) \in A(\theta_0) \Leftrightarrow \theta_0 \in C(x_1, \dots, x_N) \ , \tag{5.88}$$

with a function A describing the acceptance region for the sample $X = (x_1, \dots, x_N)$ and a function C describing the confidence region for the true parameter θ_0.

6. Time-dependent analysis

Despite the detected coincidence of the flaring Blazar TXS 0506+056 and a single ultra-high-energy neutrino together with the evidence for a temporally constrained neutrino flux about three years earlier, lasting 110 days, no other significant result of neutrino point source searches were obtained so far. Most prominent examples are the generic all-sky search, which scans the whole sky for an unknown neutrino emitter with a large amount of data. Three analyses stand out in this scenario. One is testing the whole sky using seven years of data with no prior assumptions [Aar+17a] and the other one is probing only the northern sky with priors obtained from the most recent diffuse flux measurement in the muon track channel [HW18; Rei18]. Both analyses could not find a significant contribution, mostly because the large trial factor from scanning the whole sky is lowering the significance. Another analysis of this kind is using the high energy starting event sample directly to test for a clustering of these events, assuming at least some of them originate from the same source region, again with no significant result [Aar+13a]. Therefore, many different approaches tried to search with more bias but potentially better significance by introducing a priori knowledge of emission scenarios. One class of searches relevant here is the stacked search approach. Expecting that individual sources are too weak to be detected as a single source, it is tested for multiple sources of the same source class, which are assumed to have similar intrinsic emission mechanisms. Popular and well-motivated choices are, for example, Blazars and other sources known from source catalogues created by other high energy astrophysical observatories like, for example, FERMI [Aar+18a; Aar+17c; Aar+17d; Aar+17b]. To further reduce the background, additional timing information can be taken into account. Several source classes exist for transient events and neutrino emission is then also expected only on a corresponding time scale [Bia+07; Kom15; Kat16]. All of the shortly summarized analyses above could not find a significant contribution of the expected neutrino signal. The non-detection seen in so many analyses may also have the reason that emission scenarios are not understood well enough yet, so that the searched catalogues are not specific enough or biased towards non-matching models, resulting in worsened sensitivity. Another problem might be that there are simply not enough events collected so far to make significant statements about weak source populations.

However, due to the lack of proper models, a generic approach is used here, under the following assumptions. As the HESE events on their own show a clear astrophysical signal and therefore should originate from some sources, also a lower energy neutrino flux

should be produced during the emission of the high energy events [Mes14; Mur15]. Here, a search for a clustering of events within the high statistics muon neutrino track sample around the track-like high energy starting event locations is conducted. A stacking search is used, because no significant signal can be seen by examining the HESE positions in the aforementioned single source all-sky searches. This indicates that possible emitters are likely too weak to reveal themselves within the large sample background. Additionally, in this first analysis in this thesis, the possibility of a time-dependent emission, which might, for example, originate from a flaring state, is considered [MNF11; Goo+07; ESR12]. This also further reduces the expected background and would be very sensitive to a time-constrained emission scenario.

The analysis method uses the time-dependent, unbinned Likelihood approach as described in section 5.3, which is similar to the one used for example in [Aar+18a] but with some major methodical differences. The required test statistics to obtain final significances on data are built on experimental data. Each source is always unique in its time window and is also only present in a single sample, so all sources are treated independently of each other. Because of the low amount of background in the tested, quite small time windows, only a single free parameter, the expected signal strength is fitted. To further differentiate between signal and background, instead of only using the spatial and temporal clustering, energy information is used with the assumption, that all sources inject neutrinos with energies following a generic E^{-2} power-law flux.

6.1. Per event distribution modelling

Spatial PDF

Here, the spatial signal PDF is modelled using a two dimensional, symmetric Kent distribution, to take into account the per event uncertainties. The PDF is

$$f(\Psi|\kappa) = \frac{4\pi \sinh(\kappa)}{\kappa} \exp\left(\kappa(\cos(\Psi) - 1)\right) \quad , \tag{6.1}$$

where

$$\Psi_{i,k} = \cos(\delta_k)\cos(\delta_i)\cos(\alpha_k - \alpha_i) + \sin(\delta_k)\sin(\delta_i) \tag{6.2}$$

is the space angle between the positions of source k and event i in equatorial coordinates δ, α. Instead of using the Gaussian uncertainty σ directly, the Kent distribution uses the transformation $\kappa \approx {}^1/_{\sigma^2}$ which holds up to $\sigma \approx 40°$ [YT14; Jak12]. The Kent distribution is used here, because it is correctly normalized on the sphere and virtually indistinguishable from the two-dimensional Gaussian PDF for the small angular uncertainties of the track-like events considered here.

Background PDFs are constructed in equatorial coordinates as well and the distribution is estimated from data, using only the off-time dataset to avoid signal contamination. By using equatorial coordinates, the right ascension distribution is assumed to be flat, which translates to a flat distribution in local azimuth coordinates. This holds well for larger time windows, in which the detector rotation relative to the sky smooths out any irregularities in the local azimuth PDF. For smaller time windows the assumption may break down, and alternatively, an azimuth background PDF could be used as a drop-in replacement. Here the PDF is only declination independent for simplicity and can be written as

$$f(\delta_i|t_k) = \frac{1}{2\pi} \cdot P(\delta_i|t_k) \ , \tag{6.3}$$

where t_k is the time of source k used to account for varying background strengths due to seasonal variations. This considers that a source occurring in a time of lower than average background rate has a higher chance of seeing a signal contribution, which is not influenced by the change in background rate. Seasonal variations in the atmospheric neutrino flux are directly correlated to the variation in temperature in the upper atmosphere layers. The resulting change of the atmospheric density hinders or promotes the interaction probabilities of pions and kaons from the primary cosmic ray interactions with the air, so that the resulting shifted ratios of decay and interaction probabilities influence the neutrino production [Bar+52; DG10; Gai13; Gra+10].

To build a custom background PDF for each source in its respective sample, first all events in each sample are binned in 20 $\sin(\delta)$ bins. The 14 innermost bins around the horizon region, defined as $\delta \in [-30°, 30°]$, are more tightly spaced. Around the horizon, the sample selection models are usually switched between dedicated models for the Northern and Southern sky and the finer binning resolution helps to catch the important features in the distributions, however, at the cost of higher variances. To capture the time dependence of the declination dependent background rate, it is calculated by using the runtime information from the samples. Due to a lack of proper runtime information, the run lengths are estimated from data by subtracting the earliest from the latest event time per bin[12]. The rate information is smoothed beforehand by re-binning the per run rate bins using a monthly binning, ensuring more stable fits.

To get a continuous description for the background expectation per bin, a phenomenologic model

$$f(t) = A \cdot \sin\left(\frac{2\pi}{T}\,(t - t_0)\right) + R_0 \tag{6.4}$$

is fitted to the re-binned time bin centres. The free parameters are amplitude A and average rate R_0, both in units 1/s. For the fit in each bin the period length T is fixed to 365 days, the natural scale for the seasonal variations and the time offset t_0 is fixed from

[12]This overestimates the background rate, because the earliest and latest events can only be close to the real runtimes, which yields a slightly less performance of this analysis, but introduces no further bias.

a global fit with more statistics using the whole dataset. The model is adapted to the rates at the bin centres from the monthly bins in a standard weighted χ^2 fit using the loss

$$\sum_{i=1}^{N_{\text{bins}}} \left(w_i \left(y_i - f(t_i)\right)\right)^2 \quad . \tag{6.5}$$

The weights $w_i := {}^1/_{\sigma_i}$ are defined as the standard deviations of the underlying Poisson distributions per bins n the large expectation limit, which is slightly biased, but a commonly used and stable weight definition. See figures (B.7,B.8,B.9,B.10) for the run rates and the fitted models per bin and per sample.

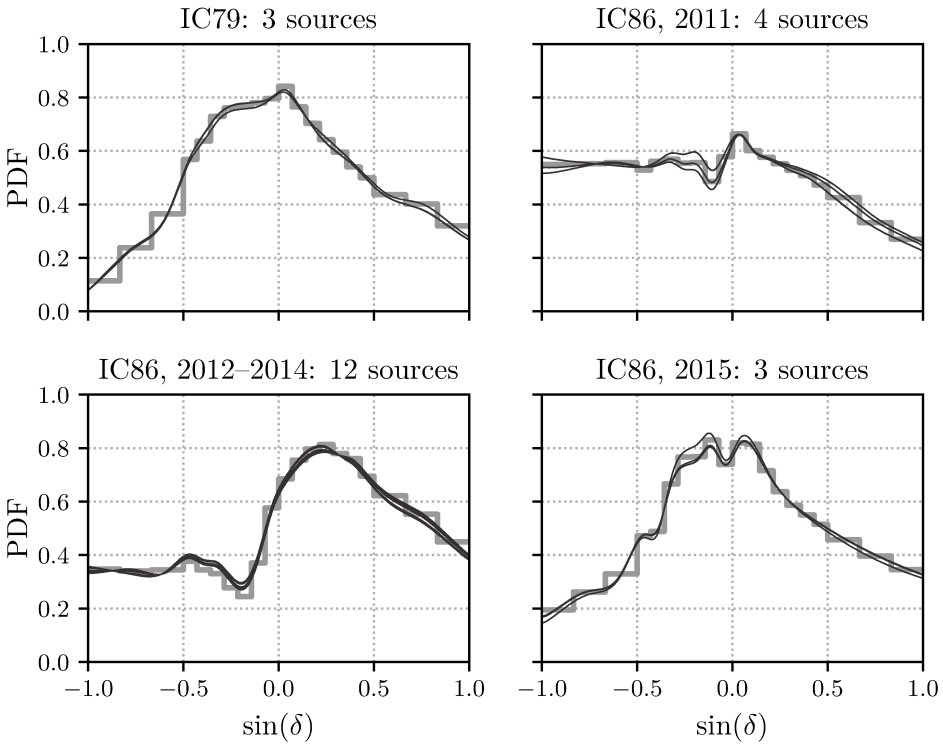

Figure 6.1.: Resulting background PDFs in $\sin(\delta)$ for each source per sample, for the largest time window. The PDFs for the smaller time windows are almost identical and not separately shown. The distributions are built by integrating the background rate over the current time window for the specific rate model at the sources temporal location. The rate model parameters are taken from the splines in figure (B.4). Each spline is normalised only across the $\sin(\delta)$ dimension in the plots, but the normalisation across the right ascension dimension is a constant of 2π anyway due to the assumption of having a symmetric right ascension PDF.

Having obtained the set of discrete background expectations from the two fit parameters per rate model, a smoothing spline is used to continuously model the fit parameter

dependence on declination. To obtain a reasonable fit of the spline function to the data points a weighted χ^2 fit is used here, too. The weights are chosen again as $1/\sigma_i^{\text{par}}$, where the standard deviations of the fit parameters are estimated from Likelihood landscape scans of the rate model fits per bin. For the sake of simplicity it is assumed that Wilks' theorem holds for the test statistics[13] and the parameter uncertainties are not obtained using a profile scan, but rather by simply using the edge values of the $1\,\sigma$ boundary box around the minima. The fit parameters of the splines are tuned, so that the resulting loss has approximately the value of

$$\sum_{i=1}^{N_{\text{bins}}} \left(w_i \left(y_i - f(t_i)\right)\right)^2 \approx N_{\text{bins}} \ , \tag{6.6}$$

which yields reasonable and stable results. The spline fits to the set of discrete parameters for the amplitude and baseline of the sine model can be found in figure (B.4). Finally, to get the background PDFs per source, the set of rate model parameters is read off from the built splines on a fine $\sin(\delta)$ grid and plugged into the rate model (6.4). For each parameter set, the model is integrated over the sources time window to obtain an average background PDF per source. To evaluate the PDF for each events' declination, an interpolating spline is used to include the dense grid in a continuous model. Figure (6.1) shows the normalized spline PDFs for each source per sample.

Energy PDF

The energy PDFs introduces a significant amount of separation power compared to using the spatial clustering only [Bra+08]. The integral values

$$\int_{-1}^{1}\int_{0}^{\infty} P(E_i, \sin\delta_i | E_\nu, \sin\delta_\nu) \cdot P(E_\nu, \sin\delta_\nu | \gamma) \mathrm{d}E_\nu \mathrm{d}\sin\delta_\nu \tag{6.7}$$

can be found using simulation if the conditional probabilities $P(E_i, \delta_i | E_\nu)$ are analytically unknown. This is done by directly estimating the convolved integral values. Here, a two dimensional histogram in $\sin(\delta)$ and in $\log_{10}$ of an energy proxy variable with 30 equidistant bins between $\lfloor \min \log_{10}(E_{\text{proxy}}) \rfloor$ and $\lceil \max \log_{10}(E_{\text{proxy}}) \rceil$ is used.

To directly obtain the needed signal over background ratio $\sim S^E/B^E$ used in the test statistic formula (5.48), two histograms with the same binning are used, one by using data to obtain the background PDF and the signal one by using signal simulation weighted to the assumed power law fluence with index $\gamma = 2$. The bin volumes then cancel, leading to

[13] Which seems reasonable, as the landscapes turn out to be quite Gaussian-shaped around the minima.

a correctly normalized ratio. The number of events normalized to the bin volume $\Delta E \Delta \Omega$ for the signal simulation histogram is obtained using OneWeight as shown before,

$$N(\Delta E, \Delta\delta) = \sum_{(i|E_{\nu,i} \in \Delta E, \delta_i \in \Delta\delta)} \frac{\text{OneWeight}'_i \cdot \Phi(E_i)}{\Delta\delta \Delta E} \quad . \tag{6.8}$$

OneWeight$'$ is a slight modification of OneWeight, as it is already divided by the total number of total generated simulation events OneWeight$' :=$ OneWeight$/N_{\text{gen}}$, where N_{gen} counts all particle types combined and Φ is also the combined neutrino and anti-neutrino fluence.

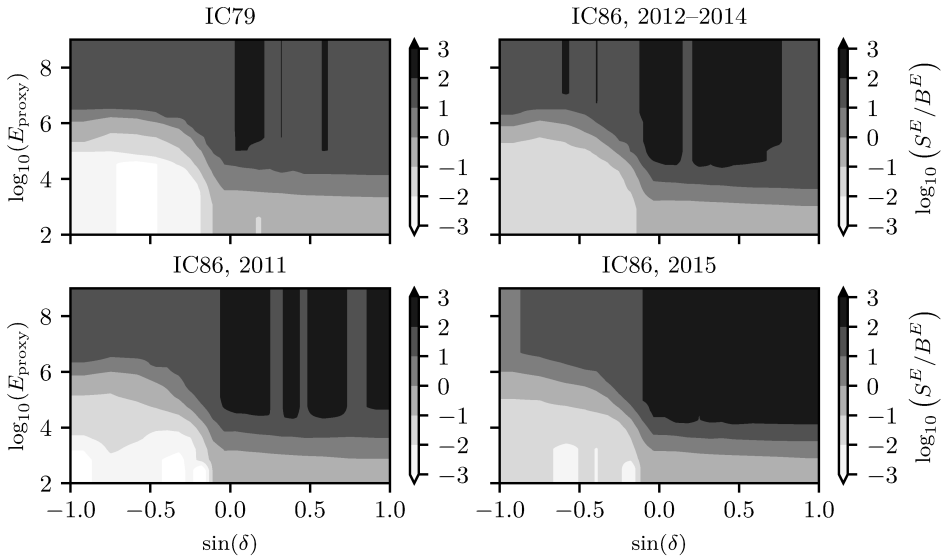

Figure 6.2.: Two-dimensional ratio of signal and background energy PDF in $\log_{10}(E_{\text{proxy}})$ and sin(δ) for each sample. The underlying binning is the same for the signal and background histogram and for each sample. The energy distribution per column in sin(δ) is forced to be ascending, which is justified by the fixed power law with index $\gamma = 2$. Higher energies are always favoured by the signal hypothesis then.

For bins missing either data, simulation or both entries, the ratio is not valid. To obtain reasonable ratios a two-step strategy is used. First the outermost energy bins per sin(δ) column is filled with the lowest, at small energies, or highest, at high energies, ratio value per column. The invalid ratios are then linearly interpolated from the previously valid and new edge values. To smooth out unexpected high ratios coming from limited statistics, the ratio is required to monotonically increase in each sin(δ) column, which is valid only for the fixed power law and energy range chosen here. To get a continuous representation of the ratio, a linear, regular grid interpolator is used to continuously

describe the ratios. No extra smoothing, for example, with a Gaussian kernel is applied here. The resulting two-dimensional PDFs are shown in figure (6.2) for each sample.

A more general strategy could be to fill missing values conservatively to the lowest non-zero entry per signal and background histogram separately and then taking the ratio. To average out fluctuations, a smoothing spline could be fitted to the ratio histogram using the statistical errors as smoothing conditions. This would also automatically yield analytic derivatives in both axes, which can prove useful when fitting more parameters than the single signal strength.

Temporal PDF

The time PDFs are defined as simple rectangle functions

$$S_{i,k}^{T} = B_{i,k}^{T} = T_k(t_i) := \text{rect}\left(\frac{t_i - \frac{t_k^1 - t_k^0}{2}}{t_k^1 - t_k^0}\right) \tag{6.9}$$

for both signal and background. For signal, this resembles a generic choice for an unknown per-burst emission process. For background, the same sine function rate model used for the spatial PDFs could more accurately be used. But as the amplitudes are small, even at the largest time window the resulting PDF would be virtually indistinguishable from a uniform distribution. So for code simplicity, a simple rectangle model is used for the background PDF. This also means that no extra sensitivity is coming from the temporal term, it is merely there to select events within the time windows and alters the amount of total background contribution which is almost zero for the smallest time windows and grows approximately linearly for the larger ones.

In this analysis, 21 time windows with total widths from two seconds to five days are tested. This corresponds to typical scales of fast and medium burst length transient sources with the potential of also having neutrino emission, like Gamma Ray or Fast Radio Bursts [GF17; Hes17]. The time windows are spaced symmetrically around each source. All sources are given the same time window and all time windows are tested independently of each other. This is done to avoid an unstable resource consuming fitting of the time window size but comes at the cost of an additional trial factor for testing multiple windows and selecting the best one. The time window intervals can be found in table (6.1).

Table 6.1.: Used time windows $\Delta T = [T_0, T_1]$ in seconds relative to each source event's detection-time in the time-dependent analysis. Each time window is tested independently from the others and all sources share the same time window length in a single emission model set-up.

ID	ΔT in s	ID	ΔT in s	ID	ΔT in s
1	[−1.0, 1.0]	8	[−73.6, 73.6]	15	[−5421.4, 5421.4]
2	[−1.8, 1.8]	9	[−136.0, 136.0]	16	[−10 019.3, 10 019.3]
3	[−3.4, 3.4]	10	[−251.4, 251.4]	17	[−18 516.6, 18 516.6]
4	[−6.3, 6.3]	11	[−464.7, 464.7]	18	[−34 220.4, 34 220.4]
5	[−11.6, 11.6]	12	[−858.9, 858.9]	19	[−63 242.4, 63 242.4]
6	[−21.5, 21.5]	13	[−1587.3, 1587.3]	20	[−116 877.5, 116 877.5]
7	[−39.8, 39.8]	14	[−2933.5, 2933.5]	21	[−216 000.0, 216 000.0]

6.2. Background estimation and stacking weights

The estimates of the number of background events per source, $\langle \lambda_{k,B} \rangle$, are not fitted in this analysis but fixed from a priori estimates on data. The values are obtained by fitting the sine rate model to the whole off-time data on the whole sky, again using monthly bins. The rate model for each sample is then integrated over each sources time window in that sample, to obtain the average number of background events. As before, the amplitudes are quite flat, so the exact integral is almost the same as just using the product of time window length and average rate. The all-sky total run rates for each sample and the fitted rate model can be seen in figure (B.5).

The a priori fixed stacking weights should resemble the expected signal emission as closely as possible to the true case, otherwise it is unlikely that the analysis leads to significant results on data. Because this analysis makes no explicit assumption on the emission model, the weights are computed using a generic power law with index $\gamma = 2$. This also implies that sources are assumed to emit the same intrinsic fluence. This is a strong assumption, though justified by demanding an test as unbiased as possible and being more conservative with regard to the unknown underlying source types.

The declination-dependent signal efficiency weight for each source in a specific sample can be obtained by histogramming the declination values from signal simulation with weights

$$w_i = \Phi(E_{\nu,i}) \cdot \text{OneWeight}'_i \ . \tag{6.10}$$

Here $\Phi(E_{\nu,i})$ is the combined fluence of both neutrinos and anti-neutrinos the simulation shall be weighted to. The histogram entries are then normalized by diving by the bin width $\Delta\Omega_{\text{bin}}$ to obtain a proper number density. If a fluence $\Phi(E_{\nu,i}, p)$ per particle type p is used, then an additional factor f_p for the OneWeight needs to be considered, which

gives the fraction of simulated particle types in the data set. Usually, the simulation files are produced with $f_p = 0.5$, so that $N_{\text{gen}} \to f_p N_{\text{gen}}$ [GK05].

Here, an equidistant binning is used to model the signal distribution and the bin widths are chosen to have at least 100 events in each bin. To obtain a continuous representation of the expected events per declination model, a smoothing spline is fitted to the histogram bin centres. For reasonable boundary conditions, values at the outermost bin edges are added by linearly extrapolating the values from the two outermost bin centres at each edge. The smoothing spline is created using a least squares minimization. The weights are the inverse $\sqrt{N_i}$ Poisson uncertainties of each bin i and the least squares sum constraint is set to the number of bins, so that the $\chi^2/\text{dof} \approx 1$ approximately holds if the spline can reasonably describe the data. This gives a stable estimation of the number of events per declination from the given Monte Carlo simulation, although the choice of the $\sqrt{N_i}$ weights again leads to slightly biased fit results. From this spline, the signal efficiency weights are read off for each exact source location. For each sample, this procedure is repeated and the source weights are taken from the spline belonging to the sample they fall into. The splines and the resulting source weights are shown in figure (B.6).

6.3. Note on LLH minimization

When minimizing the Likelihood to find the best-fit parameter $\hat{n}_S$, the small background in short time windows can be taken advantage of to solve the Likelihood minimization analytically and save computation time. For small time windows, mostly no event, a single event or two events actually have a significant contribution in the Likelihood minimization. For these cases, an analytic result of the test statistic fit can be obtained. Below are the analytic solutions for zero, one and two events with the single sample Likelihood, where the number of events means the effective number of the non-zero signal over background ratios, which is defined here by the removal of all events that have a signal over background ratio of less than $1 \cdot 10^{-3}$ from the Likelihood computation. This measure only slightly distorts the Likelihood function around the minimum, because zero terms would drop out anyway. However, due to the gained speed in trial computation, more trials can be generated for more stable test statistic estimations. The same reasoning holds for the multi-sample Likelihood where only a bit more bookkeeping is necessary to entangle the contributions from each single sample Likelihood.

As a reminder, the single sample test statistic that is fitted is

$$-2\ln\Lambda = -2n_S + 2\sum_{i=1}^{N}\ln\left(n_S \cdot R_i + 1\right) \quad , \tag{6.11}$$

where

$$R_i = \frac{\sum_{k=1}^{N_{\text{srcs}}} w_k S_{i,k}}{\sum_{k=1}^{N_{\text{srcs}}} \langle \lambda_{k,B} \rangle B_{i,k}} \tag{6.12}$$

is introduced as a short-cut for the fixed signal over background ratios per event i. The gradient in the single fit parameter n_S then reads

$$\frac{\partial(-2\ln \Lambda)}{\partial n_S} = -2 + 2\sum_{i=1}^{N} \frac{R_i}{n_S R_i + 1} \ . \tag{6.13}$$

For zero events, the case is trivial because the "fit" is directly zero, as under-fluctuations for $n_S < 0$ are excluded in this analysis and it is only fitted for over-fluctuations. This might result in slightly worse sensitivity and limits due to compressing the complete test statistic in a delta peak at $-2\ln\Lambda = 0$. Though, for code and fit procedure simplicity, this is accepted in this analysis [Aar+17d]. For zero events, no sum term is surviving and the analytic solution is

$$\ln \Lambda = -n_S \ \Rightarrow\ \hat{n}_S = 0\,, \quad \ln \hat{\Lambda} = 0 \ . \tag{6.14}$$

For a single surviving event, a single sum term is left and the linear equation needs to be solved for $\hat{n}_S$ in the gradient and re-inserted in the Likelihood to obtain the best-fit test statistic. The best-fit $\hat{n}_S$ is

$$0 = -1 + \frac{R_1}{n_S \cdot R_1 + 1} \ \Rightarrow\ \hat{n}_S = \frac{R_1 - 1}{R_1} \ , \tag{6.15}$$

which yields

$$-2\ln\hat{\Lambda} = -2\hat{n}_S + 2\ln\left(\hat{n}_S \cdot R_1 + 1\right) = -2\hat{n}_S + 2\ln(R_1) \tag{6.16}$$

for the best-fit test statistic value.

The last analytic case handled is the one with two events left, which leaves a quadratic equation to solve in $\hat{n}_S$

$$0 = -1 + \frac{R_1}{n_S \cdot R_1 + 1} + \frac{R_2}{n_S \cdot R_2 + 1} \tag{6.17}$$

$$\Leftrightarrow 0 = n_S^2 + n_S\left(\frac{R_1 + R_2}{R_1 R_2} - 2\right) + \frac{1}{R_1 R_2} - \frac{R_1 + R_2}{R_1 R_2} \ . \tag{6.18}$$

With the short-cut $\frac{R_1+R_2}{R_1 R_2} := \tilde{c}$, the best-fit is obtained solving the quadratic equation

$$\hat{n}_S = -\frac{1}{2}\tilde{c} + 1 + \sqrt{\frac{\tilde{c}^2}{4} + 1 - \frac{1}{R_1 R_2}} \tag{6.19}$$

The solution with the negative sign always resembles the fit for $n_S < 0$ and is not considered here. Re-inserting into $-2 \ln \Lambda$ yields the best-fit test statistic

$$-2 \ln \hat{\Lambda} = -2\hat{n}_S + 2 \ln (\hat{n}_S \cdot R_1 + 1) + 2 \ln (\hat{n}_S \cdot R_2 + 1) \quad . \tag{6.20}$$

6.4. Trial generation

The Likelihood ratio test performs a discrimination between the null hypothesis, stating that only diffuse background is present in the data, versus the alternative, stating that also localized signal events are mixed in. In order to decide whether a fit on actual data shows a significant signal, the behaviour or test statistic of pure background needs to be known. The distribution is generally unknown when no further assumption like the validity of Wilks' theorem is made. However, it can be empirically estimated from sampling background-like data and testing the hypotheses multiple times in pseudo-experiments. This builds a distribution of test statistic values the final fit on data can be compared against. To estimate the analysis' performance before looking at the measured data, simulated signal can be injected into the pseudo background samples.

Background trials

To obtain background-like pseudo-event samples, the experimental off-time data is re-sampled in this analysis to avoid bias from mismatching simulation data [Aar+17d]. By re-sampling data, it is either assumed that only a fraction of the sample is made from true signal events, or that only data from off regions is used, so in regions where no signal is assumed anyway. The first case uses randomized data and assumes that, when scrambled, the few potential signal events don't interfere with the larger portion of background like events. The latter case only uses a fraction of the data in regions that are not tested for a signal contribution. The first case is justified when only a few signal events are expected in a large background sample, the second one, while being more rigorous, is only convenient to do if a large and representative number of events survive after cutting out the signal regions. Here the latter approach is used because the 22 sources only cover a small fraction of the full livetime. Trials are generated and PDFs are built using only the off-region data, holding the data from the largest time windows back. The on-time data is only used once at the end, to do a single fit to obtain the analysis' results

To generate a single pseudo background sample for a single trial run, the PDFs described in section 6.1 are sampled to match the built models. First, for each source, the number of background events to inject on the whole sky is drawn from a Poisson distribution with a mean equal to the expected number of background events per source. For the requested

number of events, the $\sin(\delta)$ PDF is sampled so a different declination dependency is sampled for each source, according to the models. The existing data events are sampled with different declination distributions by re-weighting them to the current declination PDF. The weights are computed using the ratio of a spline fitted to the intrinsic distribution and the desired $\sin(\delta)$ distribution spline. Right ascension values are randomly assigned between 0 and 2π to match the assumed flat model. Next, new times are sampled from the previously built rate models per source. The sampling is done uniformly because the time windows are too short to explore the slight non-uniformity of the rate model. The other used attributes are the estimated event energy and estimated spatial uncertainty and are kept as-are from each re-sampled data event.

For each generated pseudo background dataset, the Likelihood is fitted in the free n_S parameter to build the estimate of the test statistic distribution for a sample of expected background. Note, that it is important not to tweak the seed for the fit parameter depending on the trial type, background or injected signal, but to leave the seed selection routine equal for all trials. Otherwise, a bias is obtained because the fitter might perform better or worse for a special scenario which may not be known on pure data.

For this analysis, 10^8 trials with pure background pseudo data are performed to build an independent test statistic per time window. The high number of trials is necessary to compensate for the low background in the smaller time windows, in combination with the truncation of n_S at zero explained below. For the smallest time window the expected number of background events in the whole sky is in the order of a single event, which makes it rare to find any event in the vicinity of the tested source positions. Additionally, an event candidate gets a high test statistic value only, if it is sufficiently close to one of the source positions or has a high estimated energy. With larger time windows, this effect gets less severe and more events are available to obtain test statistics with longer tails and higher test statistic values. The larger a time window gets, the more the shape of the corresponding test statistic resembles the χ^2_1 distribution expected from Wilks' theorem.

Note that signal under-fluctuations are not regarded here, which means that any values $n_S < 0$ are truncated at $n_S = 0$. This yields to a compactification of under-fluctuating trials at a test statistic value of zero. This behaviour is more prominent for smaller time windows, as the background events have a low chance to fake a signal-like contribution, so the amount of under-fluctuations is much larger than the expected 50 % for a pure-background sample. Another way to look at this is, that for Wilks' theorem to hold and to get about 50 % under- as well as over-fluctuations, both the signal and background PDFs must be sampled equally well. If the time windows are small, then the probability of having an event close by any source is small, so the signal PDF is almost never sampled in the signal-like region. This leads to a lot of trials with test statistic values of zero, the more, the smaller the time window length. Here, for the smallest time window over 99 %

of all trials have a test statistic value of zero. For the largest time window, about 71 % of all trials still come with a zero test statistic value. This is not a fundamental problem per-se, but leads to worse performance estimates and limits, the worse the more zero trials there are. Because of the compactification at the test statistic value of zero, the limits can only start at values with a higher test statistic values for a meaningful estimate. For example, if there are 99 % zero trials, then the smallest meaningful confidence level that can be applied is about $2.5\,\sigma$, which leads to larger or worse limits than necessary for any sought-after smaller confidence level. On the other hand, the small time windows have such a low background, that any number of somewhat signal-like events showing up, will lead to a high and close-to-detection significance.

The large number of generated trials allows to use the samples directly as an empirical PDF representation up to approximately $4\,\sigma$, which leaves on average 6300 events in the tails for robust quantile estimations. In principle, 10^8 samples would allow to empirically estimate the significance up to about $5.7\,\sigma$, but with very poor statistics in the high confidence regime. To make the p-value estimation more robust for large test statistic values, the tail of each time windows test statistic is fitted with an exponential distribution. To find a robust set of PDF parameters for the exponential tail, the PDF is fitted with an unbinned Likelihood fit to the tail of the distribution starting from a threshold scanned on a grid between $3\,\sigma$ and $4.5\,\sigma$ of the background test statistic. The best-fit is selected using a Kolmogorov-Smirnov test [Hor77] and using the first threshold that no longer supports the null hypothesis, that the fitted tail describes the empirical PDF well enough, at 50 % confidence level. While being a somewhat arbitrary argument, this procedure yields quite robust tails even for the test statistics in the smallest time windows. For the larger time windows, the distributions become more similar to the χ^2_1 PDFs expected from Wilks' theorem and are naturally described by the exponential tails. The resulting hybrid test statistic PDFs and the parameter scan for the Kolmogorov-Smirnov test are shown in figures (6.3,6.4) for the three smallest and largest time windows and in figures (B.14–B.18) for the other ones. An independent set of trials is used to verify the validity of the tail fits, which reveals a slight, but not severe mismatch between the built models and the independent trials, as shown in figure (B.11). The resulting PDFs are then a hybrid made from the empirical distribution and the exponential PDF, which continuously describes the distribution tails, and are used to estimate p-values for further evaluations.

As a technical note for multiple samples, every single injector can be sampled individually, because each source is unique in its corresponding dataset. The used multi sample background injector thus simply loops over all individual background injectors.

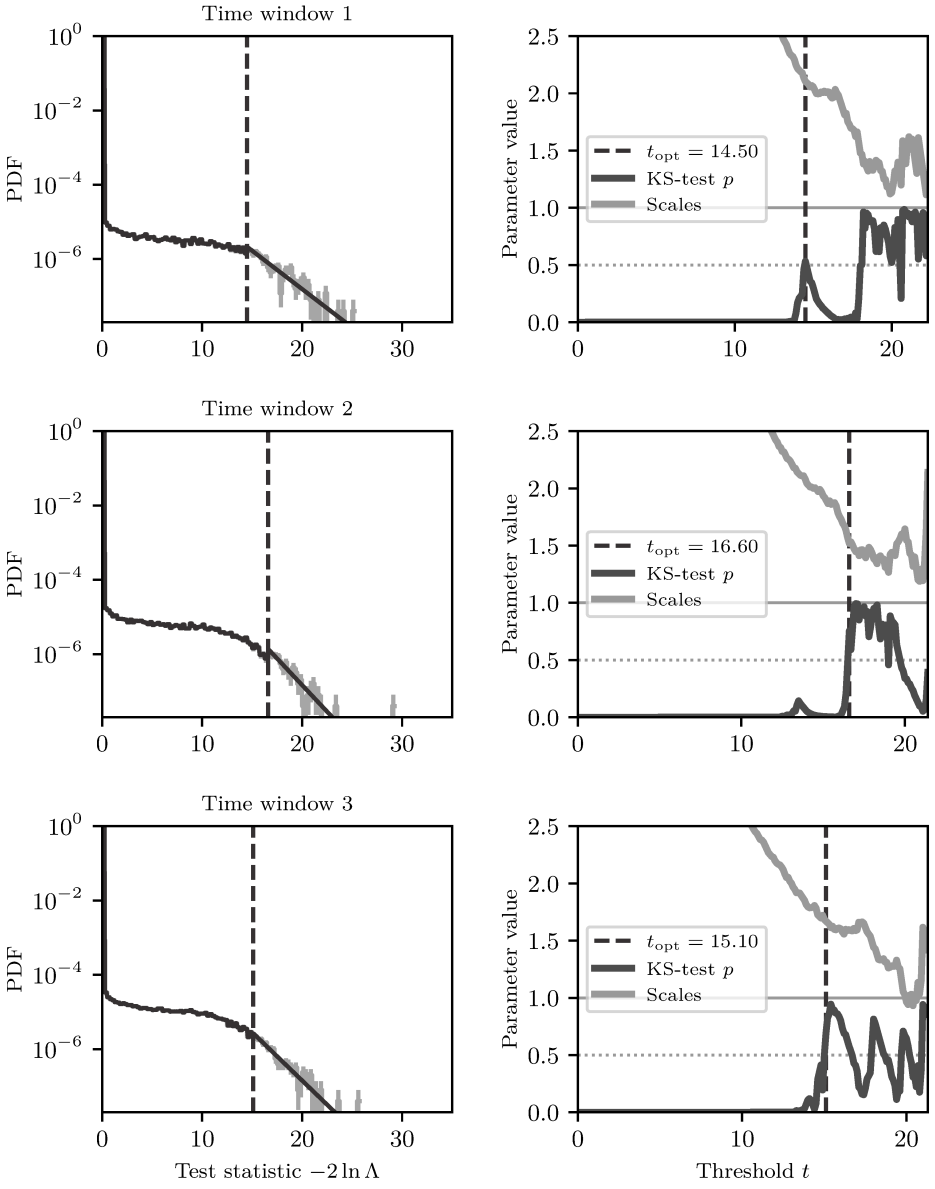

Figure 6.3.: Background-only test statistics for the time windows 1, 2 and 3 on the left and the parameter scan using the Kolmogorov-Smirnov (KS) test for the best threshold position on the right. The sampled PDF is described empirically up to the threshold value and with an exponential tail after that. The KS test is used to decide when the tail describes the sampled data sufficiently accurate.

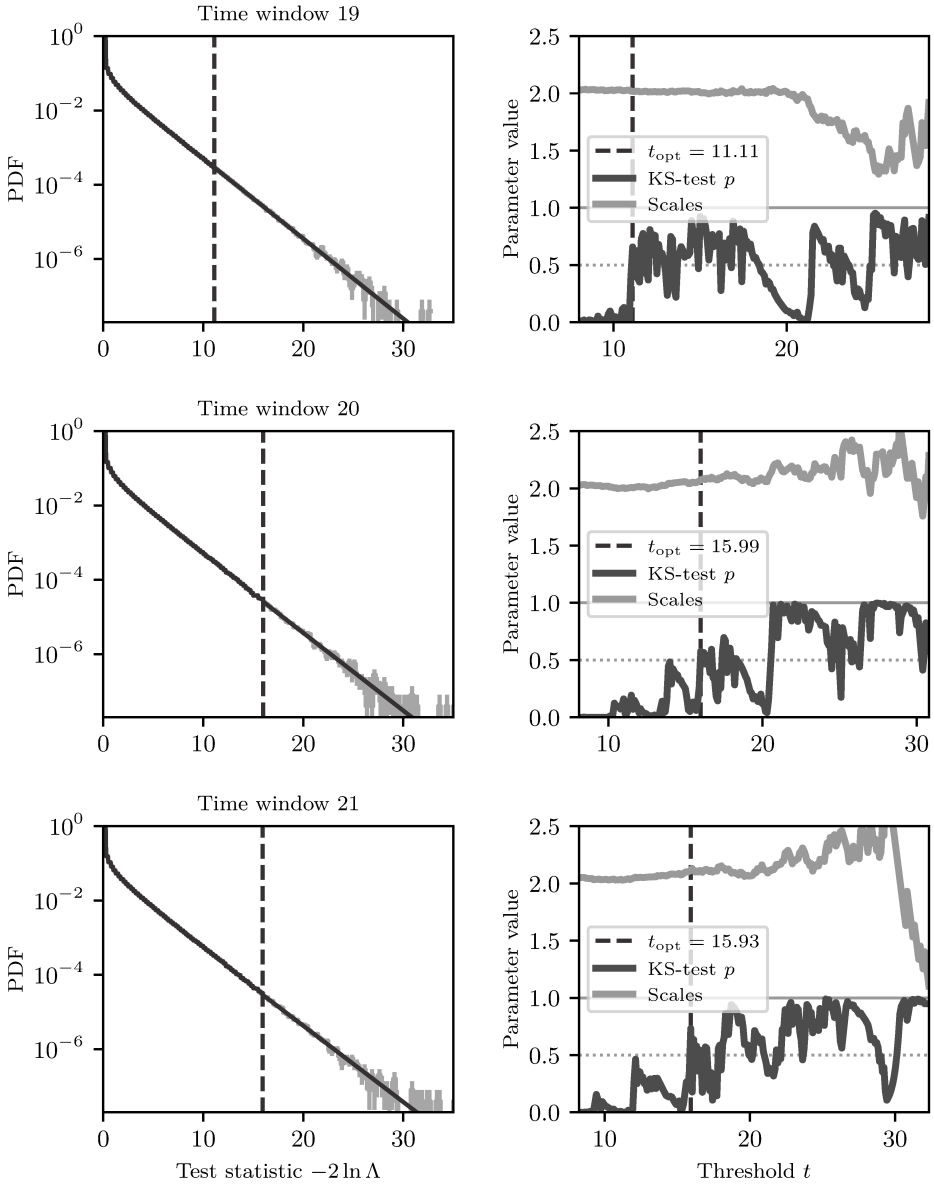

Figure 6.4.: Background-only test statistics for the time windows 19, 20 and 21 on the left and the parameter scan using the Kolmogorov-Smirnov (KS) test for the best threshold position on the right. The sampled PDF is described empirically up to the threshold value and with an exponential tail after that. The KS test is used to decide when the tail describes the sampled data sufficiently accurate.

Signal trials

To estimate the analysis' performance and to compute limits or constraints for a specific choice of a source flux model, the Likelihood response to signal-like events need to be tested. Because it is unknown which and if any events in the data are true signal events, signal-like events have to be injected from simulation data. Using the already known weighting scheme, any source emission scenario can be modelled. The injection mode should mimic the emission scenario to obtain realistic estimates.

The used simulation approach is to select a pool of simulated signal events from a region close to the source that shall be simulated. These events get rotated to the desired location using the true simulation coordinates. This assures that events that are representative for a source location on the sky are used from existing simulation. The signal simulation is weighted to a per-burst emission to describe the tested emission scenario. Per-burst emission means that the total number of expected signal events is independent of the emission-time window, which is also reflected by the rectangle function PDFs in the Likelihood. To correctly insert events corresponding to the desired target fluence, the already shown weighting scheme using OneWeight is used

$$w_{i,k} = w_k^{\mathrm{src}} \frac{\mathrm{OneWeight}'_i \cdot \Phi(E_{\nu,i})}{\Omega_k} \quad . \tag{6.21}$$

where k indicates the source, the event was selected from and w_k^{src} the intrinsic source weight, normalized over all sources in the sample. The detection efficiency weight which was used as a stacking weight in the Likelihood description is automatically intrinsically included in the sample weights because the signal simulation sample was processed with the same selection as the measured data set. The diffuse power-law fluence $\Phi(E_{\nu,i})$ used here is normalized to a point source fluence by dividing out the selection solid angle Ω_k and is left with units $1/(\mathrm{GeV\,cm}^2)$. Events can be selected multiple times if they fall in multiple source selection regions. All weights for each event in the whole pool of events then get normalized, $\sum_{i,k} \tilde{w}_{i,k} = 1$, so the weights are prepared for a weighted random choice sampling procedure.

Usually, the injection is set up to rotate the true event coordinates to the source locations and use the reconstructed coordinates in the Likelihood testing. Here, this would overestimate the sensitivity because of the unknown source locations in this analysis. As the source positions themselves are taken from reconstructed high energy neutrinos, they also have a spatial reconstruction uncertainty. It is possible to take these uncertainties into account in the Likelihood formulation, which would lead to a much more complicated fit procedure and requires a lot of neutrino events to test against, because per source two new free parameters would be introduced. In this time-dependent analysis, this is not possible due to low statistics in the small time windows tested. However, in the

performance calculation, this lack of information can be incorporated by simulating these uncertainties during the signal injection.

The whole process is then done as follows: For each source, the pool of simulation events is selected in a declination band around the best-fit source positions, which are also tested against in the Likelihood formulation. The bands' upper and lower boundaries around each source are chosen by scanning the $3\,\sigma$ contour from the corresponding source prior map and selecting the minimum and maximum declinations from the contour line. The choice of using a $3\,\sigma$ band width is arbitrary but resembles a good compromise of having enough statistics for the actual signal event injection per source and selection regions that are representative for the PDFs describing the event properties at the sources' locations in the sky. A more precise approach would be to re-select events at each drawn new source position, which comes with additional computational cost. For all selected events, the injection weights are computed as shown in equation (6.21). For the actual injection during trial sampling, the events from the prepared pool are sampled randomly, automatically respecting each sources contribution due to the weight construction and the intrinsically simulated signal efficiency. The number of events drawn in total is given as a Poisson mean number of signal events and the actual number of events drawn in each trial fluctuates accordingly. To account for the unknown source positions, new point-like source positions are drawn on the HEALPix grid for each trial as shown in figure (B.12). The positions are drawn independently from each sources reconstruction prior PDF map so that the most likely position is still the tested best-fit position. All drawn events are rotated to their new source position in their true spatial coordinates. Lastly, a random uniformly sampled new MJD time is assigned per event within the time window for each source. As the time PDFs have no separation power the new time values could also be chosen to have a constant value here. When time PDFs with real separation power are chosen for an analysis, the signal time PDF must be properly sampled anyway, so the more general approach is chosen here.

The sampled events are finally stripped from all Monte Carlo truth information, appended to the background data, which is independently drawn for the trial, and the Likelihood is fitted to the combined pseudo-sample. Doing this repeatedly creates a test statistic distribution for a given mean true signal strength. This injection mode worsens the analysis performance and limits but represents a more realistic performance estimation in light of the unknown but constrained source positions.

6.4.1. Signal injection from multiple samples

The combination of several injectors per sample to simulate the signal for the multi-sample Likelihood is done by distributed sampling from each single sample injector. For a proper distribution of the requested number signal events to each injector, a similar

weighting ansatz is used as for the multi-Likelihood n_S splitting weights. The relative amount of signal per emitter depends on the total fluence expected to be emitted from a particular set of sources in a single sample. For a single injector, each event has weights as shown in (6.21). To construct a multi-injector, which basically injects from a combined, virtual sample, the intrinsic source weights need to be re-normalized to all sources in all injectors. This catches the circumstance, that each source is unique in each sample. The multi-injector construction for the steady state emission scenario described in chapter 7 works similarly, but with a different assumption on the source emission.

The new, re-normalized weights per sample can then be expressed by

$$\tilde{w}_{i,k} = \tilde{w}_k^{\mathrm{src}} w_k^{\mathrm{det}} \frac{\mathrm{OneWeight}_i' \cdot \Phi(E_{\nu,i})}{\Omega_k} \ , \tag{6.22}$$

where $\tilde{w}_k^{\mathrm{src}}$ are the intrinsic source weights normalized over all samples

$$\sum_{j=1}^{N_{\mathrm{sam}}} \sum_{k=1}^{N_{\mathrm{j,srcs}}} \tilde{w}_k^{\mathrm{src}} = 1 \tag{6.23}$$

and the inner sum runs over all sources in sample j. Using the total number of expected events from each sample by summing all re-normalized weights $\tilde{w}_{i,k}$ per sample, the relative event distribution can be computed. During sampling, the split number of events for the current trial is sampled from a multinomial distribution with the distribution weights as expectation values and each injector is requested to sample the distributed amount of signal. The connection between the Poisson and the multinomial distribution can be found in [BZ14].

6.5. Performance estimation

To estimate the analysis performance, the fluence needed from the whole source collection in order to obtain a given significance in the final analysis result must be estimated. This can be done by injecting a mean number of events for a given grid of mean signal strength values and doing a number of trials at each grid point to construct the Neyman plane[14]. In each trial, the actual number of injected signal events is drawn from a Poisson distribution with the currently selected mean number of events from the source to simulate the measurement process. These trials are used to obtain Neyman upper limits for the needed fluence strength. The method described here, can be used to obtain a performance estimation for the normalization of a given global fluence model.

[14] See section 5.6 for a short introduction on confidence intervals and hypothesis testing.

After sampling an empirical test statistic for all tested signal strengths, instead of using the empirical CDFs directly, a generic χ^2 CDF is fit to the discrete sample points for smooth interpolation and to find a more robust estimate of the desired performance value. While not having a deeply justified connection to the sampled distributions, the function is variable enough to smoothly describe the sampled points. The desired performance values over a given test statistic value from the pure background trials can then be obtained from the analytic χ^2 CDF.

The fit is done using an unweighted χ^2 fit with the loss

$$\sum_{i=1}^{N} \left(\mathrm{CDF}_i - \chi^2_{\mathrm{CDF}}(x_i|k,l,s)\right)^2 \quad , \tag{6.24}$$

where the three free fit parameters are the degrees of freedom k, the $x-$axis offset l and the scale s of the χ^2 CDF. The location and scale parameters influence the distribution with the transformations

$$y = \frac{x-l}{s} \text{ and } \chi^2(x|k,l,s) = \frac{\chi^2(y|k)}{s} \tag{6.25}$$

and make the resulting CDF quite flexible.

To ensure a proper fit, the seeds for the degrees of freedom and the location parameters are guessed as follows: For the χ^2 distribution with degrees of freedom k, the expressions

$$\mathrm{Mean}\,(x) = k \ , \ \mathrm{Var}\,(x) = 2k \tag{6.26}$$

hold and the approximation

$$\mathrm{Median}\,(x) \approx k\left(1 - \frac{2}{9k}\right)^3 \tag{6.27}$$

for large k is valid [BL13; AS74]. Using empirical estimates on the sampled distributions for the median and the standard deviation, a rough first guess estimate can be obtained using

$$k \approx \frac{d^2}{2} \quad , \tag{6.28}$$

where d is the absolute distance between the median and standard deviation positions. The scale is seeded at a value of 1 and it is also quite correlated to the degrees of freedom parameter. Therefore, when a fit is not converging, the scale is therefore fixed at 1 and only the degree of freedom parameter and the location is fitted.

The advantage of this grid sampling method is, that trials can be reused to evaluate multiple performance definitions if the statistics are high enough. Here 20 000 trials were done at each grid point, which is enough for the usual definitions of sensitivity

and discovery potential. Sensitivity is defined as the average 90 % upper limit, meaning the flux or fluence needed to shift the signal injected test statistic's 90 % quantile over a test statistic value of 0 of the background distribution. Respectively, the discovery potential is defined as the flux or fluence needed to obtain a $5\,\sigma$ result in 50 % of the trials. Another advantage is, that the whole Neyman grid construction can be visually inspected to see if any errors occurred during the minimization or trial generation and that confidence intervals for the true signal strength can be inferred from the best fit $\hat{n}_S$ value. Uncertainties on the limits or bounds themselves, resulting from the fit of χ^2 CDF to the finite sample size, could be obtained via trial bootstrapping and refitting or error propagation. This is neglected here due to the high number of trials done per grid point and the dense grid itself. The CDF fits for sensitivity and discovery potential per time window are shown in figure (B.13).

To express the performance in flux or fluence rather than injected events, the mean injection strength must be converted to a physical intrinsic fluence at the sources. This conversion follows straight from the weighting relation between the fluence and number of events

$$N = \sum_{k=1}^{N_{\mathrm{srcs}}} \sum_{(i|\Omega_i \in \Omega_k)} w_k \frac{\mathrm{OneWeight}'_i \cdot \Phi_0 \cdot f(E_{\nu,i})}{\Omega_k} \tag{6.29}$$

$$= \Phi_0 \cdot \sum_{k=1}^{N_{\mathrm{srcs}}} \sum_{(i|\Omega_i \in \Omega_k)} w'_{k,i} := \Phi_0 \cdot \sum_{k=1}^{N_{\mathrm{srcs}}} F_k = \Phi_0 \cdot F \ , \tag{6.30}$$

where the outermost sum runs over each source contribution and $w'_{k,i}$ is the whole fluence weight just without the proper fluence normalization. The sum over $F_k := w'_{i,k}$, F, then has all the properties of the final fluence except the proper normalization. This relation connects the number of events N at the detector to the combined intrinsic source fluence strength Φ_0

$$\Phi_0(N) = \frac{N}{F} \text{ or per source } \Phi_0^k(N) = \hat{w}_k^{\mathrm{src}} \cdot \Phi_0(N) \ , \tag{6.31}$$

where $\hat{w}_k^{\mathrm{src}}$ are the normalized intrinsic source weights. The reverse relation from the combined intrinsic fluence to events then yields

$$N(\Phi_0) = \Phi_0 \cdot F \text{ or per source } N(\Phi_0) = \Phi_0 \cdot F_k \ . \tag{6.32}$$

Φ_0 is to be understood as the fluence normalization at a given, fixed energy, here at 1 GeV. Another usual convention is to use the normalization at 100 TeV which doesn't change the physics result, but simply shifts the pivot point of the underlying unbroken power-law to higher energies. To express an unbroken power-law with spectral index

γ at a new normalization energy E'_0, the new fluence or flux normalization Φ'_0 can be calculated via

$$\Phi'_0 = \Phi_0 \cdot \left(\frac{E'_0}{E_0}\right)^{-\gamma} \quad . \tag{6.33}$$

Figure (6.5) shows the resulting sensitivity and discovery potential fluences for each scanned time window.

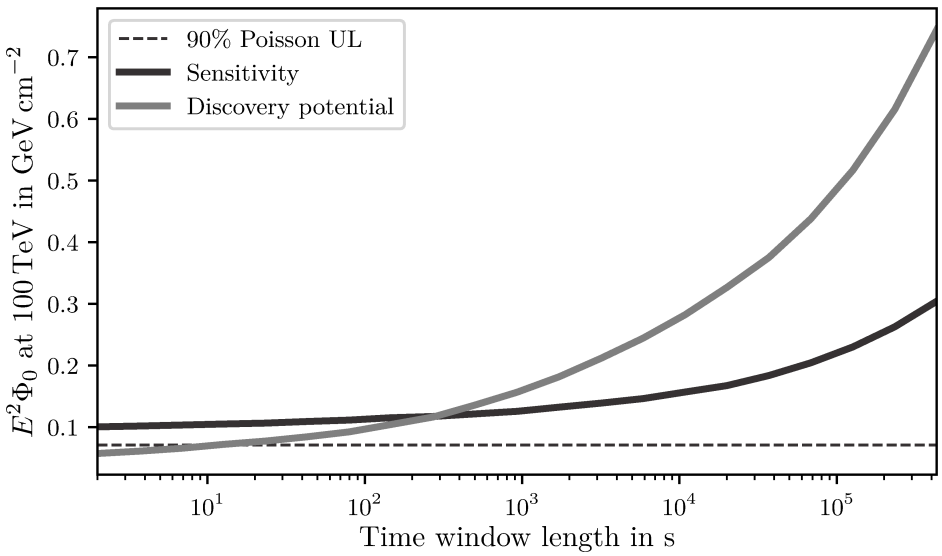

Figure 6.5.: Sensitivity and discovery potential fluences for each tested time window. The discrete points are drawn as connected lines, because the curves are not expected to show a non-smooth behaviour between the tested time window positions. For small time windows, the discovery potential fluence is actually lower than the sensitivity fluence, because of the large number of zero trials. The dashed line shows the 90 % Neyman upper limit for a Poisson distribution with zero measured events. For the small time windows, the sensitivity is close to that lower bound, because of the low amount of background on the whole sky.

6.6. Differential performance

Instead of estimating the analysis performance for a global model, it can also be estimated in a specific interval of parameters, for example in the neutrino energy. The procedure is basically the same as shown before in section 6.5, but events from the signal simulation are injected only in a specific energy range. Here, the energy is divided into logarithmic bins ΔE_j with a width of half a decade from $E_\nu = 10^2\,\mathrm{GeV}$ to $10^9\,\mathrm{GeV}$. Injecting events exclusively in a certain energy range gives an estimation for the needed fluence, if the

source would only emit events in that energy range and nowhere else. For each energy bin, a fluence normalisation which represents the fluence needed if it would only be non-zero in the current energy bins, is obtained with this procedure.

Note, that the differential performance, as described here, cannot directly be compared to a differential fluence model. This is because the tested hypothesis assumes that the fluence is only non-zero in the corresponding energy bin. Therefore, the differential performance strongly depends on the size of the chosen energy bin. Although the number of injected events stays roughly equal when the bin size is getting smaller, the resulting fluence increases because it measures events per energy. Thus, a global fluence can be made compatible with any differential fluence performance in a bin by decreasing the bin size of the differential limits. However, the limits can be used to calculate a global limit, which is directly comparable to other differential fluence models. This can be used to provide a flexible method for the reader, to obtain performances or limits for its own model creations. The differential sensitivities and discovery potentials per time window are shown in figure (6.6) and the corresponding fluence values can be found in tables (B.1, B.2). The corresponding χ^2 CDF fits for each bin and each time window used to derive the fluences can be seen in figures (B.19–B.39).

Because the differential performance fluence normalisations hold all the information of a global limit, where the only difference is, that the whole energy range would have been used in the injection procedure, it is possible to re-obtain the global performance for the same injection fluence from the differential limits. For this, the average number of events N that would have been needed to be injected on the whole energy region needs to be computed from the injected number of events N_j per bin. This can be done via a weighted sum

$$N = \sum_{j=1}^{N_{\text{bins}}} N_j \tilde{w}_j = \sum_{j=1}^{N_{\text{bins}}} N_j \frac{w_j}{\sum_{k=1}^{N_{\text{bins}}} w_k} \quad . \tag{6.34}$$

The weights can be derived by the following properties of the performance: First, the weights should be higher in bins, where more signal events are expected at detector level, thus lowering the needed fluence in presence of many signal events. This is expressed by the F_j quantity in equation (6.35), which gives the expected number of events at detector level under consideration of the functional form $f(E_\nu)$ of the underlying source spectrum. On the other hand, the weights should decrease, if a large number of actual events compared to the expected events from F_j is needed. This indicates a large background contribution in that bin and is lowering the performance, resulting in a higher fluence. Combining both properties and using the total un-normalized fluence per bin F_j, defined as F for the global model in equation (6.29),

$$F_j = \sum_{k=1}^{N_{\text{srcs}}} \sum_{(i|E_i \in \Delta E_j, \Omega_i \in \Omega_k)} w_k \frac{\text{OneWeight}'_i \cdot f(E_{\nu,i})}{\Omega_k} \quad , \tag{6.35}$$

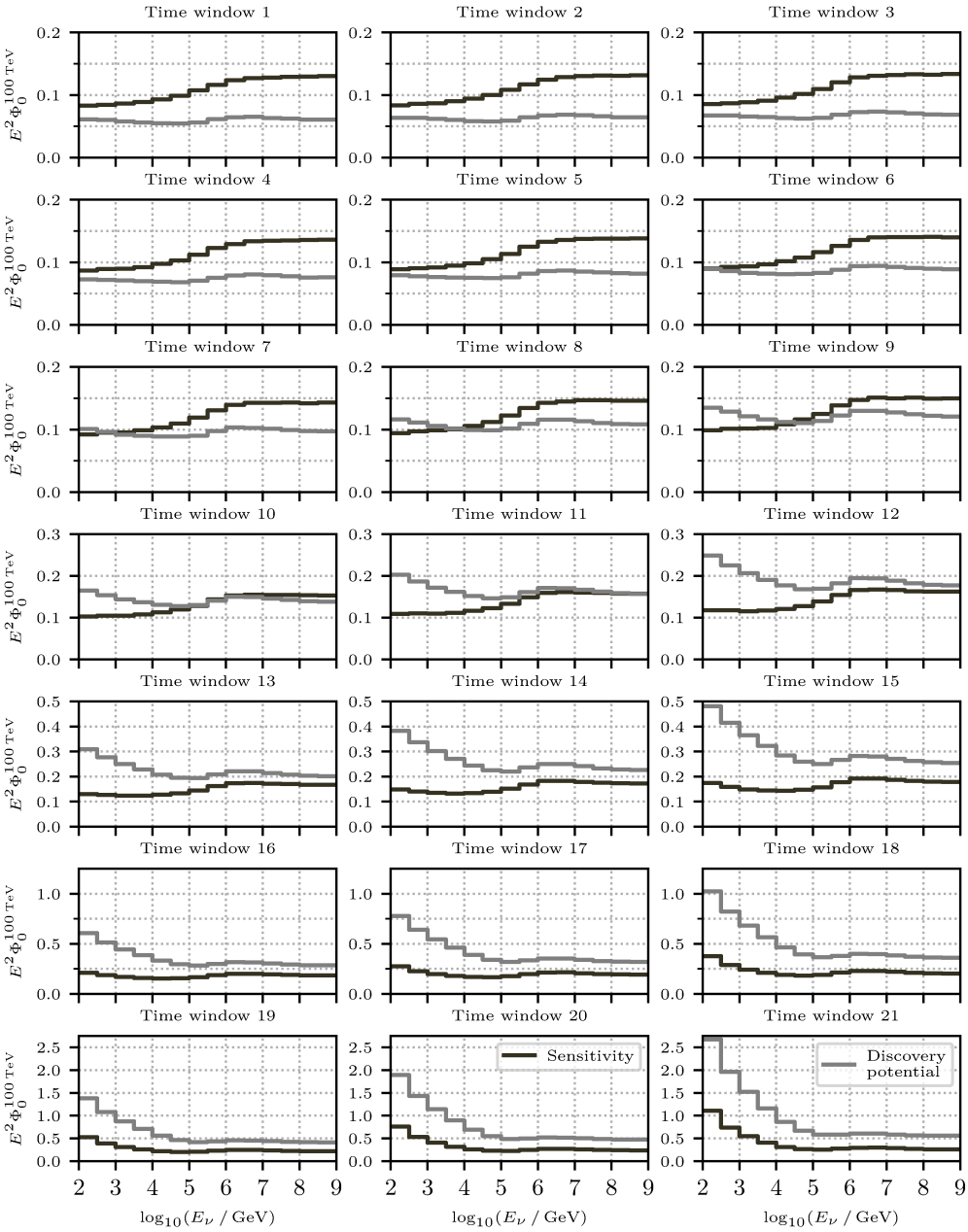

Figure 6.6.: Differential fluences per time window for sensitivity and discovery potential. The values in each bin is the fluence normalization $\Phi_0^{100\,\mathrm{TeV}}$ for an unbroken power law with index 2, $\Phi = \Phi_0^{100\,\mathrm{TeV}} \cdot (E/100\,\mathrm{TeV})^{-2}$, used for signal event injection in each bin. Because of the high number of trials with a test statistic value of 0 in the smaller time windows, the discovery potential fluence is actually below the sensitivity. This reverts to the expected behaviour the larger the time windows get. The bins are uniformly spaced in logarithmic neutrino energy with a width of half a decade.

which acts as the conversion factor from intrinsic source fluence to the measured number of events at detector level. As seen in equation (6.31), the weight w_j for each bin j can be written as

$$w_j = \frac{F_j}{N_j} = \frac{1}{\Phi_j^0} \ , \tag{6.36}$$

where Φ_j^0 is the differential performance fluence normalization, which is computed equivalently to the the global normalisation, as described in section 6.5, but for each bin independently. For the global amount of signal events that get injected proportional to $f(E_\nu)$ over the whole energy range, this further yields the expression

$$N = \sum_{j=1}^{N_{\text{bins}}} N_j \frac{w_j}{\sum_{k=1}^{N_{\text{bins}}} w_k} = \sum_{j=1}^{N_{\text{bins}}} N_j \frac{\frac{1}{\Phi_j^0}}{\sum_{k=1}^{N_{\text{bins}}} \frac{1}{\Phi_k^0}} \ . \tag{6.37}$$

Note that the global injection mode would intrinsically compute the same weights and inject events correctly distributed to their energy region accordingly.

Further, expression (6.37) can be used to additionally obtain the global fluence normalisation for the same fluence which was used to inject events per bin. This usually is the more interesting case, because it is connected to an actual physical quantity. For the total fluences F_j, the connection

$$F = \sum_{j=1}^{N_{\text{bins}}} F_j \ , \tag{6.38}$$

with the global fluence F holds, because the weighting formula (6.35) is additive across multiple bins. This is because a global model injector would internally just compute the sum over all available events i. Inserting this relation and the previously shown relation (6.36) to obtain the number of expected events from a given fluence, into equation (6.37) yields

$$N = \sum_{j=1}^{N_{\text{bins}}} N_j \frac{\frac{1}{\Phi_j^0}}{\sum_{k=1}^{N_{\text{bins}}} \frac{1}{\Phi_k^0}} = \sum_{j=1}^{N_{\text{bins}}} F_j \cdot \frac{1}{\sum_{k=1}^{N_{\text{bins}}} \frac{1}{\Phi_k^0}} = F \cdot \frac{1}{\sum_{k=1}^{N_{\text{bins}}} \frac{1}{\Phi_k^0}} \tag{6.39}$$

$$\Leftrightarrow \frac{N}{F} = \Phi_0 = \frac{1}{\sum_{k=1}^{N_{\text{bins}}} \frac{1}{\Phi_k^0}} \tag{6.40}$$

for the desired global fluence normalization Φ_0.

In addition to obtaining the the global performance on the fluence normalisation Φ_0 from the differential performance normalisations Φ_j^0 for the same flux model, global limits for any other fluence model can potentially be derived. The needed condition for this to

hold, is that the energy bins must be small enough, so that the influence of the originally injected spectrum, usually an unbroken power law, and the spectrum that the global performance shall be calculated for is negligible in the bin. This means, that the number of injected events needed to match the performance condition stays approximately the same, regardless of which functional fluence dependence is used to inject the events. If that condition is met, then the fluences per event $f(E_{\nu,i})$ in (6.35) can approximately be replaced by the average fluence model $\bar{f}$ in that bin

$$F_j = \sum_{(i|E_i \in \Delta E_j, \Omega_i \in \Omega_k)} \tilde{w}_{i,k} \cdot f(E_i) \approx \sum_{(i|E_i \in \Delta E_j, \Omega_i \in \Omega_k)} \tilde{w}_{i,k} \cdot \bar{f}_j \ . \tag{6.41}$$

The weights $\tilde{w}_{i,k}$ are introduced as a shorthand notation and the average of the model can be calculated via integration

$$\bar{f}_j = \frac{\int_{\Delta E_j} f(E)\,\mathrm{d}E}{\Delta E_j} \ . \tag{6.42}$$

This approximation allows to re-weight the raw fluxes to an arbitrary new target flux function $f'(E)$ with

$$F'_j = \sum_{(i|E_i \in \Delta E_j, \Omega_i \in \Omega_k)} \tilde{w}_{i,k} \cdot \bar{f'}_j = \sum_{(i|E_i \in \Delta E_j, \Omega_i \in \Omega_k)} \tilde{w}_{i,k} \cdot \frac{\bar{f}_j}{\bar{f}_j} \cdot \bar{f'}_j = F_j \cdot \frac{\bar{f'}_j}{\bar{f}_j} \ . \tag{6.43}$$

Using this re-weighted relation, the global number of injected events and the global new fluence normalisation Φ'_0, now for the new fluence Φ' can be computed as shown in equations (6.37) and (6.40) with

$$N = \sum_{j=1}^{N_{\mathrm{bins}}} N_j \frac{w_j}{\sum_{k=1}^{N_{\mathrm{bins}}} w_k} \tag{6.44}$$

and

$$\Phi'_0 = \frac{1}{\sum_{j=1}^{N_{\mathrm{bins}}} w_j} \ , \tag{6.45}$$

where the constant Φ'_0 can shift the whole spectrum Φ' up and down. The weights w_j are computed from

$$w_j = \frac{\int_{\Delta E_j} f'(E)\,\mathrm{d}E}{\Phi^0_j \cdot \int_{\Delta E_j} f(E)\,\mathrm{d}E} \ . \tag{6.46}$$

It can be seen, that the first case of obtaining the global normalization for the same fluence as the injection fluence, is a special case of the general weights in equation (6.46).

When having the same fluence, the weights simplify to

$$w_j = \frac{\int_{\Delta E_j} f(E)\,\mathrm{d}E}{\Phi_j^0 \cdot \int_{\Delta E_j} f(E)\,\mathrm{d}E} = \frac{1}{\Phi_j^0} \ , \tag{6.47}$$

yielding the same result as shown in equation (6.40).

6.7. Post-trial method

In this analysis, the Likelihood is only fitted for the single signal strength parameter n_S. For a two-parameter fit, the number of events is not sufficient for a meaningful fit for small time windows. Nevertheless, multiple time windows are tested because a possible true time window size is unknown. By doing the grid scan in 21 different time windows, a trial factor needs to be regarded though [GV10]. The trial factor accounts for the fact, that multiple options are trialled and a-posteriori the best one is chosen as the final result. The connection to Wilks' theorem here is as follows: Wilks' theorem states, that the difference in the number of free parameters comparing the alternative and null hypothesis is the degree of freedom of the resulting χ^2 test statistic. Fitting more parameters, adding for example the time window length as a free parameter, the test statistic would approximately follow a χ^2 distribution with higher degrees of freedom, thus incorporating a trial factor automatically. This trial factor needs to be included manually here as a penalty for trialling multiple discrete time windows in the whole allowed parameter space and picking the best result a posteriori.

The procedure to finally obtain a trial-corrected result is a follows: In the end, the best out of 21 time windows is picked. To estimate the effective trial factor, the same procedure as used to obtain the final result on data needs to be simulated by using samples following the null hypothesis distribution, so from pseudo background samples in this case. Different from the background trials per time window done before, here the trials are created correlated to each other, like it is the case with the measured dataset in the end. The largest time window is used to create a pseudo sample of pure background events. This sample is then fitted with the 21 different time window Likelihoods and all fit results are recorded per trial. From each trial, the pre-trial p-values are computed using the independent background test statistics per time window. The smallest pre-trial p-value per trial enters the final post-trial distribution against which the best p-value on the final data result is compared. For the final result, the single fit for each time window is undergoing the same procedure and the best pre-trial p-value is inserted into the post-trial distribution to obtain the final result significance.

The post-trial distribution may be described by the following PDF, which gives the probability to observe no p-value lower than a given minimal p-value x, $\min_i p_i \leq x$

from a set of N p-values $\{p_i\}$. The cumulated distribution function can be constructed using the fact that, by definition, p-values have a uniform distribution under the null hypothesis. This yields

$$P(\min_i p_i \leq x) = 1 - P(\min_i p_i > x) \tag{6.48}$$

$$= 1 - P(p_1 > x) \cdot \cdots \cdot P(p_N > x) = 1 - (1-x)^N \ , \tag{6.49}$$

by demanding, that each p-value is independent. To obtain the PDF, the derivative of the constructed CDF P needs to be taken

$$f(\hat{p}) = \left.\frac{\mathrm{d}P}{\mathrm{d}x}\right|_{x=\hat{p}} = -N(1-\hat{p})^{N-1} \ , \tag{6.50}$$

or for the often used distribution of the negative logarithm to base 10 of the p-values

$$y = -\log_{10}(\hat{p}) \rightarrow f(y) = f(\hat{p}(y)) \cdot \frac{\mathrm{d}\hat{p}}{\mathrm{d}y} = N \ (1-10^{-y}) \cdot -\ln(10) \cdot 10^{-y} \ , \tag{6.51}$$

where the rule for transforming probability densities was used [BL13].

The aforementioned independence of p-values may not hold in practice which can lead to deviations in the effective analytic trial factor. In this analysis, for example, the time windows are not independent, because each next larger time window includes all smaller ones. Therefore 10^6 post trials are done here to have a robust empirical estimate for the post-trial distribution, even for higher significances without having to assume some underlying model. Figure (6.7) shows the resulting post-trial test statistic and the connection between the pre-trial and post-trial significances.

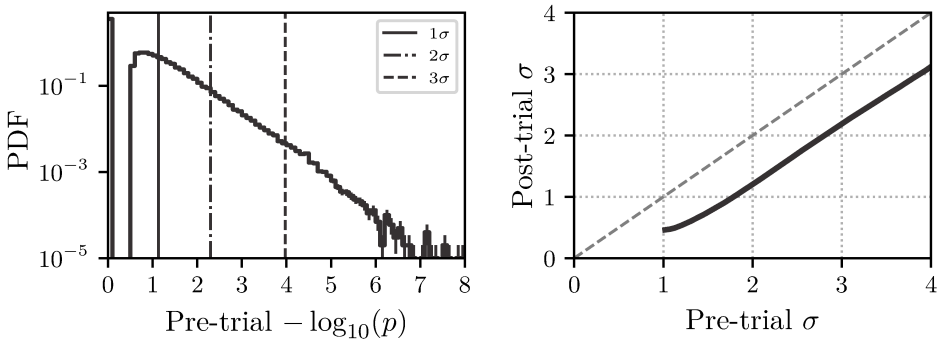

Figure 6.7.: The left plot shows the computed post-trial p-value distribution, sampled from 10^6 post trials. Using that distribution each pre-trial significance can be transformed in a post-trial, final result significance as shown on the right. Due to the still large number of zero trials even in the largest time window, the smallest non-zero pre-trial significance that can be obtained here, is approximately $1\,\sigma$.

6.8. Results

The so far held-back on-time data, containing all events within any of the largest time windows around any source are used to do a single fit per time window with the prepared Likelihood models. This yields 21 fit results, one for each time window with a single pre-trial p-value for each one. Afterwards, the post-trial significance is calculated by selecting the best p-value and comparing it to the post-trial test statistic as described in section 6.7.

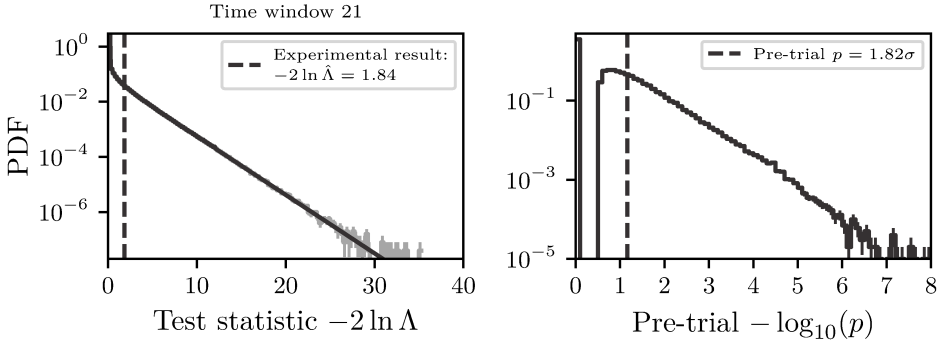

Figure 6.8.: The resulting best fit test statistic value for a single fit on the experimental muon track dataset on the left and the post-trial significance on the right. Both values are shown within their corresponding pre-trial and post-trial distributions.

No significant excess of neutrinos is seen in the stacked search around the 22 proposed

high energy starting events taken as source positions. Table (6.2) summarizes the pre-trial fit results. The best pre-trial fit was achieved for the largest time window $[-2.5, 2.5]$ days centred around each source with a pre-trial p-value of 0.068, the best-fit test statistic of 1.82 and 2.32 signal-like events. The final, trial corrected p-value is then 0.30 corresponding to $1.03\,\sigma$, obtained by inserting the smallest pre-trial value in the survival function of the empirical post-trial distribution.

Table 6.2.: Results of the time-dependent stacking search with 22 track-like high energy starting events as sources. The fit results per time window performed on held-back on-time data are shown. All p-values p are pre-trial. The most significant and only non-zero result for the largest time window 21 needs to be trial corrected.

ID	$\hat{n}_S$	$-2\ln\hat{\Lambda}$	p	ID	$\hat{n}_S$	$-2\ln\hat{\Lambda}$	p
1	0	0	1	11	0	0	1
2	0	0	1	12	0	0	1
3	0	0	1	13	0	0	1
4	0	0	1	14	0	0	1
5	0	0	1	15	0	0	1
6	0	0	1	16	0	0	1
7	0	0	1	17	0	0	1
8	0	0	1	18	0	0	1
9	0	0	1	19	0	0	1
10	0	0	1	20	0	0	1
				21	2.32	1.82	0.068

7. Time-integrated analysis

In addition to the time-dependent analysis in the previous chapter 6, a time-integrated analysis is performed to test for a potential steady flux scenario from the high energy starting event positions. This may be seen as the special case to the previous analysis using time windows as large as all samples combined across all sources. Instead of using a self-developed computing code, the calculations are mostly done using the `skylab` [Aar+17a; Coe17] module here, which is a versatile tool for performing various types of time-integrated point source searches in IceCube. Therefore the technical details of the implementation can be reviewed in the software description and only a short summary focusing on the key differences to the time-dependent search is given in this chapter. For the signal injection, the same injection code as used for the time-dependent analysis is used via a small adapter to be able to take the source position uncertainties into account with the `skylab` code.

As mentioned before, no significant excess of neutrinos at any location on the sky could be found in the extensive all-sky search with seven years of data. The results also indicate, that at each HESE position no significant source can be identified. This motivates to additionally conduct a time-independent stacked search independently of the previous time-dependent one, to check for the possibility that the sources, that have emitted the high energy starting events, are only emitting enough events for a significant detection in a combined search.

The method used in this analysis is similar to the previous one and uses the same underlying Likelihood mechanism. The detailed derivation of the used formula using different approximations suitable for large statistics samples and a steady source scenario can be seen in the dedicated section 5.4. The fact that all sources are assumed to contribute to the common neutrino flux at all times throughout all samples simplifies the construction of background PDFs and the process of trial generation. Therefore no splitting in off- and on-data regions is done beforehand. By scrambling all data events in right ascension before building any PDFs or doing trials, the experimental data is kept "blinded".

The main difference to the time-dependent analysis is the usage of an unbroken power law spectrum with a variable spectral index in the energy PDF. This introduces a second free fit parameter, namely the spectral index γ of the assumed power law flux $\propto E^{-\gamma}$ shared between all sources under the assumption of equal intrinsic emission. Due to the larger

available statistics, it is possible to reliably fit the additional parameter. From a technical point of view, the new degree of freedom is also needed to match the model to background and signal assumptions. While the specific shape of the underlying spectral model was not very important in the time-dependent analysis due to the low overall background expectation, it is necessary here to distinguish signal and background contributions more efficiently.

Performance estimation is done exactly as in the time-dependent analysis, by scanning a grid of true source strengths and building a test statistic for each grid point. This yields the Neyman plane marginalized over γ and can be used to fit a fairly general χ^2 CDF to the samples, to build the required performance parameters or limits. Also differential performances are calculated for a quite high resolution to allow for the computation of a wide range of custom models. No post trials are needed here because no grid scan is performed. Instead, the spectral index is fitted directly, which incorporates the trial factor automatically in the fitting procedure.

7.1. Per event distribution modelling

The methods to generate probability distributions from measured data and simulation, are chosen to be compliant to previously conducted IceCube point source analysis, which used the same or similar datasets for time-integrated searches. A set of rules regarding the binning and handling of these data, tuned for optimal results in time-integrated searches is therefore also used in this analysis and shortly described below.

Spatial PDF

Here, the spatial signal PDF is defined as a two-dimensional Gaussian distribution. However, this makes virtually no differences to the signal PDF for the time-dependent analysis, where the Kent distribution was used. As the dataset consists of well-reconstructed muon tracks, the angular uncertainty is small enough to avoid the regions in which both PDFs would start to severely differ.

The background PDF construction is similar to the time-dependent ones, but is simpler to compute here. Because seasonal variations are averaged out in the whole sample livetime, it is sufficient to construct a single average distribution from data to describe the background behaviour

$$f(\delta_i) = \frac{1}{2\pi} \cdot P(\delta_i) \ . \tag{7.1}$$

This is done by histogramming the data events in sine of declination and fitting an interpolating spline through the resulting bin centre points to have a smooth and

continuous representation of the PDF available. Again, for being consistent with the commonly used PDFs in IceCube, the binning is chosen a bit different than in the previous analysis, which makes almost no difference in the used PDF. The binning set-up can be looked up in the `skylab` module which collects the shared settings for the datasets. In figure (7.1) the $\sin(\delta)$ PDF for each sample and a comparison to the binning used in the time-dependent analysis can be seen.

Energy PDF

The energy PDF needs to be built and evaluated for multiple power law spectral indices because the second fit parameter is the spectral index of the assumed source flux. To avoid long computing times by re-calculating the two-dimensional PDFs in $\sin(\delta)$ and $\log_{10}\left(E_{\text{proxy}}\right)$ for every index γ occurring during the fitting procedures, the PDFs are built and cached for a fine grid of spectral indices beforehand.

For a fixed index γ the histograms are built as before from data and signal simulation with the same binning and the ratio is built to describe the signal over background ratios for the energy term. For simulated signal data, the number of events per bin can be computed using the modified OneWeight[15]

$$N(\Delta E, \Delta\delta) = T \cdot \sum_{(i|E_{\nu,i}\in\Delta E, \delta_i\in\Delta\delta)} \frac{\text{OneWeight}'_i \cdot \phi(E_i|\gamma)}{\Delta\delta\Delta E} \quad , \tag{7.2}$$

where now the spectral index γ can vary for each source flux hypothesis and each sample livetime T needs to be regarded to adapt the expected number of signal events for each sample accordingly. The binning can again be looked up in the `skylab` module. Also, a more conservative approach is followed here compared to the time-dependent analysis, which is necessary due to the flexible spectral index and the way the ratios are constructed. The ratios without valid background or signal histogram points are set to the lowest ratio and are thus made very background-like. This may worsen the sensitivity, especially for high energy proxy values and hard spectra, but cannot artificially introduce separation power based on low simulation or data statistics. An approach to resolve this would be to fill in missing values in the background and signal PDF histograms themselves using the underlying model assumptions. The ratio would then be defined in every pixel before taking the ratio. Figures (7.2) and (B.42–B.44) show the change of the signal over background PDF ratios for selected spectral indices per sample.

To cache the energy PDF dependency on the spectral index, the signal over background ratios are built for each γ on a grid, which is constrained in the interval $[1, 4]$ to cover a broad range of physically plausible hard and soft energy spectra. The stack of histograms

[15] See equation (5.72) for a more detailed description of OneWeight.

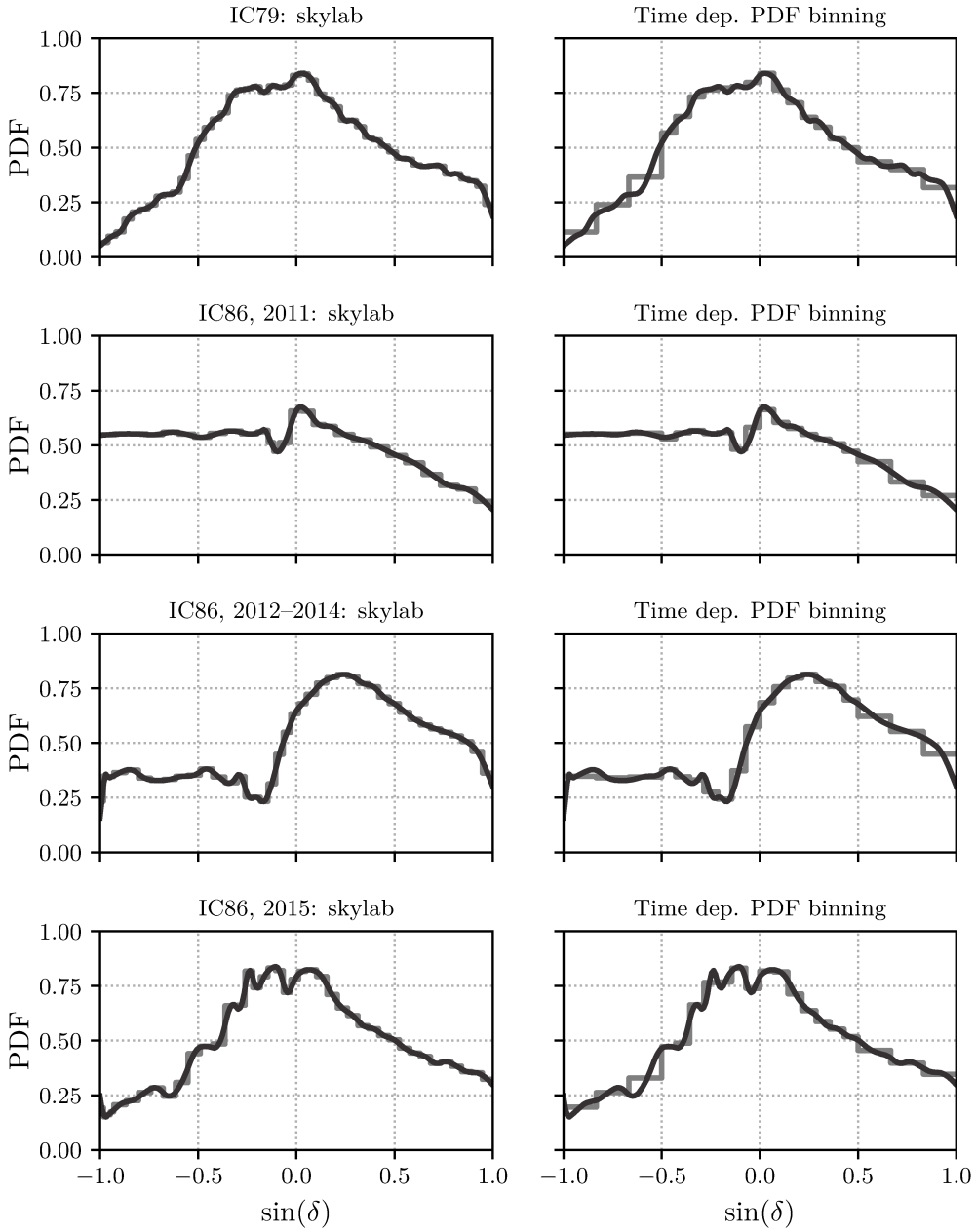

Figure 7.1.: Resulting background PDFs in $\sin(\delta)$ per sample. Because of the steady-state source emission assumption, a single average PDF is sufficient per sample for all sources. On the left plots, the `skylab` binning with the spline constructed by interpolating through the bin centres is shown. On the right, the same spline is plotted, but the histogram uses the previous binning from the time-dependent analysis to be able compare the differences. Each spline is normalised only across the $\sin(\delta)$ dimension in the plots, but the normalisation across the right ascension dimension is a constant of 2π anyway due to the assumption of having a symmetric right ascension PDF.

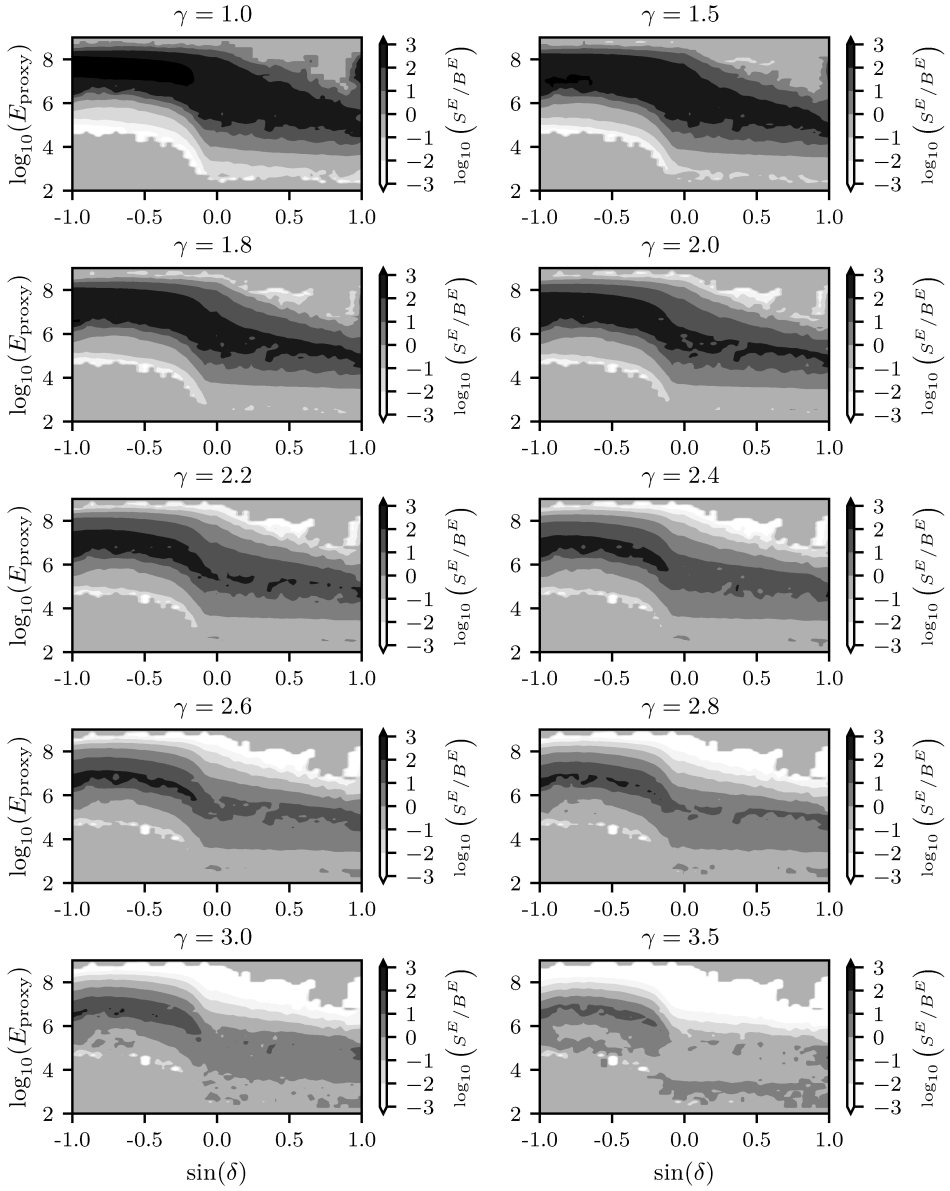

Figure 7.2.: Two-dimensional ratio of the signal and background energy PDFs in $\log_{10}\left(E_{\text{proxy}}\right)$ and $\sin(\delta)$ for the IC79 sample and for different spectral indices γ. The underlying binning is the same for the signal and background histogram. Each ratio is pre-calculated for a grid of spectral indices beforehand and used during the fitting procedure for the current realization of γ. A one-dimensional spline, which is not shown here, is used per $\left(\sin(\delta), \log_{10}\left(E_{\text{proxy}}\right)\right)$ tuple for each event to interpolate the grid and obtain the gradient information for the spectral index fit parameter.

is then used to create a one-dimensional spline in the γ direction on the fly for each pair of $\left(\sin(\delta), \log_{10}\left(E_{\text{proxy}}\right)\right)$ during the fit, to obtain a continuous description and get the needed derivatives for the fit in analytic form as well. The built splines are cached during runtime to avoid repeated construction for the same declinations and energies. Another approach would be to use multi-dimensional splines directly to parametrize the PDF. In this case, the spline would be three-dimensional, in $\log_{10}\left(E_{\text{proxy}}\right)$, $\sin(\delta)$ and γ. The advantage would be to have a single description of the PDF and obtain analytic gradients in all directions automatically. However, it might be more difficult to verify a proper description of the underlying data for higher dimensions, so a thorough verification process would be needed. Alternatively, a multidimensional kernel density estimation could be considered, which would automatically come with the possibility to directly sample the distributions for trial generation.

7.2. Stacking and multi-sample weights

Here, the source weights and the multi-sample n_S split weights both depend on the current spectral index and have to be re-evaluated each time the index changes. Otherwise, the calculation happens similar to the procedure in the time-dependent analysis, but the signal simulation needs to respect the sample lifetimes T and the current spectral index γ for the assumed power-law flux ϕ in the weights

$$w_i = T \cdot \phi(E_{\nu,i}|\gamma) \cdot \text{OneWeight}'_i \ . \tag{7.3}$$

An interpolating spline is used to continuously describe the built histogram, normalized by the bin width $\Delta\Omega_{\text{bin}}$. Though using the same spline per sample, the difference in the construction of the stacking and sample split weights, compared to the time-dependent analysis, is the normalization procedure. Stacking weights only consider how a given signal is split according to the expectation within one sample and are normalized accordingly

$$\sum_{k=1}^{N_{\text{src}}} w_{k,j} = 1 \ , \tag{7.4}$$

whereas the n_S sample split weights w_j follow the normalization rule from the aforementioned law of total probabilities (5.12)

$$\sum_{j=1}^{N_{\text{sam}}} w_j(\gamma) = \sum_{j=1}^{N_{\text{sam}}} \sum_{k=1}^{N_{\text{src}}} P(j|k,\gamma) \cdot P(k|\gamma) = 1 \ , \tag{7.5}$$

where $P(j|k,\gamma)$ and $P(k|\gamma)$ can again be obtained by the number of expected events depending on the current spectral index γ and have to be adapted accordingly during a fitting procedure. The dependency on the spectral index is not strong though, as can be seen in figure (B.40).

7.3. Note on LLH minimization

The extra fit parameter γ makes it necessary to calculate an additional analytical gradient $\partial\gamma$ to avoid costly Likelihood evaluations for numeric gradient calculations and to obtain precise gradients. For the full multi-sample Likelihood (5.64), the gradients are

$$\frac{\partial(-2\ln\Lambda)}{\partial n_S} = \frac{\partial}{\partial n_S}\left\{2\sum_{j=1}^{N_{\text{sam}}}\left[\sum_{i=1}^{N_j}\ln\left(\frac{n_S}{N_j}\left(R_{i,j}-1\right)+1\right)\right]\right\} \tag{7.6}$$

$$= 2\sum_{j=1}^{N_{\text{sam}}}\left[\sum_{i=1}^{N_j}\frac{R_{i,j}-1}{n_S\left(R_{i,j}-1\right)+N_j}\right] \tag{7.7}$$

for n_S and

$$\frac{\partial(-2\ln\Lambda)}{\partial \gamma} = \frac{\partial}{\partial \gamma}\left\{2\sum_{j=1}^{N_{\text{sam}}}\left[\sum_{i=1}^{N_j}\ln\left(\frac{n_S}{N_j}\left(R_{i,j}-1\right)+1\right)\right]\right\} \tag{7.8}$$

$$= 2\sum_{j=1}^{N_{\text{sam}}}\left[\sum_{i=1}^{N_j}\frac{n_S}{n_S\left(R_{i,j}-1\right)+N_j}\cdot\frac{\partial R_{i,j}}{\partial\gamma}\right] \tag{7.9}$$

for γ respectively, where

$$R_{i,j} = R_{i,j}(\gamma) := \frac{\sum_{k=1}^{N_{\text{srcs}}}(w_j(\gamma)w_{k,j}(\gamma)S_{i,k,j}(\gamma))}{B_{i,j}} \tag{7.10}$$

was introduced for a shorter notation. The $\partial\gamma$ derivatives of the signal over background ratios $R_{i,j}$ can be evaluated using the analytic spline derivatives used to construct the weights and PDFs and the application of the product derivation rule

$$\frac{\partial R_{i,j}}{\partial\gamma} = \frac{1}{B_{i,j}}\cdot\sum_{k=1}^{N_{\text{srcs}}}\left(\frac{\partial w_j}{\partial\gamma}w_{k,j}S_{i,k,j} + w_j\frac{\partial w_{k,j}}{\partial\gamma}S_{i,k,j} + w_j w_{k,j}\frac{\partial S_{i,k,j}}{\partial\gamma}\right) \quad . \tag{7.11}$$

7.4. Trial generation

Trial generation is similar to the method in the time-dependent analysis. The main differences here are the easier background trial generation, by using the full set of spatially scrambled background data and the different signal injection mode due to the time-integrated flux.

Here, the added fit parameter γ leads to a better conversion to a χ^2 background only test statistic as expected from Wilks' theorem. Using a fixed index would result in many

test statistic values of zero during background trials because a larger set of background events follows a much steeper energy spectrum than predicted signal and thus makes it hard to properly sample a rather flat spectrum from the given experimental dataset. The variable index results in almost 50 % over- and under-fluctuations in background trials with spectral indices preferably getting fitted in the more steep spectral region with indices $\gamma_{\mathrm{BG}} \in [2.7, 3.7]$. These are shifted a bit from the expected atmospheric index of roughly 3.7 indicating a small bias in the fit parameter from the background scrambles.

Background trials

In this analysis, pure background pseudo data samples are generated by using the experimental data for the same reason of avoiding bias from mismatches between data and background simulation. To obtain a pseudo background sample, it is sufficient to assign a new right ascension value, sampled uniformly in $[0, 2\pi]$ to each event per trial. The usage of experimental data as background is justified by the assumption of expecting a low amount of signal in the sample and that the spatial scrambling of the event positions in right ascension ensures the removal of any potential signal clustering. Additionally, because the Likelihood works with the approximation of having a constant number of events by dropping the Poisson term, the number of background events stays constant in each trial.

10^6 background-only trials where performed to describe the test statistic distribution sufficiently accurate. Again, no under-fluctuations are fitted and the fit parameter n_S is truncated at zero. Due to the variable index, this is not as large an issue as previously described. The test statistic follows the expected χ^2 distribution well and is therefore analytically described with a modified χ^2 PDF, which is a common choice for a time-integrated search. The number of degrees of freedom of the χ^2 PDF turns out to be slightly higher than its expected value of 1 from Wilks' theorem. This is because for very background-like samples, which means $n_S = 0$, the spectral index of the signal energy PDF has no relevance any more and is degenerate, leading to the slightly different effective number of degrees of freedom $\hat{n}$. The distribution fitted to the test statistic is a split PDF model catching the compactified under-fluctuations at zero with a delta peak and the tail with a χ^2 distribution

$$f(x := -2 \ln \hat{\Lambda}) = \begin{cases} \eta \cdot \chi^2_{\hat{n}}(x) & \text{, for} \quad x > 0 \\ (1 - \eta) & \text{, for} \quad x = 0 \end{cases} . \tag{7.12}$$

The PDF is fitted to the test statistic by only varying the effective number of degrees of freedom $\hat{n}$ with a best fit of 1.17. The fraction of non-zero trials $\eta = 0.54$ is directly deduced by simple counting. The comparison to the fitted χ^2 model and the hybrid solution that was used in the time-dependent analysis can be seen in figure (B.45). The

distribution of the fitted signal strengths and spectral indices for the background trials are shown in figure (B.46). As the median of the spectral index fit values lies around 3, a small bias towards slightly harder indices than expected from the simplified atmospheric expectation of $\gamma_{\text{atmo}} \approx 3.7$ can be seen. However, this has no influence on the final result, as this type of analysis is not well suited to really measure the astrophysical spectral index, but it is rather treated as a nuisance parameter to adapt the signal model in a flexible way to the data.

Signal trials

The signal injection is set up to simulate a steady flux scenario. This comes with two main differences to the time-dependent part. First, all sources contribute in every sample and are no longer unique and only present in a single sample. Second, the expected flux is directly proportional to the data livetime in each sample. Both properties need to be reflected by the signal injector. The weights for the signal event sampling are constructed with

$$w_{i,k} = w_k \frac{\text{OneWeight}'_i \cdot \phi(E_{\nu,i})}{\Omega_k} \cdot T \ , \tag{7.13}$$

where k is the source the event was selected at, w_k the combined source weight and T the sample livetime in seconds. The simulated diffuse flux $\phi(E_{\nu,i})$ is normalized to a point source flux by dividing out the solid angle Ω_k of the selected regions around each source and has units $1/(\text{GeV}\,\text{cm}^2\,\text{s})$. The sampling itself stays the same and is also used with the same HEALPix injection mode to account for the source position uncertainties. No time information is sampled or needed in this steady-state scenario.

To combine multiple signal injectors, the distribution weights need to be adapted to account for the fact that all sources are present in every sample. Here, it is sufficient to distribute the samples according to their expected events in total, without a need to re-normalize the source weights

$$w_j = \frac{N_j}{\sum_{m=1}^{N_{\text{sam}}} N_m} \ . \tag{7.14}$$

7.5. Performance

The a priori estimation of the analysis performance is performed analogue to the procedure in section 6.5. Because the performance flux is just a single value for the full analysis, a finely binned differential performance is computed here. The differential performance is estimated in logarithmic energy bins, uniformly spaced with an eighth of a decade

between 10^2 GeV and 10^9 GeV. Additionally the differential performance is computed for two injection spectra, with indices $\gamma_{\text{inj}} = 2$ and $\gamma_{\text{inj}} = 3$ to validate if the bin size is sufficiently small to justify the creation of arbitrary flux performances and limits as explained in section 6.6. The differential fluxes can be seen in figure (7.3). In figure (B.41), the number of actually injected events per bin to reach the performance definition is shown. The amount of signal events needed is almost identical for both injection models. This is one requirement needed to be able to derive global performances and limits from the differential fluxes. The corresponding χ^2 CDF fits to the discrete test statistic points used to estimate the performance fluxes are shown in figures (B.47, B.48) for $\gamma_{\text{inj}} = 2$ and in figures (B.49, B.50) for $\gamma_{\text{inj}} = 3$. The numerical values for the differential sensitivity fluxes can be found in tables (B.3, B.4).

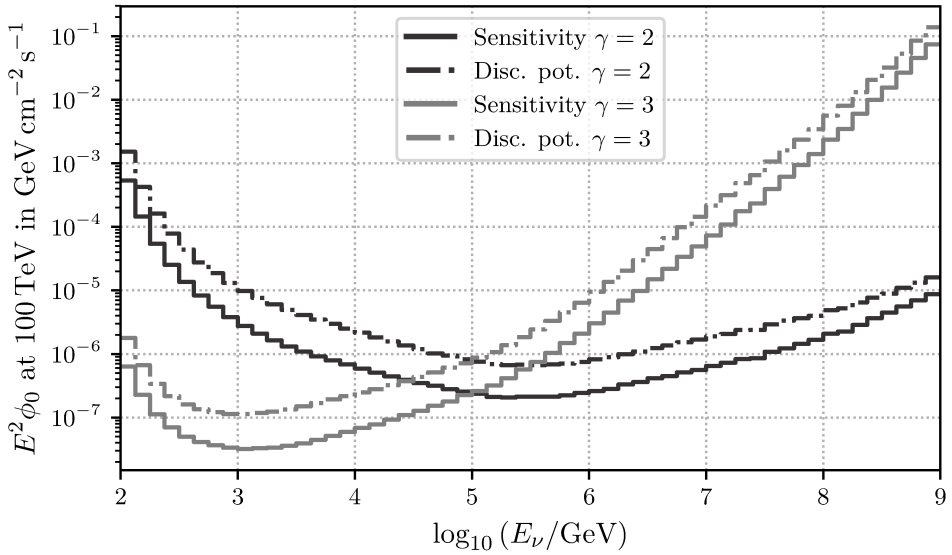

Figure 7.3.: Shown are the differential sensitivity and discovery potential fluxes for the time-integrated analysis. Both performances are computed once with an injection spectrum with a spectral index of $\gamma_{\text{inj}} = 2$ and once with $\gamma_{\text{inj}} = 3$ to validate the aforementioned subtleties when using differential performances. The bins are uniformly spaced in logarithmic neutrino energy with a width of one eight of a decade in order to minimize the spectral dependency in each bin.

The connection between the flux normalisation ϕ_0 and the model flux F is slightly different here. Because of the steady-state emission scenario, the expected number of events can

be calculated using

$$N = T \cdot \sum_{k=1}^{N_{\mathrm{srcs}}} \sum_{(i|\Omega_i \in \Omega_k)} w_k \frac{\mathrm{OneWeight}'_i \cdot \phi_0 \cdot f(E_{\nu,i})}{\Omega_k} \tag{7.15}$$

$$= \phi_0 \cdot \sum_{k=1}^{N_{\mathrm{srcs}}} \sum_{(i|\Omega_i \in \Omega_k)} w'_{k,i} := \phi_0 \cdot \sum_{k=1}^{N_{\mathrm{srcs}}} F_k = \phi_0 \cdot F \ , \tag{7.16}$$

where T is the sample livetime. A global flux normalization ϕ'_0 can equivalently be obtained from the differential performance normalizations ϕ^0_j using

$$\phi'_0 = \frac{1}{\sum_{j=1}^{N_{\mathrm{bins}}} w_j} \ , \tag{7.17}$$

where the weights w_j are computed from

$$w_j = \frac{\int_{\Delta E_j} f'(E)\,\mathrm{d}E}{\phi^0_j \cdot \int_{\Delta E_j} f(E)\,\mathrm{d}E} \ . \tag{7.18}$$

7.6. Results

The analysis result is obtained by doing a single Likelihood fit on the unscrambled experimental dataset. The resulting test statistic value is compared to the background only test statistic model to obtain the final p-value

No significant excess of neutrinos is seen in the test for a steady state flux scenario. The best-fit test statistic is 0.057 with best-fit parameters $\hat{n}_S = 5.57$ and $\hat{\gamma} = 2.8$. This results in a p-value of $p = 0.47$ and a significance of $0.73\,\sigma$. The best fit test statistic value together with the background only distribution can be seen in figure (7.4). No post-trial correction needs to be applied.

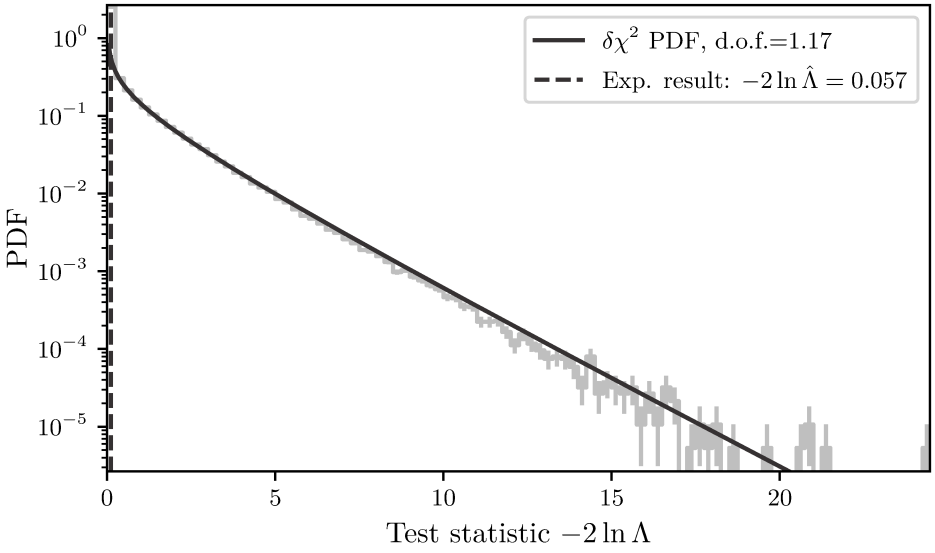

Figure 7.4.: Background only test statistic together with the unblinded experimental result. The best test statistic value of 0.057 was shifted to twice its value to be visible in the plot. In solid, the fitted χ^2 PDF model is overlaid, which is used to estimate the p-value.

8. Discussion

Both analyses conducted in this thesis do not yield a significant measurement of the sought-after, additional neutrino event clustering at the 22 proposed high energy starting event positions. Fluence and flux limits based on the non-detection are calculated for each analysis and presented in this chapter, serving as the final analyses results.

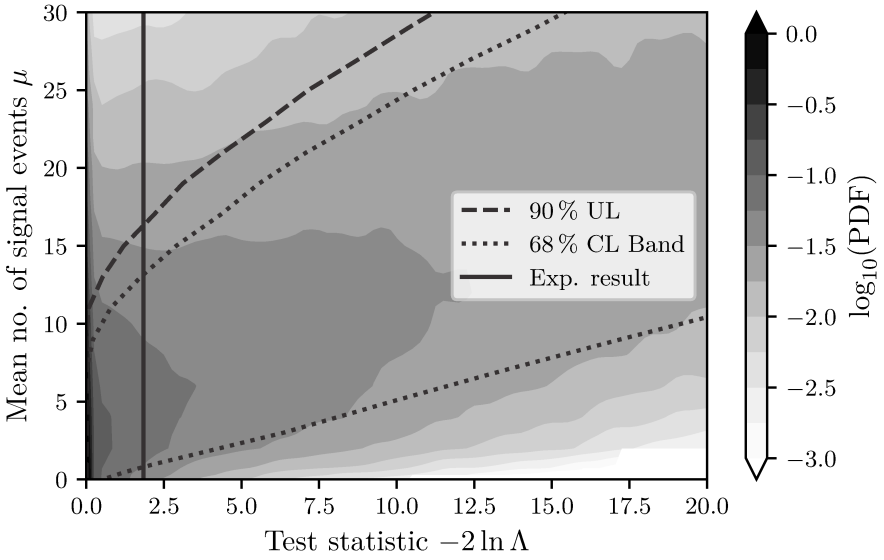

Figure 8.1.: Neyman plane scan for the true but unknown signal strength parameter μ for the time-dependent analysis for the largest time window. Each row is constructed by doing a number of signal trials injecting the mean number of true signal events. The upper limit on the true signal strength parameter can be read of by vertically intersecting the upper limits line with the experimental result test statistic value. The plane is smoothed with a Gaussian kernel for viewing purposes only, the bands are constructed from the pure empirical test statistics.

Time-dependent search

In the time dependent-search, a single parameter fit for the global signal strength is done in combination with a scan over 21 logarithmically increasing time-windows from two

seconds to five days. After trial-correction, the measurement in the largest time window yielded a non-significant result of $1.03\,\sigma$.

The true signal strength parameter μ, which is estimated by the fitted signal strength parameter n_S, is constrained by the construction of Neyman upper limits. For this, the full plane and limit construction is shown in figure (8.1). The construction yields a central $1\,\sigma$ interval with boundaries $[0.8, 13.2]$ and a 90 % upper limit of 16.3 These are pre-trial limits in a sense, that they are computed against the pre-trial significance and the single background test statistic for the largest time window only. If the significance would have been closer to an actual detection, the extra effort of taking the trial factor into account should be taken and the bounds would get wider respectively. This could be done similar to the post-trial method used for the background trials. Events correlated over all time windows must be drawn for both the pseudo signal and background samples and then the best fit per trial would be incorporated into the post-trial test statistic.

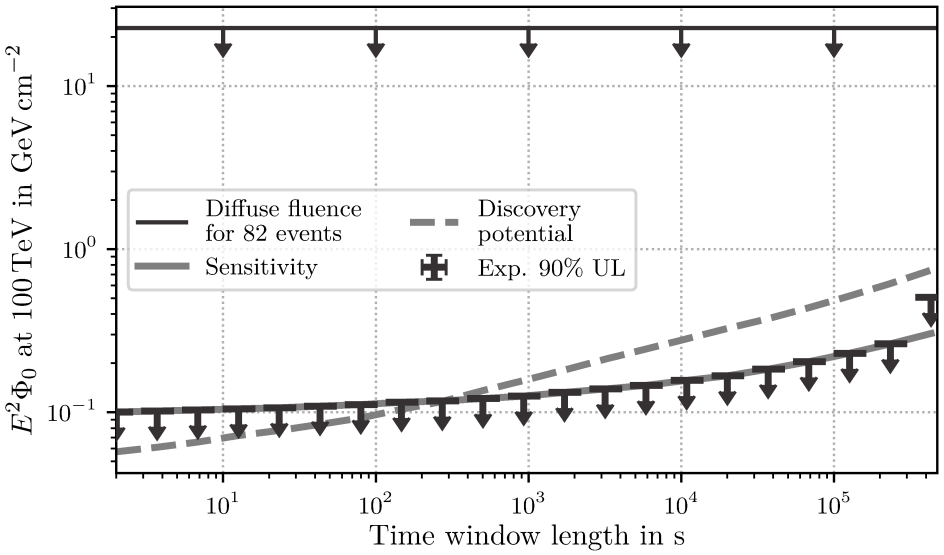

Figure 8.2.: 90 % Neyman upper limits per time window on the fluence normalisation at 100 TeV. All limits are equal to the sensitivity except for the largest time window which shows an overfluctuation in the best fit test statistic value with respect to the background expectation. The dark solid line indicates the expected fluence, if the whole astrophysical flux component measured in [HW18] would have been emitted in a burst scenario. Any fluence above that line would lead to a higher diffuse flux than measured.

Upper limits for the assumed power law fluence with a spectral index of $\gamma = 2$ are calculated against the measured number of signal events for each time window separately. This is done to show the flux constraints if each window would not have been scanned, but a priori fixed. To compute the limits for a confidence level α, the amount of signal

needs to be found, so that the test statistic with injected signal events has its $1 - \alpha$ percentile at the measured test statistic value in the corresponding time window. Here, upper limits at the usual 90 % confidence level are chosen. The resulting upper limits for each time window can be seen in figure (8.2). For each time window with a test statistic of zero, the sensitivity is per definition the upper limit. For the largest time window, the upper limit is higher because of the non-zero significance in that region.

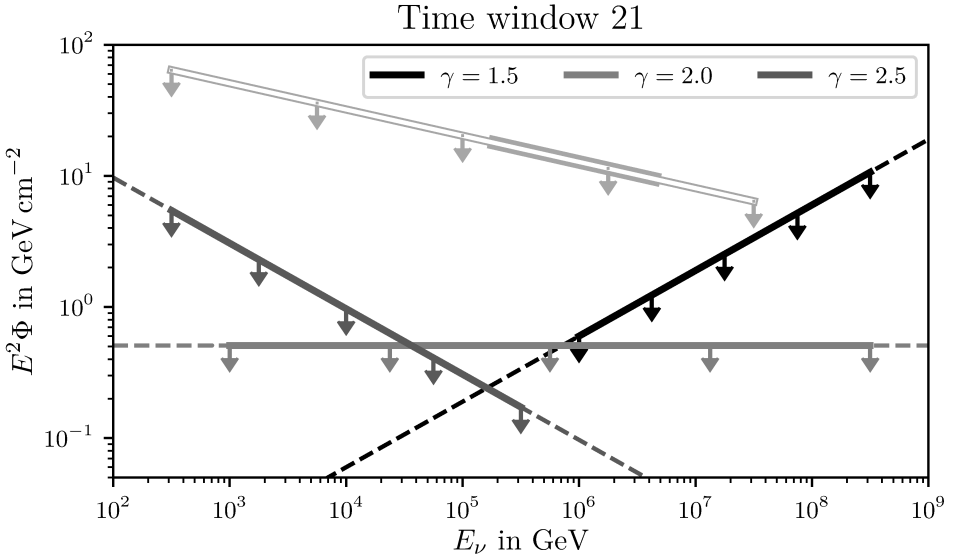

Figure 8.3.: 90 % Neyman upper limits for the largest time window for a selection of spectral indices γ. The solid region gives the central 90 % interval with the best sensitivity for the given spectral index. The range is derived from the differential performances and the weight PDFs can be found in figure (B.51). The double light grey solid line shows the fluence limits derived from the diffuse flux measurement scaled to a burst fluence as explained in the text. The thicker portion of the line shows the valid region given in the original work, the thinner portion the 90 % central interval obtained from the differential fluence limits.

The calculated limits are not directly comparable to a specific model, as models that predict a time-dependent neutrino flux or a per-burst emission from a possible source of high energy starting events do not exist so far. Time-dependent and burst models are primarily built for Gamma Ray Bursts, which have been tested in a dedicated time-dependent analysis similar to this work [Aar+15a; Abb+12]. However, it is possible to generically compare the limits against the current diffuse astrophysical muon neutrino flux measurement made in IceCube [HW18]. The used flux model is an unbroken power-law and the best fit is given as

$$\phi^{\nu_\mu+\bar{\nu}_\mu} = 1.01 \cdot \left(\frac{E_\nu}{100\,\mathrm{TeV}}\right)^{-2.19} \cdot 10^{-18}\,\frac{1}{\mathrm{GeV\,cm^2\,s\,sr}}\ . \tag{8.1}$$

This can be used to calculate a fluence upper limit that can be compared against this analysis' upper limits. Under the assumption, that the whole diffuse flux from (8.1) is accounted for by burst emission originating from the $N_{\text{srcs}} = 22$ track-like high energy starting event positions in $T_{\text{tot}} = 2071.13$ days of lifetime[16], this leads to a burst rate of

$$R_{\text{HESE}} = \frac{N_{\text{srcs}}}{4\pi \cdot T_{\text{tot}}} \approx \frac{22}{4\pi \cdot 2071.13 \cdot 86\,400} \frac{1}{\text{s sr}} \approx 9.78 \cdot 10^{-9} \, \frac{1}{\text{s sr}} \tag{8.2}$$

for a single direction per second. The E_ν^2 weighted diffuse flux normalisation at 100 TeV

$$E_\nu^2 \phi_0^{\nu_\mu + \bar{\nu}_\mu} = 1.01 \cdot 10^{-8} \, \frac{\text{GeV}}{\text{cm}^2 \, \text{s sr}} \tag{8.3}$$

can then be scaled to a per-burst fluence with

$$E_\nu^2 \Phi_{\text{HESE}}^{\text{diff}} = \frac{\Delta T \cdot E_\nu^2 \phi_0^{\nu_\mu + \bar{\nu}_\mu} \cdot 4\pi}{\Delta T \cdot R_{\text{HESE}} \cdot 4\pi} = \frac{E_\nu^2 \phi_0^{\nu_\mu + \bar{\nu}_\mu}}{R_{\text{HESE}}} \ . \tag{8.4}$$

Note, that the dependence on the burst time window ΔT and the factor 4π for the isotropic integration over the whole sky is cancelled, because the burst rate scales accordingly. This leads to a potential E_ν^2 weighted per-burst fluence of

$$E_\nu^2 \Phi_{\text{HESE, burst}}^{\text{diff}} \approx 1.03 \, \frac{\text{GeV}}{\text{cm}^2} \text{ or a total fluence of } E_\nu^2 \Phi_{\text{HESE}}^{\text{diff}} \approx 22.71 \, \frac{\text{GeV}}{\text{cm}^2} \tag{8.5}$$

at at a normalisation energy of 100 TeV. Any fluence higher than $\Phi_{\text{HESE}}^{\text{diff}}$ would mean that more than the total observed diffuse astrophysical muon neutrino flux would originate from a possible per-burst emission at the HESE positions, which is a highly unlikely scenario. As seen in figure (8.2), the limits set by this analysis are sane and well below the diffuse limits, indicating a smaller contribution to the diffuse flux.

To obtain limits for a wider range of spectra and not only the one that is explicitly tested against, limits are calculated for several different spectral indices for the assumed sources and for all time-windows. It is always tested against the largest time-window with the highest significance. The resulting upper limits can be seen in figure (8.3). The central solid interval indicates the energy region in which the analysis has the most potential sensitivity for the given spectral hypothesis. These intervals can be computed from the inverse differential fluences as explained in section 6.6 and the resulting weight distribution is shown in figure (B.51). Additionally to the shown selection of three power-laws, a fine grid scan of spectral indices is done. Figure (B.52) shows the resulting limits. Instead of plotting the power law energy dependent, only the fluence normalisations are shown

[16] As total fluences are compared in the end, the per-source normalisation cancels out again, but was put through the calculation for clarity here.

for two pivot energies, 1 GeV and 100 TeV. The fluence shapes, that can be inferred from these two reference points again indicate the low background contribution even for the largest time windows. For the normalisation at 100 TeV the limit fluence for the E^{-2} power law is actually the highest among the tested indices. This can be understood regarding the low number of background events and the relatively low influence of the energy PDF. The energy point at which the energy PDF in combination with a few events close to any source leads to high signal over background ratios, is lower than the shown 100 TeV. Harder spectra still gain from the in general higher energy events, but also the softer power-laws gain lower limits, because they can counter the lack of higher energy events with more medium energy events, that are sufficient to yield high test statistics in the absence of many background events.

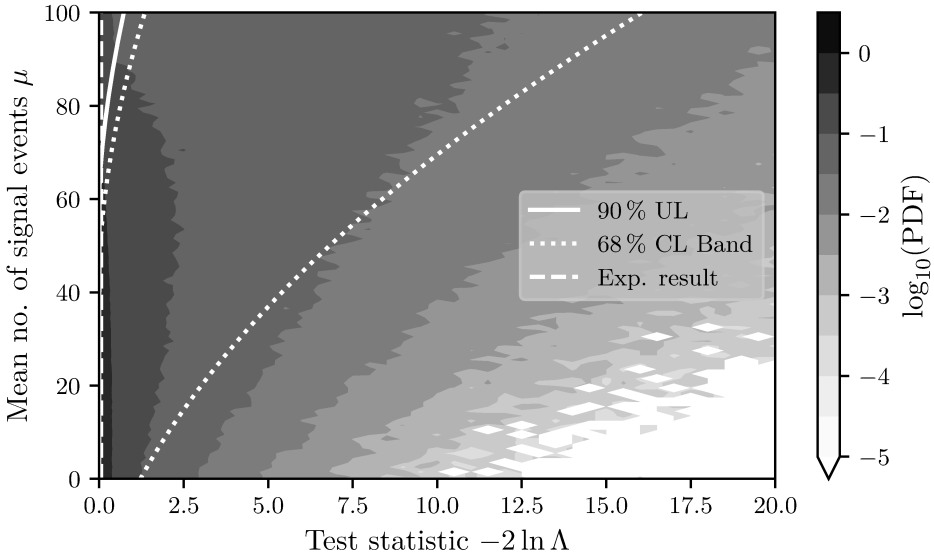

Figure 8.4.: Neyman plane scan for the true but unknown signal strength parameter μ for the time-integrated analysis. Each row is constructed by doing a number of signal trials, injecting the mean number of true signal events. The upper limit on the true signal strength parameter can be read of by vertically intersecting the upper limits line with the experimental result test statistic value. The bands are constructed from spline fits to the discrete empirical quantiles for smoothing. The splines can be found in figure (B.53)

Time-integrated search

The search for a steady flux emission originating from the 22 high energy starting event positions also yields no significant result. A slight over-fluctuation of $0.73\,\sigma$ over the

expected background could be measured in six years of muon track data. Limits are constructed and shown as the main physics results in this section.

Equivalently to the Neyman plane constructed in the time-dependent analysis, the bounds for the true signal strength parameters can be computed here too. Because of the quite insignificant result, the central $1\,\sigma$ bounds, $[0, 52.7]$, are compatible with a true signal strength of zero as shown in figure (8.4). The resulting 90 % upper limit is at a signal strength of 68.1 expected events for all sources. As a technical note, the bands are constructed by fitting smoothing splines to the discrete quantiles of the empirical test statistics to counter the effects of finite statistics used for the scan. As the results are non-significant anyway, this has no influence on any result. The constructed splines and more information on the fitting procedure can be found in figure (B.53).

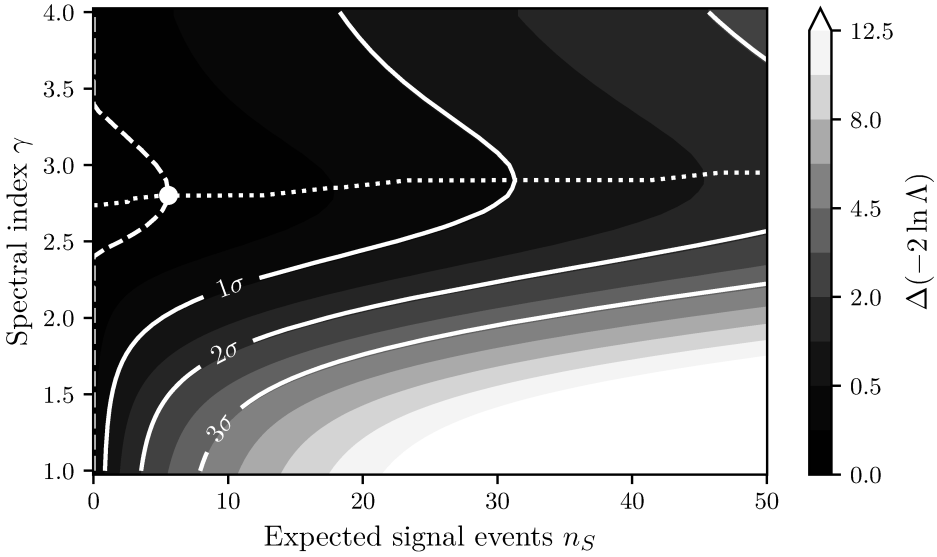

Figure 8.5.: 2D Likelihood scan around the experimental best-fit position in spectral index γ and expected signal events n_S, with the experimental result marked by the white dot. The contours are calculated under the assumption that Wilks' theorem holds, describing the test statistic with a χ^2 distribution with two degrees of freedom. 39 % of probability is enclosed by the $1\,\sigma$ contour. The dashed line gives the marginal scan line for fixing the spectral index and only fitting n_S, the dotted line vice versa for a fixed n_S.

Additionally to the Neyman plane scan for the signal strength parameter, a Likelihood landscape scan in both fit parameters is done. This serves as a tool to inspect the correlation between the two parameters and can also be used to derive limits on the underlying true parameters. The interval estimation is only approximately done here under the assumption that Wilks' theorem holds for connecting the measured with the true values and only serves visualisation purposes. Figure (8.5) shows the scanned

parameter region, where the non-solid lines are marginal scans in each parameter. For each marginal scan, one parameter is fixed at a specific value, while the best fit Likelihood value is only obtained by fitting the other one, yielding one-dimensional parameter confidence intervals. The scan confirms the low significance result from the comparison with the test statistic. The spectral index best fit tends only slightly to harder, signal-like spectra and is close to the median spectral index obtained from the background only trials, shown in figure (B.46), indicating a very background-like dataset.

Power-law flux limits are calculated equivalently to the time-dependent analysis. The differential limits, shown in figure (B.54) were used to calculate global flux limits for a selection of power-law fluxes. Also, the same argumentation used for comparing the time-dependent limits to an effective point source flux from the diffuse flux can be applied. This time, the density of the source events only depends on the sky area

$$R_{\mathrm{HESE}} = \frac{N_{\mathrm{srcs}}}{4\pi} \ , \tag{8.6}$$

so the E_ν^2 weighted point source flux normalisation at 100 TeV per source can be obtained via

$$\phi^{\mathrm{diff}}_{\mathrm{HESE}} = \frac{\phi_0^{\nu_\mu+\bar{\nu}_\mu} \cdot 4\pi}{R_{\mathrm{HESE}} \cdot 4\pi} = \frac{\phi_0^{\nu_\mu+\bar{\nu}_\mu} \cdot 4\pi}{N_{\mathrm{srcs}}} \ , \tag{8.7}$$

which yields

$$E_\nu^2 \phi^{\mathrm{diff}}_{\mathrm{HESE,\ src}} \approx 5.71 \cdot 10^{-9} \, \frac{\mathrm{GeV}}{\mathrm{cm}^2\,\mathrm{s}} \ , \tag{8.8}$$

or a total flux of

$$E_\nu^2 \phi^{\mathrm{diff}}_{\mathrm{HESE}} \approx 1.26 \cdot 10^{-7} \, \frac{\mathrm{GeV}}{\mathrm{cm}^2\,\mathrm{s}} \ . \tag{8.9}$$

Additionally, the limits can be directly compared to the most optimistic sensitivity flux for the seven year single point source search analysis in [Aar+17a]

$$E_\nu^2 \phi^{\nu_\mu+\bar{\nu}_\mu}_{\mathrm{PS,\ sens.}} \approx 4 \cdot 10^{-13} \, \frac{\mathrm{TeV}}{\mathrm{cm}^2\,\mathrm{s}} \ , \tag{8.10}$$

which yields a total flux for all 22 high energy starting events of

$$N_{\mathrm{srcs}} E_\nu^2 \phi^{\nu_\mu+\bar{\nu}_\mu}_{\mathrm{PS,\ sens.}} = 8.8 \cdot 10^{-9} \, \frac{\mathrm{GeV}}{\mathrm{cm}^2\,\mathrm{s}} \ . \tag{8.11}$$

The limits for this analysis are slightly above that potential detection threshold of the single point source search. This does not necessarily mean, that at least one of the source locations should have already shown up in the dedicated analysis. However, as the limits here are penalized by considering the unknown source positions and in the point source analysis a perfectly known position is assumed, that is not a problem per-se. Ignoring

the source uncertainties here, would push the limits below the single source analysis sensitivity again. Also the limits are compared against the most optimistic point source sensitivity flux and the average case, taking into account the source distribution, has worse sensitivity and the dedicated single source search incorporates a seventh year of lifetime instead of the six years used here. In figure (8.6) the limits from this analysis are compared to the one from the diffuse flux measurement and the point source search sensitivity, both scaled to be comparable to the tested case here. As a technical note, for supporting the claim, that the global limits do not depend on the injection spectrum for the fine binning used here, figure (B.57) shows the same limits, but derived from an injection spectrum with index $\gamma_{\text{inj}} = 3$. Also, the weight distributions to obtain the central most significant intervals are shown in figures (B.55, B.56).

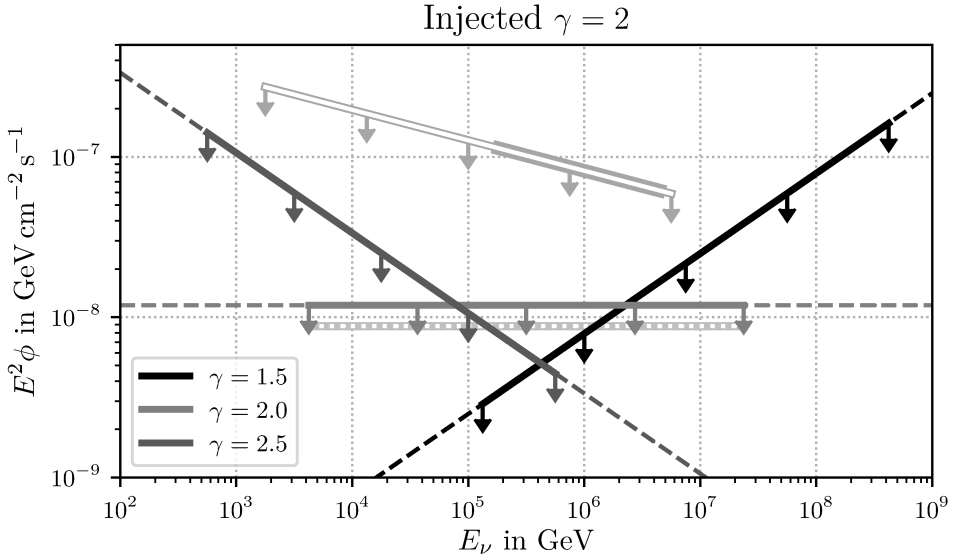

Figure 8.6.: This analysis' power-law limits compared to generic limits derived from the diffuse muon neutrino track flux measurement in [HW18] and the all-sky point source search from [Aar+17a] using seven years of muon neutrino track data. The global limits are derived from the differential limits shown in figure (B.54) with an injection index of $\gamma_{\text{inj}} = 2$. The double light grey solid line shows the flux limits derived from the diffuse flux measurement scaled to a point source flux. The thicker portion of the line shows the valid region given in the original work, the thinner portion the 90 % central interval obtained from the differential flux limits. The double light grey dotted line shows the scaled sensitivity flux from the all-sky point source analysis.

9. Outlook

Both measurements done in this thesis independently show an insignificant but slight over-fluctuation, although the tested regimes are placed at quite opposite ends of the possible source emission scenarios with respect to the temporal source behaviour. In the time-dependent analysis, small to medium sized time windows are tested in a per-burst emission scenario. The underlying temporal emission is not modelled in detail here, in favour of a more generic test. However, the resulting small background leads to a high sensitivity of catching any event at all. On the other end, in the time-integrated analysis, a test for a steady flux assumed to originate from all source positions simultaneously is done. Upper limits and parameter space scans are done in absence of a significant measurement as the main physics results.

For the time-dependent analysis, the largest time window with a total width of five days yielded the most significant result from the 21 tested time ranges, with a post-trial significance of $1.03\,\sigma$ and is therefore compatible with pure background. The resulting limits are calculated for various generic power-law neutrino fluence models and a Neyman upper limit on the number of signal events from the sources could be set. Differential limits were provided if limits for a new model need to be calculated by the reader at some time. For the time-integrated analysis, the final significance was $0.73\,\sigma$ with a best fit spectral index of $\hat{\gamma} \approx 2.8$ which is also well compatible with background. The same family of limits has been calculated as for the time-dependent analysis and finely binned differential flux limits are provided.

In the light of the recent discovery of the correlation between the flaring Blazar TXS 0506+056 with an extremely-high-energy event measured in IceCube [Aar+18b], the results in this thesis seem to fit in the picture, under the assumption, that the detected extremely high energy neutrino may only be the single visible peak energy event. A time window of about 110 days has been found in which a significant neutrino emission from TXS could be measured. Comparing the results from [Aar+18c; Aar+18b] to the results from this thesis, it seems likely that also the high energy starting events have an associated lower energy neutrino contribution, but on emission scales somewhere between the time window lengths tested in this work.

Although the results from this thesis are only a hint, it justifies the increasing efforts in multi-messenger observations, where, in the case of IceCube, real-time alerts from high energy events are sent out [Aar+17f]. Usually immediate follow-up observations are done

for these alerts, if the current observation conditions for the respective instruments are good [Ans+16] and as mentioned before, one of these alert events lead to the observation of the correlated flaring Blazar [Aar+18c]. A second confirmed neutrino source would further constrain the parameter space of the neutrino production mechanisms in astrophysical sources. Therefore, this analysis aims at a similar approach with a multi-messenger background in mind, although neutrinos are not tested against other messenger particles but against neutrinos from a different energy range that are very likely from astrophysical origin. Finding a localized neutrino flux in multiple energy ranges would certainly mean a big step forward in the understanding of the source physics. In this light, several approaches may be followed to improve on the analyses strategies presented in this thesis.

In chapter 5, an extensive theoretic foundation is laid out for the extended, unbinned Likelihood framework used for searches for neutrino sources in the sky. A detailed derivation from the general Likelihood definition and the underlying mechanisms to construct the per-event probability distributions is given. The formulas are partly specified for the special location of the IceCube detector but should have been introduced generalised enough to transform the procedure to other, similar environments. Also, two of the more prominent Likelihood formulas used for the general per-burst search and the time-integrated search are derived, both for the single and multi-sample case. All formulas include the often used stacking generalisation. Chapter 5 therefore gives an extensive review of the used Likelihood formalism for further studies.

The two dedicated analyses described in chapter 6 and 7 use information from two different neutrino event selections to search for a correlated emission of the few high energy neutrino events and an expected, less energetic neutrino contribution. For the time-dependent case, a detailed method to model per-event and source distributions for the Likelihood framework has been worked out. Especially the time dependent background modelling has not been included in any analysis of this kind before, taking into account the rate dependency on the naturally occurring seasonal variations. Also, the method of using differential flux limits to obtain global model limits has been developed. This may be useful for the reader if a specific model limit was not calculated by the analyser. With finely binned differential performance values, it should be possible to obtain global limits from these values alone for quite arbitrary flux models.

But, for the two searches done here, two improvements may also be suggested. First, for each high energy starting event, a *signalness* parameter can be obtained from dedicated simulation, which estimates the probability of the single event being a true astrophysical signal. Some high energy starting events have a low signalness, indicating, that these events may rather be atmospheric high-energy background muons instead of astrophysical particles. A cut on the signalness parameter can be scanned to further improve the

sensitivities[17]. A tighter cut ensures that the surviving events originate more likely from astrophysical sources which are expected to have an additional lower energy neutrino contribution. However, the fewer sources are left, the more the sensitivity approaches the single source search described in [Aar+17a], in which the potential sources could not be detected. Therefore, an optimal cut has to be found. Also, an additional neutrino event selection of *extremely high energy events* (EHE) exists[YI18; Aar+16b]. It may be useful to also include these event positions to increase the catalogue size and thus decrease the needed signal flux per source for a discovery.

Another approach may be to increase the time window size and construct an analysis, which transfers smoothly from the per-burst scenario to the time-integrated search, which is, in principle, just a special case of burst time-windows of the size of the sample livetime. However, current analysis frameworks, including the one that was developed for this work, cannot handle that smooth transition automatically yet. A useful task would be the development of such a flexible and robust framework for future analyses.

In conclusion, this thesis can serve as a starting reference to construct more generalized analysis frameworks for future searches for neutrino sources. Several new analysis approaches have been developed and utilized in this thesis, however, the two conducted analyses lead to no detection of neutrino sources. Currently, the IceCube detector is taking data with an uptime of over 99 % and therefore, the awaited further detections of neutrino sources and the direct characterisation of source properties may only be a matter of time.

[17] Note that introducing an intrinsic source stacking weight proportional to the signalness would not work as maybe expected, because the single events can either be of astrophysical origin or come from interactions in the atmosphere.

A. Further references

The appendix is mainly used to show additional plots, for example for distributions for other time windows than shown in the main matter. These are often similar to each other and would otherwise clutter the main part too much.

The code written to enable the computational part of this analysis was mainly done in the `Python` programming language, making heavy use of the scientific computing and visualization libraries `numpy` [Oli15], `scipy` [JOP+01], `matplotlib` [Hun07] and `healpy` [Gor+05].

A.1. Notes on reproducibility

The author tried to leave the analysis code in a state that hopefully allows to reproduce the distributions and results in this analysis. `Python` is used as the programming language for both the core analysis code and for the scripts using that core code. The scripts and data for both analysis can be found on the computing cluster of the IceCube collaboration at the University of Wisconsin-Madison (UW-Madison). A numbering scheme is used to guide the execution order of the scripts. Help strings are included, when additional command line argument are needed.

The core analysis code for the time-dependent analysis was written from scratch, but it was tried to keep a close connection to the existing `skylab` code base used for many other IceCube point-source searches. At the time of writing this thesis, the `skylab` module wasn't capable of handling the needed time-dependent variations of the extended Likelihood formalism though, making the self developed code necessary. The code can be found in the `github` repository at `www.github.com/mennthor/tdepps`. This repository also includes spline and statistics related methods to provide the tools used during the evaluation of the analysis in the `tdepps/utils` submodule. The installation manual can be found in the modules `Readme` file. The scripts for the time-dependent analysis can be found on the UW-Madison cluster's file system under

```
/home/tmenne/analysis/hese_transient_stacking_analysis
```

An additional `Readme` file is provided with a short install manual. The analysis folder itself is a `git` repository so all changes can be tracked. For the first setup, the required

Python dependencies can be installed using the `pip` package manager and the provided `py2_requirements.txt` file. In this analysis the branch `original_hese` is used. The `master` branch was intended to use an improved HESE sample event selection, "Pass2", which was not ready at the time of this thesis and the original selection was used instead. In general, the analysis folder uses `git` branches and their names for the whole folder tree. For this, a `_loader.py` and `_paths.py` module is provided. These modules are used to handle all relative path dependencies and automatically set a new folder structure in the analysis folder and in the users data storage folder when a new branch is created. This way, new tests cannot easily overwrite existing data or results and experiments can be done by `git` branching. The processing order loosely follows the steps presented in the analysis chapters 6and 7. Some of the scripts simply run by themselves directly on the gateway machine. However, trial generation takes quite some computing time. The trial generation scripts are therefore usually split into three parts, where the first one creates job files for the `dagman` distributed computing system, the second one resembles the actual code to be executed in each job and the last one is usually a script that collects and combines all the results from the job files in a more compact data structure. For this analysis, all results are stored in a human readable form in the `JSON` file format. Because the format has no compression and can be quite verbose for a large datasets, the `gzip` compression algorithm is used to compress the files if necessary. The handling of these files in Python is quite easy as demonstrated in the following listing

```
import json
import gzip
fname = "path/to/file.json.gz"
# 'gzip' may be optional, use just 'open(...)' then
with gzip.open(fname, "r") as fp:
  data_dict = json.load(fp)
```

For the time-integrated search, the existing `skylab` core analysis code was used. Apart from that, the analysis is structured as explained above for the time-dependent analysis. The Likelihood map signal injector was not available to the date when it was needed in the `skylab` core code. Due to the similar code structure between the self-developed `tdepps` and the `skylab` code, a simple adapter method was used to inject the signal events in a format needed by the `skylab` code. The analysis folder can also be found on the UW-Madison cluster file system at the path

```
/home/tmenne/analysis/hese_time_independent_stacking_fit_index
```

Unfortunately, the code to perform certain post-processing analysis steps, as the χ^2 fits or code for producing the plots in this thesis completely resides in `IPython` notebooks. Although these have been copied to the respective analysis folders on the UW-Madison machine, this is not very beneficial for reproducibility. The author can only recommend

the reader to proceed otherwise with his analysis and make these accessible in standard scripts too.

A.2. Acknowledgements

It would not have been possible to finish this thesis without the help and support of many people. Trying to thank each and everyone of them would consequently lead to missing acknowledgement for sure. Therefore, I only want to address some of them directly at this place, but also express my gratitude to everyone who participated in any way during the creation of this work and in general during my studies at TU Dortmund.

Firstly, I want to thank my parents for making it possible in the first place, with every small decision they made, for me to finish the physics education and the doctoral studies. I also want to thank my wife for her support even though the writing of this thesis did take much longer than expected.

Furthermore, I want to thank my supervisor Dr. Dr. Wolfgang Rhode for his professional and the financial support, as well as Dr. Bernhardt Spaan in his role as second corrector and the other two members of the defence committee Dr. Bärbel Siegmann and Dr. Mirko Cinchetti.

Also, particular thanks to the IceCube group at Drexel university, lead by Dr.Kurahashi Neilson, where I had a great stay and learned a lot about the needed analysis techniques and to the DAAD for its financial support during the scholarship.

Lastly, many thanks go to my colleagues at the astroparticle physics chair at TU Dortmund, who helped me with many details and problems over the years and went through the pain of proof-reading this thesis.

B. Supplementary material

This chapter includes supplementary material, mostly additional figures, that would otherwise clutter the main chapters too much, but provide useful additional information.

B.1. Datasets

This appendix chapter includes additional figures for chapter 4.

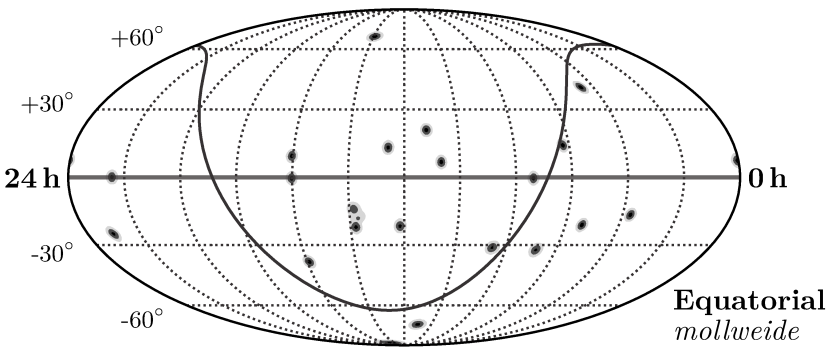

Figure B.1.: Skymap in equatorial coordinates and Mollweide projection of the combination of all Likelihood reconstruction maps from the track-like high energy starting events.

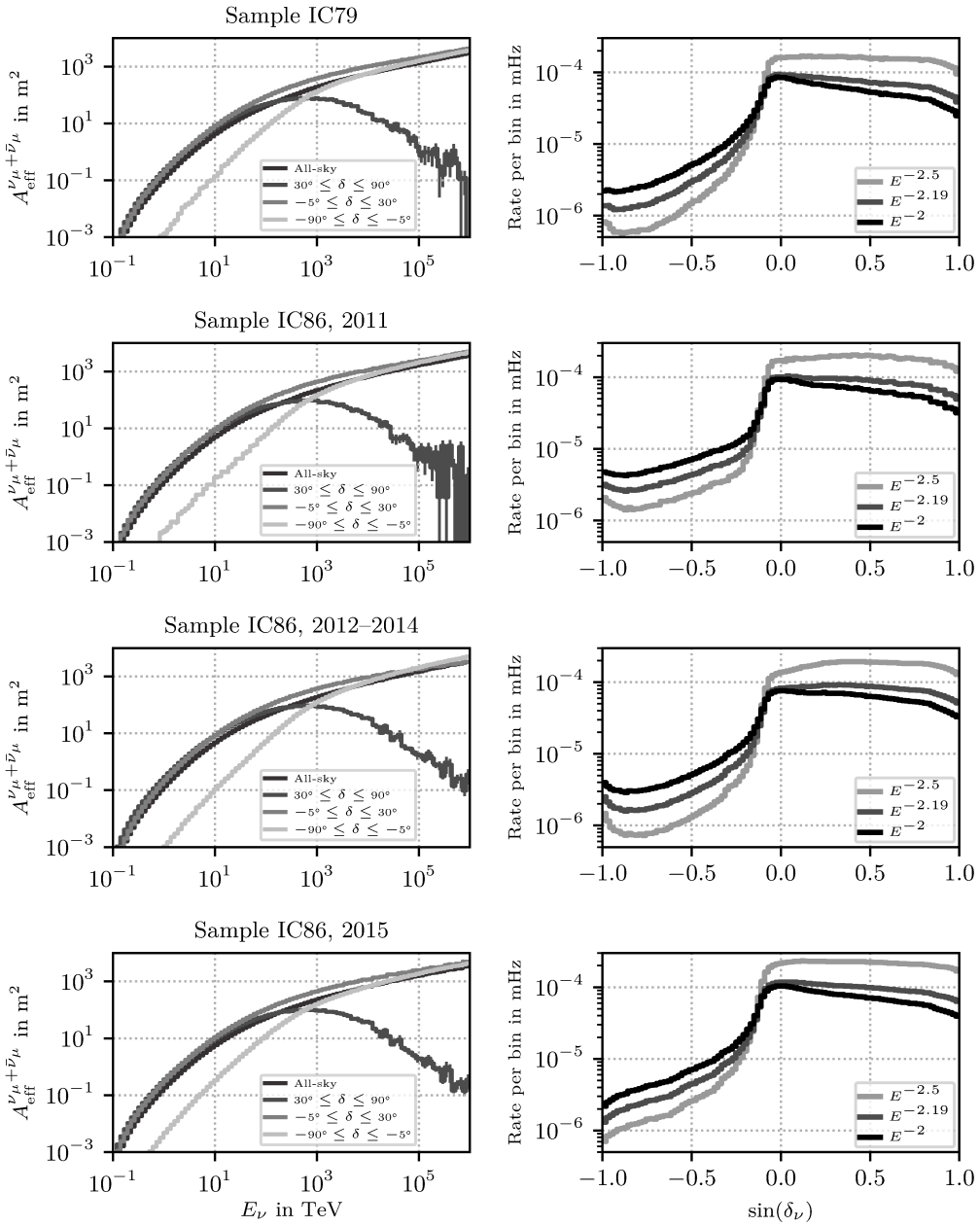

Figure B.2.: Effective areas and $\sin(\delta_\nu)$ distributions for for the samples IC79, IC86, 2011, IC86, 2012–2014 and IC86, 2015 in the muon neutrino test dataset. The effective areas are shown for multiple declination bands to capture the main features of the underlying sample selection efficiencies. The $\sin(\delta_\nu)$ distributions are weighted to generic power law fluxes with indices 2 and 2.5 and to the current measurement from [HW18] all with the same normalisation constant of $\phi_0 = 10^{-18}\,\mathrm{GeV}^{-1}\,\mathrm{cm}^{-2}\,\mathrm{sr}^{-1}\,\mathrm{s}^{-1}$.

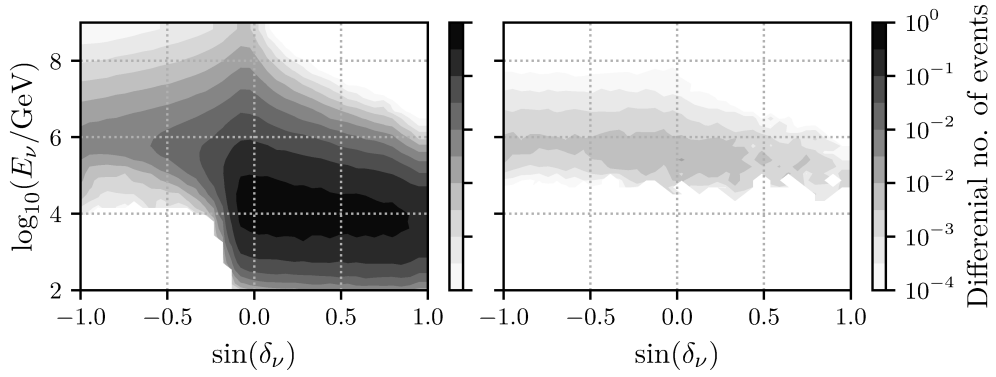

(a) Sample IC79

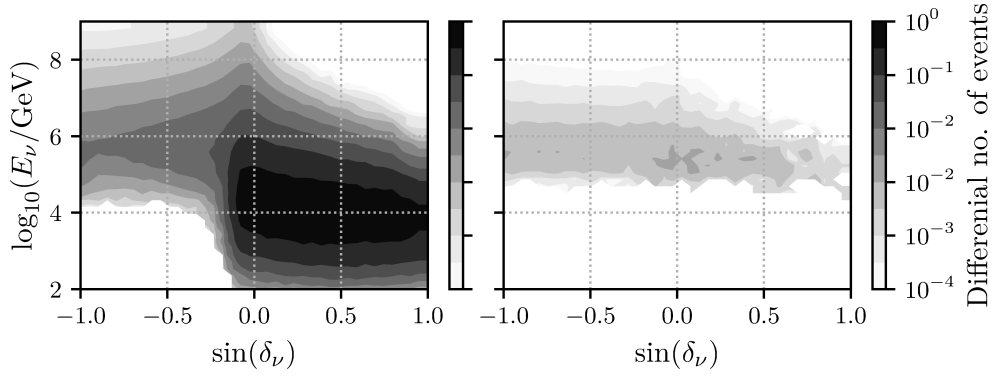

(b) Sample IC86, 2011

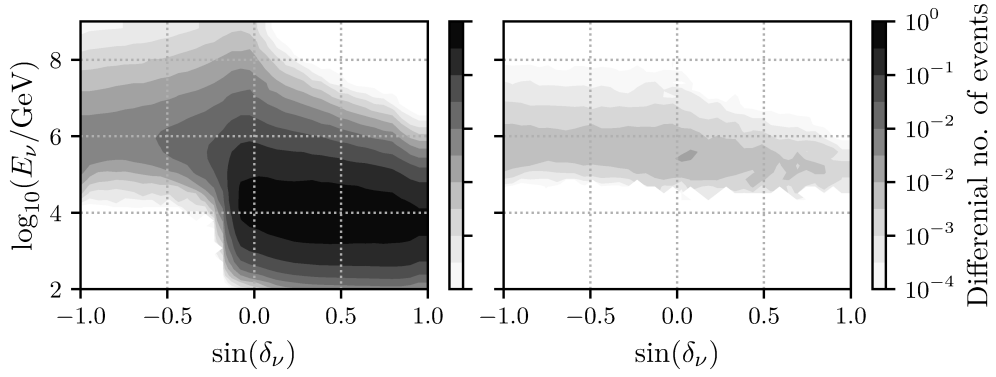

(c) Sample IC86, 2012–2014

Figure B.3.: Plot showing the filtered out HESE-like events in the simulation files used for each sample on the right and the full simulation sample on the left. The samples are weighted to the flux model in [HW18] equally normalized to a livetime of 365 days. To obtain the total number of events, the integral over the parameter space needs to be taken, shown are differential number of events.

B.2. Time-dependent analysis

This chapter includes additional figures and tables for the time-dependent analysis chapter.

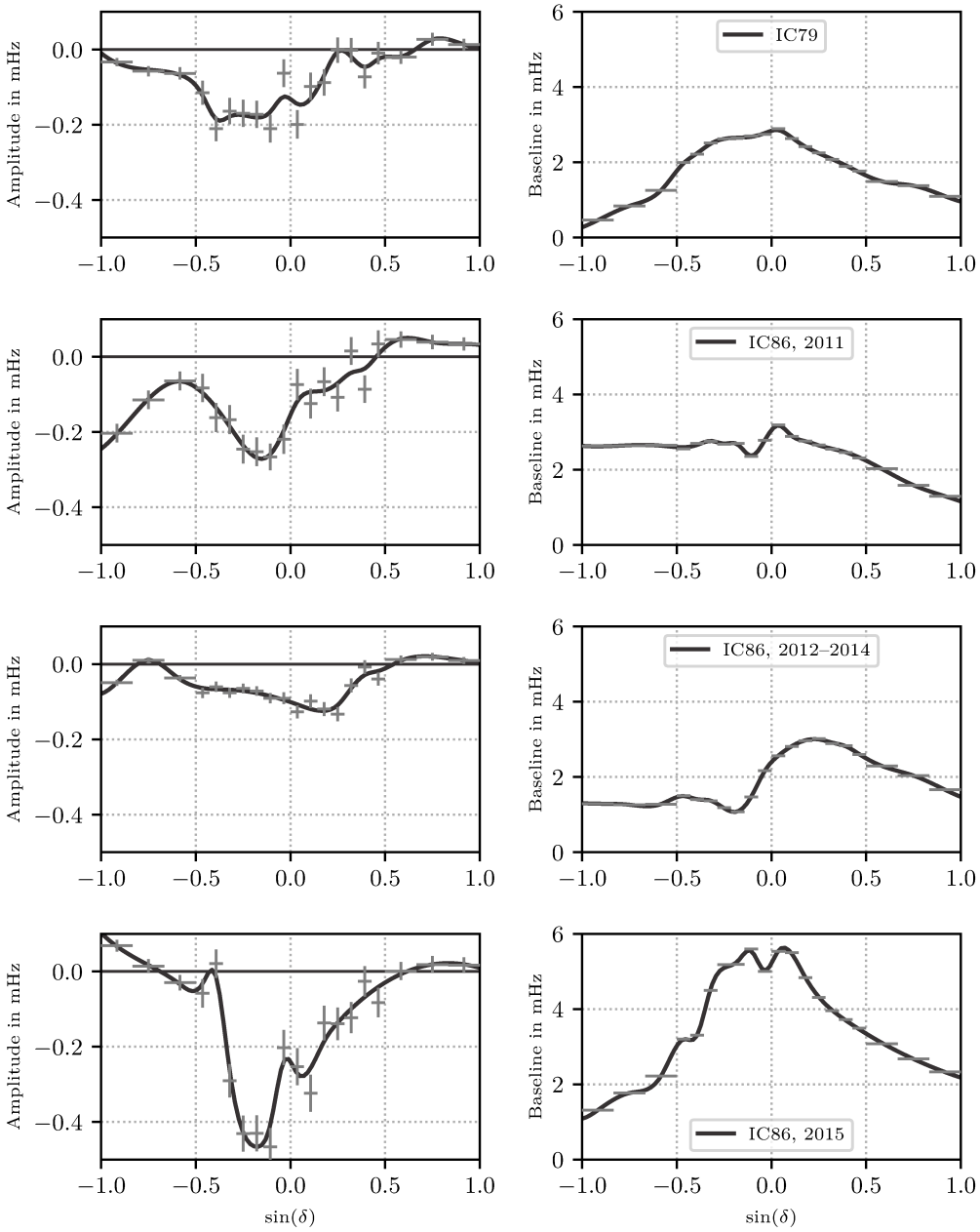

Figure B.4.: Spline models fitted to the discrete fit parameters from the rate models in figures (B.7–B.10). The splines are used to obtain the set of rate model parameters used to tailor the model for the source locations in time. On the left the splines for the amplitude parameter A and on right the splines for the baseline parameter R_0 for the model (6.4) are shown.

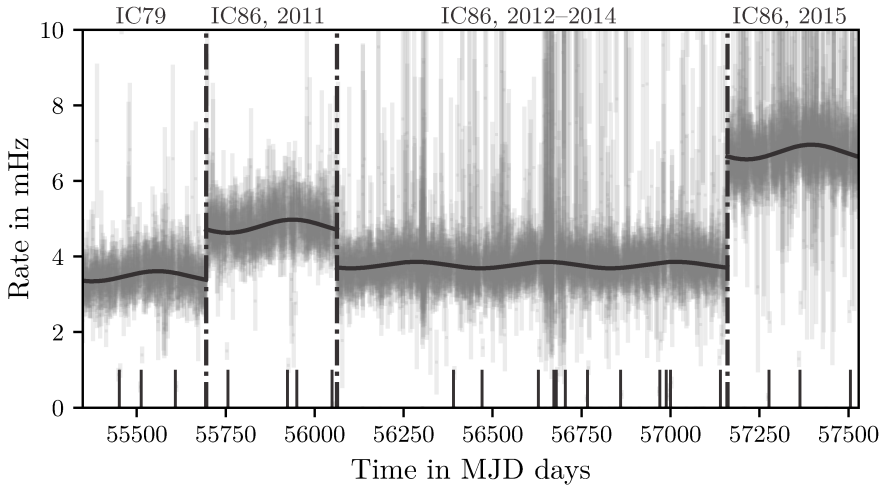

Figure B.5.: Measured run rates and fitted allsky rate models for all four muon track data samples. The rates per run are rebinned in monthly bins and a sine model is fitted to the bin centres per sample. This global model is integrated over each source's time window to estimate the expected number of background events, which is a priori fixed in the Likelihood fit.

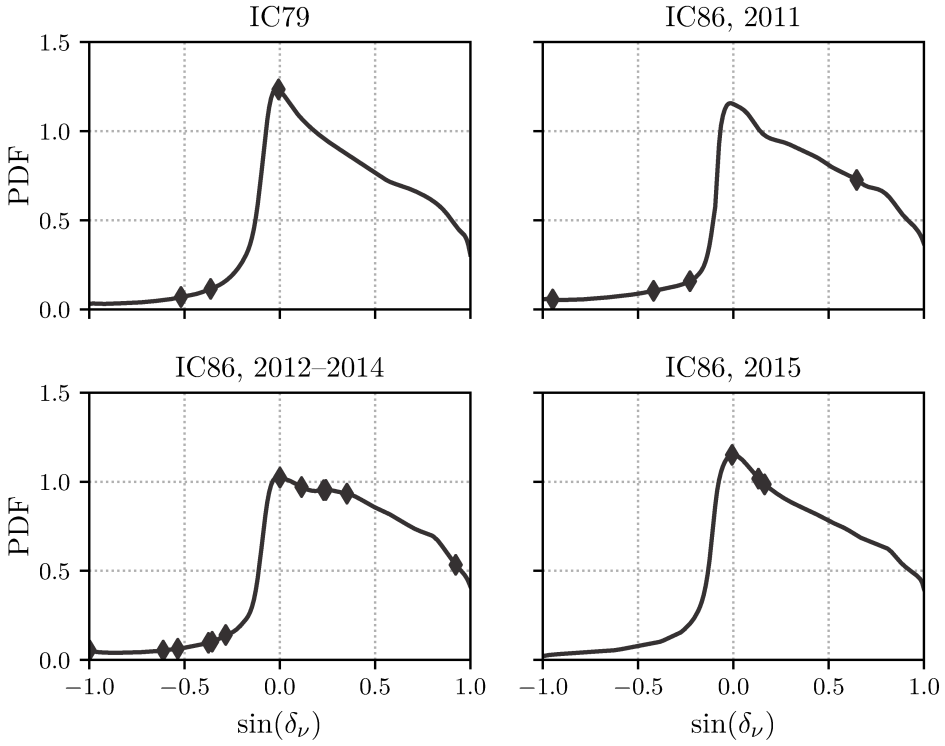

Figure B.6.: Source stacking detection efficiency weights for all source per sample. The spline is constructed from the distribution of simulated signal-like events at the same processing level as the measured dataset. The weights per source are read of at the corresponding source declinations and are independently normalized per sample.

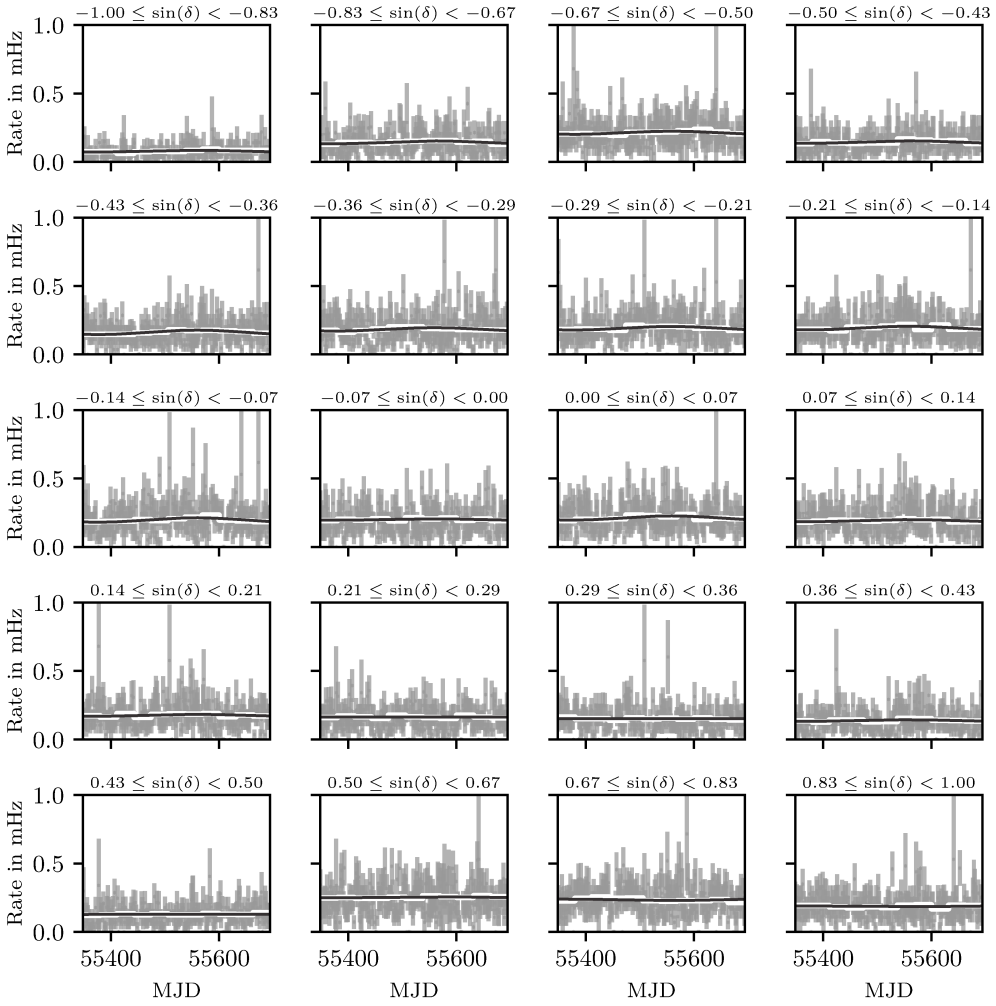

Figure B.7.: Measured run rates and fitted models for the IC79 sample. In each bin, the rates per run are rebinned in monthly bins and a sine model is fitted to the bin centres.

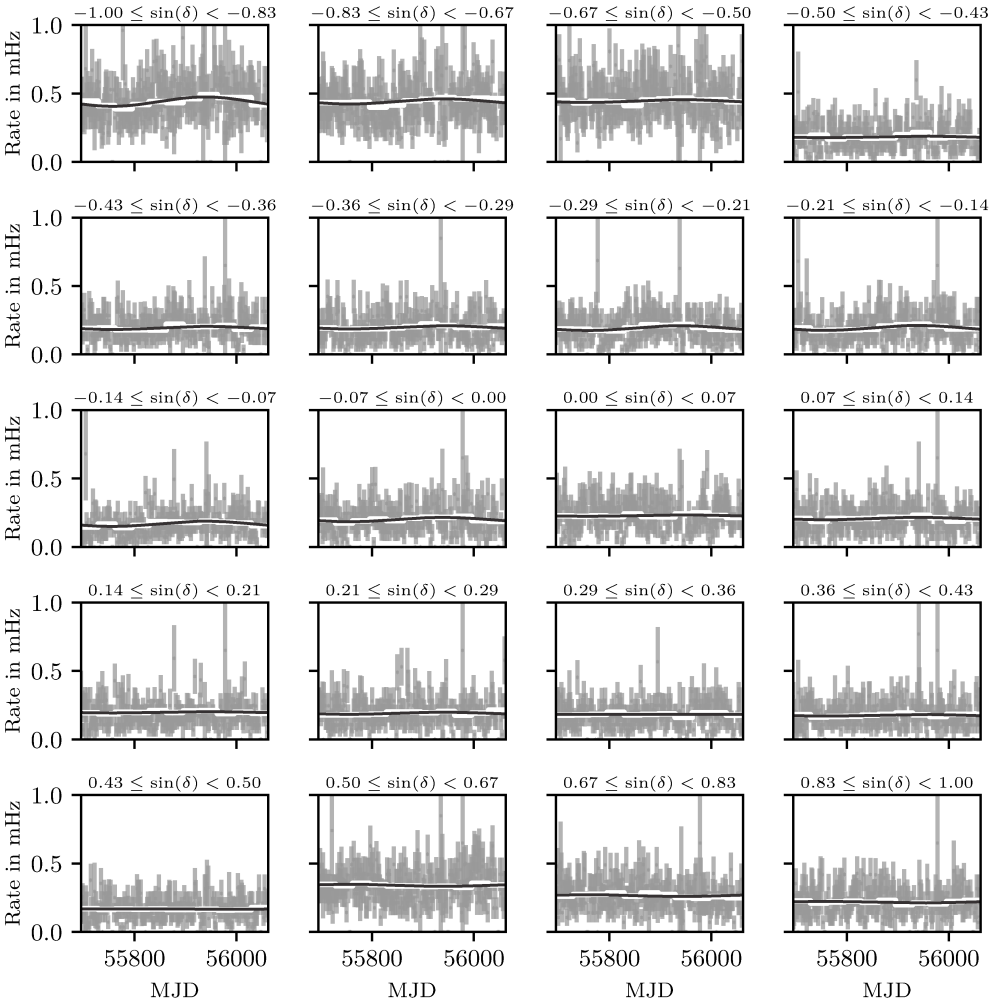

Figure B.8.: Measured run rates and fitted models for the IC86, 2011 sample. In each bin, the rates per run are rebinned in monthly bins and a sine model is fitted to the bin centres.

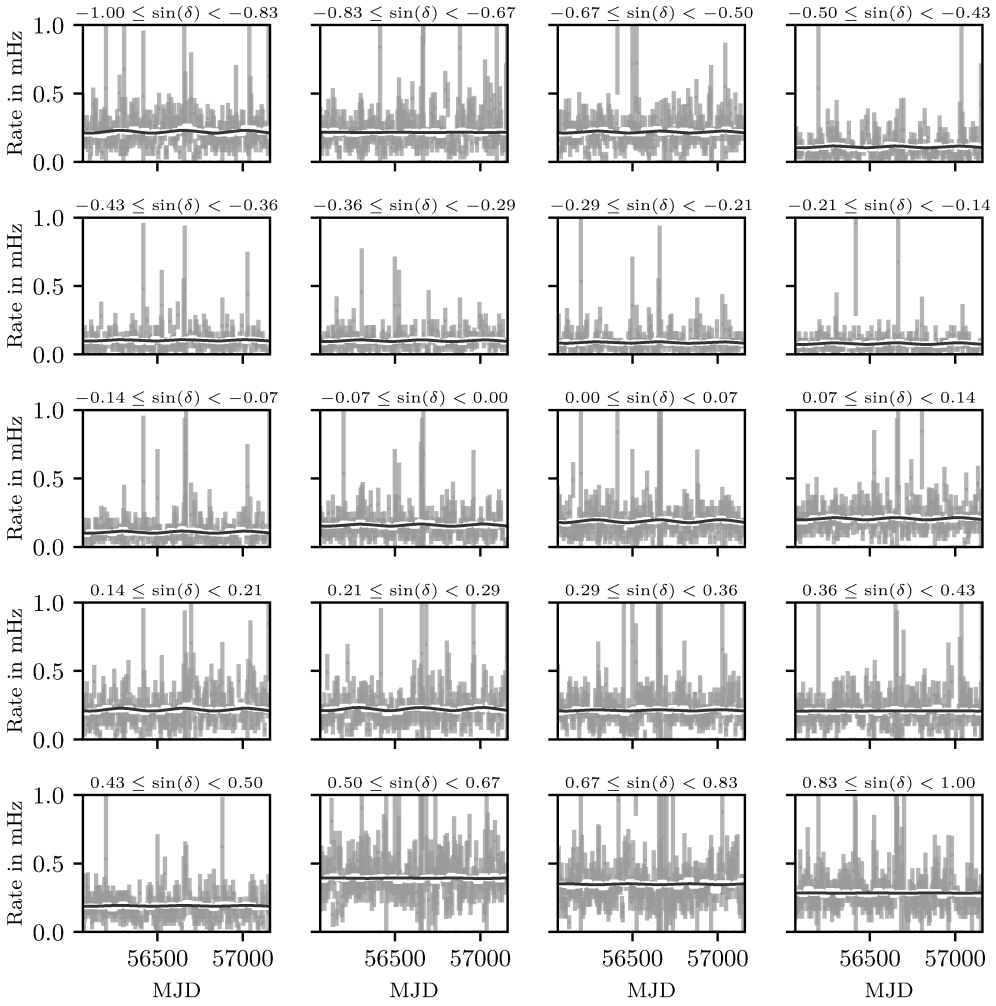

Figure B.9.: Measured run rates and fitted models for the IC86, 2012–2014 sample. In each bin, the rates per run are rebinned in monthly bins and a sine model is fitted to the bin centres.

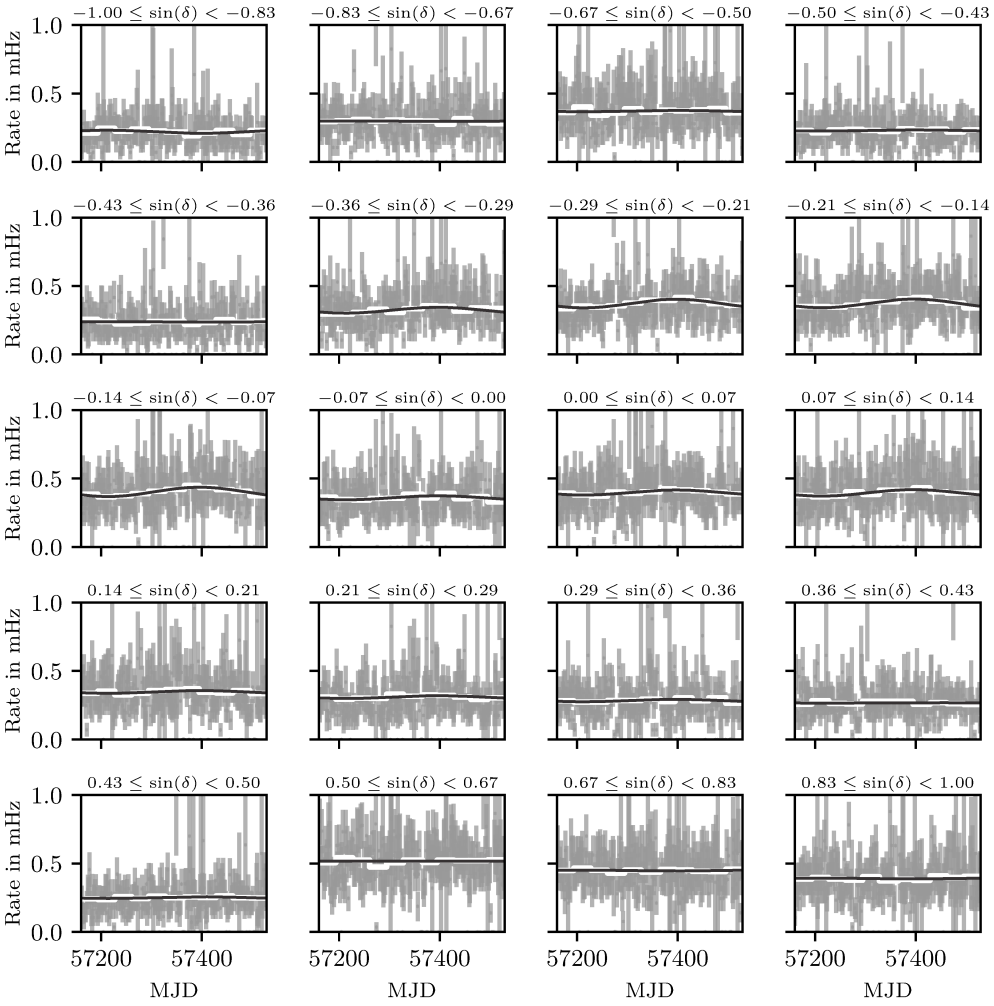

Figure B.10.: Measured run rates and fitted models for the IC86, 2015 sample. In each bin, the rates per run are rebinned in monthly bins and a sine model is fitted to the bin centres.

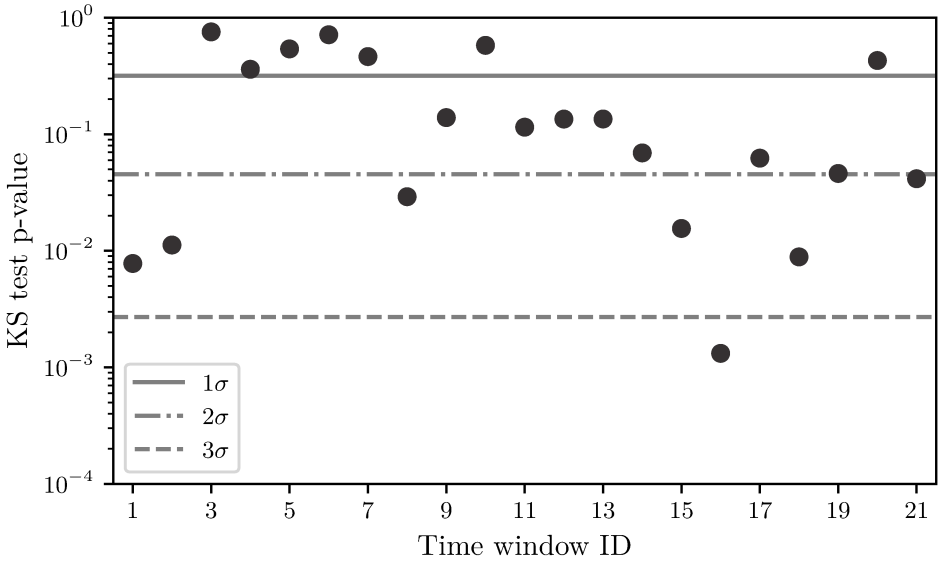

Figure B.11.: Kolmogorov-Smirnov test results per time-window, testing the exponential tail for the background test statistics against a set of independently sampled distributions. A small tendency for a mismatch at larger time windows can be seen, but overall the fitted tails describe the sampled distributions sufficiently well.

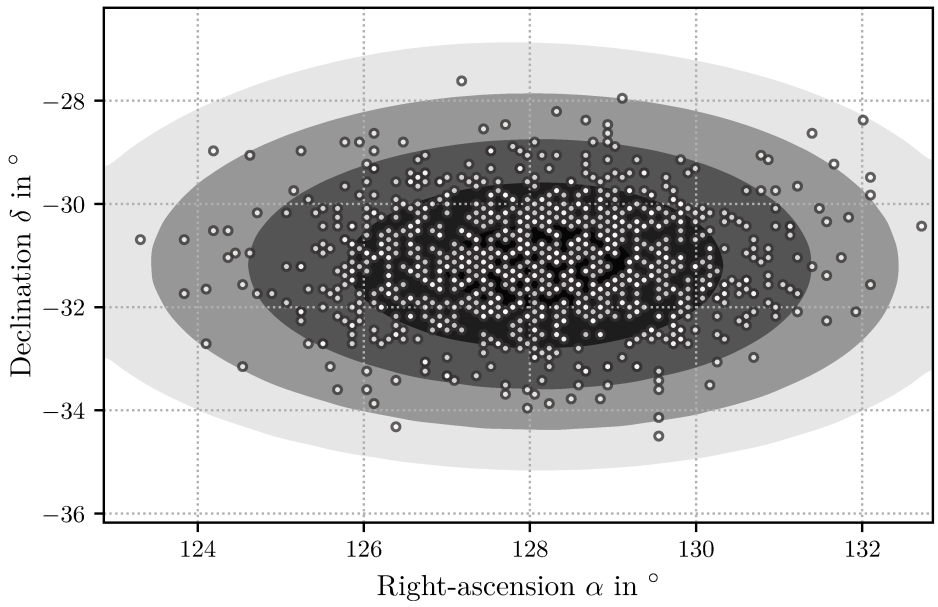

Figure B.12.: Likelihood map for the high energy starting event 1 as used in the analysis. The dots are the sampled source positions from the signal injector module for 10^3 trials. Per trial one new source location is sampled per source. The actually injected signal events are rotated to the new source positions in their true coordinates prior to injection and added to the separately sampled background event sample.

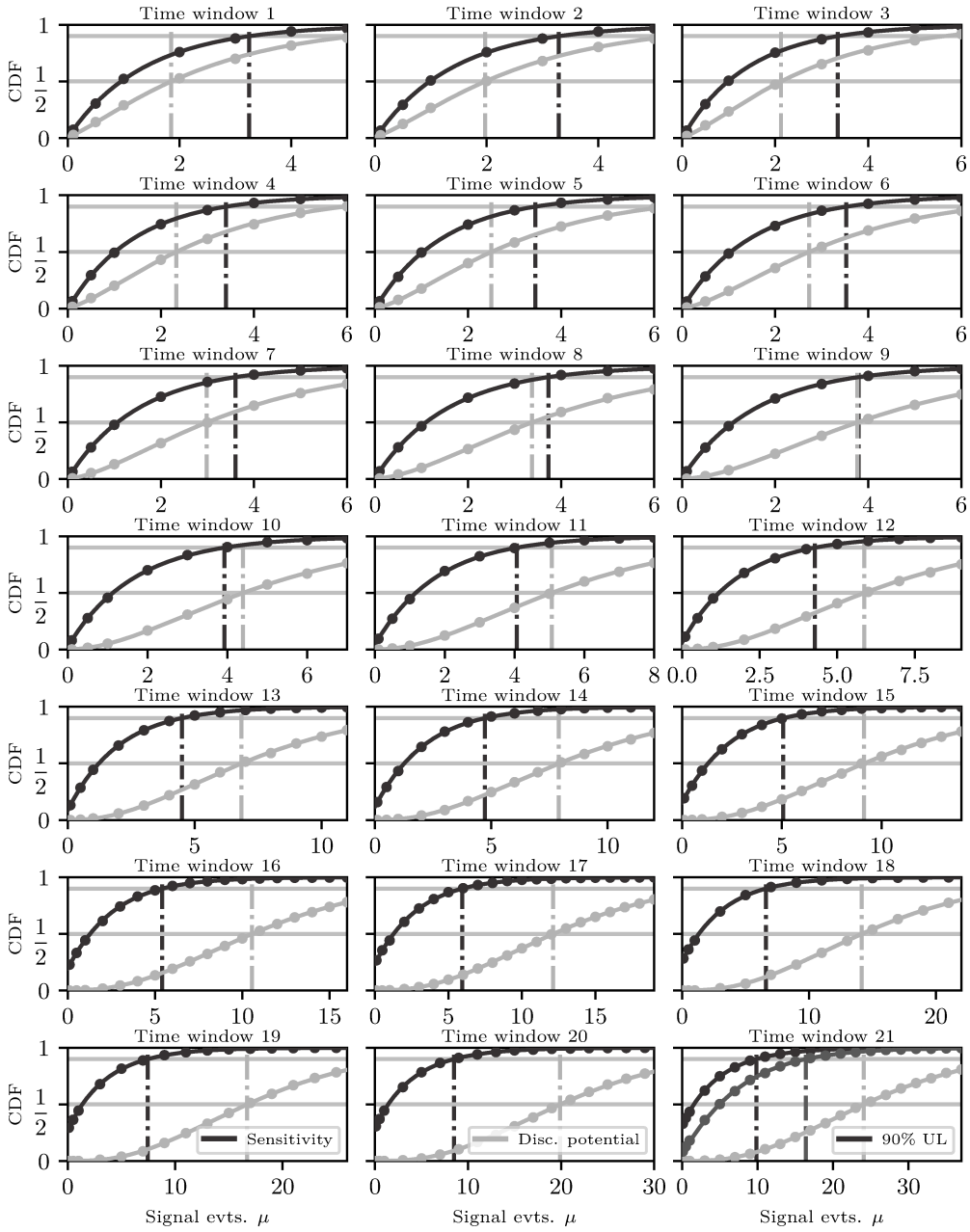

Figure B.13.: χ^2 CDF fits to the discrete set of test statistic quantiles from the signal injection trials over the mean number of injected signal events μ parameter scan for all time windows. For each point, the quantile for the currently sampled test statistic over the desired test statistic value from the background distribution is calculated from the empiric PDF. The the χ^2 CDF is fitted to all grid points to obtain a more reliable estimate of the needed quantile. The density of the sampled grid points in μ is adapted to the needed quantity in each bin. Each set of trials is reused for the sensitivity and discovery potential definitions. The injection is done with a unbroken power law with index $\gamma = 2$ over the whole available simulation dataset true neutrino energy range.

Background test statistics

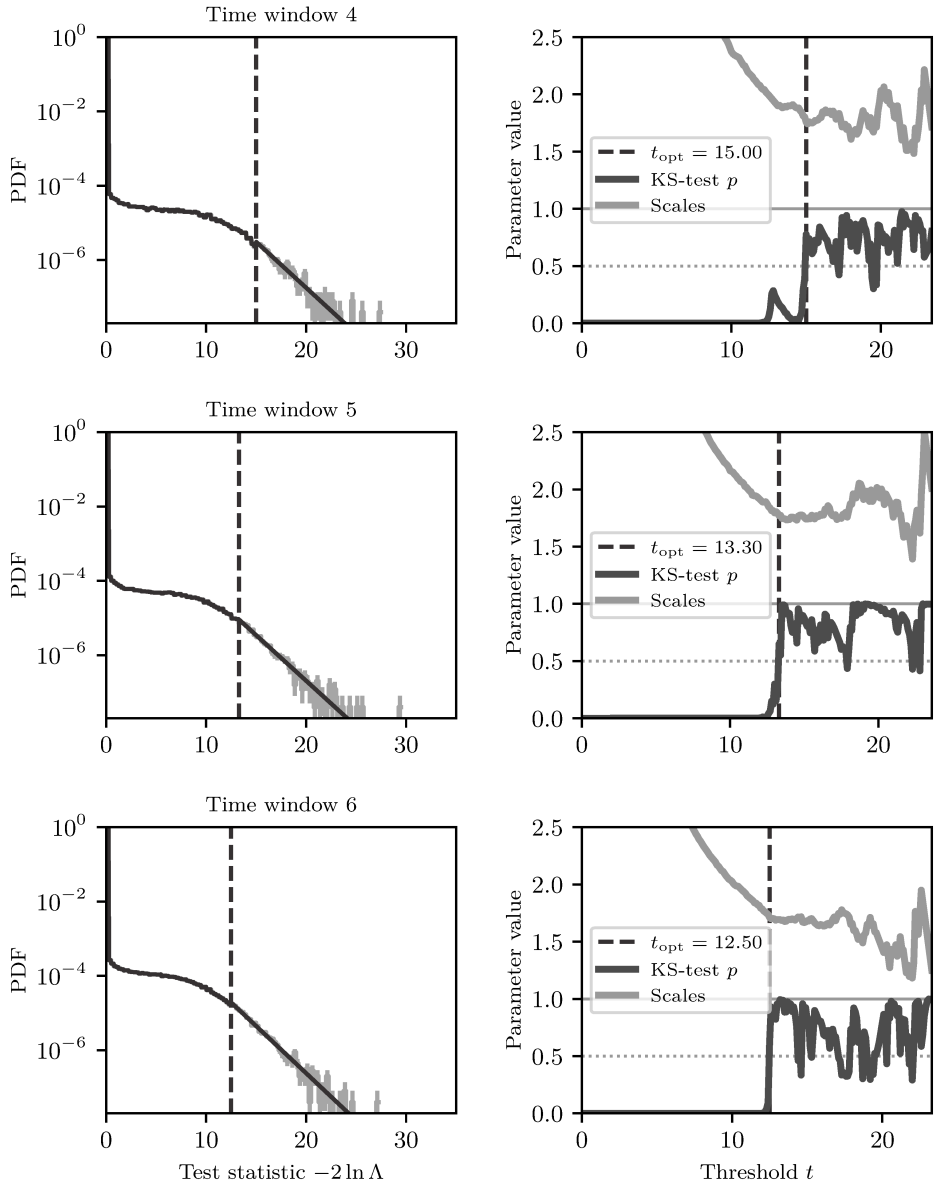

Figure B.14.: Background only test statistics for the time windows 4, 5 and 6 on the left and the parameter scan using the Kolmogorov-Smirnov (KS) test for the best threshold position on the right. The sampled PDF is described empirically up to the threshold value and with an exponential tail after that. The KS test is used to decide when the tail describes the sampled data sufficiently accurate.

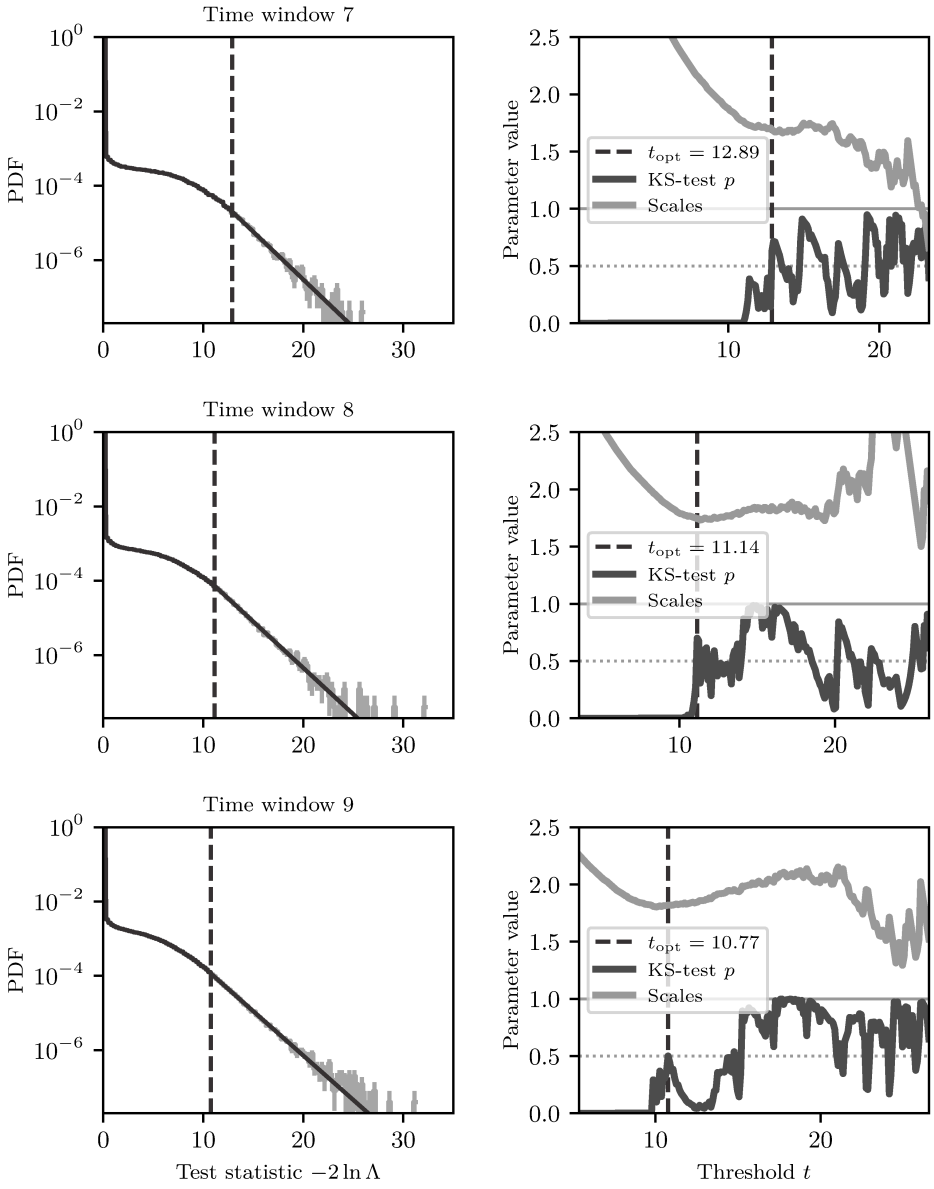

Figure B.15.: Background only test statistics for the time windows 7, 8 and 9 on the left and the parameter scan using the Kolmogorov-Smirnov (KS) test for the best threshold position on the right. The sampled PDF is described empirically up to the threshold value and with an exponential tail after that. The KS test is used to decide when the tail describes the sampled data sufficiently accurate.

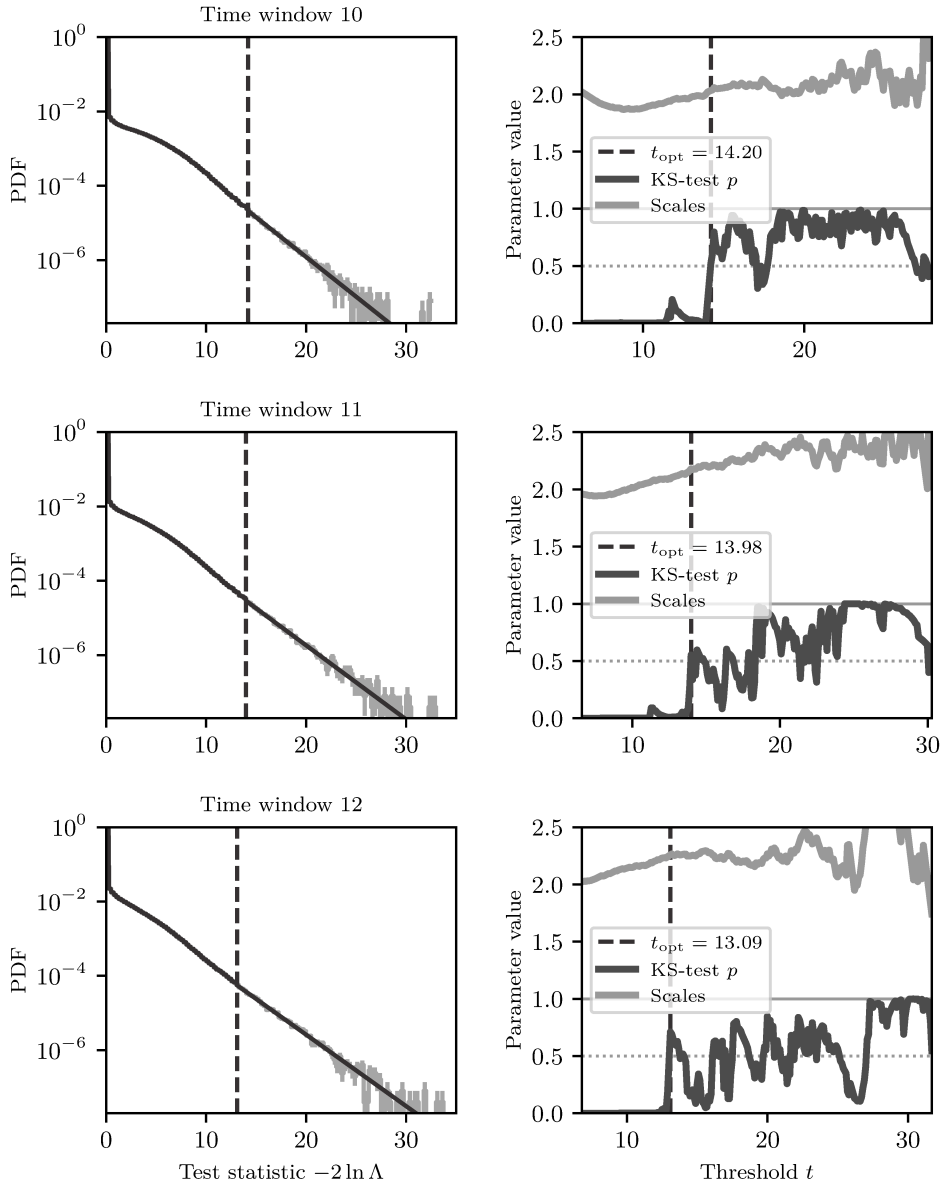

Figure B.16.: Background only test statistics for the time windows 10, 11 and 12 on the left and the parameter scan using the Kolmogorov-Smirnov (KS) test for the best threshold position on the right. The sampled PDF is described empirically up to the threshold value and with an exponential tail after that. The KS test is used to decide when the tail describes the sampled data sufficiently accurate.

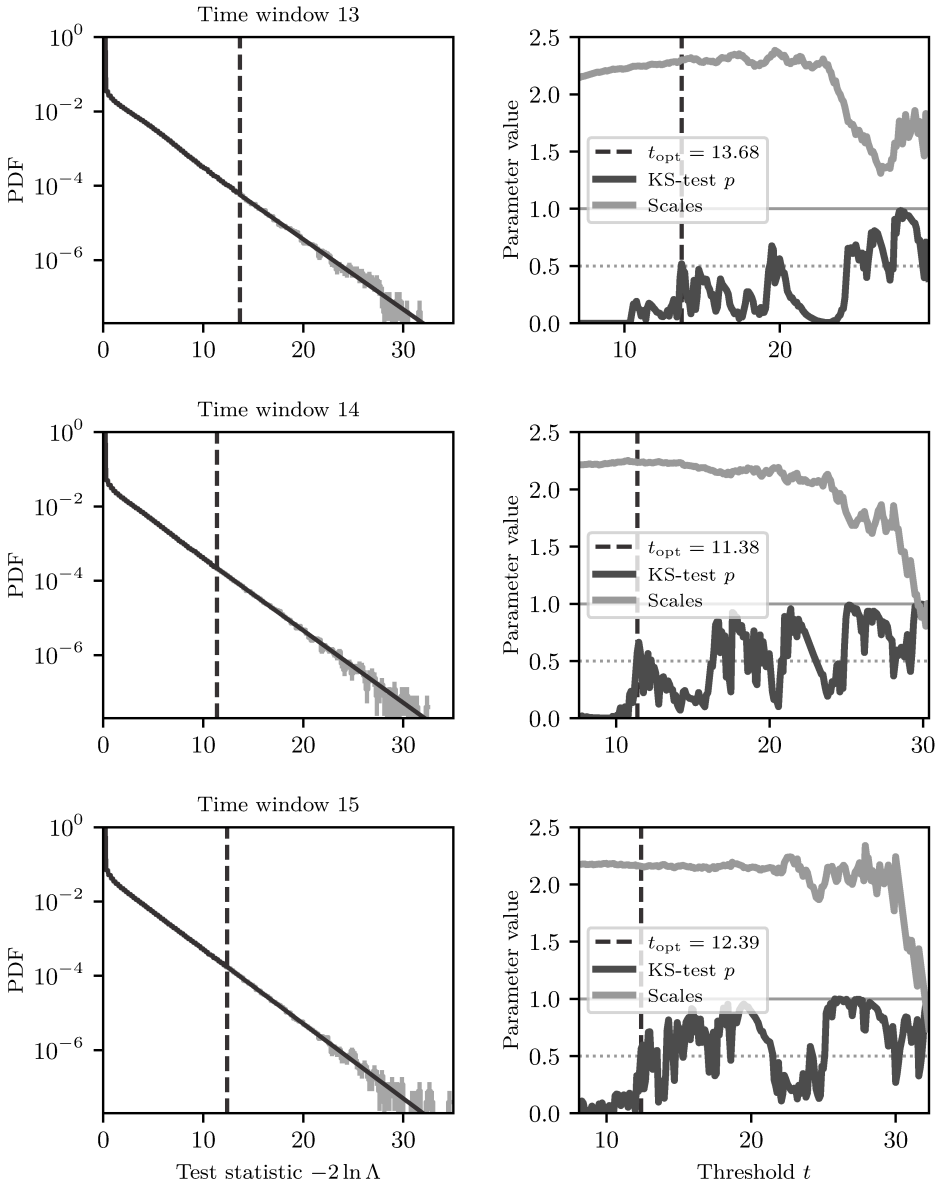

Figure B.17.: Background only test statistics for the time windows 13, 14 and 15 on the left and the parameter scan using the Kolmogorov-Smirnov (KS) test for the best threshold position on the right. The sampled PDF is described empirically up to the threshold value and with an exponential tail after that. The KS test is used to decide when the tail describes the sampled data sufficiently accurate.

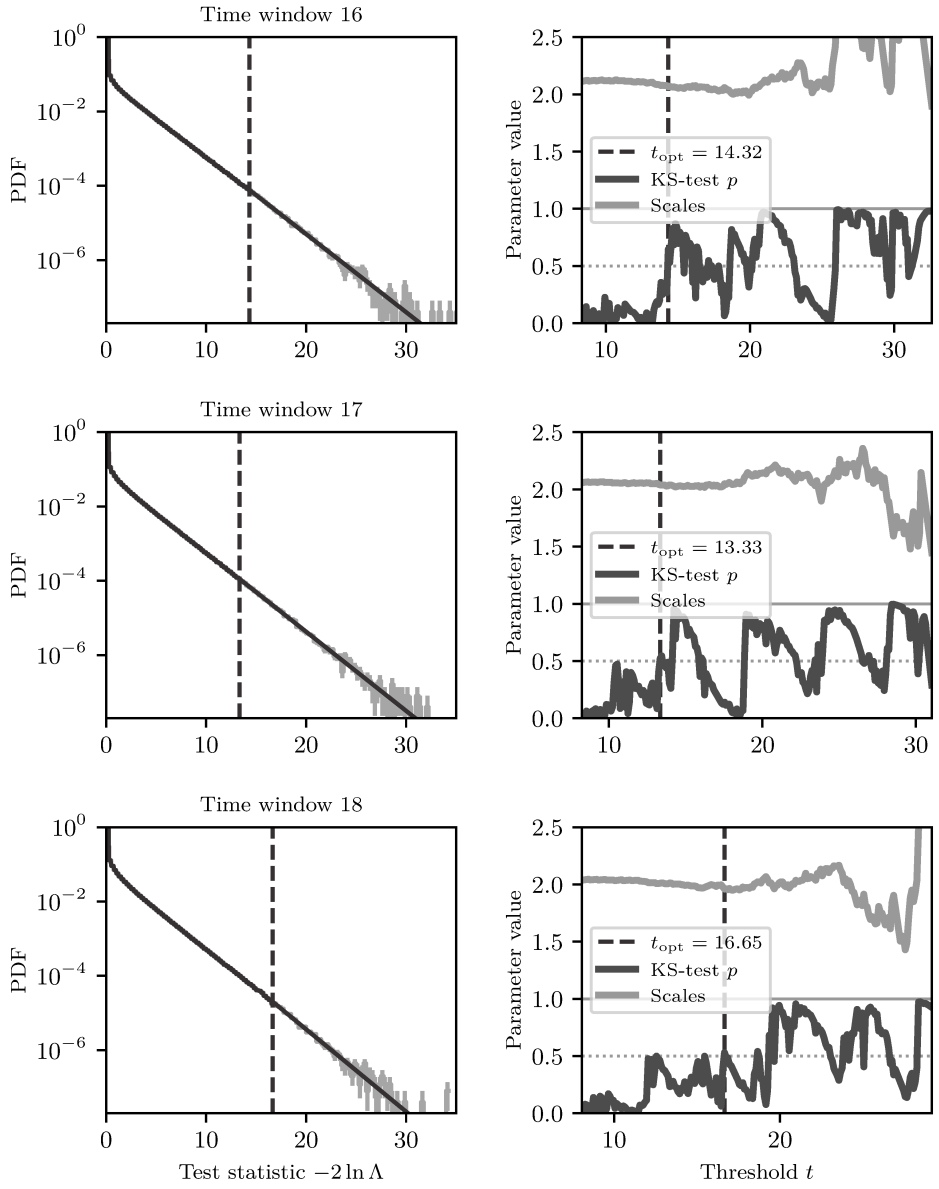

Figure B.18.: Background only test statistics for the time windows 16, 17 and 18 on the left and the parameter scan using the Kolmogorov-Smirnov (KS) test for the best threshold position on the right. The sampled PDF is described empirically up to the threshold value and with an exponential tail after that. The KS test is used to decide when the tail describes the sampled data sufficiently accurate.

Differential performances χ^2 CDF fits

Table B.1.: E^2 weighted numerical values for the differential sensitivity fluence normalisations at 100 TeV in GeV/cm^2. The values correspond to the differential performance curves shown in figure (6.6). The field ID corresponds to the time window ID as defined in table (6.1). See table (B.2) for the other energy bins. Note: the unweighted fluence values are obtained by dividing by $(100\,\mathrm{TeV})^2$.

ID	Left bin edge $\log_{10}(E_\nu/\mathrm{GeV})$						
	2.0	2.5	3.0	3.5	4.0	4.5	5.0
0	0.083	0.084	0.086	0.089	0.093	0.099	0.107
1	0.084	0.086	0.087	0.090	0.094	0.100	0.108
2	0.086	0.087	0.088	0.091	0.096	0.102	0.110
3	0.087	0.089	0.090	0.092	0.098	0.103	0.112
4	0.089	0.090	0.092	0.095	0.098	0.105	0.113
5	0.090	0.093	0.093	0.097	0.102	0.108	0.116
6	0.092	0.095	0.096	0.099	0.103	0.110	0.119
7	0.094	0.097	0.099	0.101	0.106	0.112	0.123
8	0.099	0.101	0.102	0.103	0.108	0.116	0.125
9	0.103	0.105	0.105	0.108	0.113	0.120	0.129
10	0.109	0.110	0.110	0.111	0.117	0.123	0.133
11	0.118	0.117	0.116	0.117	0.121	0.127	0.139
12	0.130	0.127	0.124	0.124	0.127	0.133	0.144
13	0.148	0.140	0.135	0.132	0.134	0.139	0.152
14	0.174	0.159	0.149	0.145	0.144	0.148	0.157
15	0.212	0.187	0.169	0.159	0.154	0.156	0.166
16	0.276	0.227	0.199	0.180	0.169	0.168	0.176
17	0.378	0.290	0.241	0.210	0.190	0.183	0.190
18	0.528	0.388	0.310	0.258	0.218	0.203	0.206
19	0.761	0.532	0.407	0.318	0.257	0.230	0.227
20	1.105	0.739	0.548	0.409	0.309	0.262	0.253

Table B.2.: E^2 weighted numerical values for the differential sensitivity fluence normalisations at 100 TeV in GeV/cm^2. The values correspond to the differential performance curves shown in figure (6.6). The field ID corresponds to the time window ID as defined in table (6.1). See table (B.1) for the other energy bins. Note: the unweighted fluence values are obtained by dividing by $(100\,\mathrm{TeV})^2$.

ID	Left bin edge $\log_{10}(E_\nu/\mathrm{GeV})$						
	5.5	6.0	6.5	7.0	7.5	8.0	8.5
0	0.116	0.124	0.127	0.128	0.129	0.129	0.130
1	0.117	0.125	0.129	0.130	0.131	0.131	0.132
2	0.120	0.128	0.131	0.132	0.133	0.132	0.134
3	0.123	0.129	0.133	0.135	0.135	0.136	0.136
4	0.125	0.133	0.136	0.137	0.138	0.138	0.138
5	0.126	0.136	0.140	0.140	0.140	0.141	0.140
6	0.131	0.140	0.143	0.143	0.143	0.142	0.143
7	0.134	0.143	0.145	0.147	0.147	0.146	0.146
8	0.139	0.147	0.151	0.150	0.151	0.149	0.150
9	0.144	0.153	0.155	0.154	0.154	0.154	0.153
10	0.149	0.160	0.161	0.160	0.160	0.158	0.158
11	0.154	0.166	0.167	0.166	0.163	0.162	0.162
12	0.162	0.174	0.175	0.171	0.170	0.168	0.167
13	0.168	0.183	0.183	0.179	0.175	0.173	0.173
14	0.178	0.192	0.192	0.187	0.183	0.180	0.179
15	0.187	0.202	0.202	0.196	0.190	0.186	0.184
16	0.197	0.215	0.215	0.206	0.199	0.196	0.192
17	0.213	0.230	0.229	0.220	0.210	0.206	0.204
18	0.230	0.250	0.248	0.239	0.225	0.219	0.217
19	0.248	0.270	0.270	0.259	0.246	0.239	0.236
20	0.273	0.293	0.297	0.285	0.268	0.261	0.259

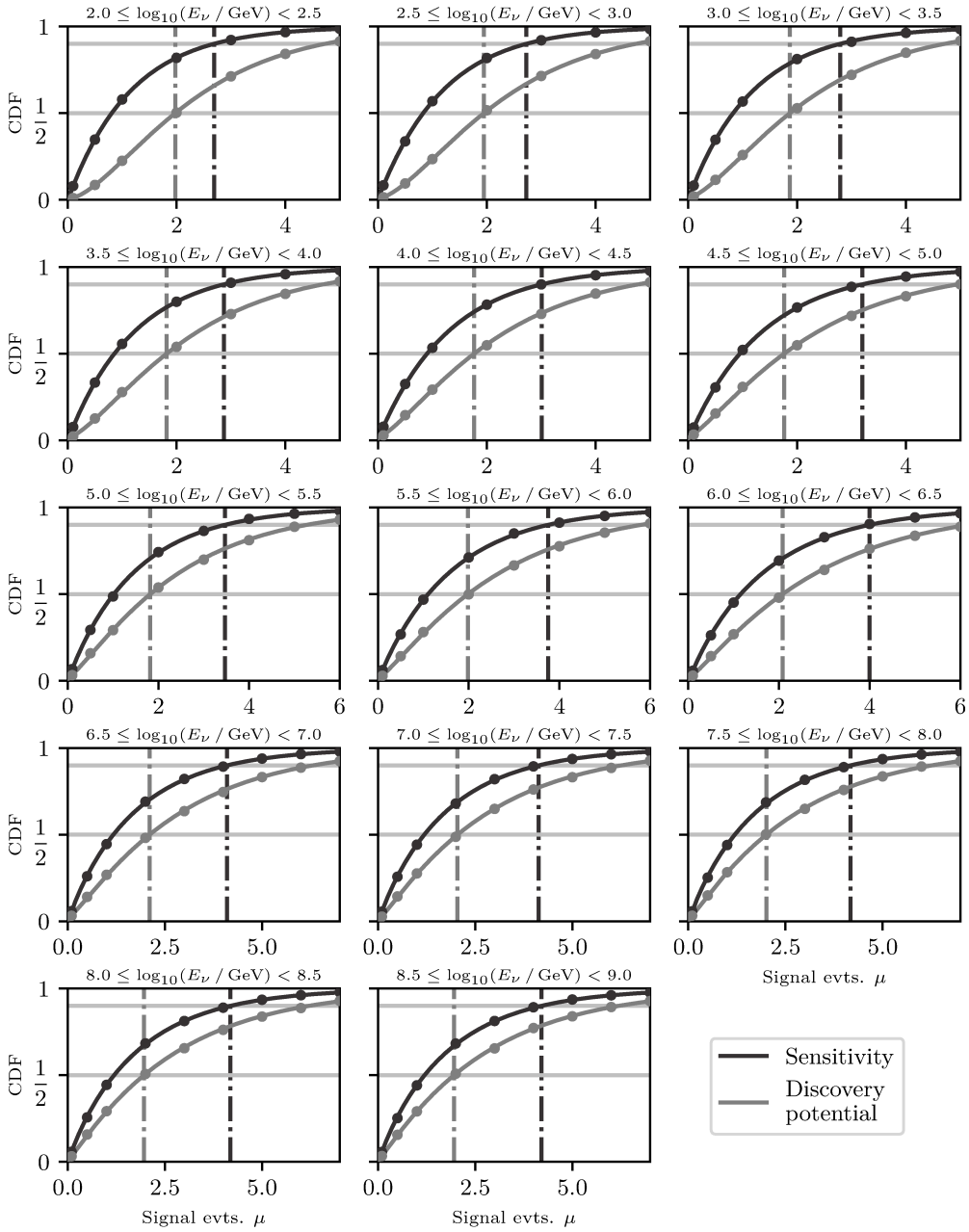

Figure B.19.: χ^2 CDF fits to the discrete set of test statistic quantiles from the signal injection trials over the mean number of injected signal events μ parameter scan for the first time window. For each point, the quantile for the currently sampled test statistic over the desired test statistic value from the background distribution is calculated from the empiric PDF. The χ^2 CDF is fitted to the points to obtain a more reliable estimate of the needed quantile. The density of the sampled grid point in μ is adapted to the needed quantity in each bin. Each set of trials is reused for the sensitivity and discovery potential definitions.

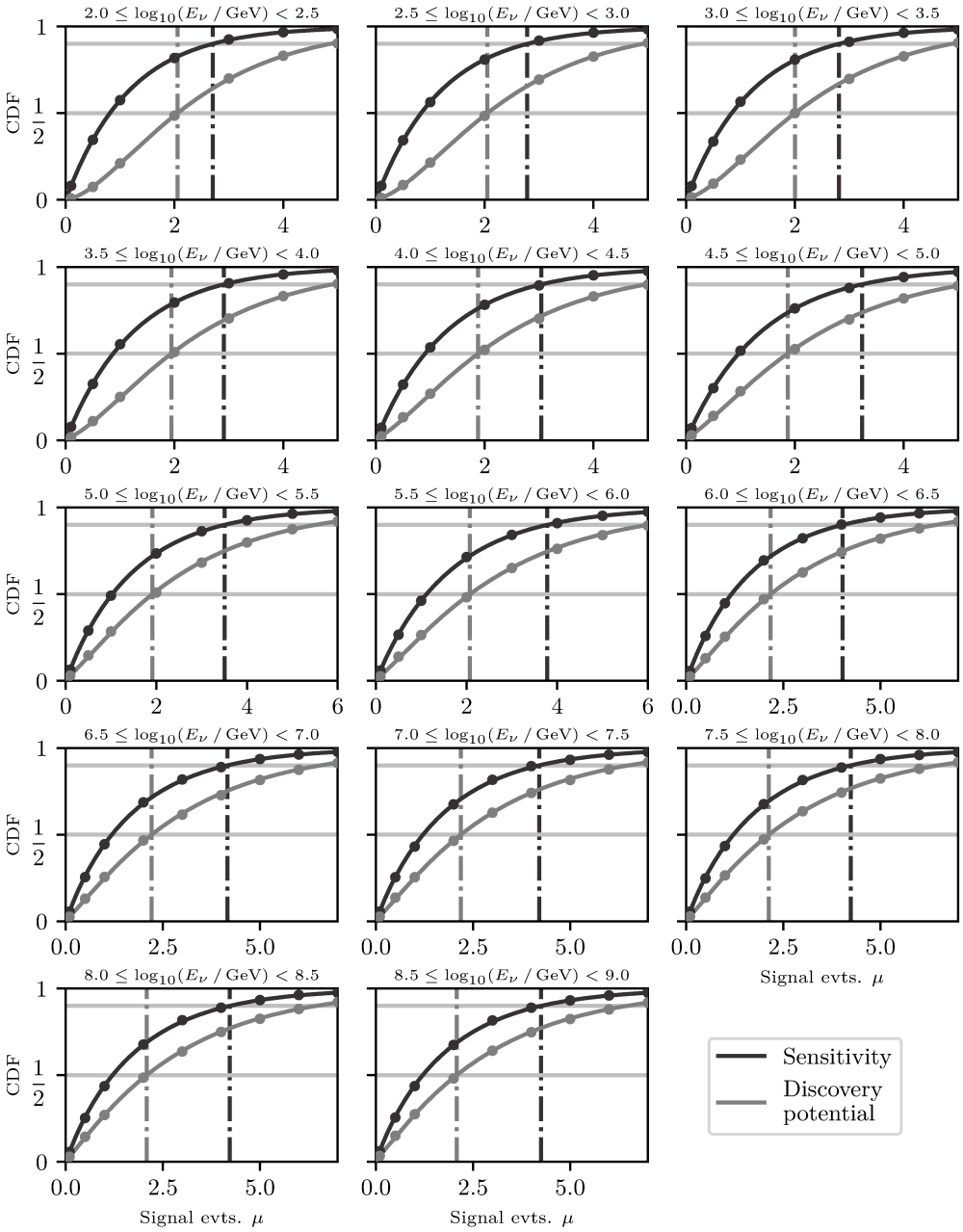

Figure B.20.: χ^2 CDF fits to the discrete set of test statistic quantiles from the signal injection trials over the mean number of injected signal events μ parameter scan for the second time window. For each point, the quantile for the currently sampled test statistic over the desired test statistic value from the background distribution is calculated from the empiric PDF. The χ^2 CDF is fitted to the points to obtain a more reliable estimate of the needed quantile. The density of the sampled grid point in μ is adapted to the needed quantity in each bin. Each set of trials is reused for the sensitivity and discovery potential definitions.

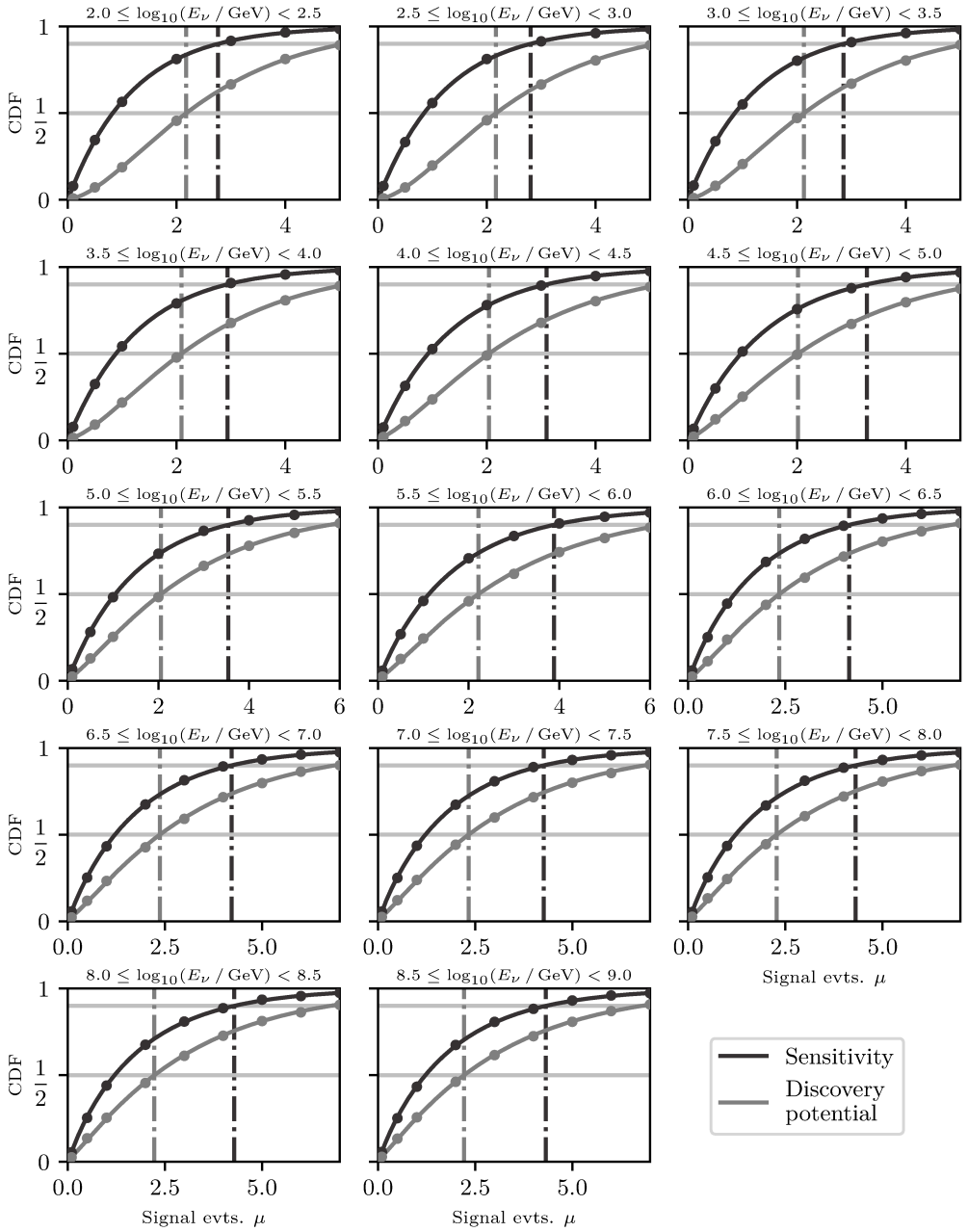

Figure B.21.: χ^2 CDF fits to the discrete set of test statistic quantiles from the signal injection trials over the mean number of injected signal events μ parameter scan for the third time window. For each point, the quantile for the currently sampled test statistic over the desired test statistic value from the background distribution is calculated from the empiric PDF. The χ^2 CDF is fitted to the points to obtain a more reliable estimate of the needed quantile. The density of the sampled grid point in μ is adapted to the needed quantity in each bin. Each set of trials is reused for the sensitivity and discovery potential definitions.

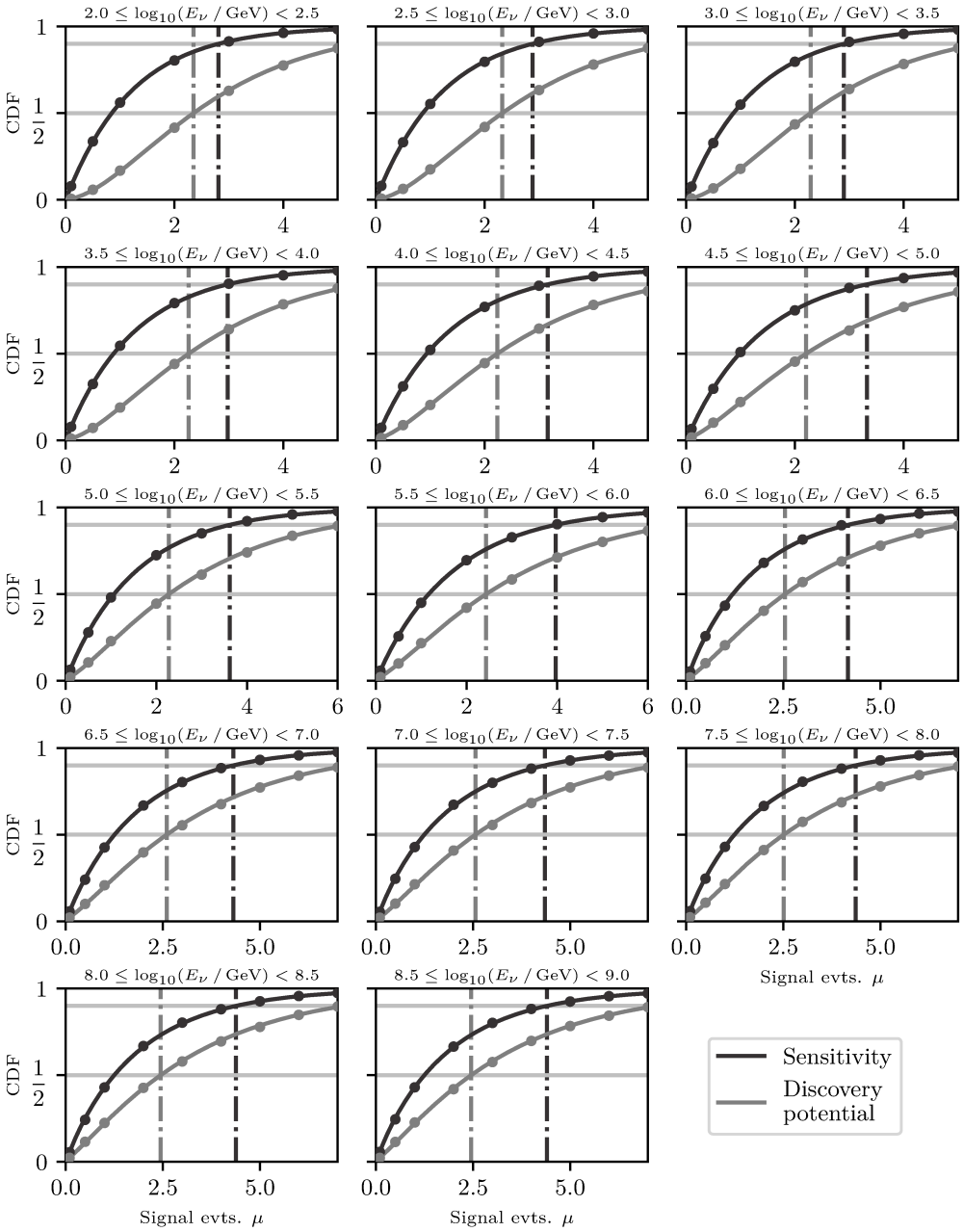

Figure B.22.: χ^2 CDF fits to the discrete set of test statistic quantiles from the signal injection trials over the mean number of injected signal events μ parameter scan for the fourth time window. For each point, the quantile for the currently sampled test statistic over the desired test statistic value from the background distribution is calculated from the empiric PDF. The χ^2 CDF is fitted to the points to obtain a more reliable estimate of the needed quantile. The density of the sampled grid point in μ is adapted to the needed quantity in each bin. Each set of trials is reused for the sensitivity and discovery potential definitions.

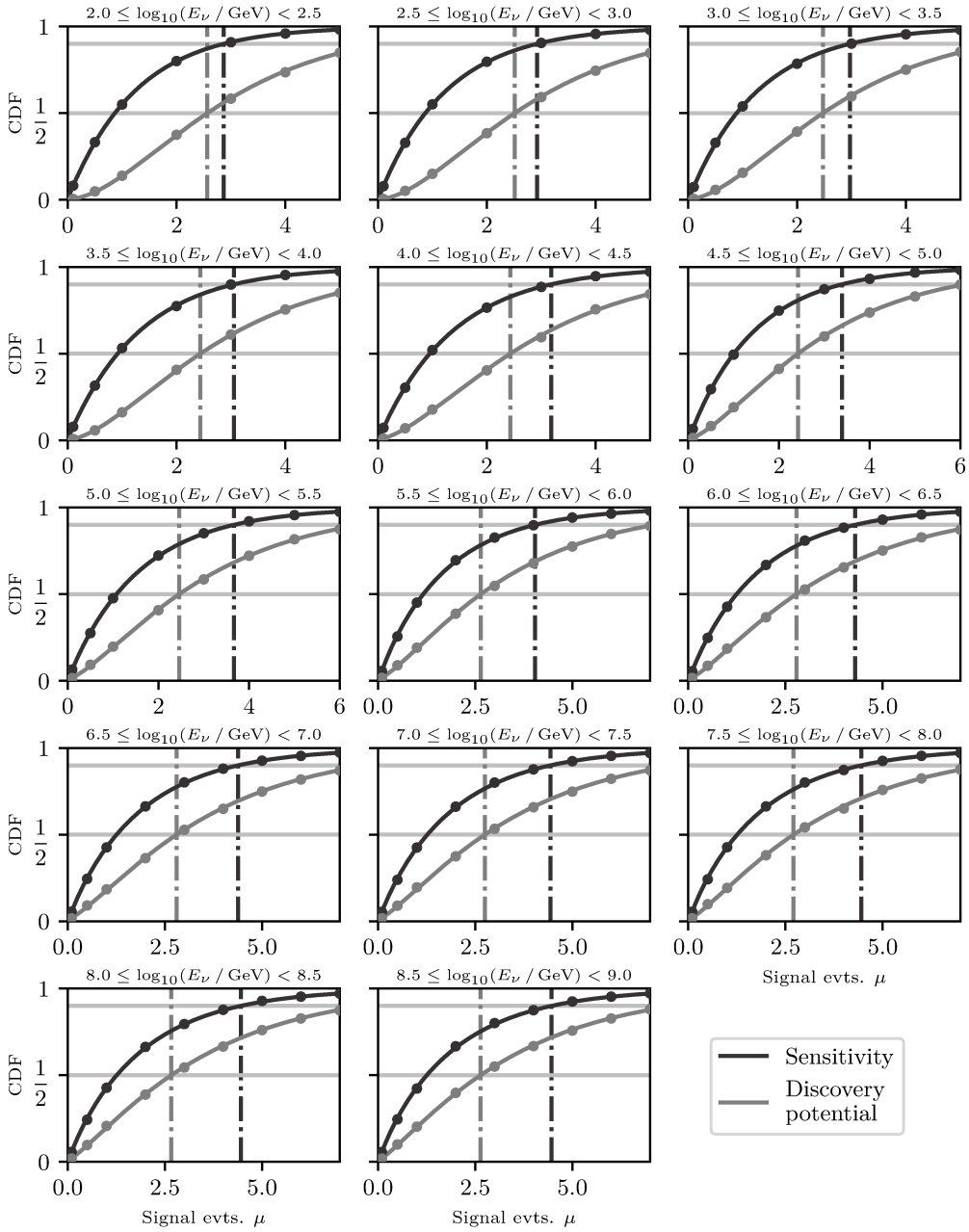

Figure B.23.: χ^2 CDF fits to the discrete set of test statistic quantiles from the signal injection trials over the mean number of injected signal events μ parameter scan for the fifth time window. For each point, the quantile for the currently sampled test statistic over the desired test statistic value from the background distribution is calculated from the empiric PDF. The χ^2 CDF is fitted to the points to obtain a more reliable estimate of the needed quantile. The density of the sampled grid point in μ is adapted to the needed quantity in each bin. Each set of trials is reused for the sensitivity and discovery potential definitions.

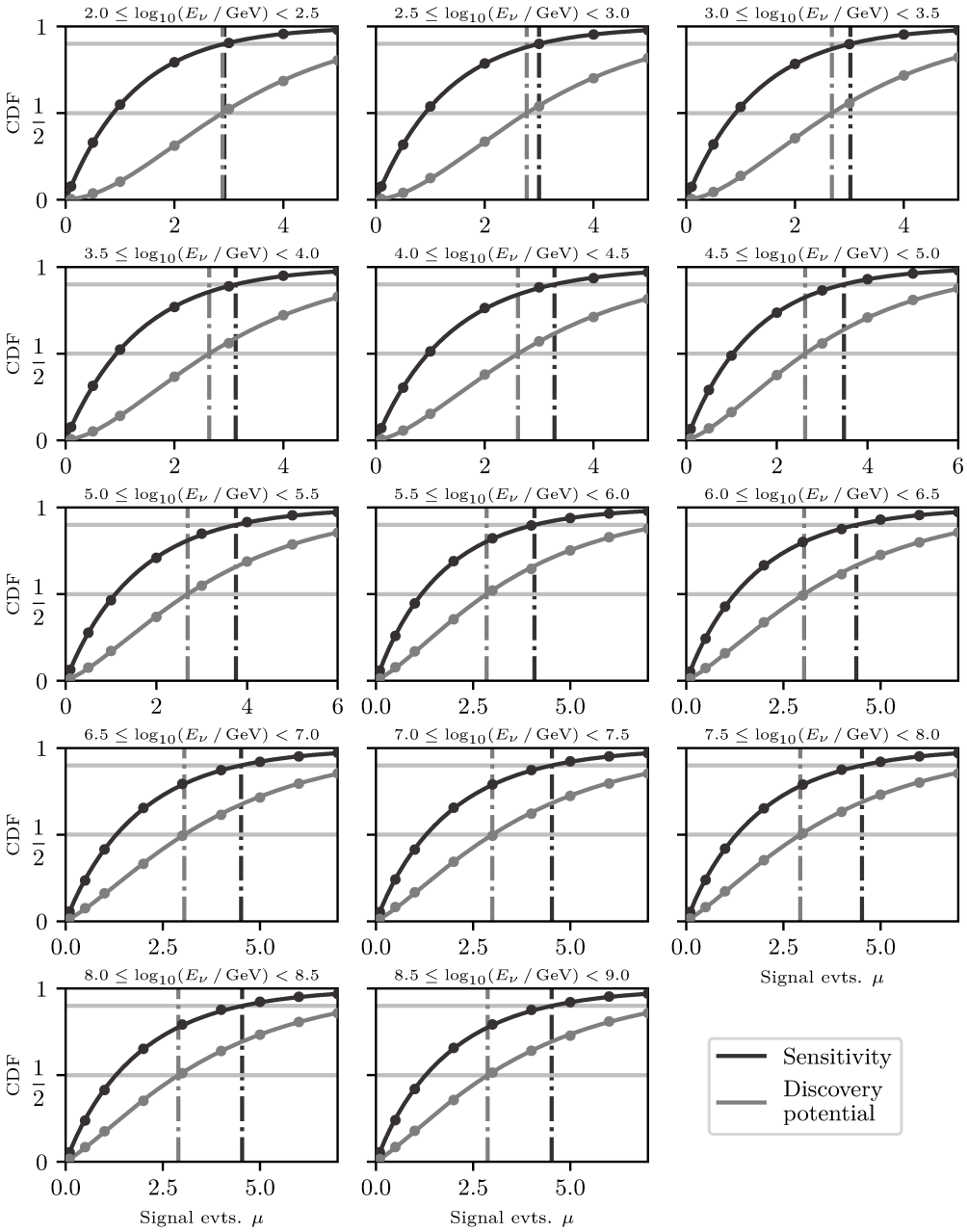

Figure B.24.: χ^2 CDF fits to the discrete set of test statistic quantiles from the signal injection trials over the mean number of injected signal events μ parameter scan for the sixth time window. For each point, the quantile for the currently sampled test statistic over the desired test statistic value from the background distribution is calculated from the empiric PDF. The χ^2 CDF is fitted to the points to obtain a more reliable estimate of the needed quantile. The density of the sampled grid point in μ is adapted to the needed quantity in each bin. Each set of trials is reused for the sensitivity and discovery potential definitions.

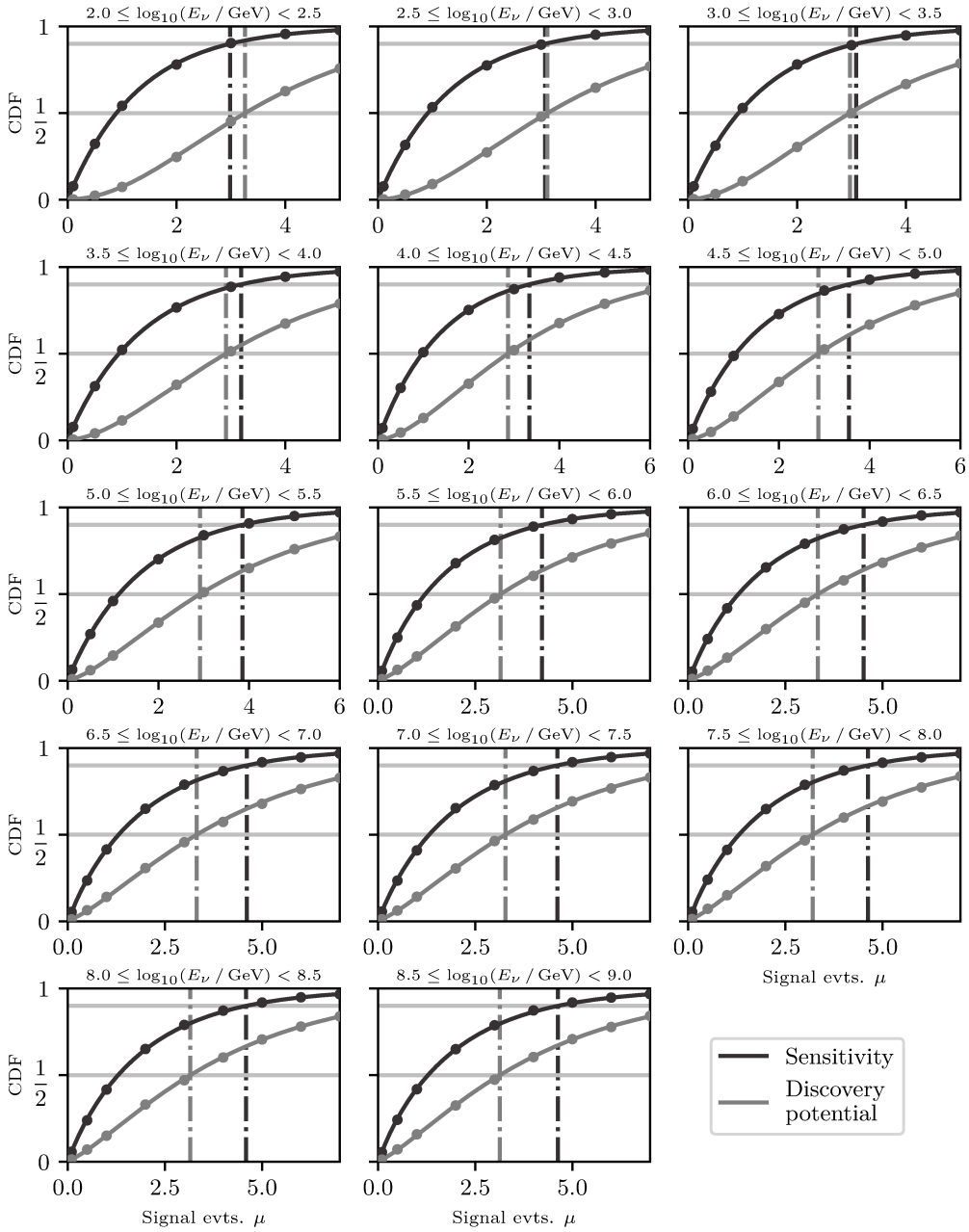

Figure B.25.: χ^2 CDF fits to the discrete set of test statistic quantiles from the signal injection trials over the mean number of injected signal events μ parameter scan for the seventh time window. For each point, the quantile for the currently sampled test statistic over the desired test statistic value from the background distribution is calculated from the empiric PDF. The χ^2 CDF is fitted to the points to obtain a more reliable estimate of the needed quantile. The density of the sampled grid point in μ is adapted to the needed quantity in each bin. Each set of trials is reused for the sensitivity and discovery potential definitions.

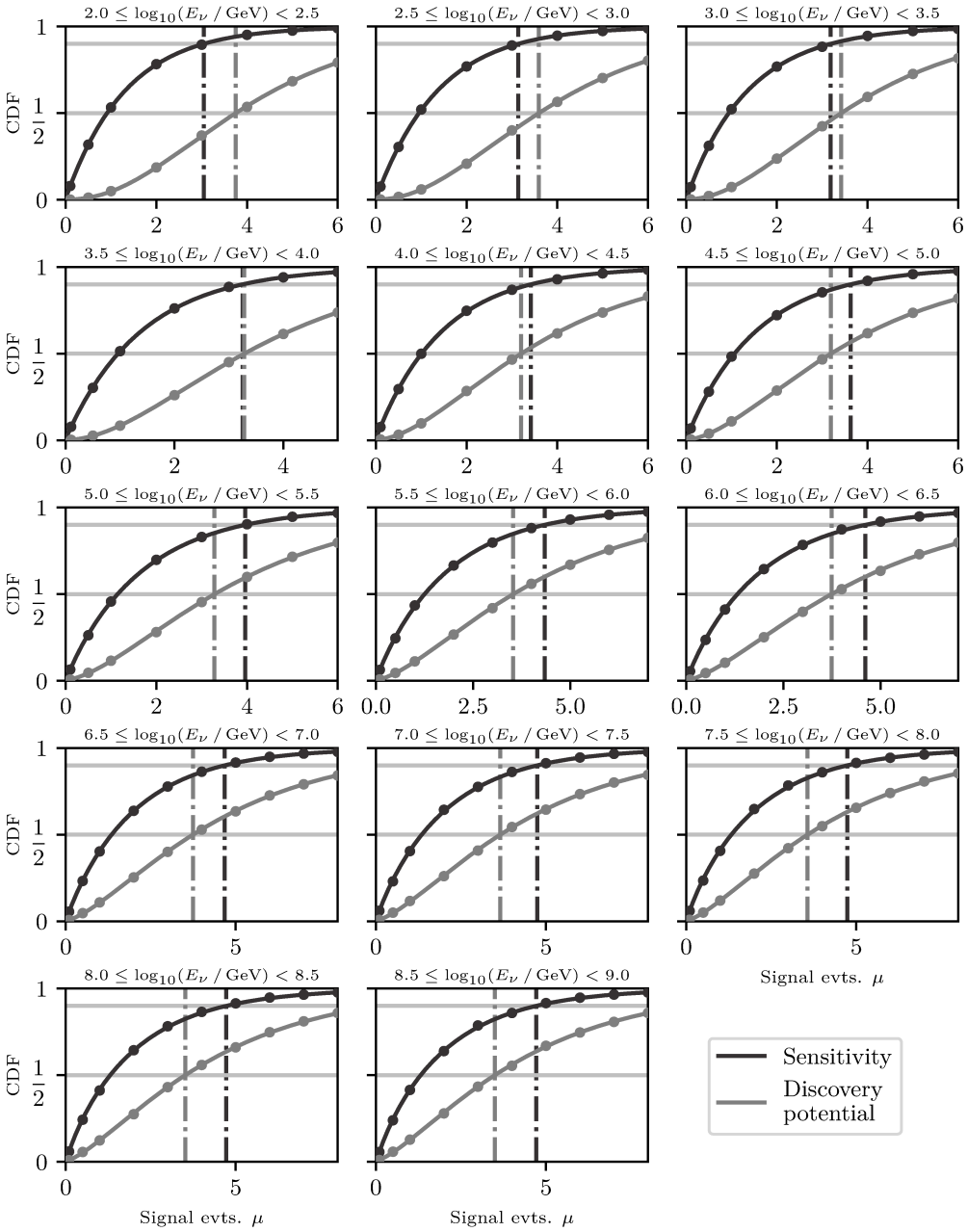

Figure B.26.: χ^2 CDF fits to the discrete set of test statistic quantiles from the signal injection trials over the mean number of injected signal events μ parameter scan for the eighth time window. For each point, the quantile for the currently sampled test statistic over the desired test statistic value from the background distribution is calculated from the empiric PDF. The χ^2 CDF is fitted to the points to obtain a more reliable estimate of the needed quantile. The density of the sampled grid point in μ is adapted to the needed quantity in each bin. Each set of trials is reused for the sensitivity and discovery potential definitions.

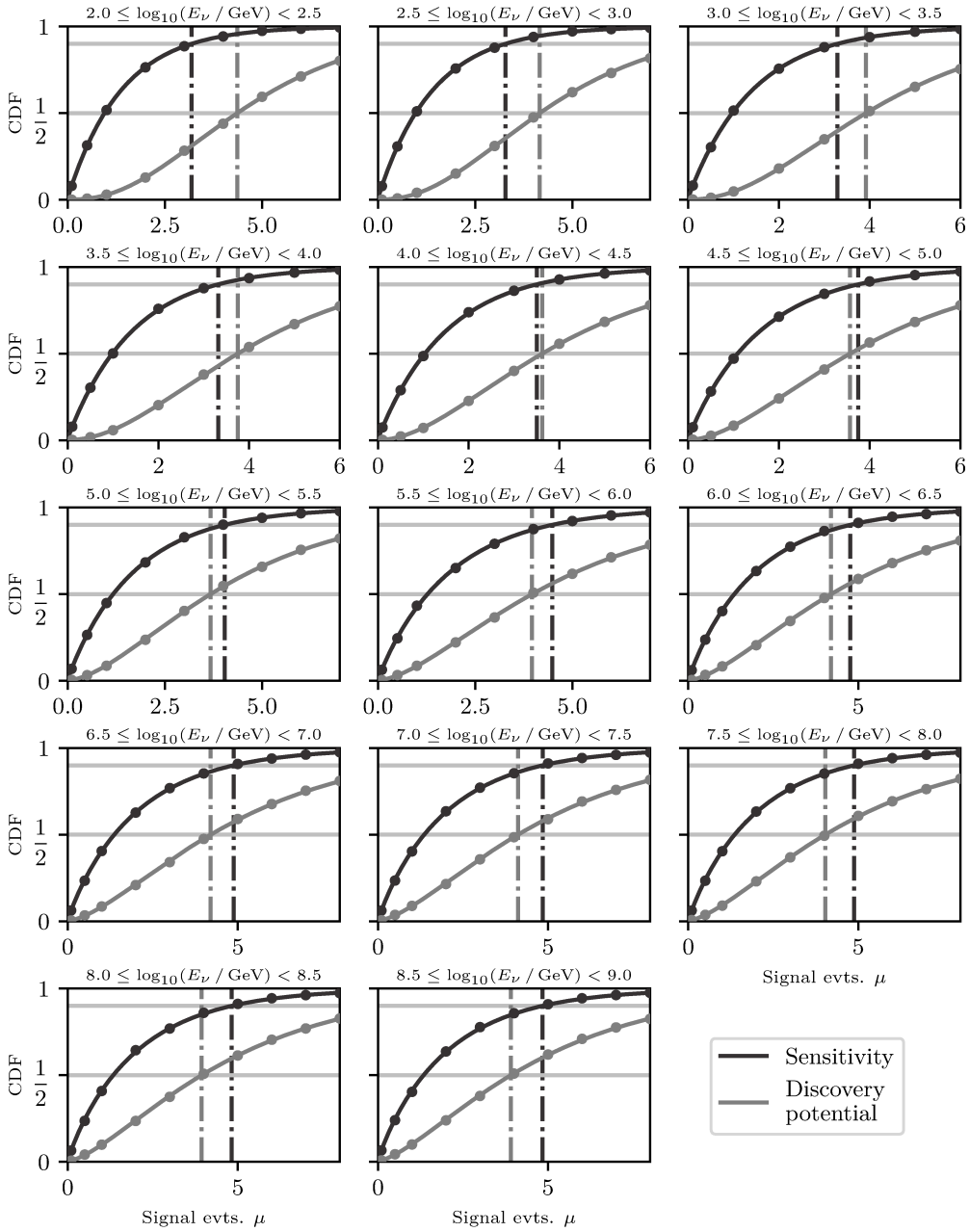

Figure B.27.: χ^2 CDF fits to the discrete set of test statistic quantiles from the signal injection trials over the mean number of injected signal events μ parameter scan for the ninth time window. For each point, the quantile for the currently sampled test statistic over the desired test statistic value from the background distribution is calculated from the empiric PDF. The χ^2 CDF is fitted to the points to obtain a more reliable estimate of the needed quantile. The density of the sampled grid point in μ is adapted to the needed quantity in each bin. Each set of trials is reused for the sensitivity and discovery potential definitions.

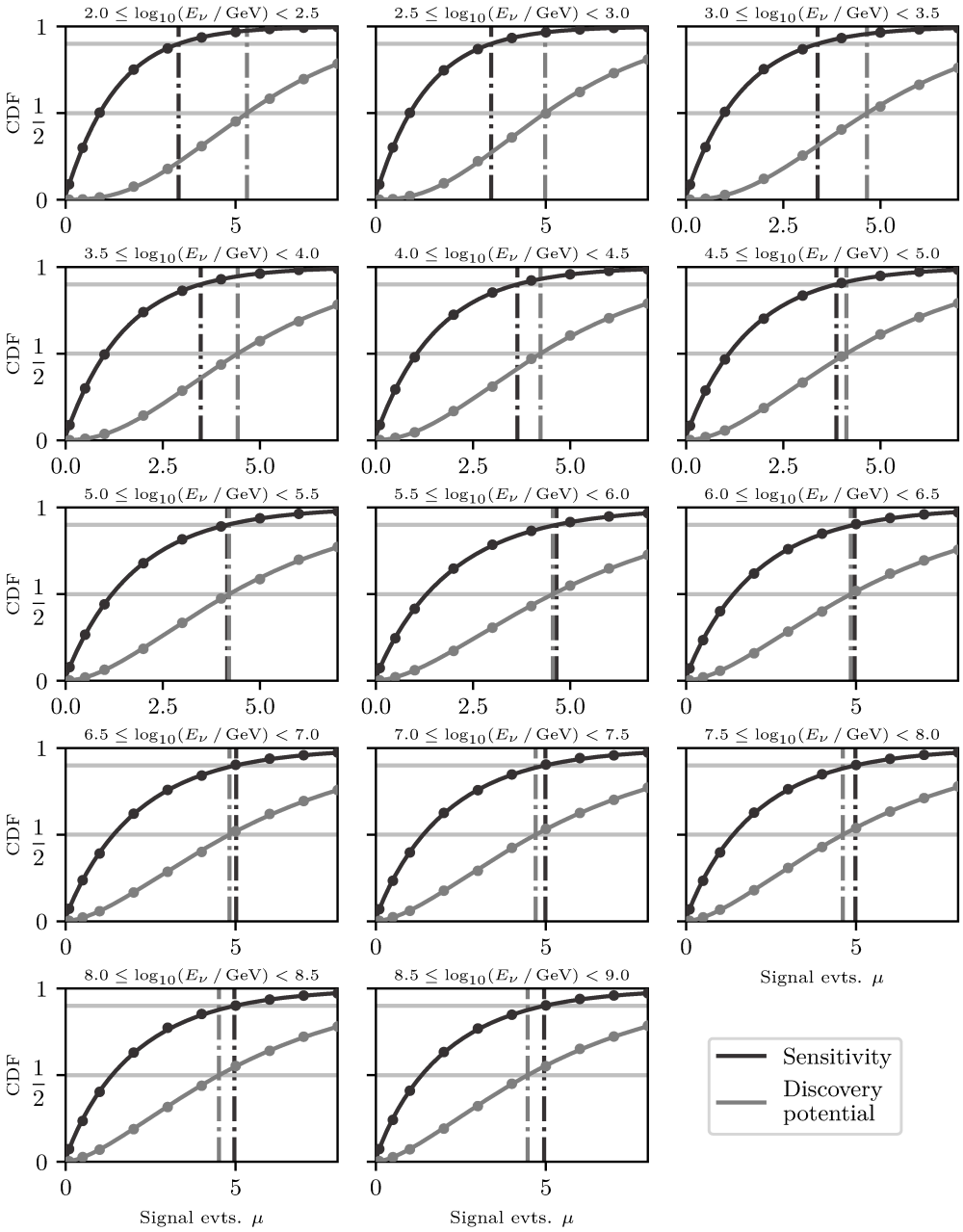

Figure B.28.: χ^2 CDF fits to the discrete set of test statistic quantiles from the signal injection trials over the mean number of injected signal events μ parameter scan for the tenth time window. For each point, the quantile for the currently sampled test statistic over the desired test statistic value from the background distribution is calculated from the empiric PDF. The χ^2 CDF is fitted to the points to obtain a more reliable estimate of the needed quantile. The density of the sampled grid point in μ is adapted to the needed quantity in each bin. Each set of trials is reused for the sensitivity and discovery potential definitions.

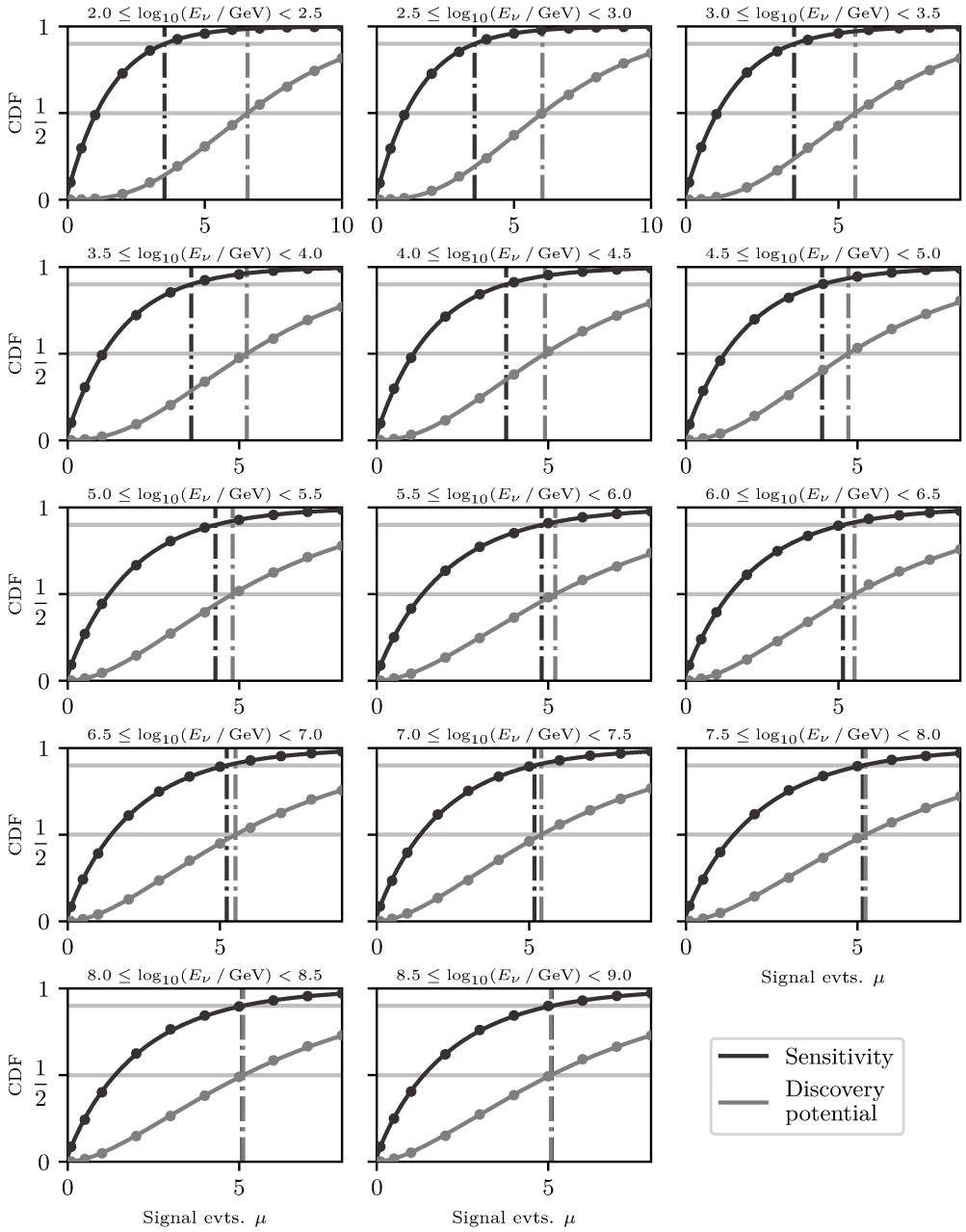

Figure B.29.: χ^2 CDF fits to the discrete set of test statistic quantiles from the signal injection trials over the mean number of injected signal events μ parameter scan for the 11th time window. For each point, the quantile for the currently sampled test statistic over the desired test statistic value from the background distribution is calculated from the empiric PDF. The χ^2 CDF is fitted to the points to obtain a more reliable estimate of the needed quantile. The density of the sampled grid point in μ is adapted to the needed quantity in each bin. Each set of trials is reused for the sensitivity and discovery potential definitions.

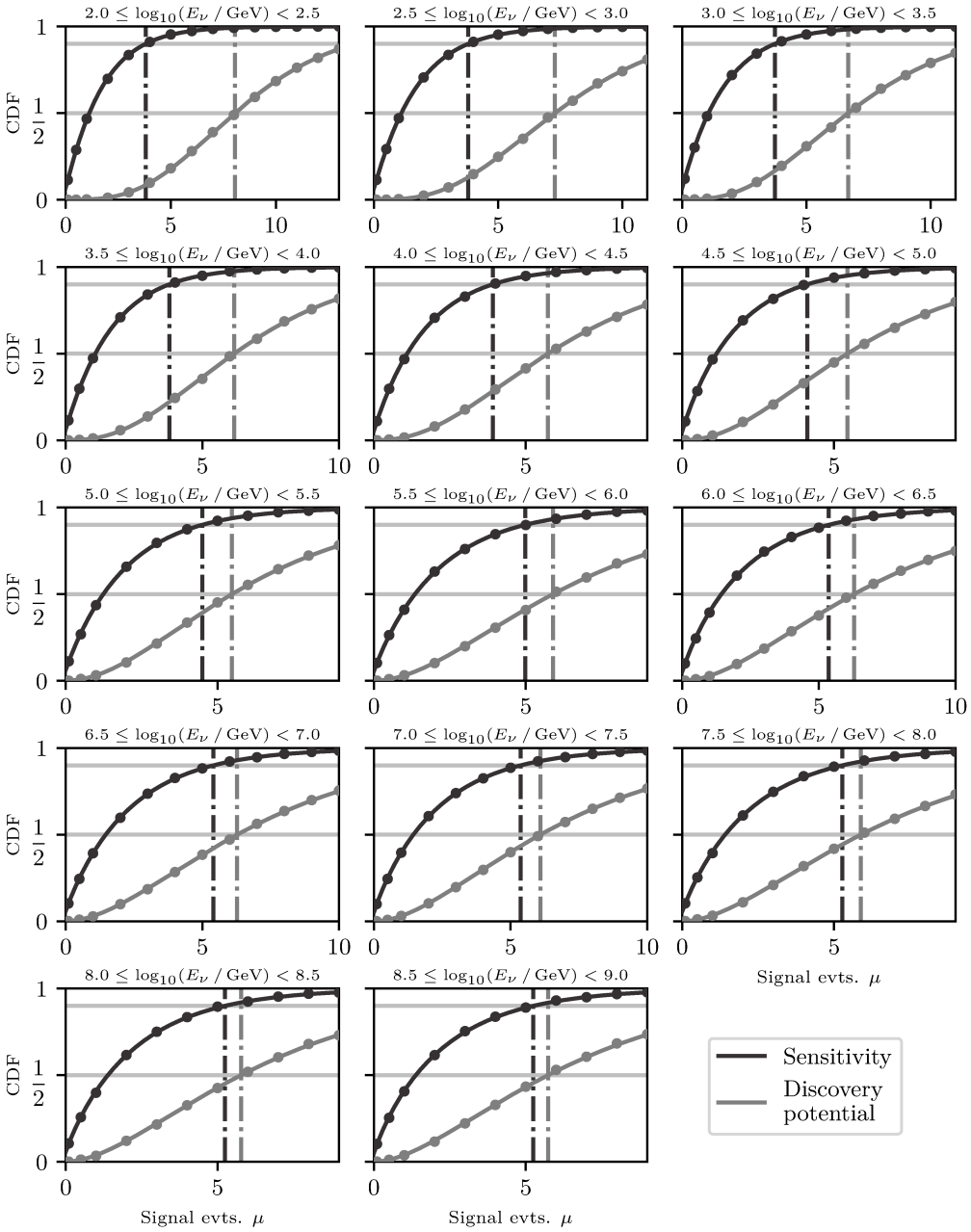

Figure B.30.: χ^2 CDF fits to the discrete set of test statistic quantiles from the signal injection trials over the mean number of injected signal events μ parameter scan for the 12th time window. For each point, the quantile for the currently sampled test statistic over the desired test statistic value from the background distribution is calculated from the empiric PDF. The χ^2 CDF is fitted to the points to obtain a more reliable estimate of the needed quantile. The density of the sampled grid point in μ is adapted to the needed quantity in each bin. Each set of trials is reused for the sensitivity and discovery potential definitions.

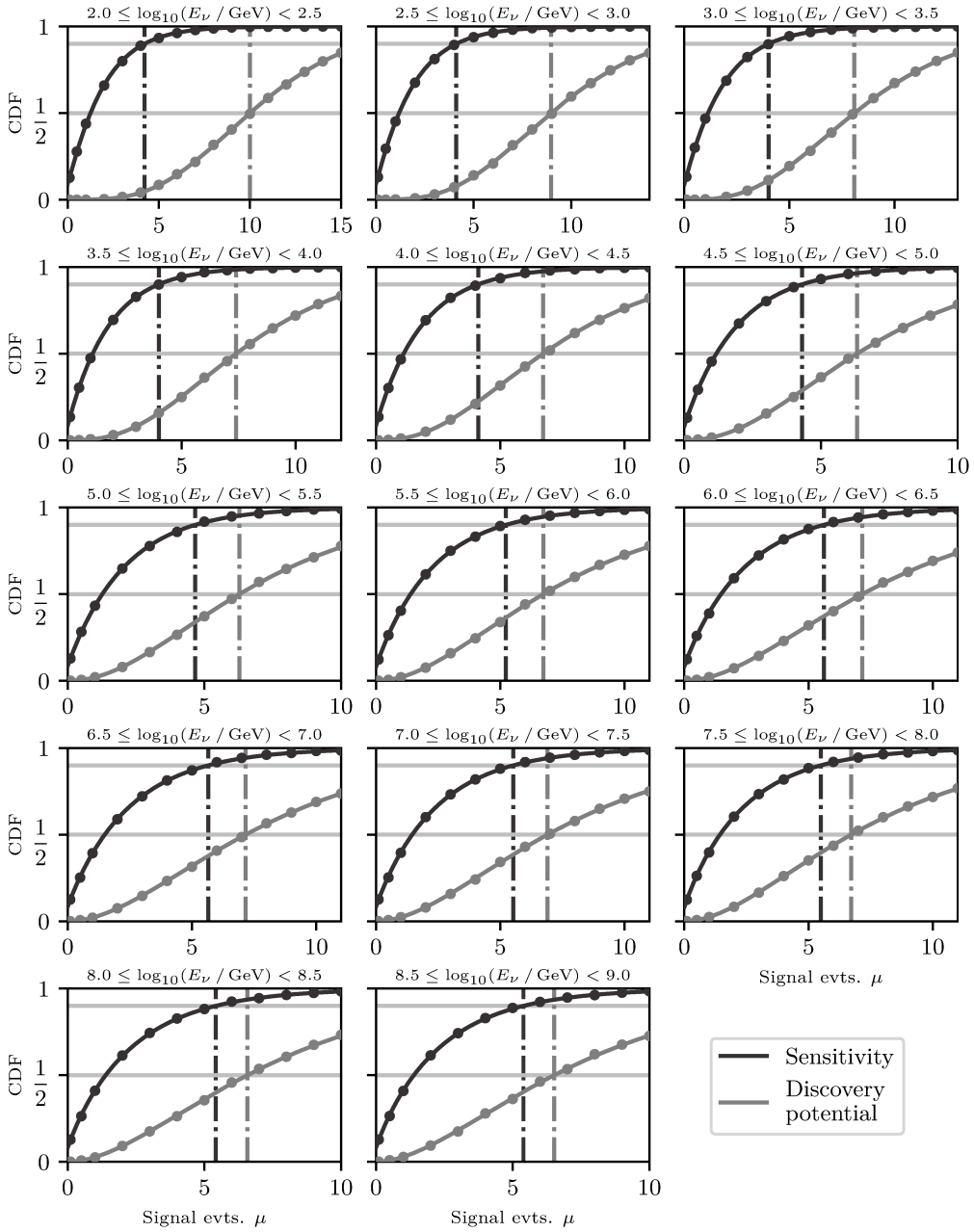

Figure B.31.: χ^2 CDF fits to the discrete set of test statistic quantiles from the signal injection trials over the mean number of injected signal events μ parameter scan for the 13th time window. For each point, the quantile for the currently sampled test statistic over the desired test statistic value from the background distribution is calculated from the empiric PDF. The χ^2 CDF is fitted to the points to obtain a more reliable estimate of the needed quantile. The density of the sampled grid point in μ is adapted to the needed quantity in each bin. Each set of trials is reused for the sensitivity and discovery potential definitions.

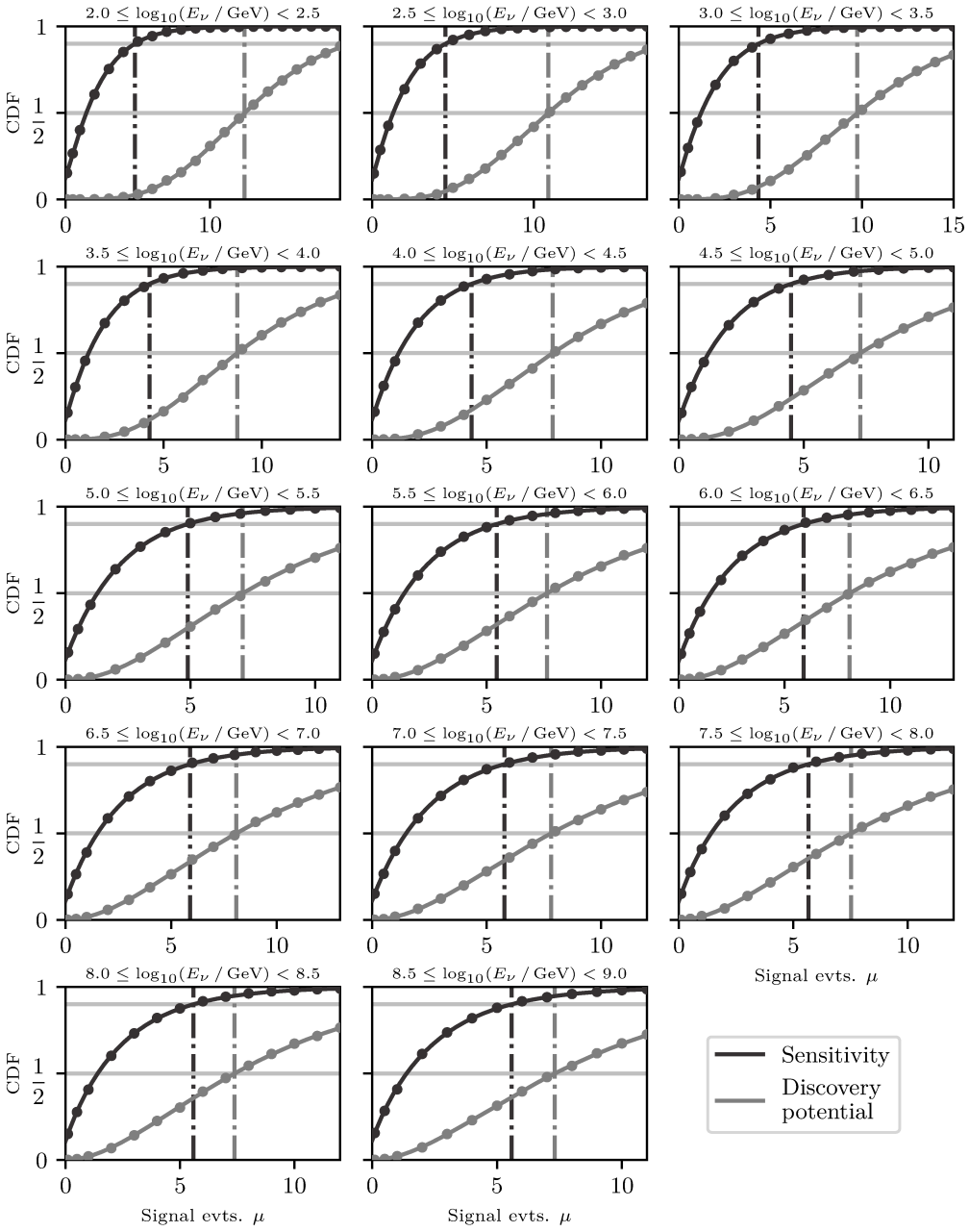

Figure B.32.: χ^2 CDF fits to the discrete set of test statistic quantiles from the signal injection trials over the mean number of injected signal events μ parameter scan for the 14th time window. For each point, the quantile for the currently sampled test statistic over the desired test statistic value from the background distribution is calculated from the empiric PDF. The χ^2 CDF is fitted to the points to obtain a more reliable estimate of the needed quantile. The density of the sampled grid point in μ is adapted to the needed quantity in each bin. Each set of trials is reused for the sensitivity and discovery potential definitions.

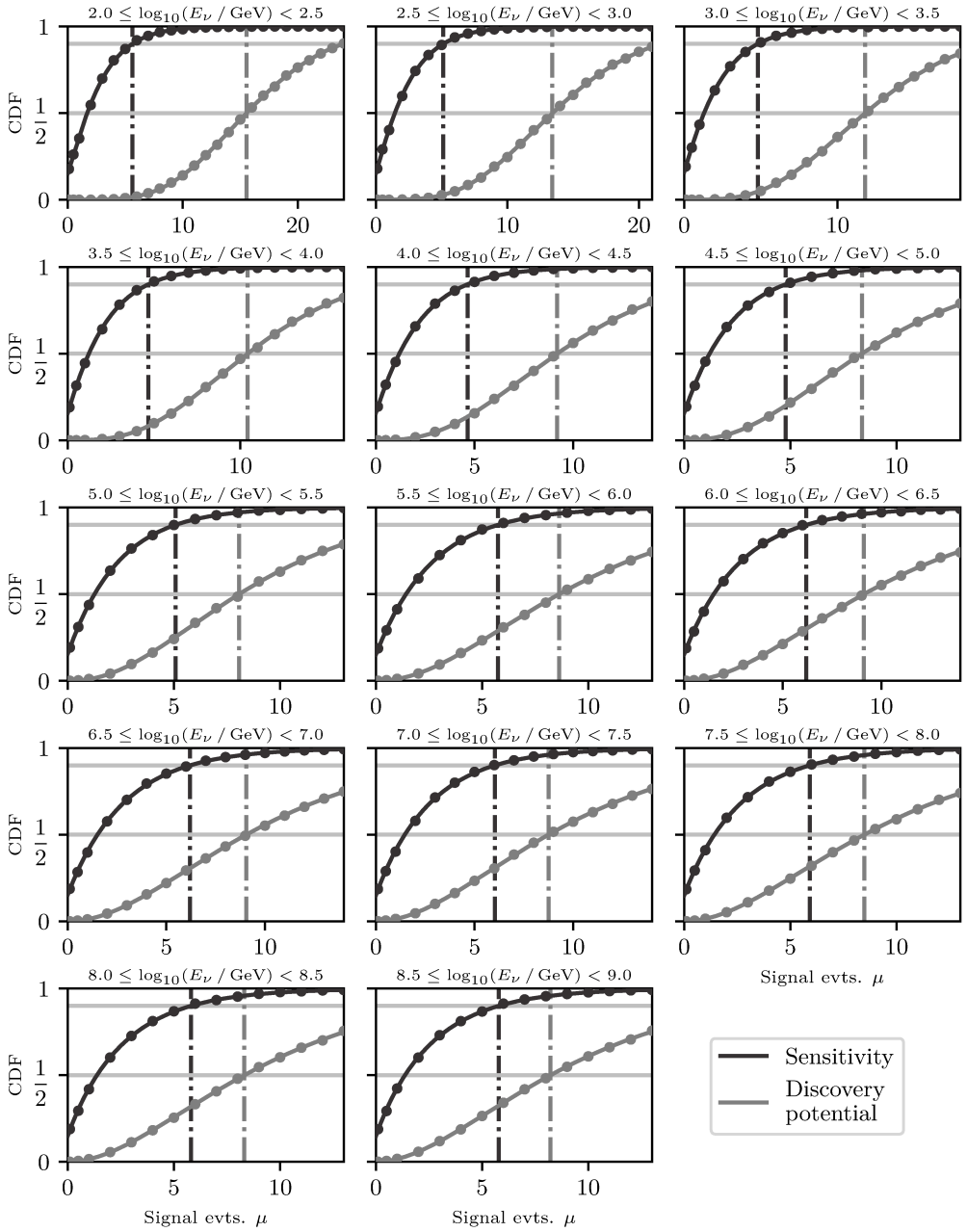

Figure B.33.: χ^2 CDF fits to the discrete set of test statistic quantiles from the signal injection trials over the mean number of injected signal events μ parameter scan for the 15th time window. For each point, the quantile for the currently sampled test statistic over the desired test statistic value from the background distribution is calculated from the empiric PDF. The χ^2 CDF is fitted to the points to obtain a more reliable estimate of the needed quantile. The density of the sampled grid point in μ is adapted to the needed quantity in each bin. Each set of trials is reused for the sensitivity and discovery potential definitions.

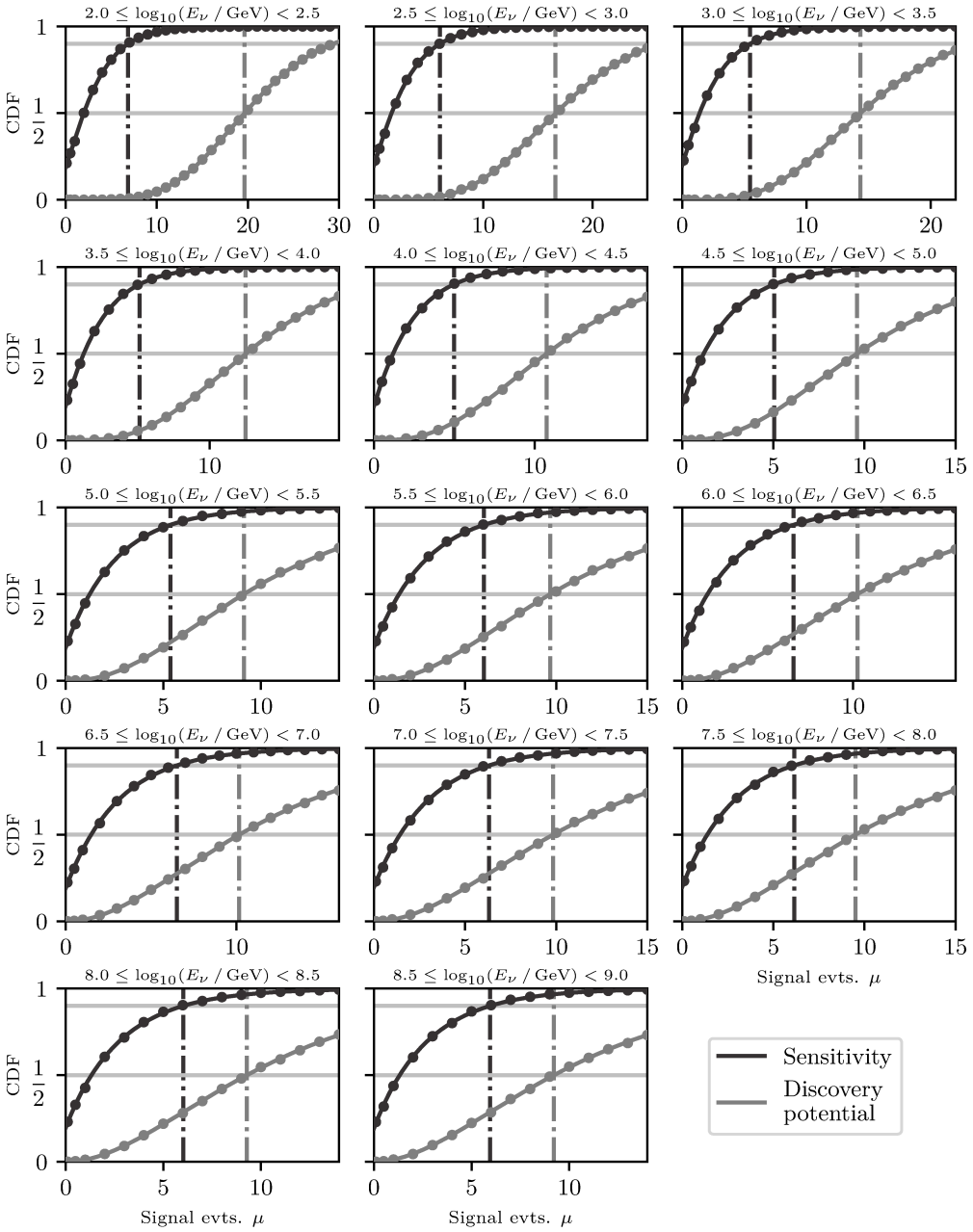

Figure B.34.: χ^2 CDF fits to the discrete set of test statistic quantiles from the signal injection trials over the mean number of injected signal events μ parameter scan for the 16th time window. For each point, the quantile for the currently sampled test statistic over the desired test statistic value from the background distribution is calculated from the empiric PDF. The χ^2 CDF is fitted to the points to obtain a more reliable estimate of the needed quantile. The density of the sampled grid point in μ is adapted to the needed quantity in each bin. Each set of trials is reused for the sensitivity and discovery potential definitions.

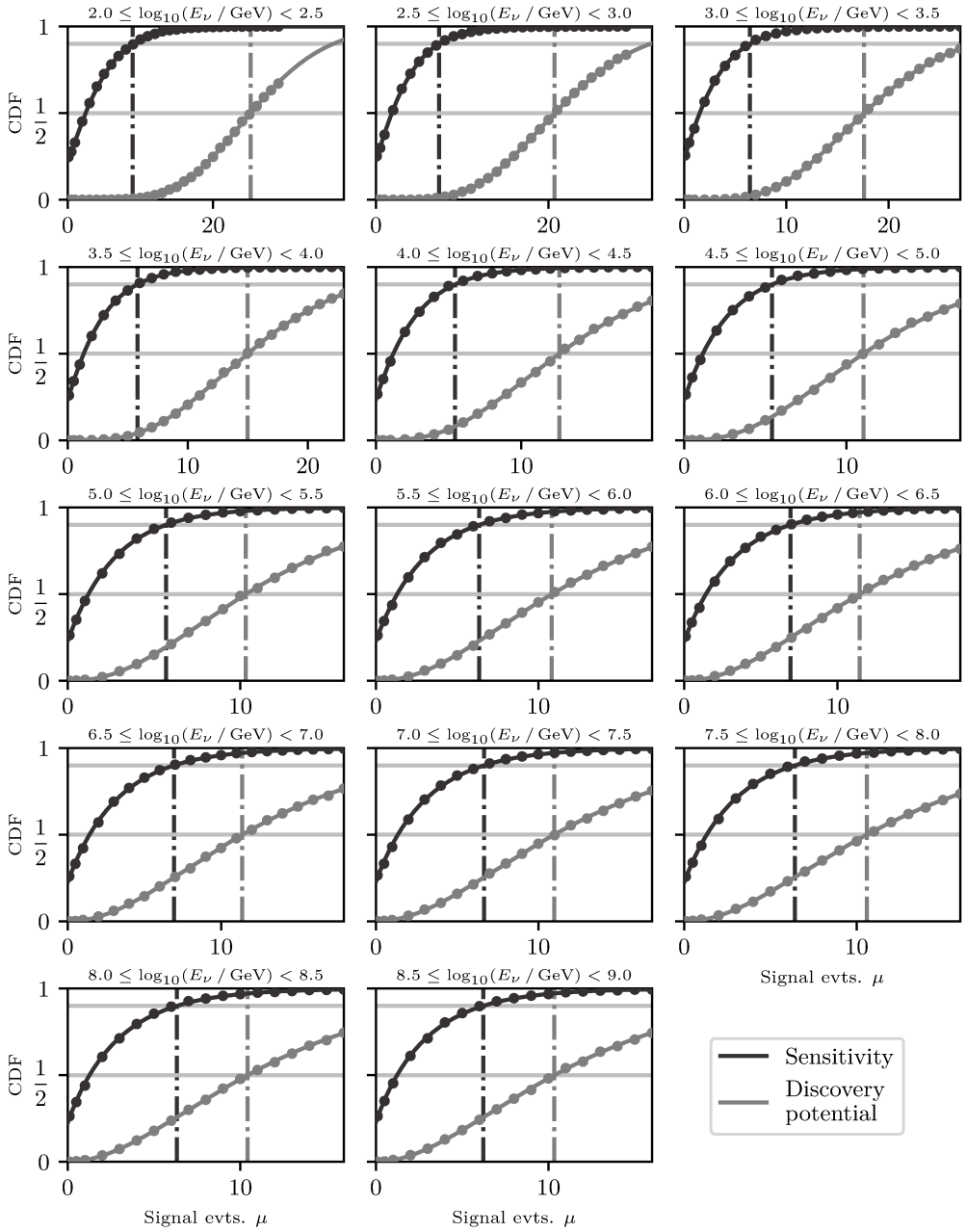

Figure B.35.: χ^2 CDF fits to the discrete set of test statistic quantiles from the signal injection trials over the mean number of injected signal events μ parameter scan for the 17th time window. For each point, the quantile for the currently sampled test statistic over the desired test statistic value from the background distribution is calculated from the empiric PDF. The χ^2 CDF is fitted to the points to obtain a more reliable estimate of the needed quantile. The density of the sampled grid point in μ is adapted to the needed quantity in each bin. Each set of trials is reused for the sensitivity and discovery potential definitions.

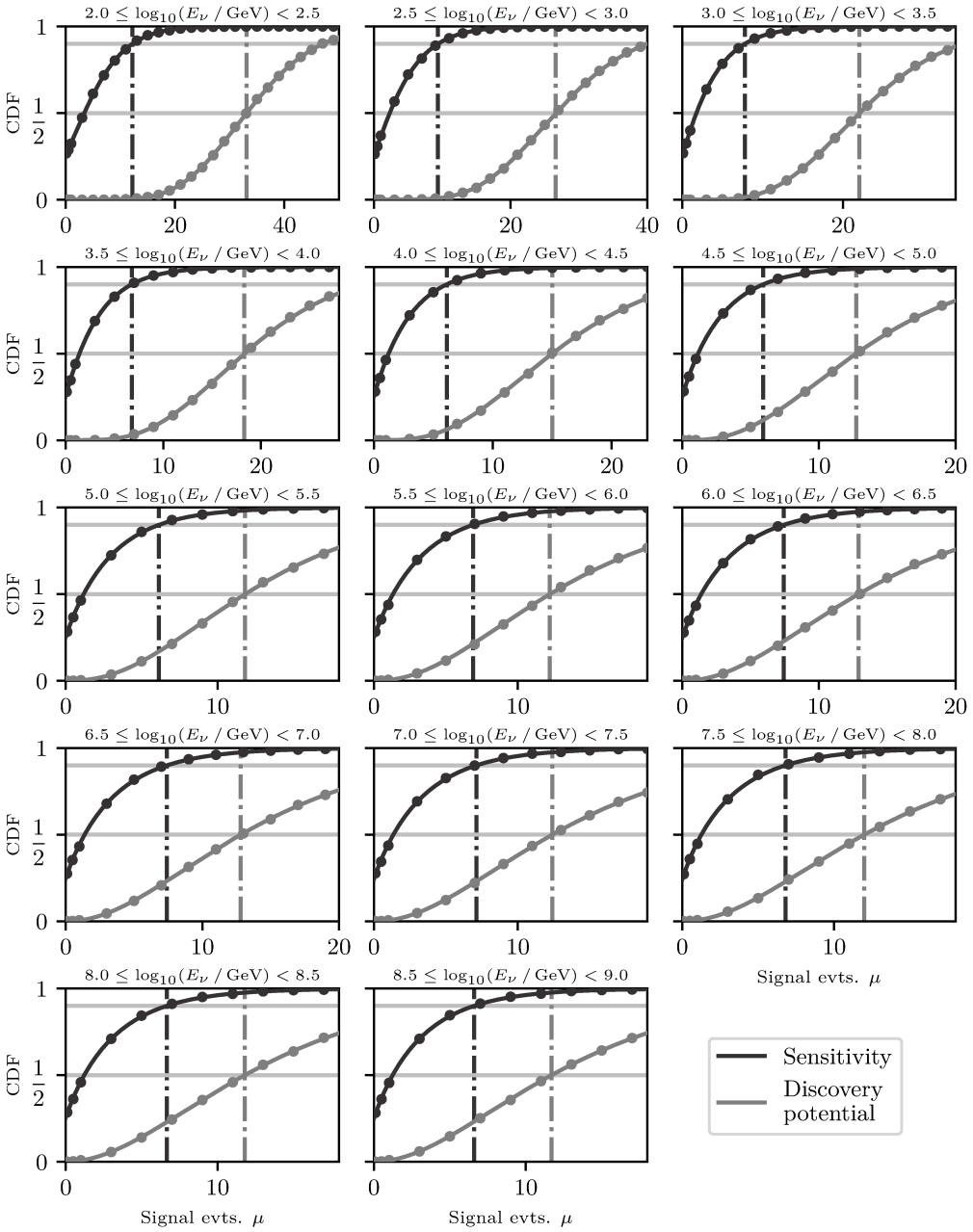

Figure B.36.: χ^2 CDF fits to the discrete set of test statistic quantiles from the signal injection trials over the mean number of injected signal events μ parameter scan for the 18th time window. For each point, the quantile for the currently sampled test statistic over the desired test statistic value from the background distribution is calculated from the empiric PDF. The χ^2 CDF is fitted to the points to obtain a more reliable estimate of the needed quantile. The density of the sampled grid point in μ is adapted to the needed quantity in each bin. Each set of trials is reused for the sensitivity and discovery potential definitions.

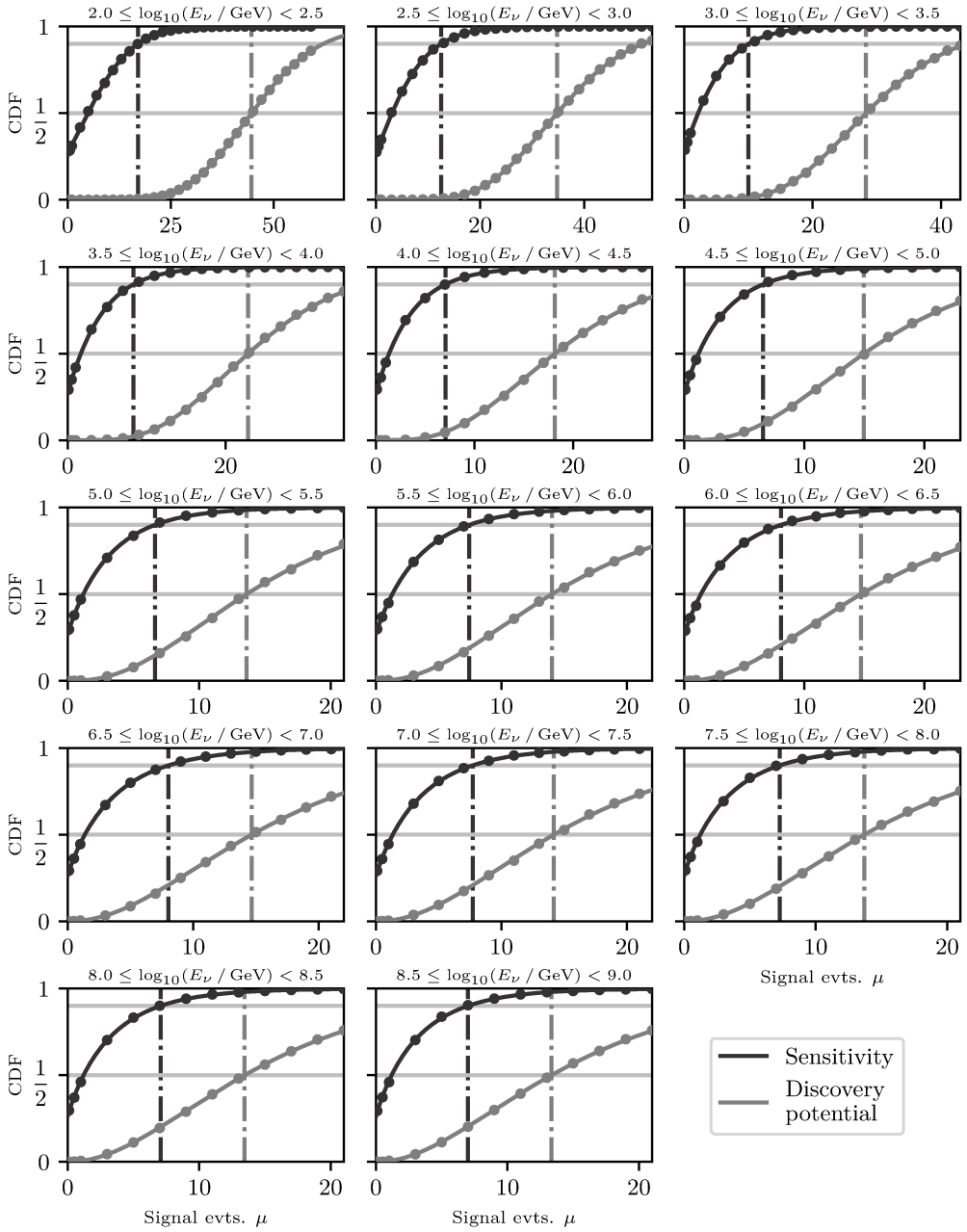

Figure B.37.: χ^2 CDF fits to the discrete set of test statistic quantiles from the signal injection trials over the mean number of injected signal events μ parameter scan for the 19th time window. For each point, the quantile for the currently sampled test statistic over the desired test statistic value from the background distribution is calculated from the empiric PDF. The χ^2 CDF is fitted to the points to obtain a more reliable estimate of the needed quantile. The density of the sampled grid point in μ is adapted to the needed quantity in each bin. Each set of trials is reused for the sensitivity and discovery potential definitions.

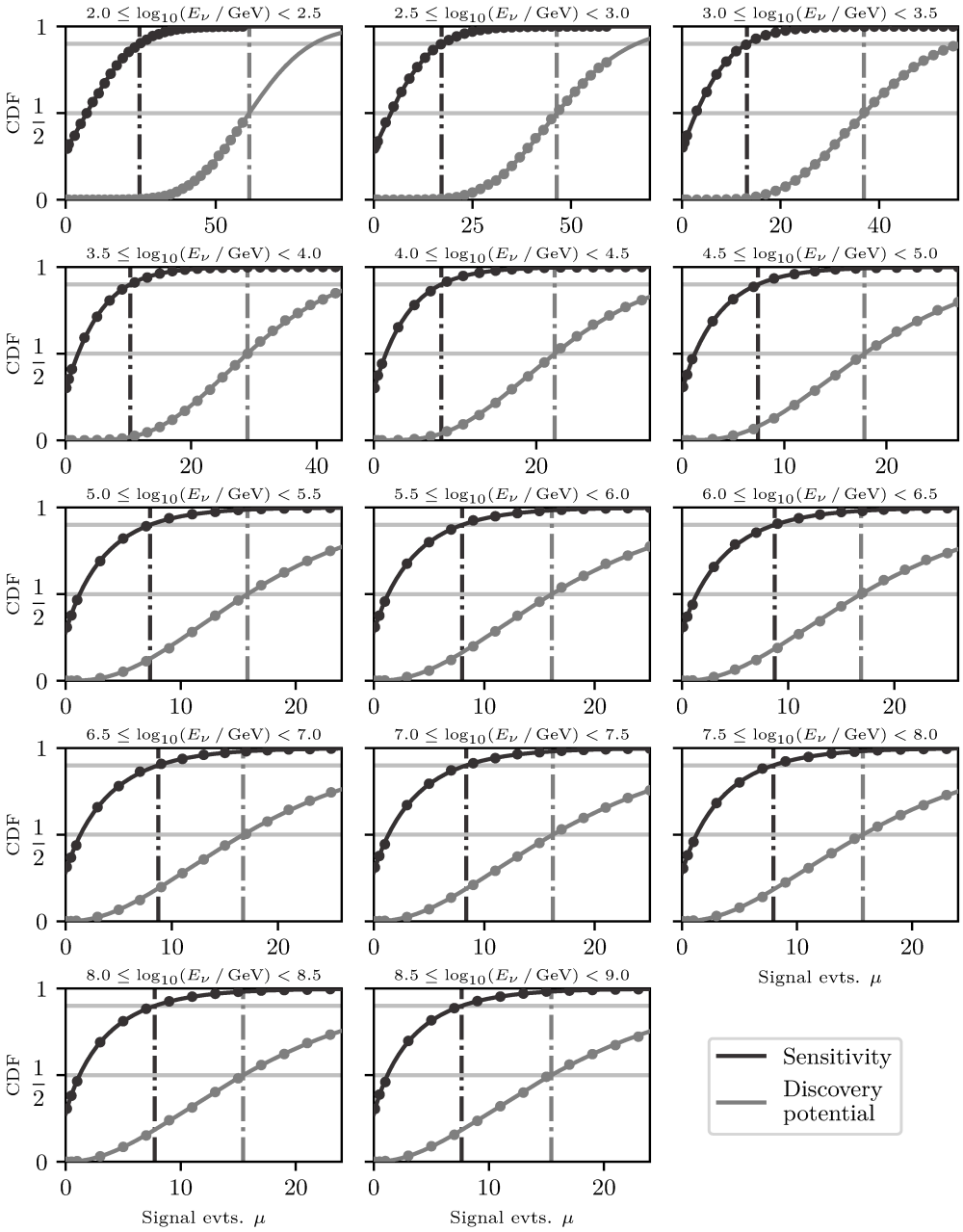

Figure B.38.: χ^2 CDF fits to the discrete set of test statistic quantiles from the signal injection trials over the mean number of injected signal events μ parameter scan for the 20th time window. For each point, the quantile for the currently sampled test statistic over the desired test statistic value from the background distribution is calculated from the empiric PDF. The χ^2 CDF is fitted to the points to obtain a more reliable estimate of the needed quantile. The density of the sampled grid point in μ is adapted to the needed quantity in each bin. Each set of trials is reused for the sensitivity and discovery potential definitions.

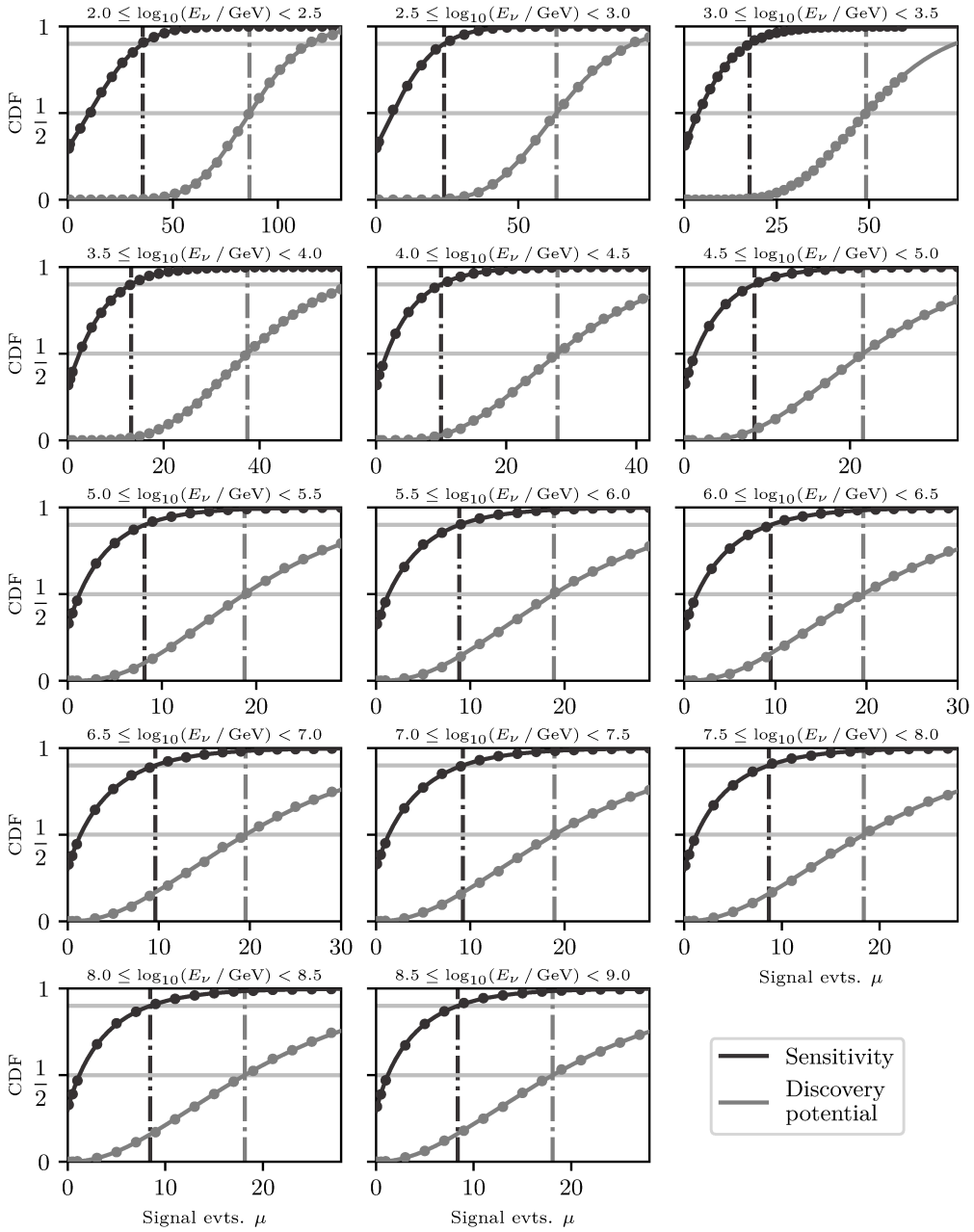

Figure B.39.: χ^2 CDF fits to the discrete set of test statistic quantiles from the signal injection trials over the mean number of injected signal events μ parameter scan for the 21st time window. For each point, the quantile for the currently sampled test statistic over the desired test statistic value from the background distribution is calculated from the empiric PDF. The χ^2 CDF is fitted to the points to obtain a more reliable estimate of the needed quantile. The density of the sampled grid point in μ is adapted to the needed quantity in each bin. Each set of trials is reused for the sensitivity and discovery potential definitions.

B.3. Time-integrated analysis

This chapter includes additional figures and tables for the time-integrated analysis chapter.

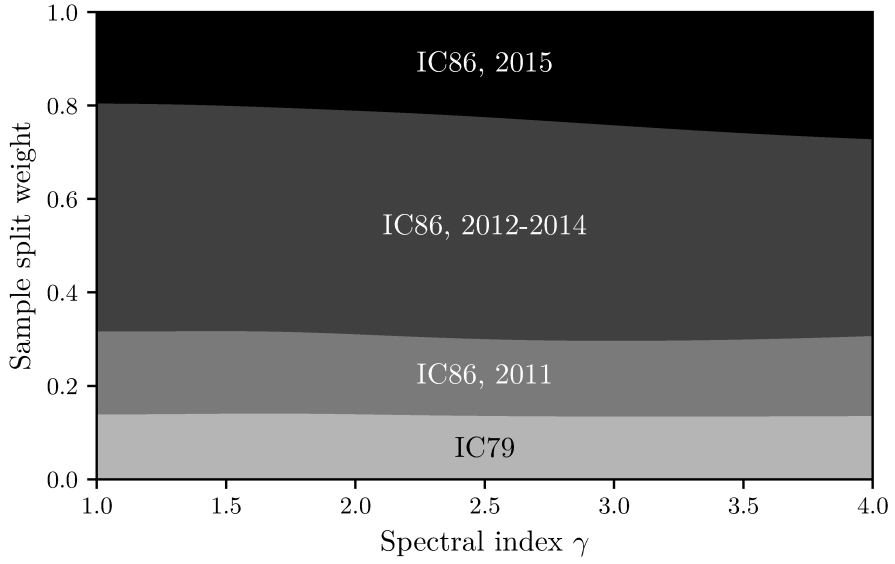

Figure B.40.: Weights w_j to split the global n_S fit parameter across the single Likelihoods in the multi-sample Likelihood (5.64). The weights depend on the spectral index γ that currently describes the signal flux hypothesis and are selected accordingly during the fitting procedure.

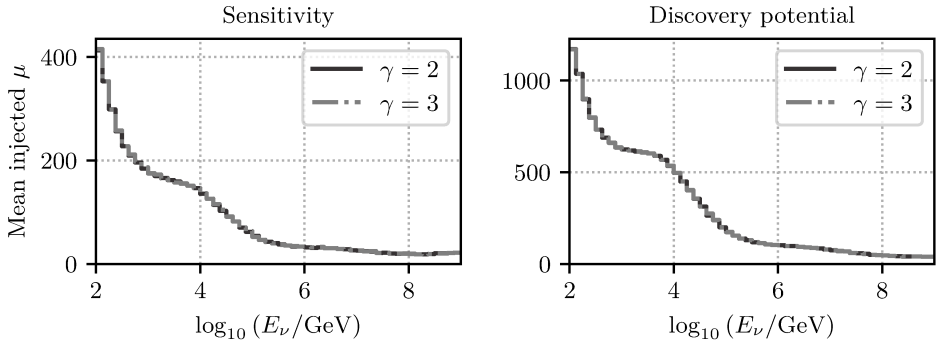

Figure B.41.: The number of needed injected signal events is almost identical for both injection models and for sensitivity and discovery potential fluxes due to the used small bin sizes. This quasi independence on the injection model is one prerequisite to justify the calculation of global flux performances or limits of almost arbitrary flux models from the differential fluxes.

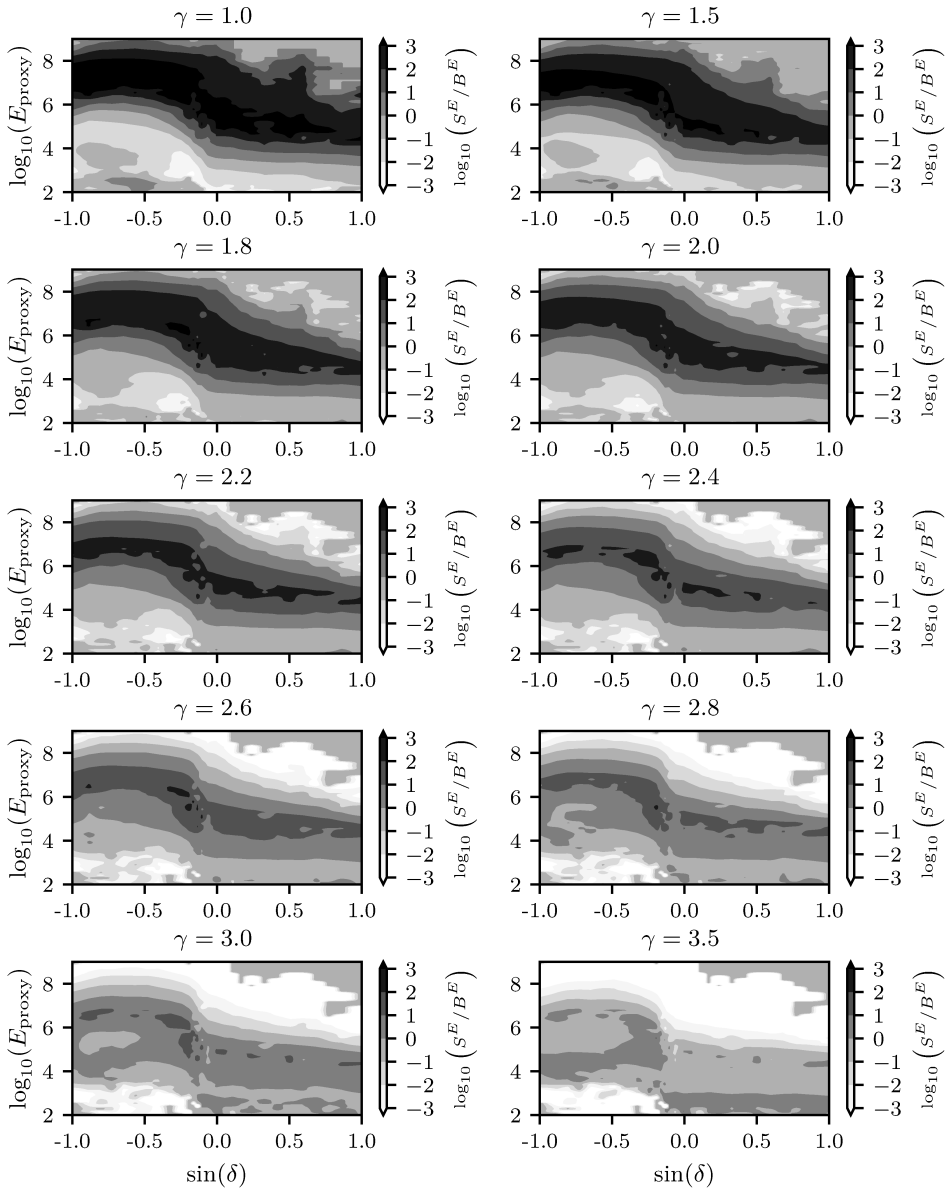

Figure B.42.: Two-dimensional ratio of the signal and background energy PDFs in $\log_{10}(E_{\mathrm{proxy}})$ and $\sin(\delta)$ for the IC86, 2011 sample and for different spectral indices γ. The underlying binning is the same for the signal and background histogram. Each ratio is pre-calculated for a grid of spectral indices beforehand and used during the fitting procedure for the current realization of γ. A one-dimensional spline, which is not shown here, is used per $\left(\sin(\delta), \log_{10}(E_{\mathrm{proxy}})\right)$ tuple for each event to interpolate the grid and obtain the gradient information for the spectral index fit parameter.

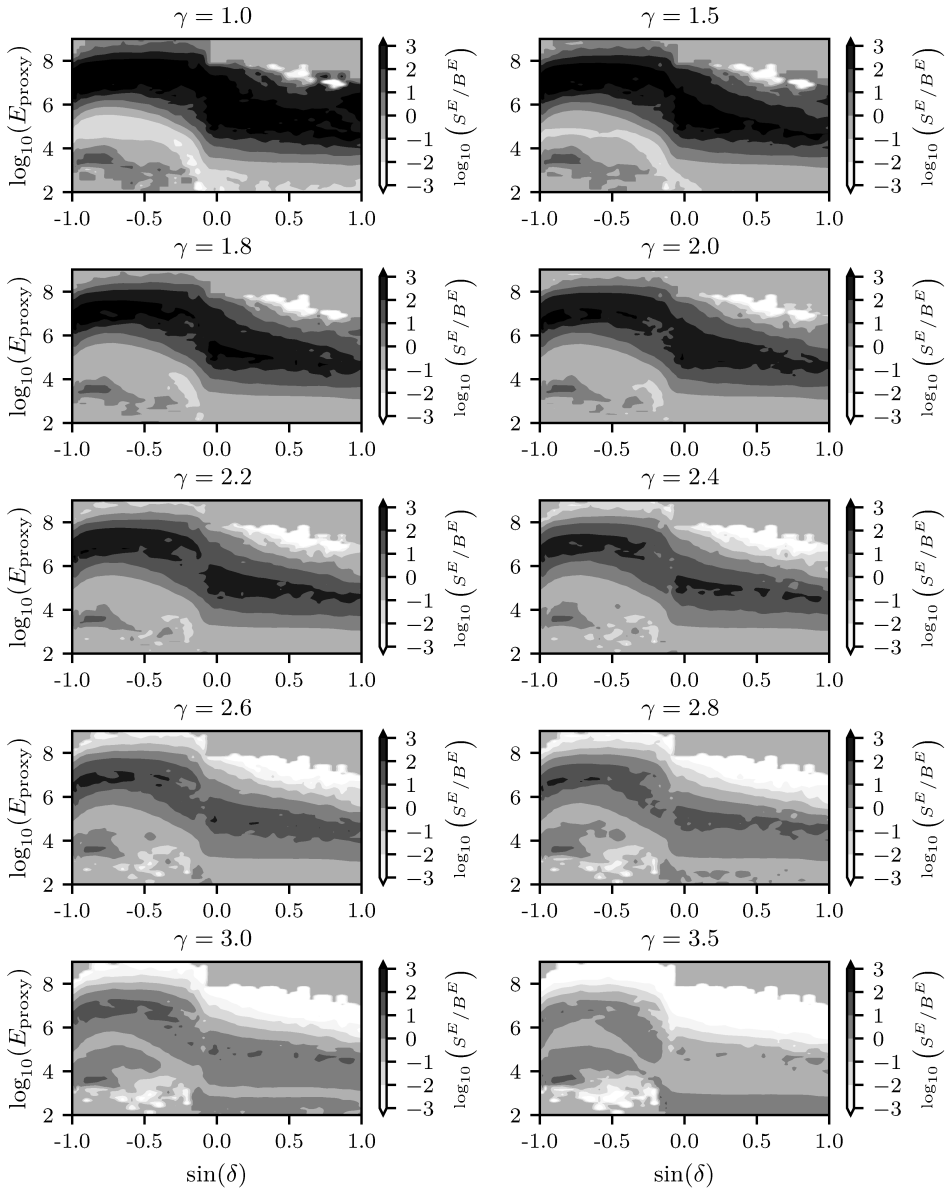

Figure B.43.: Two-dimensional ratio of the signal and background energy PDFs in $\log_{10}\left(E_{\mathrm{proxy}}\right)$ and $\sin(\delta)$ for the IC86, 2012–2014 sample and for different spectral indices γ. The underlying binning is the same for the signal and background histogram. Each ratio is pre-calculated for a grid of spectral indices beforehand and used during the fitting procedure for the current realization of γ. A one-dimensional spline, which is not shown here, is used per $\left(\sin(\delta), \log_{10}\left(E_{\mathrm{proxy}}\right)\right)$ tuple for each event to interpolate the grid and obtain the gradient information for the spectral index fit parameter.

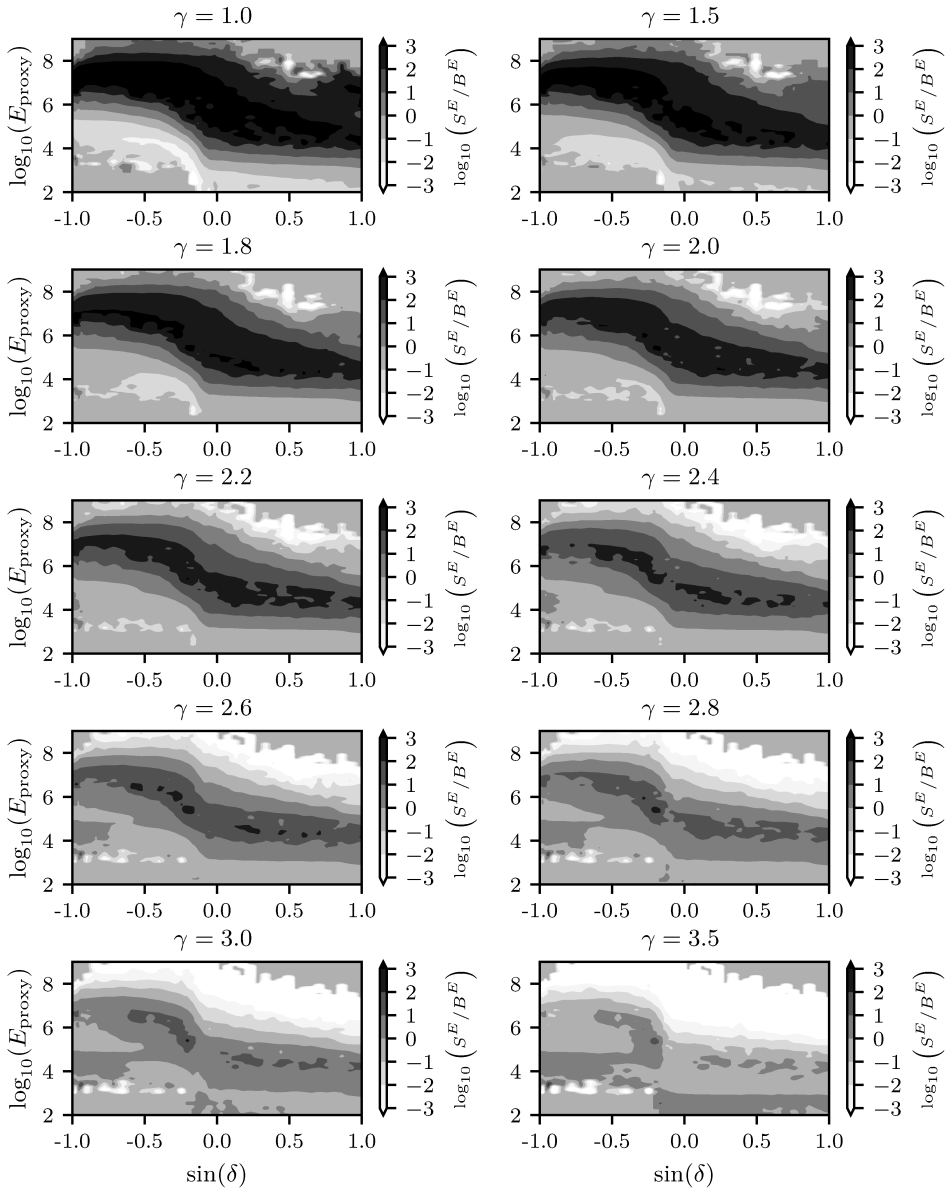

Figure B.44.: Two-dimensional ratio of the signal and background energy PDFs in $\log_{10}(E_{\mathrm{proxy}})$ and $\sin(\delta)$ for the IC86, 2015 sample and for different spectral indices γ. The underlying binning is the same for the signal and background histogram. Each ratio is pre-calculated for a grid of spectral indices beforehand and used during the fitting procedure for the current realization of γ. A one-dimensional spline, which is not shown here, is used per $\left(\sin(\delta), \log_{10}(E_{\mathrm{proxy}})\right)$ tuple for each event to interpolate the grid and obtain the gradient information for the spectral index fit parameter.

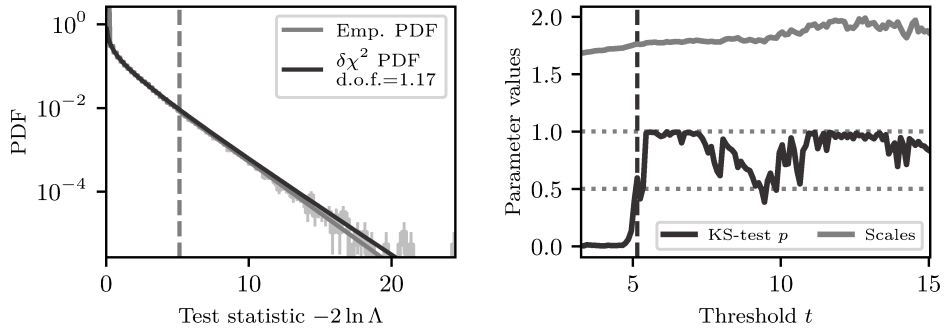

Figure B.45.: Background test statistic for the time-integrated analysis with both the direct χ^2 model and the hybrid model used in the time-dependent analysis for comparison. Only the effective degrees of freedom are fitted in the χ^2 model, the number of non-zero trials η is obtained by simple counting. On the right, the threshold scan for the hybrid model is shown. For the final p-value estimation, the χ^2 model is used.

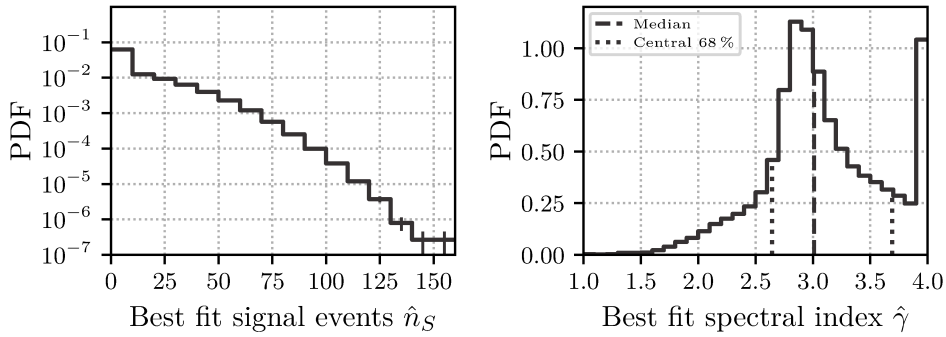

Figure B.46.: On the left plot, the n_S distribution for pure background trials is shown. On the right plot, the same for the second fit parameter, the spectral index γ of the assumed signal flux. A slight bias can be seen towards slightly harder spectra than expected from the common atmospheric neutrino flux model. However, the spectral index is handled more than a nuisance parameter in this type of analysis, so a slight bias has no negative consequence on the final result.

Differential performances χ^2 CDF fits

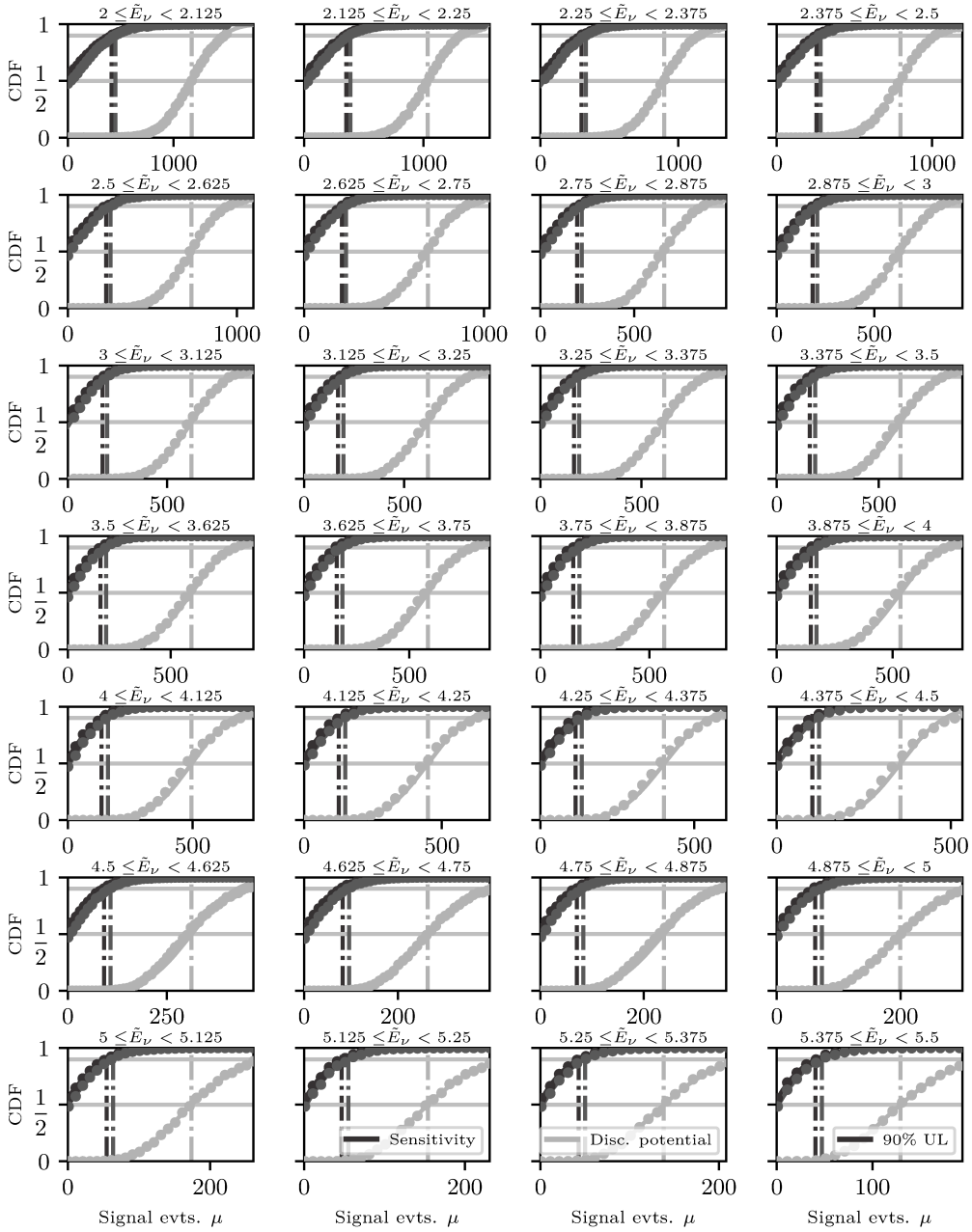

Figure B.47.: χ^2 CDF fits to the discrete set of test statistic quantiles from the signal injection trials over the mean number of injected signal events μ parameter scan for the injection model with spectral index $\gamma_{\text{inj}} = 2$ and the lower half of neutrino energy bins. For each point, the quantile for the currently sampled test statistic over the desired test statistic value from the background distribution is calculated from the empiric PDF. The χ^2 CDF is fitted to the points to obtain a more reliable estimate of the needed quantile. The density of the sampled grid point in μ is adapted to the needed quantity in each bin. The fits for the other half of the bins can be seen in figure (B.48)

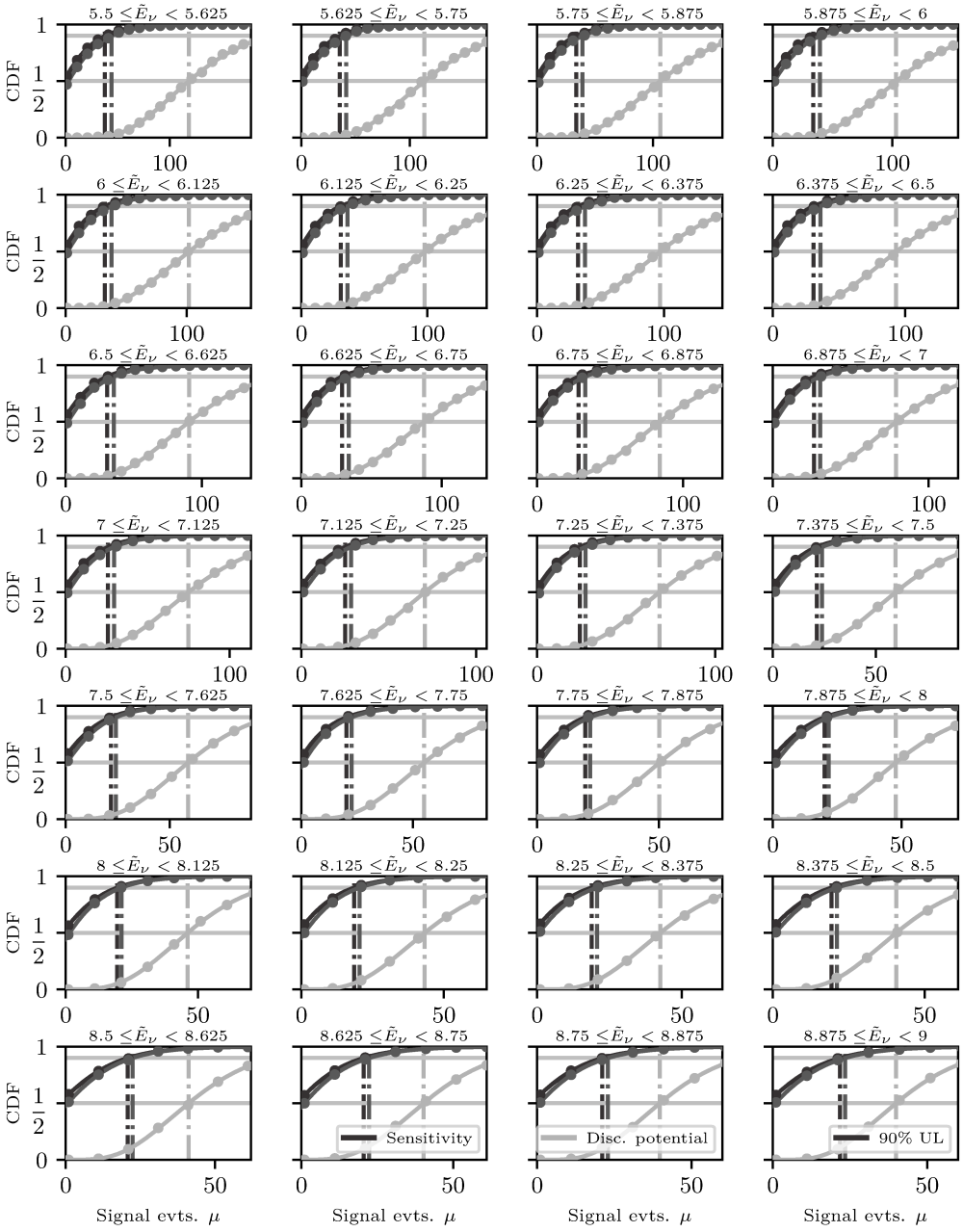

Figure B.48.: χ^2 CDF fits to the discrete set of test statistic quantiles from the signal injection trials over the mean number of injected signal events μ parameter scan for the injection model with spectral index $\gamma_{\text{inj}} = 2$ and the upper half of neutrino energy bins. For each point, the quantile for the currently sampled test statistic over the desired test statistic value from the background distribution is calculated from the empiric PDF. The χ^2 CDF is fitted to the points to obtain a more reliable estimate of the needed quantile. The density of the sampled grid point in μ is adapted to the needed quantity in each bin. The fits for the other half of the bins can be seen in figure (B.47)

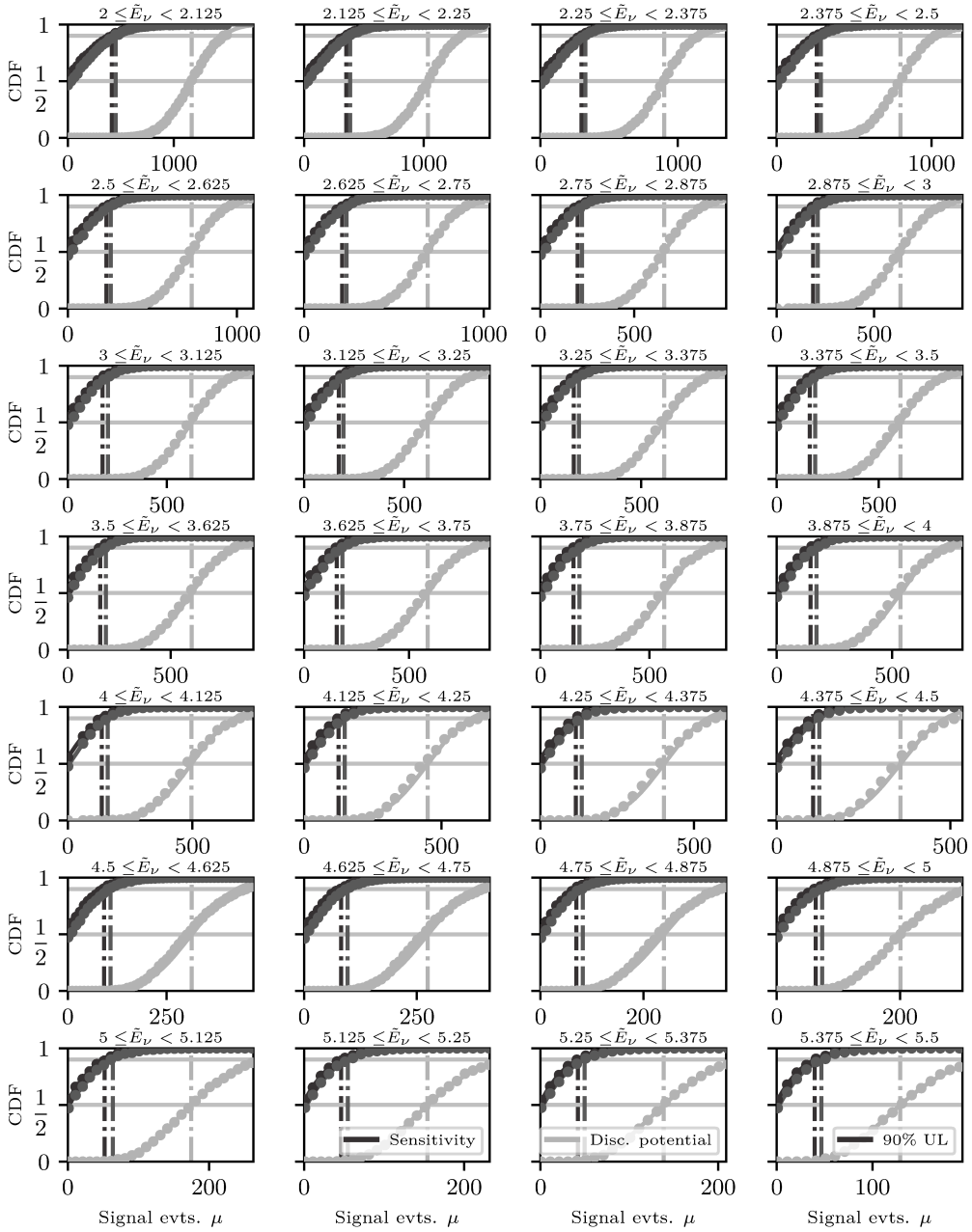

Figure B.49.: χ^2 CDF fits to the discrete set of test statistic quantiles from the signal injection trials over the mean number of injected signal events μ parameter scan for the injection model with spectral index $\gamma_{\text{inj}} = 3$ and the lower half of neutrino energy bins. For each point, the quantile for the currently sampled test statistic over the desired test statistic value from the background distribution is calculated from the empiric PDF. The χ^2 CDF is fitted to the points to obtain a more reliable estimate of the needed quantile. The density of the sampled grid point in μ is adapted to the needed quantity in each bin. The fits for the other half of the bins can be seen in figure (B.50)

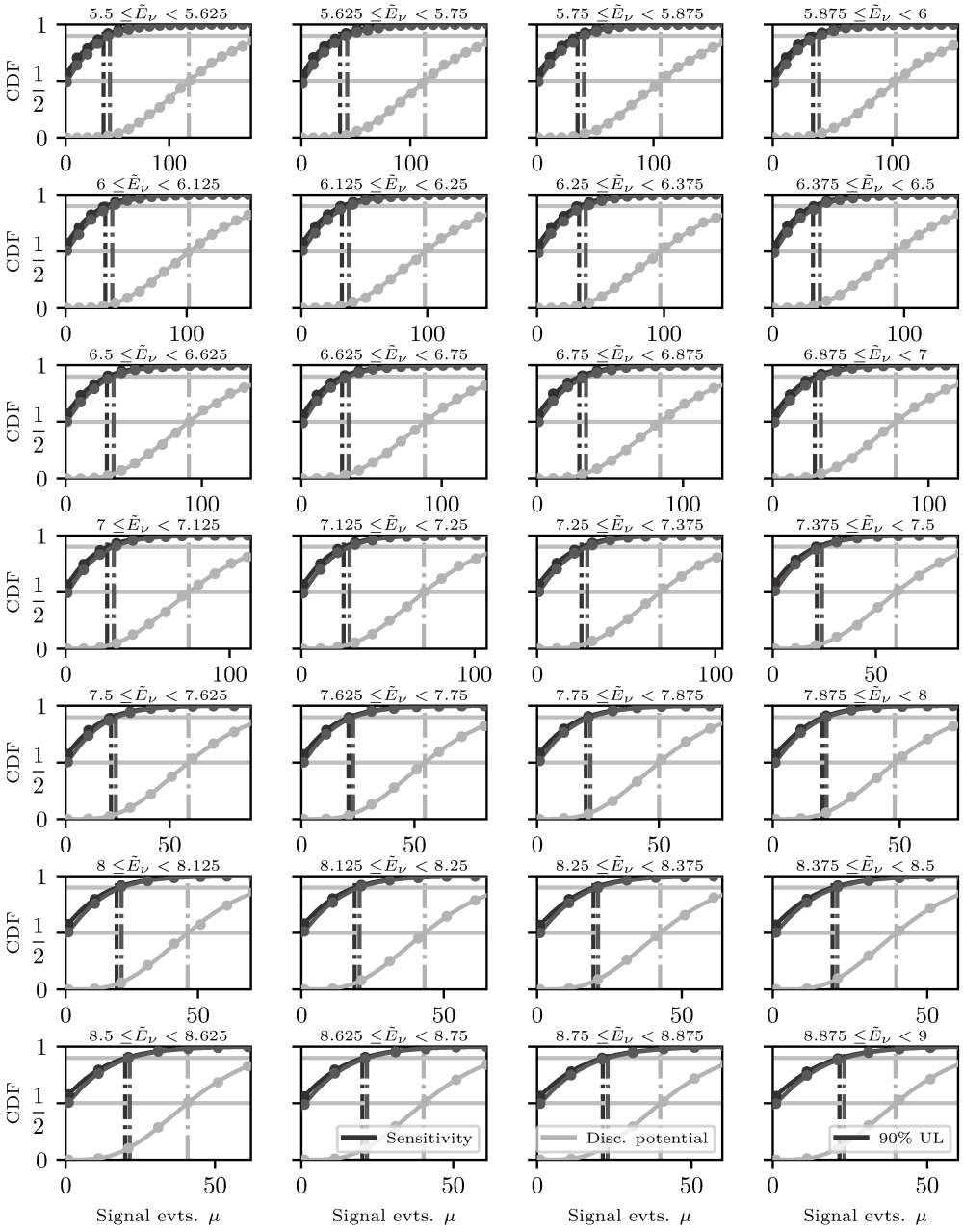

Figure B.50.: χ^2 CDF fits to the discrete set of test statistic quantiles from the signal injection trials over the mean number of injected signal events μ parameter scan for the injection model with spectral index $\gamma_{\text{inj}} = 3$ and the upper half of neutrino energy bins. For each point, the quantile for the currently sampled test statistic over the desired test statistic value from the background distribution is calculated from the empiric PDF. The χ^2 CDF is fitted to the points to obtain a more reliable estimate of the needed quantile. The density of the sampled grid point in μ is adapted to the needed quantity in each bin. The fits for the other half of the bins can be seen in figure (B.49)

Table B.3.: Numerical values for the differential sensitivity flux normalisations $E^2\phi_0^{100\,\mathrm{TeV}}$ at 100 TeV in $\mathrm{GeV\,cm^{-2}\,s^{-1}}$. The values correspond to the differential performance curve shown in figure (7.3) for the injection model with spectral index $\gamma_{\mathrm{inj}} = 2$. The $\log_{10}(E_\nu/\mathrm{GeV})$ columns are the left energy bin borders. See table (B.4) for the flux values calculated with the injection index $\gamma_{\mathrm{inj}} = 3$. Note: the unweighted flux values are obtained by dividing by $(100\,\mathrm{TeV})^2$.

$\log_{10}(E_\nu/\mathrm{GeV})$	$\phi_0^{100\,\mathrm{TeV}}$	$\log_{10}(E_\nu/\mathrm{GeV})$	$\phi_0^{100\,\mathrm{TeV}}$
2.000	$5.34 \cdot 10^{-4}$	5.500	$2.12 \cdot 10^{-7}$
2.125	$1.45 \cdot 10^{-4}$	5.625	$2.14 \cdot 10^{-7}$
2.250	$5.41 \cdot 10^{-5}$	5.750	$2.24 \cdot 10^{-7}$
2.375	$2.52 \cdot 10^{-5}$	5.875	$2.44 \cdot 10^{-7}$
2.500	$1.36 \cdot 10^{-5}$	6.000	$2.62 \cdot 10^{-7}$
2.625	$8.35 \cdot 10^{-6}$	6.125	$2.83 \cdot 10^{-7}$
2.750	$5.55 \cdot 10^{-6}$	6.250	$3.31 \cdot 10^{-7}$
2.875	$3.80 \cdot 10^{-6}$	6.375	$3.61 \cdot 10^{-7}$
3.000	$2.75 \cdot 10^{-6}$	6.500	$4.15 \cdot 10^{-7}$
3.125	$2.09 \cdot 10^{-6}$	6.625	$4.50 \cdot 10^{-7}$
3.250	$1.64 \cdot 10^{-6}$	6.750	$5.15 \cdot 10^{-7}$
3.375	$1.31 \cdot 10^{-6}$	6.875	$5.59 \cdot 10^{-7}$
3.500	$1.09 \cdot 10^{-6}$	7.000	$6.50 \cdot 10^{-7}$
3.625	$9.13 \cdot 10^{-7}$	7.125	$7.29 \cdot 10^{-7}$
3.750	$7.93 \cdot 10^{-7}$	7.250	$8.30 \cdot 10^{-7}$
3.875	$6.85 \cdot 10^{-7}$	7.375	$8.55 \cdot 10^{-7}$
4.000	$5.89 \cdot 10^{-7}$	7.500	$1.08 \cdot 10^{-6}$
4.125	$5.11 \cdot 10^{-7}$	7.625	$1.23 \cdot 10^{-6}$
4.250	$4.46 \cdot 10^{-7}$	7.750	$1.44 \cdot 10^{-6}$
4.375	$3.92 \cdot 10^{-7}$	7.875	$1.67 \cdot 10^{-6}$
4.500	$3.48 \cdot 10^{-7}$	8.000	$2.08 \cdot 10^{-6}$
4.625	$3.17 \cdot 10^{-7}$	8.125	$2.25 \cdot 10^{-6}$
4.750	$2.78 \cdot 10^{-7}$	8.250	$2.86 \cdot 10^{-6}$
4.875	$2.56 \cdot 10^{-7}$	8.375	$3.65 \cdot 10^{-6}$
5.000	$2.36 \cdot 10^{-7}$	8.500	$4.48 \cdot 10^{-6}$
5.125	$2.11 \cdot 10^{-7}$	8.625	$5.59 \cdot 10^{-6}$
5.250	$2.07 \cdot 10^{-7}$	8.750	$6.99 \cdot 10^{-6}$
5.375	$2.12 \cdot 10^{-7}$	8.875	$8.75 \cdot 10^{-6}$

Table B.4.: Numerical values for the differential sensitivity flux normalisations $E^2\phi_0^{100\,\mathrm{TeV}}$ at 100 TeV in $\mathrm{GeV\,cm^{-2}\,s^{-1}}$. The values correspond to the differential performance curve shown in figure (7.3) for the injection model with spectral index $\gamma_{\mathrm{inj}} = 3$. The $\log_{10}(E_\nu/\mathrm{GeV})$ columns are the left energy bin borders. See table (B.3) for the flux values calculated with the injection index $\gamma_{\mathrm{inj}} = 2$. Note: the unweighted flux values are obtained by dividing by $(100\,\mathrm{TeV})^2$.

$\log_{10}(E_\nu/\mathrm{GeV})$	$\phi_0^{100\,\mathrm{TeV}}$	$\log_{10}(E_\nu/\mathrm{GeV})$	$\phi_0^{100\,\mathrm{TeV}}$
2.000	$6.37 \cdot 10^{-7}$	5.500	$7.49 \cdot 10^{-7}$
2.125	$2.27 \cdot 10^{-7}$	5.625	$1.04 \cdot 10^{-6}$
2.250	$1.12 \cdot 10^{-7}$	5.750	$1.48 \cdot 10^{-6}$
2.375	$7.01 \cdot 10^{-8}$	5.875	$2.08 \cdot 10^{-6}$
2.500	$5.01 \cdot 10^{-8}$	6.000	$3.04 \cdot 10^{-6}$
2.625	$4.13 \cdot 10^{-8}$	6.125	$4.46 \cdot 10^{-6}$
2.750	$3.65 \cdot 10^{-8}$	6.250	$6.91 \cdot 10^{-6}$
2.875	$3.35 \cdot 10^{-8}$	6.375	$9.77 \cdot 10^{-6}$
3.000	$3.19 \cdot 10^{-8}$	6.500	$1.49 \cdot 10^{-5}$
3.125	$3.29 \cdot 10^{-8}$	6.625	$2.18 \cdot 10^{-5}$
3.250	$3.35 \cdot 10^{-8}$	6.750	$3.39 \cdot 10^{-5}$
3.375	$3.60 \cdot 10^{-8}$	6.875	$4.91 \cdot 10^{-5}$
3.500	$3.93 \cdot 10^{-8}$	7.000	$7.32 \cdot 10^{-5}$
3.625	$4.46 \cdot 10^{-8}$	7.125	$1.09 \cdot 10^{-4}$
3.750	$5.14 \cdot 10^{-8}$	7.250	$1.76 \cdot 10^{-4}$
3.875	$5.92 \cdot 10^{-8}$	7.375	$2.33 \cdot 10^{-4}$
4.000	$6.85 \cdot 10^{-8}$	7.500	$3.93 \cdot 10^{-4}$
4.125	$7.82 \cdot 10^{-8}$	7.625	$6.13 \cdot 10^{-4}$
4.250	$9.23 \cdot 10^{-8}$	7.750	$9.35 \cdot 10^{-4}$
4.375	$1.10 \cdot 10^{-7}$	7.875	$1.40 \cdot 10^{-3}$
4.500	$1.27 \cdot 10^{-7}$	8.000	$2.35 \cdot 10^{-3}$
4.625	$1.54 \cdot 10^{-7}$	8.125	$3.47 \cdot 10^{-3}$
4.750	$1.78 \cdot 10^{-7}$	8.250	$6.02 \cdot 10^{-3}$
4.875	$2.26 \cdot 10^{-7}$	8.375	$9.91 \cdot 10^{-3}$
5.000	$2.60 \cdot 10^{-7}$	8.500	$1.55 \cdot 10^{-2}$
5.125	$3.20 \cdot 10^{-7}$	8.625	$2.65 \cdot 10^{-2}$
5.250	$4.17 \cdot 10^{-7}$	8.750	$4.54 \cdot 10^{-2}$
5.375	$5.69 \cdot 10^{-7}$	8.875	$7.44 \cdot 10^{-2}$

B.4. Discussion

This chapter includes additional figures for the discussion chapter.

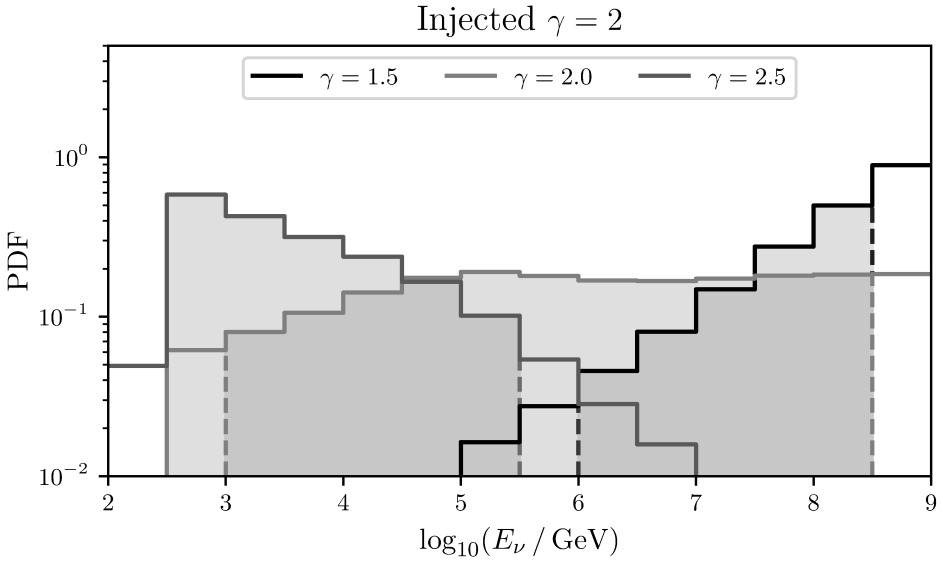

Figure B.51.: Weights constructed from the inverse differential performance curve for the largest time window in the time-dependent analysis, as shown in figure (6.6). The 90 % central interval is used to give an impression of the most sensitive region for each power-law hypothesis. See section 6.6 for a derivation of the formulas.

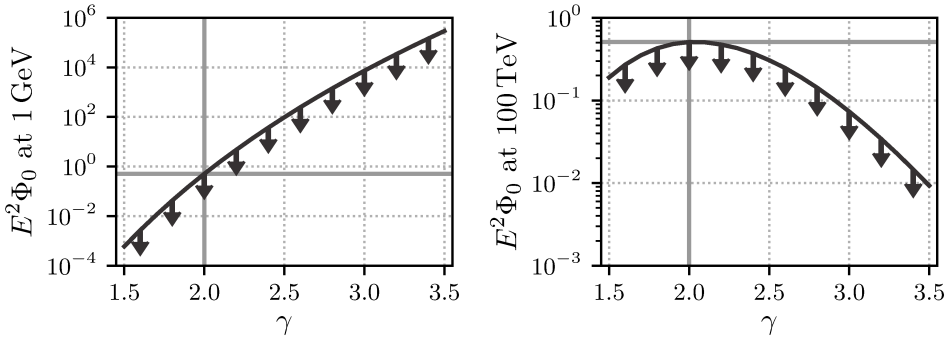

Figure B.52.: 90 % Neyman upper limits for the largest time window in the time-dependent analysis, scanned for a grid of power-laws with different spectral indices. The normalisations are shown at two different energies to be able to infer the spectral behaviour.

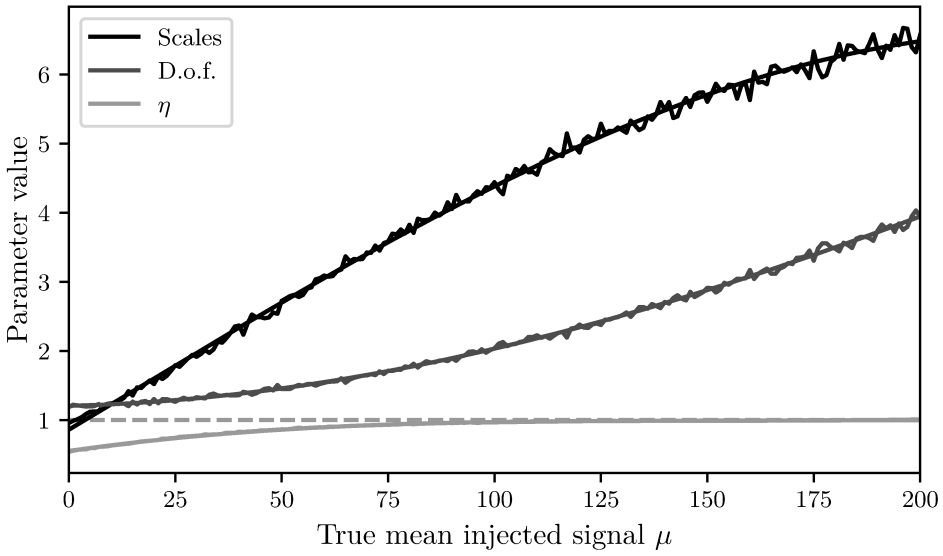

Figure B.53.: Smoothing spline fits to the discrete test statistic quantiles for the time-integrated analysis. The splines are evaluated to construct more smooth confidence intervals and upper limits than possible from the sampled data alone. The parameters are obtained by fitting the modified χ^2 PDF to each slice of the plane. The fit parameters are the number of non-zero trials η, the degrees of freedom d.o.f. and the scale of the distribution. The model is defined in formula (7.12).

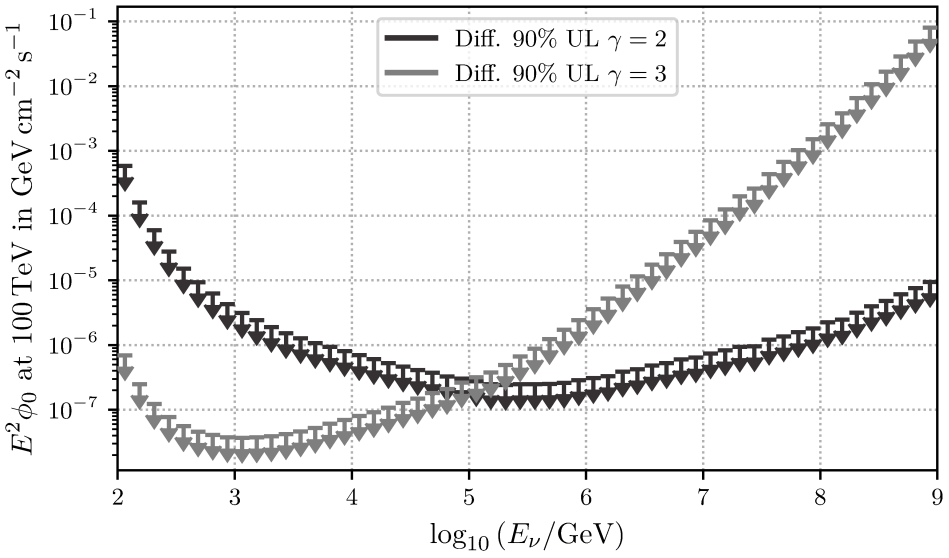

Figure B.54.: Differential limits for the time-integrated analysis for two injection spectra with indices $\gamma_{\text{inj}} = 2$ and $\gamma_{\text{inj}} = 3$. The differential limits are not directly comparable to other flux models, because they depend on the binning and the injection index but they can give an overview of the sensitive regions of the analysis. The bins are uniformly spaced in logarithmic neutrino energy with a width of one eight of a decade in order to minimize the spectral dependency in each bin.

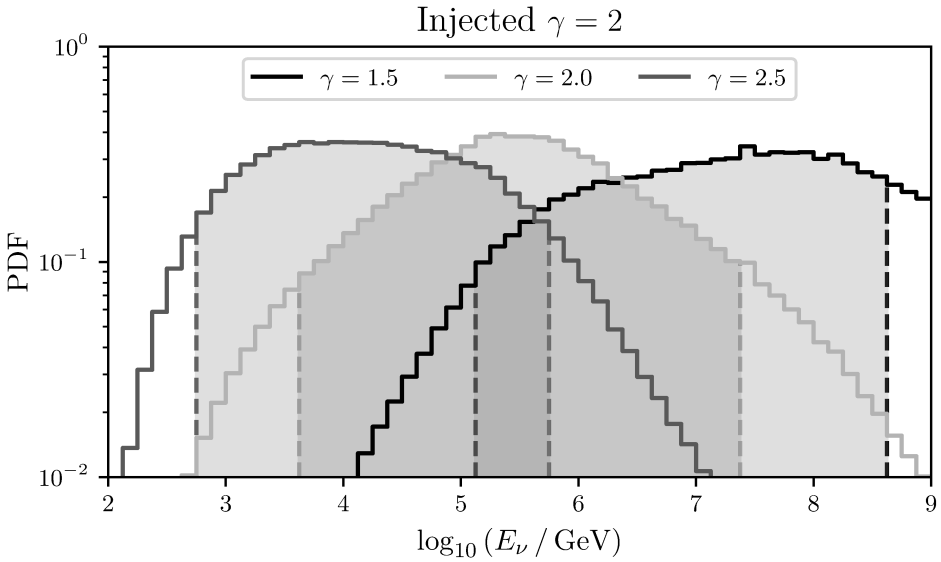

Figure B.55.: Weights constructed from the inverse differential performance curve for the injection index $\gamma_{\mathrm{inj}} = 2$ in the time-integrated analysis. The 90 % central interval is used to give an impression of the most sensitive region for each power-law hypothesis. See section 6.6 for a derivation of the formulas.

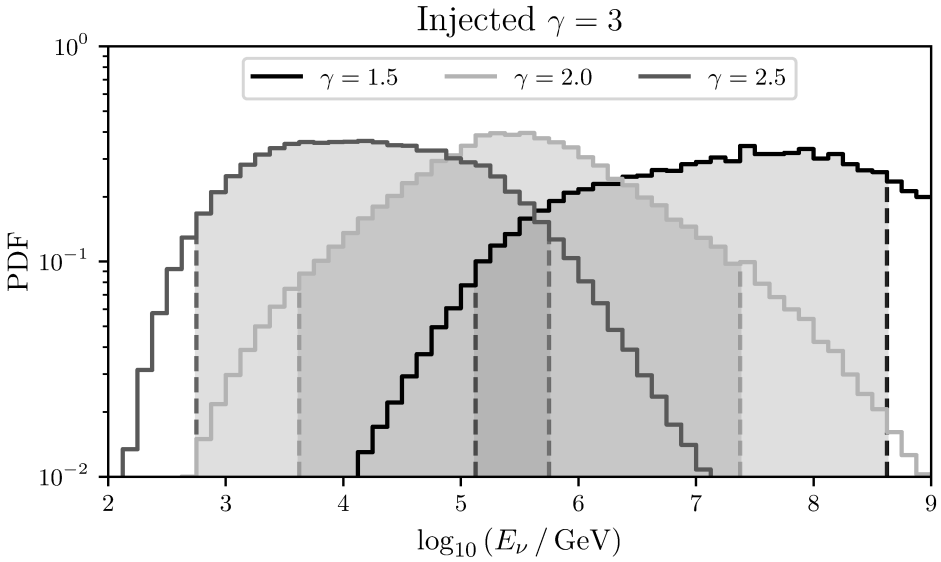

Figure B.56.: Weights constructed from the inverse differential performance curve for the injection index $\gamma_{\mathrm{inj}} = 3$ in the time-integrated analysis. The 90 % central interval is used to give an impression of the most sensitive region for each power-law hypothesis. See section 6.6 for a derivation of the formulas.

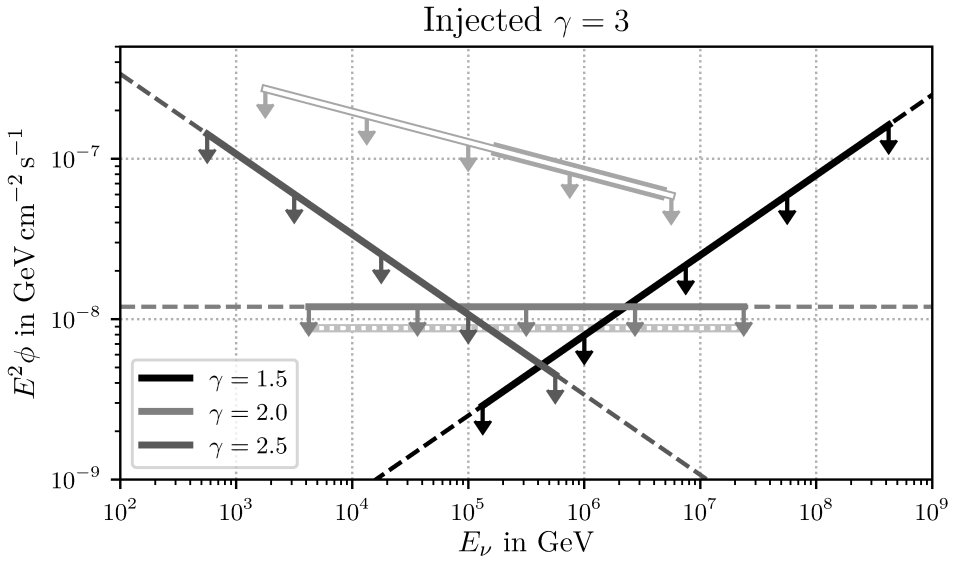

Figure B.57.: This analysis' power-law limits compared to limits derived from the diffuse muon neutrino track flux measurement in [HW18] and the all-sky point source search from [Aar+17a] using seven years of muon neutrino track data. The global limits are derived from the differential limits shown in figure (B.54) with an injection index of $\gamma_{\text{inj}} = 3$. The double light grey solid line shows the flux limits derived from the diffuse flux measurement scaled to a point source flux. The thicker portion of the line shows the valid region given in the original work, the thinner portion the 90 % central interval obtained from the differential flux limits. The double light grey dotted line shows the scaled sensitivity flux from the all-sky point source analysis.

Bibliography

[Chi11] Dmitry Chirkin. "Study of South Pole ice transparency with IceCube flashers". In: *Proceedings, 32nd International Cosmic Ray Conference (ICRC 2011): Beijing, China, August 11-18, 2011*. Vol. 4. 2011, p. 161. DOI: 10.7529/ICRC2011/V04/0333.

[Gai13] Thomas Gaisser. "Seasonal variation of atmospheric neutrinos in IceCube". In: *Proceedings, 33rd International Cosmic Ray Conference (ICRC2013): Rio de Janeiro, Brazil, July 2-9, 2013*. 2013, p. 0492. URL: http://www.cbpf.br/%7Eicrc2013/papers/icrc2013-0492.pdf.

[Aar+13a] M. G. Aartsen et al. "Evidence for High-Energy Extraterrestrial Neutrinos at the IceCube Detector". In: *Science* 342 (2013), p. 1242856. DOI: 10.1126/science.1242856. arXiv: 1311.5238 [astro-ph.HE].

[Aar+13b] M. G. Aartsen et al. "Measurement of South Pole ice transparency with the IceCube LED calibration system". In: *Nucl. Instrum. Meth.* A711 (2013), pp. 73–89. DOI: 10.1016/j.nima.2013.01.054. arXiv: 1301.5361 [astro-ph.IM].

[Aar+13c] M. G. Aartsen et al. "Probing the origin of cosmic rays with extremely high energy neutrinos using the IceCube Observatory". In: *Phys. Rev.* D88 (2013), p. 112008. DOI: 10.1103/PhysRevD.88.112008. arXiv: 1310.5477 [astro-ph.HE].

[Aar+13d] M. G. Aartsen et al. "Search for Time-independent Neutrino Emission from Astrophysical Sources with 3 yr of IceCube Data". In: *Astrophys. J.* 779 (2013), p. 132. DOI: 10.1088/0004-637X/779/2/132. arXiv: 1307.6669 [astro-ph.HE].

[Aar+14a] M. G. Aartsen et al. "Energy Reconstruction Methods in the IceCube Neutrino Telescope". In: *JINST* 9 (2014), P03009. DOI: 10.1088/1748-0221/9/03/P03009. arXiv: 1311.4767 [physics.ins-det].

[Aar+14b] M. G. Aartsen et al. "Observation of High-Energy Astrophysical Neutrinos in Three Years of IceCube Data". In: *Phys. Rev. Lett.* 113 (2014), p. 101101. DOI: 10.1103/PhysRevLett.113.101101. arXiv: 1405.5303 [astro-ph.HE].

[Aar+14c] M. G. Aartsen et al. "Observation of the cosmic-ray shadow of the Moon with IceCube". In: *Phys. Rev.* D89.10 (2014), p. 102004. DOI: 10.1103/PhysRevD.89.102004. arXiv: 1305.6811 [astro-ph.HE].

[Aar+15a] M. G. Aartsen et al. "Search for Prompt Neutrino Emission from Gamma-Ray Bursts with IceCube". In: *Astrophys. J.* 805.1 (2015), p. L5. DOI: 10.1088/2041-8205/805/1/L5. arXiv: 1412.6510 [astro-ph.HE].

[Aar+15b] M. G. Aartsen et al. "Searches for Time Dependent Neutrino Sources with IceCube Data from 2008 to 2012". In: *Astrophys. J.* 807.1 (2015), p. 46. DOI: 10.1088/0004-637X/807/1/46. arXiv: 1503.00598 [astro-ph.HE].

[Aar+16a] M. G. Aartsen et al. "An All-Sky Search for Three Flavors of Neutrinos from Gamma-Ray Bursts with the IceCube Neutrino Observatory". In: *Astrophys. J.* 824.2 (2016), p. 115. DOI: 10.3847/0004-637X/824/2/115. arXiv: 1601.06484 [astro-ph.HE].

[Aar+16b] M. G. Aartsen et al. "Constraints on Ultrahigh-Energy Cosmic-Ray Sources from a Search for Neutrinos above 10 PeV with IceCube". In: *Phys. Rev. Lett.* 117.24 (2016). [Erratum: Phys. Rev. Lett.119,no.25,259902(2017)], p. 241101. DOI: 10.1103/PhysRevLett.117.241101. arXiv: 1607.05886 [astro-ph.HE].

[Aar+16c] M. G. Aartsen et al. "Lowering IceCube's Energy Threshold for Point Source Searches in the Southern Sky". In: *Astrophys. J.* 824.2 (2016), p. L28. DOI: 10.3847/2041-8205/824/2/L28. arXiv: 1605.00163 [astro-ph.HE].

[Aar+16d] M. G. Aartsen et al. "Search for correlations between the arrival directions of IceCube neutrino events and ultrahigh-energy cosmic rays detected by the Pierre Auger Observatory and the Telescope Array". In: *JCAP* 1601.01 (2016), p. 037. DOI: 10.1088/1475-7516/2016/01/037. arXiv: 1511.09408 [astro-ph.HE].

[Aar+16e] M. G. Aartsen et al. "Very High-Energy Gamma-Ray Follow-Up Program Using Neutrino Triggers from IceCube". In: *JINST* 11.11 (2016), P11009. DOI: 10.1088/1748-0221/11/11/P11009. arXiv: 1610.01814 [hep-ex].

[Aar+17a] M. G. Aartsen et al. "All-sky Search for Time-integrated Neutrino Emission from Astrophysical Sources with 7 yr of IceCube Data". In: *Astrophys. J.* 835.2 (2017), p. 151. DOI: 10.3847/1538-4357/835/2/151. arXiv: 1609.04981 [astro-ph.HE].

[Aar+17b] M. G. Aartsen et al. "Constraints on Galactic Neutrino Emission with Seven Years of IceCube Data". In: *Astrophys. J.* 849.1 (2017), p. 67. DOI: 10.3847/1538-4357/aa8dfb. arXiv: 1707.03416 [astro-ph.HE].

[Aar+17c] M. G. Aartsen et al. "Extending the search for muon neutrinos coincident with gamma-ray bursts in IceCube data". In: *Astrophys. J.* 843.2 (2017), p. 112. DOI: 10.3847/1538-4357/aa7569. arXiv: 1702.06868 [astro-ph.HE].

[Aar+17d] M. G. Aartsen et al. "The contribution of Fermi-2LAC blazars to the diffuse TeV-PeV neutrino flux". In: *Astrophys. J.* 835.1 (2017), p. 45. DOI: 10.3847/1538-4357/835/1/45. arXiv: 1611.03874 [astro-ph.HE].

[Aar+17e] M. G. Aartsen et al. "The IceCube Neutrino Observatory: Instrumentation and Online Systems". In: *JINST* 12.03 (2017), P03012. DOI: 10.1088/1748-0221/12/03/P03012. arXiv: 1612.05093 [astro-ph.IM].

[Aar+17f] M. G. Aartsen et al. "The IceCube Realtime Alert System". In: *Astropart. Phys.* 92 (2017), pp. 30–41. DOI: 10.1016/j.astropartphys.2017.05.002. arXiv: 1612.06028 [astro-ph.HE].

[Aar+18a] M. G. Aartsen et al. "A Search for Neutrino Emission from Fast Radio Bursts with Six Years of IceCube Data". In: *Astrophys. J.* 857.2 (2018), p. 117. DOI: 10.3847/1538-4357/aab4f8. arXiv: 1712.06277 [astro-ph.HE].

[Aar+18b] M. G. Aartsen et al. "Multimessenger observations of a flaring blazar coincident with high-energy neutrino IceCube-170922A". In: *Science* 361.6398 (2018), eaat1378. DOI: 10.1126/science.aat1378. arXiv: 1807.08816 [astro-ph.HE].

[Aar+18c] M. G. Aartsen et al. "Neutrino emission from the direction of the blazar TXS 0506+056 prior to the IceCube-170922A alert". In: *Science* 361.6398 (2018), pp. 147–151. DOI: 10.1126/science.aat2890. arXiv: 1807.08794 [astro-ph.HE].

[Aar+14d] M. G. Aartsen et al. "Searches for Extended and Point-like Neutrino Sources with Four Years of IceCube Data". In: ApJ 796, 109 (Dec. 2014), p. 109. DOI: 10.1088/0004-637X/796/2/109. arXiv: 1406.6757 [astro-ph.HE].

[Abb+09] R. Abbasi et al. "Search for high-energy muon neutrinos from the 'naked-eye' GRB 080319B with the IceCube neutrino telescope". In: *Astrophys. J.* 701 (2009). [Erratum: Astrophys. J.708,911(2010)], pp. 1721–1731. DOI: 10.1088/0004-637X/701/2/1721,10.1088/0004-637X/708/1/911. arXiv: 0902.0131 [astro-ph.HE].

[Abb+12] R. Abbasi et al. "An absence of neutrinos associated with cosmic-ray acceleration in γ-ray bursts". In: *Nature* 484 (2012), pp. 351–353. DOI: 10.1038/nature11068. arXiv: 1204.4219 [astro-ph.HE].

[Abb+13] R. Abbasi et al. "IceTop: The surface component of IceCube". In: *Nucl. Instrum. Meth.* A700 (2013), pp. 188–220. DOI: 10.1016/j.nima.2012.10.067. arXiv: 1207.6326 [astro-ph.IM].

[Abb+10] R. Abbasi et al. "Search for Muon Neutrinos from Gamma-ray Bursts with the IceCube Neutrino Telescope". In: ApJ 710 (Feb. 2010), pp. 346–359. DOI: 10.1088/0004-637X/710/1/346. arXiv: 0907.2227 [astro-ph.HE].

[Abb+16] B. P. Abbott et al. "Observation of Gravitational Waves from a Binary Black Hole Merger". In: *Phys. Rev. Lett.* 116.6 (2016), p. 061102. DOI: 10.1103/PhysRevLett.116.061102. arXiv: 1602.03837 [gr-qc].

[Abb+17] B. P. Abbott et al. "GW170817: Observation of Gravitational Waves from a Binary Neutron Star Inspiral". In: *Phys. Rev. Lett.* 119.16 (2017), p. 161101. DOI: 10.1103/PhysRevLett.119.161101. arXiv: 1710.05832 [gr-qc].

[Abr+09] J. Abraham et al. "The Fluorescence Detector of the Pierre Auger Observatory". In: July 2009. arXiv: 0907.4282 [astro-ph.IM].

[AS74] M. Abramowitz and I. A. Stegun. *Handbook of Mathematical Functions, With Formulas, Graphs, and Mathematical Tables,* New York, NY, USA: Dover Publications, Inc., 1974. ISBN: 0486612724.

[Ada+16] R. Adam et al. "Planck 2015 results. I. Overview of products and scientific results". In: *Astron. Astrophys.* 594 (2016), A1. DOI: 10.1051/0004-6361/201527101. arXiv: 1502.01582 [astro-ph.CO].

[Adr+16a] S. Adrian-Martinez et al. "High-energy Neutrino follow-up search of Gravitational Wave Event GW150914 with ANTARES and IceCube". In: *Phys. Rev.* D93.12 (2016), p. 122010. DOI: 10.1103/PhysRevD.93.122010. arXiv: 1602.05411 [astro-ph.HE].

[Adr+16b] S. Adrian-Martinez et al. "The First Combined Search for Neutrino Point-sources in the Southern Hemisphere With the Antares and Icecube Neutrino Telescopes". In: *Astrophys. J.* 823.1 (2016), p. 65. DOI: 10.3847/0004-637X/823/1/65. arXiv: 1511.02149 [hep-ex].

[AH14] Markus Ahlers and Francis Halzen. "Pinpointing Extragalactic Neutrino Sources in Light of Recent IceCube Observations". In: *Phys. Rev.* D90.4 (2014), p. 043005. DOI: 10.1103/PhysRevD.90.043005. arXiv: 1406.2160 [astro-ph.HE].

[Ahr+04] J. Ahrens et al. "Muon track reconstruction and data selection techniques in AMANDA". In: *Nucl. Instrum. Meth.* A524 (2004), pp. 169–194. DOI: 10.1016/j.nima.2004.01.065. arXiv: astro-ph/0407044 [astro-ph].

[Aje+17] M. Ajello et al. "3FHL: The Third Catalog of Hard Fermi-LAT Sources". In: *Astrophys. J. Suppl.* 232.2 (2017), p. 18. DOI: 10.3847/1538-4365/aa8221. arXiv: 1702.00664 [astro-ph.HE].

[All+08] I. Allekotte et al. "The Surface Detector System of the Pierre Auger Observatory". In: *Nucl. Instrum. Meth.* A586 (2008), pp. 409–420. DOI: 10.1016/j.nima.2007.12.016. arXiv: 0712.2832 [astro-ph].

[Anc+14] Luis A. Anchordoqui et al. "Cosmic Neutrino Pevatrons: A Brand New Pathway to Astronomy, Astrophysics, and Particle Physics". In: *JHEAp* 1-2 (2014), pp. 1–30. DOI: 10.1016/j.jheap.2014.01.001. arXiv: 1312.6587 [astro-ph.HE].

[Ans+16] Stefano Ansoldi et al. "MAGIC electromagnetic follow-up of gravitational wave alerts". In: *IAU Symp.* 324 (2016), pp. 287–290. DOI: 10.1017/S1743921317001430.

[Arg+18] Carlos A. Argüelles et al. "Unified atmospheric neutrino passing fractions for large-scale neutrino telescopes". In: *JCAP* 1807.07 (2018), p. 047. DOI: 10.1088/1475-7516/2018/07/047. arXiv: 1805.11003 [hep-ph].

[AJY00] H. Athar, M. Jezabek, and O. Yasuda. "Effects of neutrino mixing on high-energy cosmic neutrino flux". In: *Phys. Rev.* D62 (2000), p. 103007. DOI: 10.1103/PhysRevD.62.103007. arXiv: hep-ph/0005104 [hep-ph].

[AKL06] H. Athar, C. S. Kim, and Jake Lee. "The Intrinsic and oscillated astrophysical neutrino flavor ratios". In: *Mod. Phys. Lett.* A21 (2006), pp. 1049–1066. DOI: 10.1142/S021773230602038X. arXiv: hep-ph/0505017 [hep-ph].

[Bar97] Matthew G. Baring. "Diffusive shock acceleration: The Fermi mechanism". In: *Very high-energy phenomena in the universe. Proceedings, 32nd Rencontres de Moriond, Les Arcs, France, January 18-25, 1997*. 1997, pp. 97–106. arXiv: astro-ph/9711177 [astro-ph].

[Bar89] Roger J Barlow. *Statistics: a guide to the use of statistical methods in the physical sciences*. Vol. 29. John Wiley & Sons, 1989.

[Bar+52] Paul H. Barrett et al. "Interpretation of Cosmic-Ray Measurements Far Underground". In: *Rev. Mod. Phys.* 24 (3 July 1952), pp. 133–178. DOI: 10.1103/RevModPhys.24.133. URL: https://link.aps.org/doi/10.1103/RevModPhys.24.133.

[Bay+10] R. C. Bay et al. "South Pole paleowind from automated synthesis of ice core records". In: *Journal of Geophysical Research (Atmospheres)* 115.D14, D14126 (July 2010), p. D14126. DOI: 10.1029/2009JD013741.

[BS13] Volker Beckmann and Chris R. Shrader. "The AGN phenomenon: open issues". In: *Proceedings: 9th INTEGRAL Workshop* (2013). arXiv: 1302.1397 [astro-ph.HE].

[Bel78a] A. R. Bell. "The acceleration of cosmic rays in shock fronts – II". In: *Monthly Notices of the Royal Astronomical Society* 182.3 (Mar. 1978), pp. 443–455. DOI: 10.1093/mnras/182.3.443.

[Bel78b] A. R. Bell. "The acceleration of cosmic rays in shock fronts. I". In: MNRAS 182 (Feb. 1978), pp. 147–156. DOI: 10.1093/mnras/182.2.147.

[Bia+07] Carlo Luciano Bianco et al. "The Fireshell model and the canonical GRB scenario". In: *AIP Conf. Proc.* 966 (2007), pp. 12–15. DOI: 10.1063/1.2836983. arXiv: 0712.0495 [astro-ph].

[BSY14] Roger Blandford, Paul Simeon, and Yajie Yuan. "Cosmic Ray Origins: An Introduction". In: *Nuclear Physics B - Proceedings Supplements* 256-257 (2014). Cosmic Ray Origin – Beyond the Standard Models, pp. 9–22. ISSN: 0920-5632. DOI: https://doi.org/10.1016/j.nuclphysbps.2014.10.002.

[BL13] Volker Blobel and Erich Lohrmann. *Statistische und numerische Methoden der Datenanalyse*. Springer-Verlag, 2013.

[BZ14] G. Bohm and G. Zech. "Statistics of weighted Poisson events and its applications". In: *Nuclear Instruments and Methods in Physics Research Section A: Accelerators, Spectrometers, Detectors and Associated Equipment* 748 (2014), pp. 1–6. ISSN: 0168-9002. DOI: https://doi.org/10.1016/j.nima.2014.02.021.

[BZ10] Gerhard Bohm and Günter Zech. *Introduction to statistics and data analysis for physicists*. Vol. 1. DESY Hamburg, 2010.

[Bos+15] F. Bos et al. "Observation of the Cosmic-Ray Shadow of the Moon and Sun with IceCube". In: *ASTRA Proceedings* 2 (2015), pp. 5–8. DOI: 10.5194/ap-2-5-2015. URL: https://www.astra-proc.net/2/5/2015/.

[Bra16] M. Branchesi. "Multi-messenger astronomy: gravitational waves, neutrinos, photons, and cosmic rays". In: *Journal of Physics Conference Series*. Vol. 718. Journal of Physics Conference Series. May 2016, p. 022004. DOI: 10.1088/1742-6596/718/2/022004.

[Bra+10] J. Braun et al. "Time-dependent point source search methods in high energy neutrino astronomy". In: *Astroparticle Physics* 33 (Apr. 2010), pp. 175–181. DOI: 10.1016/j.astropartphys.2010.01.005. arXiv: 0912.1572 [astro-ph.IM].

[Bra+08] Jim Braun et al. "Methods for point source analysis in high energy neutrino telescopes". In: *Astropart. Phys.* 29 (2008), pp. 299–305. DOI: 10.1016/j.astropartphys.2008.02.007. arXiv: 0801.1604 [astro-ph].

[Bro14] Paul A. Bromiley. *Products and Convolutions of Gaussian Probability Density Functions*. Tech. rep. 2014. URL: https://www.semanticscholar.org/paper/Products-and-Convolutions-of-Gaussian-Probability-Bromiley/1dd7cbfe3eb496c73d560b52e68cb0526a5be12f.

[CB02] George Casella and Roger L Berger. *Statistical inference*. Vol. 2. Duxbury Pacific Grove, CA, 2002.

[Cas+14] K.A. Casey et al. "The 1500 m South Pole ice core: recovering a 40 ka environmental record". In: *Annals of Glaciology* 55.68 (2014), pp. 137–146. DOI: 10.3189/2014AoG68A016.

[Che37] P. A. Cherenkov. "Visible Radiation Produced by Electrons Moving in a Medium with Velocities Exceeding that of Light". In: *Phys. Rev.* 52 (4 Aug. 1937), pp. 378–379. DOI: 10.1103/PhysRev.52.378.

[Cir08] Vanessa Cirkel-Bartelt. "History of Astroparticle Physics and its Components". In: *Living Reviews in Relativity* 11.1 (May 2008), p. 2. ISSN: 1433-8351. DOI: 10.12942/lrr-2008-2.

[Coe17] Stefan Coenders. *skylab*. June 2017. URL: https://github.com/coenders/skylab.

[Col18] IceCube Collaboration/NSF. *IceCube Neutrino Telescope Diagrams*. 2018. URL: http://gallery.icecube.wisc.edu/web/var/albums/WWW_GALLERY/Diagrams/1-blueTopArray_black.jpg?m=1425997119 (visited on 09/06/2018).

[CMS11] Amanda Cooper-Sarkar, Philipp Mertsch, and Subir Sarkar. "The high energy neutrino cross-section in the Standard Model and its uncertainty". In: *JHEP* 08 (2011), p. 042. DOI: 10.1007/JHEP08(2011)042. arXiv: 1106.3723 [hep-ph].

[CI07] D. F. Cowen and Ice Cube Collaboration. "Tau Neutrinos in IceCube". In: *Journal of Physics Conference Series*. Ed. by F. Halzen, A. Karle, and T. Montaruli. Vol. 60. Journal of Physics Conference Series. Mar. 2007, pp. 227–230. DOI: 10.1088/1742-6596/60/1/048.

[Dal+17] Neal Dalal et al. *Fundamental Physics with the Hubble Space Telescope*. 2017. arXiv: 1712.04928 [astro-ph.CO].

[Der07] Charles D. Dermer. "Best-Bet Astrophysical Neutrino Sources". In: *J. Phys. Conf. Ser.* 60 (2007), pp. 8–13. DOI: 10.1088/1742-6596/60/1/002. arXiv: astro-ph/0611191 [astro-ph].

[DG16] Charles Dennison Dermer and Berrie Giebels. "Active galactic nuclei at gamma-ray energies". In: *Comptes Rendus Physique* 17 (2016), pp. 594–616. DOI: 10.1016/j.crhy.2016.04.004. arXiv: 1602.06592 [astro-ph.HE].

[DG10] Paolo Desiati and Thomas K. Gaisser. "Seasonal Variation of Atmospheric Leptons as a Probe of Charm". In: *Phys. Rev. Lett.* 105 (12 Sept. 2010), p. 121102. DOI: 10.1103/PhysRevLett.105.121102.

[ESR12] B. Eichmann, R. Schlickeiser, and W. Rhode. "On the Duration of Blazar Synchrotron Flares". In: *The Astrophysical Journal* 744.2 (2012), p. 153. URL: http://stacks.iop.org/0004-637X/744/i=2/a=153.

[ERS08] Rikard Enberg, Mary Hall Reno, and Ina Sarcevic. "Prompt neutrino fluxes from atmospheric charm". In: *Phys. Rev. D* 78 (4 Aug. 2008), p. 043005. DOI: 10.1103/PhysRevD.78.043005.

[Fer49] Enrico Fermi. "On the Origin of the Cosmic Radiation". In: *Phys. Rev.* 75 (8 Apr. 1949), pp. 1169–1174. DOI: 10.1103/PhysRev.75.1169.

[FS82] H E Fisk and F Sciulli. "Charged-Current Neutrino Interactions". In: *Annual Review of Nuclear and Particle Science* 32.1 (1982), pp. 499–573. eprint: https://doi.org/10.1146/annurev.ns.32.120182.002435.

[FGS97] G. M. Frichter, T. K. Gaisser, and T. Stanev. "Inelasticity in p - nucleus collisions and its application to high-energy cosmic ray cascades". In: *Phys. Rev.* D56 (1997), pp. 3135–3142. DOI: 10.1103/PhysRevD.56.3135. arXiv: astro-ph/9704061 [astro-ph].

[Gai90] T. K. Gaisser. *Cosmic rays and particle physics*. 1990. ISBN: 9780521339315. URL: http://www.cambridge.org/uk/catalogue/catalogue.asp?isbn=0521326672.

[Gai10] T. K. Gaisser. "Cosmic rays: current status, historical context". In: *ArXiv e-prints* (Oct. 2010). arXiv: 1010.5996 [astro-ph.HE].

[GH02] T. K. Gaisser and M. Honda. "Flux of atmospheric neutrinos". In: *Ann. Rev. Nucl. Part. Sci.* 52 (2002), pp. 153–199. DOI: 10.1146/annurev.nucl.52.050102.090645. arXiv: hep-ph/0203272 [hep-ph].

[Gai12] Thomas K. Gaisser. "Spectrum of cosmic-ray nucleons, kaon production, and the atmospheric muon charge ratio". In: *Astroparticle Physics* 35.12 (2012), pp. 801–806. ISSN: 0927-6505. DOI: https://doi.org/10.1016/j.astropartphys.2012.02.010.

[GER16] Thomas K. Gaisser, Ralph Engel, and Elisa Resconi. *Cosmic Rays and Particle Physics*. Cambridge University Press, 2016. ISBN: 9781316598917. URL: http://www.cambridge.org/de/academic/subjects/physics/cosmology-relativity-and-gravitation/cosmic-rays-and-particle-physics-2nd-edition?format=HB.

[GST13] Thomas K. Gaisser, Todor Stanev, and Serap Tilav. "Cosmic Ray Energy Spectrum from Measurements of Air Showers". In: *Front. Phys.(Beijing)* 8 (2013), pp. 748–758. DOI: 10.1007/s11467-013-0319-7. arXiv: 1303.3565 [astro-ph.HE].

[Gan+96] Raj Gandhi et al. "Ultrahigh-energy neutrino interactions". In: *Astropart. Phys.* 5 (1996), pp. 81–110. DOI: 10.1016/0927-6505(96)00008-4. arXiv: hep-ph/9512364 [hep-ph].

[Gao+18] Shan Gao et al. *Interpretation of the coincident observation of a high energy neutrino and a bright flare*. 2018. arXiv: 1807.04275 [astro-ph.HE].

[GK05] Askhat Gazizov and Marek P. Kowalski. "ANIS: High energy neutrino generator for neutrino telescopes". In: *Comput. Phys. Commun.* 172 (2005), pp. 203–213. DOI: 10.1016/j.cpc.2005.03.113. arXiv: astro-ph/0406439 [astro-ph].

[Gil+09] R. C. Gilmore et al. "GeV gamma-ray attenuation and the high-redshift UV background". In: MNRAS 399 (Nov. 2009), pp. 1694–1708. DOI: 10.1111/j.1365-2966.2009.15392.x. arXiv: 0905.1144.

[Gio09] F. Giovannelli. "Astroparticle physics (a short review)". In: *Frontier Objects in Astrophysics and Particle Physics*. Ed. by F. Giovannelli and G. Mannocchi. 2009, p. 3.

[Gol02] A. Goldschmidt. "Scientific Goals of the IceCube Neutrino Detector at the South Pole". In: *Nuclear Physics B - Proceedings Supplements* 110 (2002), pp. 516–518. ISSN: 0920-5632. DOI: https://doi.org/10.1016/S0920-5632(02)01552-9.

[GF17] B. P. Gompertz and A. S. Fruchter. "Magnetars in Ultra-Long Gamma-Ray Bursts and GRB 111209A". In: *Astrophys. J.* 839.1 (2017), p. 49. DOI: 10.3847/1538-4357/aa6629. arXiv: 1702.05507 [astro-ph.HE].

[GIT96] P. Gondolo, G. Ingelman, and M. Thunman. "Charm production and high-energy atmospheric muon and neutrino fluxes". In: *Astropart. Phys.* 5 (1996), pp. 309–332. DOI: 10.1016/0927-6505(96)00033-3. arXiv: hep-ph/9505417 [hep-ph].

[Goo+07] Rene W. Goosmann et al. "X-ray variability of AGN and the flare model". In: *ASP Conf. Ser.* 360 (2007), p. 277. arXiv: astro-ph/0410079 [astro-ph].

[Gor+05] K. M. Gorski et al. "HEALPix - A Framework for high resolution discretization, and fast analysis of data distributed on the sphere". In: *Astrophys. J.* 622 (2005), pp. 759–771. DOI: 10.1086/427976. arXiv: astro-ph/0409513 [astro-ph].

[Gra+10] E.W. Grashorn et al. "The atmospheric charged kaon/pion ratio using seasonal variation methods". In: *Astroparticle Physics* 33.3 (2010), pp. 140–145. ISSN: 0927-6505. DOI: https://doi.org/10.1016/j.astropartphys.2009.12.006.

[GV10] Eilam Gross and Ofer Vitells. "Trial factors for the look elsewhere effect in high energy physics". In: *Eur. Phys. J.* C70 (2010), pp. 525–530. DOI: 10.1140/epjc/s10052-010-1470-8. arXiv: 1005.1891 [physics.data-an].

[Gru05] C. Grupen. *Astroparticle physics*. Springer, 2005. ISBN: 9783540253129. URL: http://www.springer.com/book/3-540-25312-2.

[HW18] Christian Haack and Christopher Wiebusch. "A measurement of the diffuse astrophysical muon neutrino flux using eight years of IceCube data." In: *PoS* ICRC2017 (2018), p. 1005. DOI: 10.22323/1.301.1005.

[Hal16] Francis Halzen. "High-energy neutrino astrophysics". In: *Nature Phys.* 13.3 (2016), pp. 232–238. DOI: 10.1038/nphys3816.

[Her99] M. Herrero. "The Standard model". In: *NATO Sci. Ser. C* 534 (1999), pp. 1–59. DOI: 10.1007/978-94-011-4689-0_1. arXiv: hep-ph/9812242 [hep-ph].

[Hes17] J. W. T. Hessels. "Fast Radio Bursts and their Possible Neutron Star Origins". In: *J. Phys. Conf. Ser.* 932 (2017), p. 012025. arXiv: 1804.06149 [astro-ph.HE].

[Hoh+92] C. Y. Hohenkerk et al. *Explanatory Supplement to the Astronomical Almanac.* University Science Books, 1992.

[Hör03] Joerg R. Hörandel. "On the knee in the energy spectrum of cosmic rays". In: *Astropart. Phys.* 19 (2003), pp. 193–220. DOI: 10.1016/S0927-6505(02)00198-6. arXiv: astro-ph/0210453 [astro-ph].

[Hör16] Jörg R. Hörandel. "Radio detection of air showers with LOFAR and AERA". In: *JPS Conf. Proc.* 9 (2016), p. 010004. DOI: 10.7566/JPSCP.9.010004. arXiv: 1509.04960 [astro-ph.HE].

[Hor77] Susan Dadakis Horn. "Goodness-of-Fit Tests for Discrete Data: A Review and an Application to a Health Impairment Scale". In: *Biometrics* 33.1 (1977), pp. 237–247. ISSN: 0006341X, 15410420. DOI: 10.2307/2529319.

[Hub+16] Martin C. E. Huber et al. *Observing Photons in Space: A Guide to Experimental Space Astronomy.* 2nd. Springer Publishing Company, Incorporated, 2016. ISBN: 9781493946617.

[HK18] Matthias Huber and Kai Krings. "Results of IceCube searches for neutrinos from blazars using seven years of through-going muon data". In: *PoS* ICRC2017 (2018), p. 994. DOI: 10.22323/1.301.0994.

[Hun07] J. D. Hunter. "Matplotlib: A 2D graphics environment". In: *Computing In Science & Engineering* 9.3 (2007), pp. 90–95. DOI: 10.1109/MCSE.2007.55.

[Jak12] Wenzel Jakob. *Numerically stable sampling of the von Mises-Fisher distribution on S^2 (and other tricks).* 2012. URL: http://www.mitsuba-renderer.org/~wenzel/files/vmf.pdf.

[JB12] O. Jamil and M. Böttcher. "An Angle-dependent Synchrotron Self-Compton Model for Relativistic Jet Sources". In: ApJ 759, 45 (Nov. 2012), p. 45. DOI: 10.1088/0004-637X/759/1/45. arXiv: 1209.2711 [astro-ph.HE].

[Jar+11] N. Jarosik et al. "Seven-Year Wilkinson Microwave Anisotropy Probe (WMAP) Observations: Sky Maps, Systematic Errors, and Basic Results". In: *Astrophys. J. Suppl.* 192 (2011), p. 14. DOI: 10.1088/0067-0049/192/2/14. arXiv: 1001.4744 [astro-ph.CO].

[JOP+01] Eric Jones, Travis Oliphant, Pearu Peterson, et al. *SciPy: Open source scientific tools for Python*. 2001. URL: http://www.scipy.org/.

[Kat16] J. I. Katz. "Fast radio bursts — A brief review: Some questions, fewer answers". In: *Mod. Phys. Lett.* A31.14 (2016), p. 1630013. DOI: 10.1142/S0217732316300135. arXiv: 1604.01799 [astro-ph.HE].

[KS12] U. F. Katz and Ch. Spiering. "High-Energy Neutrino Astrophysics: Status and Perspectives". In: *Prog. Part. Nucl. Phys.* 67 (2012), pp. 651–704. DOI: 10.1016/j.ppnp.2011.12.001. arXiv: 1111.0507 [astro-ph.HE].

[Kei+18] A. Keivani et al. "A Multimessenger Picture of the Flaring Blazar TXS 0506+056: implications for High-Energy Neutrino Emission and Cosmic Ray Acceleration". In: ApJ 864 (84 2018). DOI: 10.3847/1538-4357/aad59a. arXiv: 1807.04537 [astro-ph.HE].

[Ken82] John T. Kent. "The Fisher-Bingham Distribution on the Sphere". In: *Journal of the Royal Statistical Society. Series B (Methodological)* 44.1 (1982), pp. 71–80. ISSN: 00359246. URL: http://www.jstor.org/stable/2984712.

[Koe+13] J.-H. Koehne et al. "PROPOSAL: A tool for propagation of charged leptons". In: *Computer Physics Communications* 184.9 (2013), pp. 2070–2090. ISSN: 0010-4655. DOI: https://doi.org/10.1016/j.cpc.2013.04.001.

[Kom15] S. Komossa. "Tidal disruption of stars by supermassive black holes: Status of observations". In: *JHEAp* 7 (2015), pp. 148–157. DOI: 10.1016/j.jheap.2015.04.006. arXiv: 1505.01093 [astro-ph.HE].

[Kop18] Claudio Kopper. "Observation of Astrophysical Neutrinos in Six Years of IceCube Data". In: *PoS* ICRC2017 (2018), p. 981. DOI: 10.22323/1.301.0981.

[KGK16] Claudio Kopper, William Giang, and Naoko Kurahashi. "Observation of Astrophysical Neutrinos in Four Years of IceCube Data". In: *PoS* ICRC2015 (2016), p. 1081. DOI: 10.22323/1.236.1081.

[Kow15] Marek Kowalski. "Status of High-Energy Neutrino Astronomy". In: *J. Phys. Conf. Ser.* 632.1 (2015), p. 012039. DOI: 10.1088/1742-6596/632/1/012039. arXiv: 1411.4385 [astro-ph.HE].

[Lal12] M. D. Lallo. "Experience with the Hubble Space Telescope: 20 years of an archetype". In: *Optical Engineering* 51.1, 011011-011011-19 (Jan. 2012). DOI: 10.1117/1.OE.51.1.011011. arXiv: 1203.0002 [astro-ph.IM].

[Lau15] R. J. Lauer. "First results from HAWC: monitoring the TeV gamma-ray sky". In: *Extragalactic Jets from Every Angle*. Ed. by F. Massaro et al. Vol. 313. IAU Symposium. Mar. 2015, pp. 70–75. DOI: 10.1017/S1743921315001891.

[LM00] J. G. Learned and K. Mannheim. "High-energy neutrino astrophysics". In: *Ann. Rev. Nucl. Part. Sci.* 50 (2000), pp. 679–749. DOI: 10.1146/annurev.nucl.50.1.679.

[LM83] T.-P. Li and Y.-Q. Ma. "Analysis methods for results in gamma-ray astronomy". In: ApJ 272 (Sept. 1983), pp. 317–324. DOI: 10.1086/161295.

[Lip08] Paolo Lipari. "Proton and Neutrino Extragalactic Astronomy". In: *Phys. Rev.* D78 (2008), p. 083011. DOI: 10.1103/PhysRevD.78.083011. arXiv: 0808.0344 [astro-ph].

[Liu+18] Jun Liu et al. "Effelsberg Monitoring of a Sample of RadioAstron Blazars: Analysis of Intra-Day Variability". In: *Galaxies* 6 (2018), p. 49. DOI: 10.3390/galaxies6020049. arXiv: 1804.09289 [astro-ph.GA].

[MD01] M. A. Malkov and P. H. Diamond. "Modern theory of Fermi acceleration: a new challenge to plasma physics". In: *Phys. Plasmas* 8 (2001), p. 2401. DOI: 10.1063/1.1345507. arXiv: astro-ph/0102373 [astro-ph].

[Mar60] M. A. Markov. "On high energy neutrino physics". In: *Proceedings, 10th International Conference on High-Energy Physics (ICHEP 60): Rochester, NY, USA, 25 Aug - 1 Sep 1960*. 1960, pp. 578–581.

[Mat+18] S. Mattila et al. "A dust-enshrouded tidal disruption event with a resolved radio jet in a galaxy merger". In: *Science* 361 (2018), p. 482. DOI: 10.1126/science.aao4669. arXiv: 1806.05717 [astro-ph.GA].

[Mea58] C. A. Mead. "Quantum Theory of the Refractive Index". In: *Phys. Rev.* 110 (2 Apr. 1958), pp. 359–369. DOI: 10.1103/PhysRev.110.359. URL: https://link.aps.org/doi/10.1103/PhysRev.110.359.

[MR18] Kevin Meagher and Christoph Raab. "Search for a cumulative neutrino signal from blazar flares using IceCube data". In: *PoS* ICRC2017 (2018), p. 957. DOI: 10.22323/1.301.0957.

[MGH98] Gustavo A. Medina-Tanco, Elisabete M. de Gouveia Dal Pino, and Jorge E. Horvath. "Deflection of ultrahigh-energy cosmic rays by the galactic magnetic field: From the sources to the detector". In: *Astrophys. J.* 492 (1998), p. 200. DOI: 10.1086/305044. arXiv: astro-ph/9707041 [astro-ph].

[MRT17] Philipp Mertsch, Mohamed Rameez, and Irene Tamborra. "Detection prospects for high energy neutrino sources from the anisotropic matter distribution in the local universe". In: *JCAP* 1703.03 (2017), p. 011. DOI: 10.1088/1475-7516/2017/03/011. arXiv: 1612.07311 [astro-ph.HE].

[Mes14] P. Meszaros. "Ultra-high Energy Cosmic Rays and Neutrinos from Gamma-Ray Bursts, Hypernovae and Galactic Shocks". In: *Nuclear Physics B - Proceedings Supplements* 256-257 (2014). Cosmic Ray Origin – Beyond the Standard Models, pp. 241–251. ISSN: 0920-5632. DOI: https://doi.org/10.1016/j.nuclphysbps.2014.10.028.

[Mes17] P. Meszaros. "Astrophysical Sources of High Energy Neutrinos in the IceCube Era". In: *Ann. Rev. Nucl. Part. Sci.* 67 (2017), pp. 45–67. DOI: 10.1146/annurev-nucl-101916-123304. arXiv: 1708.03577 [astro-ph.HE].

[Mos03] Igor V. Moskalenko. "Cosmic ray propagation and acceleration". In: *Proceedings, 28th International Cosmic Ray Conference (ICRC 2003): Tsukuba, Japan, July 31-August 7, 2003*. 2003, pp. 183–204. arXiv: astro-ph/0405532 [astro-ph].

[MNF11] C. G. Mundell, N. Nagar, and P. Ferruit. "Radio-Quiet AGN and the Transient Radio Sky". In: *ArXiv e-prints* (Feb. 2011). arXiv: 1102.3039 [astro-ph.CO].

[Mur15] Kohta Murase. "On the Origin of High-Energy Cosmic Neutrinos". In: *AIP Conf. Proc.* 1666 (2015), p. 040006. DOI: 10.1063/1.4915555. arXiv: 1410.3680 [hep-ph].

[Net15] H. Netzer. "Revisiting the Unified Model of Active Galactic Nuclei". In: ARA&A 53 (Aug. 2015), pp. 365–408. DOI: 10.1146/annurev-astro-082214-122302. arXiv: 1505.00811.

[Neu06] Till Neunhoffer. "Estimating the angular resolution of tracks in neutrino telescopes based on a likelihood analysis". In: *Astropart. Phys.* 25 (2006), pp. 220–225. DOI: 10.1016/j.astropartphys.2006.01.002. arXiv: astro-ph/0403367 [astro-ph].

[Ney37] J. Neyman. "Outline of a Theory of Statistical Estimation Based on the Classical Theory of Probability". In: *Philosophical Transactions of the Royal Society of London. Series A, Mathematical and Physical Sciences* 236.767 (1937), pp. 333–380. ISSN: 00804614. URL: http://www.jstor.org/stable/91337.

[NX18] Hans Martin Niederhausen and Yiqian Xu. "High Energy Astrophysical Neutrino Flux Measurement Using Neutrino-induced Cascades Observed in 4 Years of IceCube Data". In: *PoS* ICRC2017 (2018), p. 968. DOI: 10.22323/1.301.0968.

[ODe+10] S. L. O'Dell et al. "High-resolution x-ray telescopes". In: *Adaptive X-Ray Optics*. Vol. 7803. Proc. SPIE. Aug. 2010, 78030H. DOI: 10.1117/12.862315. arXiv: 1010.4892 [astro-ph.IM].

[Oli15] Travis E. Oliphant. *Guide to NumPy*. 2nd. USA: CreateSpace Independent Publishing Platform, 2015. ISBN: 9781517300074.

[Pat+16] C. Patrignani et al. "Review of Particle Physics". In: *Chin. Phys.* C40.10 (2016), p. 100001. DOI: 10.1088/1674-1137/40/10/100001.

[RW13] Leif Rädel and Christopher Wiebusch. "Calculation of the Cherenkov light yield from electromagnetic cascades in ice with Geant4". In: *Astroparticle Physics* 44 (2013), pp. 102–113. ISSN: 0927-6505. DOI: https://doi.org/10.1016/j.astropartphys.2013.01.015.

[Rei18] Rene Reimann. "Search for point-like sources in the astrophysical muon neutrino flux with IceCube". In: *PoS* ICRC2017 (2018), p. 997. DOI: 10.22323/1.301.0997.

[Sem99] Kenneth R. Sembach. "The far ultraviolet spectroscopic explorer: mission overview and prospects for studies of the interstellar medium and high velocity clouds". In: *ASP Conf. Ser.* 166 (1999), p. 243. arXiv: astro-ph/9811314 [astro-ph].

[SMM16] Nicholas Senno, Kohta Murase, and Peter Mészáros. "Choked jets and low-luminosity gamma-ray bursts as hidden neutrino sources". In: *Phys. Rev. D* 93 (8 Apr. 2016), p. 083003. DOI: 10.1103/PhysRevD.93.083003.

[Sio63] M. Siotani. *Tolerance Regions for a Multivariate Normal Population*. Tech. rep. Stanford University, Stanford, California, 1963. URL: https://statistics.stanford.edu/sites/default/files/OLK%20NSF%2005.pdf.

[SW09] P Sommers and S Westerhoff. "Cosmic ray astronomy". In: *New Journal of Physics* 11.5 (2009), p. 055004. URL: http://stacks.iop.org/1367-2630/11/i=5/a=055004.

[Str+09] A. W. Strong et al. "The GALPROP Cosmic-Ray Propagation Code". In: *ArXiv e-prints* (July 2009). arXiv: 0907.0559 [astro-ph.HE].

[Tib12] O. Tibolla. "Recent Results from the MAGIC Telescopes". In: *Astroparticle, Particle, Space Physics and Detectors For Physics Applications - Proceedings of the 13th ICATPP Conference., 2012*. Ed. by S. Giani and et al. World Scientific, Aug. 2012, pp. 194–203. ISBN: 9789814405072. DOI: 10.1142/9789814405072_0030. arXiv: 1201.2295 [astro-ph.HE].

[UP95] C. Megan Urry and Paolo Padovani. "Unified schemes for radio-loud active galactic nuclei". In: *Publ. Astron. Soc. Pac.* 107 (1995), p. 803. DOI: 10.1086/133630. arXiv: astro-ph/9506063 [astro-ph].

[Wer+04] M. W. Werner et al. "The Spitzer Space Telescope mission". In: *Astrophys. J. Suppl.* 154 (2004), pp. 1–9. DOI: 10.1086/422992. arXiv: astro-ph/0406223 [astro-ph].

[Wie09] C. for the IceCube Collaboration Wiebusch. "Physics Capabilities of the IceCube DeepCore Detector". In: *ArXiv e-prints* (July 2009). arXiv: 0907.2263 [astro-ph.IM].

[Wil38] S. S. Wilks. "The Large-Sample Distribution of the Likelihood Ratio for Testing Composite Hypotheses". In: *Annals Math. Statist.* 9.1 (1938), pp. 60–62. DOI: 10.1214/aoms/1177732360.

[WT09] Alwyn Wootten and A. Richard Thompson. "The Atacama Large Millimeter/submillimeter Array". In: *IEEE Proc.* 97 (2009), p. 1463. DOI: 10.1109/JPROC.2009.2020572. arXiv: 0904.3739 [astro-ph.IM].

[Xia+16] Di Xiao et al. "High-Energy Neutrino Emission from White Dwarf Mergers". In: *Astrophys. J.* 832.1 (2016), p. 20. DOI: 10.3847/0004-637X/832/1/20. arXiv: 1608.08150 [astro-ph.HE].

[Yan+12] Yang, R.-Z. et al. "Deep observation of the giant radio lobes of Centaurus A with the Fermi Large Area Telescope". In: *A&A* 542 (2012), A19. DOI: 10.1051/0004-6361/201118713.

[YT14] S. Yasutomi and T. Tanaka. "Parameter estimation for von Mises-Fisher mixture model via Gaussian distribution". In: *Signal and Information Processing Association Annual Summit and Conference (APSIPA), 2014 Asia-Pacific*. Dec. 2014, pp. 1–5. DOI: 10.1109/APSIPA.2014.7041707.

[Yoo+17] Y. S. Yoon et al. "Proton and Helium Spectra from the CREAM-III Flight". In: *Astrophys. J.* 839.1 (2017), p. 5. DOI: 10.3847/1538-4357/aa68e4. arXiv: 1704.02512 [astro-ph.HE].

[YI18] Shigeru Yoshida and Aya Ishihara. "Differential limit on an EHE neutrino flux component in the presence of astrophysical background from nine years of IceCube data". In: *PoS* ICRC2017 (2018), p. 975. DOI: 10.22323/1.301.0975.

List of figures

2.1. Neutrino source constraints and unified AGN model. 6

3.1. Schematic view of the IceCube detector 9
3.2. Two event displays from very high energy events 12

4.1. High energy starting event veto region 15
4.2. Skymap of all 22 HESE positions with season information 16
4.3. Likelihood reconstruction map before and after smoothing 18
4.4. Likelihood reconstruction map truncation after smoothing 20
4.5. Muon and neutrino contributions to the test data set 21
4.6. HESE decorrelation for IC86, 2015 24

6.1. Background PDFs per source per sample for the time-dependent analysis . 52
6.2. Energy PDFs for the time-dependent analysis 54
6.3. Background test statistics for the time windows 1, 2 and 3 62
6.4. Background test statistics for the time windows 19, 20 and 21 63
6.5. Performance fluences for each time window 69
6.6. Time-dependent differential performances 71
6.7. Connection between pre-trial and post-trial significances 76
6.8. Experimental result for the time-dependent analysis 76

7.1. Background PDFs per source per sample for the time-integrated analysis . 82
7.2. Energy PDF for the time-integrated analysis for IC79 83
7.3. Differential performance of the time-integrated analysis 88
7.4. Experimental result of the time-integrated analysis 90

8.1. Neyman plane for the time-dependent analysis 91
8.2. Fluence limits for each time windows for the time-dependent analysis . . . 92
8.3. Unbroken power-law fluence limits for the largest time window 93
8.4. Neyman plane for the time-integrated analysis 95
8.5. 2D LLH scan of n_S and γ for the time-integrated analysis 96
8.6. Time-integrated analysis global power-law limits $\gamma_{\text{inj}} = 3$ 98

B.1. Combined Likelihood skymap of the 22 HES events 107
B.2. Effective areas and $\sin(\delta_\nu)$ distributions 108

B.3. HESE decorrelation for IC79, IC86'11 and IC86'12–'14 109
B.4. Parameter splines for the sine rate model per sample 110
B.5. Total run rates and sine models for all samples 111
B.6. Source stacking weights for the time-dependent analysis 111
B.7. Rate models per bin for sample IC79 112
B.8. Rate models per bin for sample IC86, 2011 113
B.9. Rate models per bin for sample IC86, 2012–2014 114
B.10. Rate models per bin for sample IC86, 2015 115
B.11. KS test results for the independent BG trials 116
B.12. Sampling from a healpy map for the signal source injection 116
B.13. χ^2 CDF fits per time window for the analysis performance 117
B.14. Background-only test statistics for the time windows 4, 5 and 6 118
B.15. Background-only test statistics for the time windows 7, 8 and 9 119
B.16. Background-only test statistics for the time windows 10, 11 and 12 120
B.17. Background-only test statistics for the time windows 13, 14 and 15 121
B.18. Background-only test statistics for the time windows 16, 17 and 18 122
B.19. χ^2 CDF fits for the 1st time window differential performance 125
B.20. χ^2 CDF fits for the 2nd time window differential performance 126
B.21. χ^2 CDF fits for the 3rd time window differential performance 127
B.22. χ^2 CDF fits for the 4th time window differential performance 128
B.23. χ^2 CDF fits for the 5th time window differential performance 129
B.24. χ^2 CDF fits for the 6th time window differential performance 130
B.25. χ^2 CDF fits for the 7th time window differential performance 131
B.26. χ^2 CDF fits for the 8th time window differential performance 132
B.27. χ^2 CDF fits for the 9th time window differential performance 133
B.28. χ^2 CDF fits for the 10th time window differential performance 134
B.29. χ^2 CDF fits for the 11th time window differential performance 135
B.30. χ^2 CDF fits for the 12th time window differential performance 136
B.31. χ^2 CDF fits for the 13th time window differential performance 137
B.32. χ^2 CDF fits for the 14th time window differential performance 138
B.33. χ^2 CDF fits for the 15th time window differential performance 139
B.34. χ^2 CDF fits for the 16th time window differential performance 140
B.35. χ^2 CDF fits for the 17th time window differential performance 141
B.36. χ^2 CDF fits for the 18th time window differential performance 142
B.37. χ^2 CDF fits for the 19th time window differential performance 143
B.38. χ^2 CDF fits for the 20th time window differential performance 144
B.39. χ^2 CDF fits for the 21st time window differential performance 145
B.40. Signal split weights for the time-integrated analysis 146
B.41. Injected signal events for the time-integrated diff. performance fluxes . . . 146
B.42. Energy PDF for the time-integrated analysis for IC86, 2011 147
B.43. Energy PDF for the time-integrated analysis for IC86, 2012–2014 148

B.44. Energy PDF for the time-integrated analysis for IC86, 2015 149
B.45. Background test statistic for the time-integrated analysis 150
B.46. Signal strength and spectral index distribution for background trials . . . 150
B.47. χ^2 CDF fits for the time-integrated diff. performance, $\gamma_{\text{inj}} = 2$ – part 1 . . 151
B.48. χ^2 CDF fits for the time-integrated diff. performance, $\gamma_{\text{inj}} = 2$ – part 2 . . 152
B.49. χ^2 CDF fits for the time-integrated diff. performance, $\gamma_{\text{inj}} = 3$ – part 1 . . 153
B.50. χ^2 CDF fits for the time-integrated diff. performance, $\gamma_{\text{inj}} = 3$ – part 2 . . 154
B.51. Differential performance weights for the largest time window 157
B.52. Time-dependent analysis upper limit scan for spectral indices 157
B.53. Splines for Neyman interval construction in the time-integrated analysis . 158
B.54. Time-integrated analysis differential upper limits 158
B.55. Differential performance weights for $\gamma_{\text{inj}} = 2$ 159
B.56. Differential performance weights for $\gamma_{\text{inj}} = 3$ 159
B.57. Time-integrated analysis global power-law limits 160

List of tables

4.1. Times and angular positions for the 22 HESE events 19
4.2. Number of events in the test datasets 22

6.1. Time window ranges used in the time-dependent analysis 56
6.2. Pre-trial results of the time-dependent analysis 77

B.1. Differential performance fluence values per time window – Part 1 123
B.2. Differential performance fluence values per time window – Part 2 124
B.3. Time-integrated diff. performance flux values per bin, $\gamma_{\text{inj}} = 2$ 155
B.4. Time-integrated diff. performance flux values per bin, $\gamma_{\text{inj}} = 3$ 156